



COMPUTATIONS ON FULLERENES: FINDING RULES, IDENTIFYING PRODUCTS AND DISCLOSING REACTION PATHS

Núria Alegret Ramon

Dipòsit Legal: T 1234-2014

ADVERTIMENT. L'accés als continguts d'aquesta tesi doctoral i la seva utilització ha de respectar els drets de la persona autora. Pot ser utilitzada per a consulta o estudi personal, així com en activitats o materials d'investigació i docència en els termes establerts a l'art. 32 del Text Refós de la Llei de Propietat Intel·lectual (RDL 1/1996). Per altres utilitzacions es requereix l'autorització prèvia i expressa de la persona autora. En qualsevol cas, en la utilització dels seus continguts caldrà indicar de forma clara el nom i cognoms de la persona autora i el títol de la tesi doctoral. No s'autoritza la seva reproducció o altres formes d'explotació efectuades amb finalitats de lucre ni la seva comunicació pública des d'un lloc aliè al servei TDX. Tampoc s'autoritza la presentació del seu contingut en una finestra o marc aliè a TDX (framing). Aquesta reserva de drets afecta tant als continguts de la tesi com als seus resums i índexs.

ADVERTENCIA. El acceso a los contenidos de esta tesis doctoral y su utilización debe respetar los derechos de la persona autora. Puede ser utilizada para consulta o estudio personal, así como en actividades o materiales de investigación y docencia en los términos establecidos en el art. 32 del Texto Refundido de la Ley de Propiedad Intelectual (RDL 1/1996). Para otros usos se requiere la autorización previa y expresa de la persona autora. En cualquier caso, en la utilización de sus contenidos se deberá indicar de forma clara el nombre y apellidos de la persona autora y el título de la tesis doctoral. No se autoriza su reproducción u otras formas de explotación efectuadas con fines lucrativos ni su comunicación pública desde un sitio ajeno al servicio TDR. Tampoco se autoriza la presentación de su contenido en una ventana o marco ajeno a TDR (framing). Esta reserva de derechos afecta tanto al contenido de la tesis como a sus resúmenes e índices.

WARNING. Access to the contents of this doctoral thesis and its use must respect the rights of the author. It can be used for reference or private study, as well as research and learning activities or materials in the terms established by the 32nd article of the Spanish Consolidated Copyright Act (RDL 1/1996). Express and previous authorization of the author is required for any other uses. In any case, when using its content, full name of the author and title of the thesis must be clearly indicated. Reproduction or other forms of for profit use or public communication from outside TDX service is not allowed. Presentation of its content in a window or frame external to TDX (framing) is not authorized either. These rights affect both the content of the thesis and its abstracts and indexes.

Núria Alegret Ramon

Computations on Fullerenes: Finding Rules, Identifying Products and Disclosing Reaction Paths

PhD Thesis

Supervised by

Dr. Antonio Rodríguez Fortea and Prof. Josep Maria Poblet Rius

Grup de Química Quàntica
Departament de Química Física i Inorgànica



UNIVERSITAT ROVIRA I VIRGILI

Tarragona, June 2014

UNIVERSITAT ROVIRA I VIRGILI

COMPUTATIONS ON FULLERENES: FINDING RULES, IDENTIFYING PRODUCTS AND DISCLOSING REACTION PATHS

Núria Alegret Ramon

DL: T 1234-2014



Departament de Química Física i Inorgànica

Antonio Rodríguez Fortea, Professor Agregat del Departament de Química Física i Inorgànica de la Universitat Rovira i Virgili, i Josep Maria Poblet Rius, Catedràtic del Departament de Química Física i Inorgànica de la Universitat Rovira i Virgili

Fem constar que la present memoria, titulada

“Computations on Fullerenes: Finding Rules, Identifying Products and Disclosing Reaction Paths”

ha estat realitzada sota la nostra direcció al Departament de Química Física i Inorgànica de la Universitat Rovira i Virgili per Núria Alegret Ramon per a l’obtenció del títol de Doctor i que aconsegueix els requeriments per poder optar a la Menció Internacional.

Tarragona, 27 de Juny de 2014

Els directors de la tesi doctoral

Antonio Rodríguez Fortea

Josep Maria Poblet Rius

*A la Maria, la Blanca i l'Aina.
I en especial al Martu.*

Contents

CHAPTER 1. Fullerene Symphony

1.1. Bucky won the Prize	3
1.2. Knowing about the fullerene cages.....	6
1.3. Not all the fullerenes exist	9
1.2.1. The Isolated Pentagon Rule (IPR)	10
1.2.2. Breaking the Rules: the non-IPR cages.....	11
1.4. The magic of endohedral fullerenes	12
1.3.1. Pure metal clusters: M, M ₂ and M ₃	14
1.3.2. M ₃ N cluster: metallic nitrides.....	14
1.3.3. Metallic carbides, oxides and sulfides	15
1.5. Reactivity of EMFs.....	17
1.6. Potential applications of endofullerenes	19
1.7. Bibliography	21

CHAPTER 2. Aims & Scopes of this Thesis 29

CHAPTER 3. Models of Prediction

3.1. Introduction	35
3.1.1. The Ionic Model.....	36
3.1.2. Orbital Rule	37
3.1.3. The Inverse Pentagon Separation Index (IPSI).....	38
3.2. Computational Details.....	40
3.3. Maximum Pentagon Separation Rule	41
3.3.1. Stability and localization of the charge density	41
3.3.2. Non-IPR cages and the pyracylene motif	46

3.3.1. The icosahedral symmetry: the most favorable charge distribution in an anion.....	51
3.4. Connecting Orbital and Topological Rules.....	52
3.4.1. IPSI: a measure for the size and topology of the cages	52
3.4.2. Orbital and topological rules: is there a connection?.....	54
3.4.3. IPR versus non-IPR cages: the importance of the charge transfer.....	56
3.5. Conclusions	57
3.6. Bibliography.....	59

CHAPTER 4. Looking for the identity of the first non-IPR $Sc_2@C_{66}$

4.1. Discrepancies in the cage assignments	65
4.2. Computational details.....	67
4.3. Looking for the empty anionic cage.....	68
4.3.1. The 4478 isomers of C_{66}^{6-}	68
4.3.2. The carbide option: evaluation of C_{64}^{4-}	70
4.4. The endohedral fullerene.....	72
4.4.1. Relative stabilities and electronic structures of the lowest-energy EMFs	72
4.4.2. The effect of the temperature	77
4.4.3. Computational clues: predicted IR and ^{45}Sc -NMR.....	77
4.5. Conclusions	79
4.6. Bibliography.....	80

CHAPTER 5. Bingel-Hirsch Reaction on Nitride EMFs

5.1. A cyclopropanation reaction	86
5.1.1. Insights into the stationary points of the reaction	87
5.2. Computational Details	88
5.3. Addition on $Sc_3N@I_h-C_{80}$.....	89
5.3.1. Description of the system	89
5.3.2. Thermodynamics: rotation of the Sc_3N cluster in products	90
5.3.3. Step 1: intermediates formation	92
5.3.4. Step 2: going through a TS	94

5.4. Addition on $\text{Sc}_3\text{N}@D_3\text{-}^{6140}\text{C}_{68}$	96
5.4.1. Description of the system	97
5.4.2. Thermodynamics: analysis of products.....	98
5.4.3. Step 1: intermediates formation.....	99
5.4.4. Step 2: going through a TS	100
5.4.5. Looking for a "cheaper" methodology: test study for the Bingel-Hirsch reaction on $\text{Sc}_3\text{N}@C_{68}$	103
5.5. Addition on $\text{Gd}_3\text{N}@C_{2n}$ (2n=82 and 84)	105
5.5.1. Description of the systems	106
5.5.2. Thermodynamics: Rotation of the Gd_3N cluster in products	109
5.5.3. Steps 1 & 2: analysis of reaction path study.....	116
5.6. Conclusions	121
5.7. Bibliography	123

CHAPTER 6. Prato Reaction on C_{60}

6.1. Introduction	129
6.2. Methods	131
6.2.1. Experimental strategy.....	131
6.2.2. Computational details	132
6.3. Synthesis and characterization	132
6.3.1. Experimental section	132
6.3.2. Thermodynamic and kinetic aspects	136
6.4. Isomerization from 1 to 2	140
6.5. Conclusions	143
6.6. Bibliography	145

CHAPTER 7. Concluding Remarks

151

CHAPTER 8. Annexes

Annex A. Cage Dilemma with $\text{Sc}_2@C_{66}$	157
Annex B. Bingel-Hirsch Reaction on EMFs	163

Annex C. Prato Reaction on C₆₀	177
--	------------

Résumé

Publications	191
---------------------------	------------

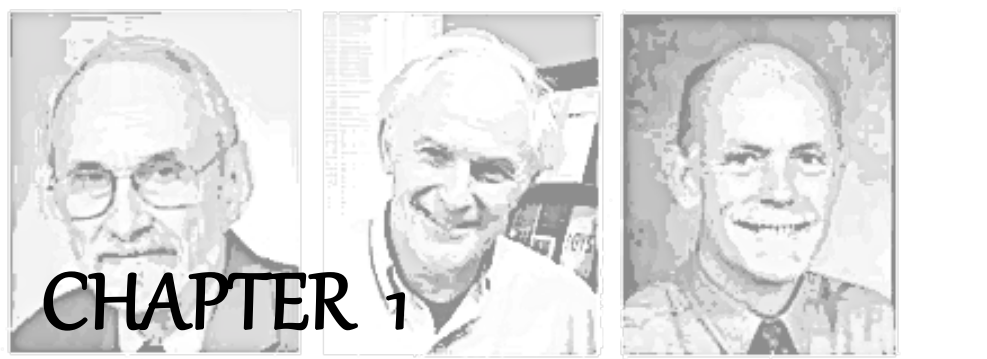
Posters and Presentations	193
--	------------

Collaborations and Research Abroad	194
---	------------

Notes and Comments	195
---------------------------------	------------

Symbols and acronyms

AM1	Austin Model 1
APP	Adjacent Pentagon Pair
BP86	Becke-Perdew 86 functional
B3LYP	Becke 3-Parameter (exchange), Lee, Yang and Parr (correlation)
COSMO	Conductor-like Screening Model
DFT	Density Functional Theory
EMF	Endohedral Metallofullerene
HOMO	Highest-Occupied Molecular Orbital
IPSI	Inverse Pentagon Separation Index
LUMO	Lowest-Unoccupied Molecular Orbital
MEP	Molecular Electrostatic Potential
M06	Minnesota functional 06
o-DCB	<i>ortho</i> -dichlorobenzene
PCM	Polarizable Continuum Model
PES	Potential Electrostatic Surface
SMD	Solvation Model based on the quantum mechanical charge Density



Fullerene Symphony

CHAPTER 1

Fullerene Symphony

Fullerenes are young molecules – only two years older than me! – and during the last four years have become the main reason I lost sleep. They were discovered accidentally and have a lot of special characteristics that made them useful in medicine and solar cells technology. Fullerenes research is not an easy path, but I wish that all the effort done will be compensated in a near future so we will all know the fullerene as the “molecule that made a better world”.

1.1. Bucky won the Prize

“The story of the discovery of C_{60} Buckminsterfullerene and the birth of Fullerene Science consists of several disparate strands which came together over ten days in September 1985.” That’s how sir Harold W. Kroto began his Nobel Lecture when he received the Nobel Prize in Chemistry in 1996, together with his colleagues Robert F. Curl and Richard E. Smalley. The first strand he referred to emerged at University of Sussex (Brighton, Great Britain), where Kroto discovered long carbon chains in the interstellar medium and aimed to reproduce the conditions of carbon nucleation at the red giant stars. Meanwhile at Rice University (Houston, Texas), Smalley developed a new machine able to generate clusters from solids by laser vaporization and subsequently analyze them by mass spectrometry. Fortune wants Curl in the middle of the story as the connection between Rice and Sussex, so the three scientists, in collaboration with Jim Heath and Sean O’Brien, spent ten days

at Rice University experimenting with graphite in Smalley's machine to accomplish Kroto's idea. Surprisingly, the resultant mass spectra showed two unexpected peaks with the highest intensity corresponding to 60 and 70 carbon atoms. The group could even optimize the experimental conditions in order to obtain a single signal 50 times more intense than the other ones, thus recording C_{60} for the first time.^[1] Their chemical intuition was enough to elucidate the spherical shape of the new molecule and its icosahedral symmetry. The scientists gave to the new molecule the name of *Buckminsterfullerene*, due to its similarity with the geodesic domes constructed by the architect Richard Buckminster Fuller (Figure 1.1). Later, the name became simply **fullerene**.



Figure 1.1. Left: Montreal's Biosphere Environmental Museum (Canada) resides inside a Geodesic Dome designed by R. Buckminster Fuller.^[2] Right: C_{60} fullerene representation.

Before the fullerene discovery, only two allotropic forms of carbon were known: diamond and graphite. Previous little theoretical studies had predicted the new allotrope of carbon although they remained in the background until the huge discovery. In 1966, D. E. H. Jones conjectured that if pentagonal defects could be introduced between the hexagons in a graphene sheet, such a sheet would close into a hollow balloon. Four years later, E. Osawa described computationally the C_{60} molecule as a stable species with the same structural pattern as a soccer ball – one pentagon surrounded by five hexagons. Gal'pem calculated such molecule concluding that it should be a closed shell system with a relatively high-energy gap between the HOMO (Highest Occupied Molecular Orbital) and the LUMO (Lowest Unoccupied Molecular Orbital). However, none of the studies predicted that the 60-carbon atoms molecule would be spontaneously synthesized from carbon vapor condensation.

Fullerenes are empty spheres with an internal radius between 4 – 10 Å. They have the intrinsic property of "storing" any molecule or atom small enough to fit inside the hole. Already in the first experiments, the scientists detected the presence of

La encapsulated inside C_{60} , which was named as $La@C_{60}$.^[3] The following years, many other atoms and molecules up to 7 atoms appeared captured inside a fullerene cage.^[4] This new family was known as **endohedral fullerenes** or **endofullerenes**.^[5] The IUPAC defined their name as $[2n]\text{fullerene-}inrar\text{-}M$, abbreviated as iMC_{2n} ; nevertheless, such complicated nomenclature is not commonly used. The first endohedral isolated was $La@C_{82}$ in 1991, but the most abundant endohedral and the third most abundant fullerene is $Sc_3N@I_h\text{-}C_{80}$. S. Stevenson and H. C. Dorn discovered it in 1999,^[6] and quickly became the first of a new family of endohedral fullerenes known as **endohedral metallofullerenes** or **EMFs**. Only EMFs with metals of groups 2, 3 and 4 are obtained in macroscopic amounts,^[7] although not all of them in enough yields to be fully characterized. From then on, any study related to endohedral metallofullerenes gained the first position in the fullerene science due to their novel chemical and physical properties, never seen in other fullerene families, that confer them high potential for applications in medicine and material science.^[5b]

Fullerene synthesis and extraction in large amounts was also accidentally achieved. Krätschmer and Huffman were trying to create interstellar rubbish by graphite vaporization under helium atmosphere. Just like the Rice experiments, the two German scientists observed the C_{60} formation by IR techniques. But then, they were able to purify it by benzene extractions and obtain around 1% of fullerene yield from the soot. Nowadays, C_{60} is sold commercially, although the production of large amounts of other fullerenes is still a pending job. In research laboratories, fullerenes are synthesized with the Krätschmer-Huffman machine by the *arc-discharged method*,^[8] unofficially known as "*arc-ing*" (Figure 1.2). The resultant soot contains a large variety of hydrocarbons, nanotubes and fullerenes, so a first extraction with carbon disulfide or other similar solvent is necessary to obtain only a fullerene mixture. That mixture is composed of different empty and endohedral fullerenes; their type and yield depend on the *arc-ing* conditions. To separate and purify each isomer, advanced HPLC techniques, such as *multistage recycling*, are used. Very recently, due to the different reactivity of the cages, it has been discovered that selective oxidations/reductions can be a useful tool to separate empty from endohedral fullerenes and even endohedrals between them.^[9] Separation is the most laborious step in fullerenes research, since the working amounts are in the order of the *mg*, and careful work is required. In order to characterize the cages, mass spectrometry, cyclic voltammetry and spectroscopic techniques (UV-VIS and NMR) are used. ^{13}C -NMR reveals information about the symmetry and the composition of the system, but not about its spatial distribution; sometimes this is not a suitable technique because of the low yield of sample or the complex spectra when paramagnetic metals are present. The most powerful technique to obtain

the geometry of the isomers is X-Ray diffraction. The obstacles are found in the crystal growth, not only because it can take months but also because the high symmetry of the cages makes them indistinguishable, so highly disordered. In order to reduce the symmetry, cages are co-crystallized with metalloporphyrins, such as the *octaethylporphyrin* or *OEP*.^[10] Even so, sometimes it is impossible to obtain a suitable crystal.

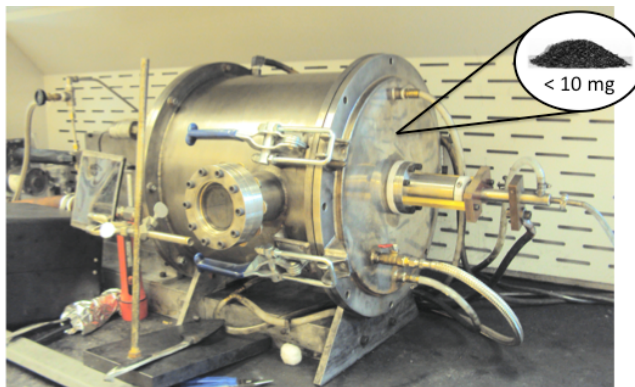


Figure 1.2. Krättschmer-Huffmann reactor or arc used for the synthesis of fullerenes. From the 100 g of soot obtained, less than 10 mg of fullerene mixture are commonly obtained.

Characterization of fullerenes is not a straightforward task due to the tiny amounts of product that are obtained. As a consequence, computational chemistry has become an important and additional tool to characterize fullerenes and to rationalize their structural and electronic properties. In fact, theoretical and computational chemists have been walking in parallel with experimental chemists since the birth of fullerenes in 1985.

1.2. Knowing about the fullerene cages

Carbon atoms constitute the fullerene cages C_{2n} by assembly of hexagonal and pentagonal rings. Note that we write $2n$ in the subscript since the number of atoms in the cage is always even. According to Euler's Theorem, the closure of a geometric figure of at least 24 vertices, such as fullerenes, is possible with exactly 12 pentagons within the structure. Additionally, in fullerene structures the number of hexagons increase with the size of the cage following the equation $m=(2n-20)/2$, while the number of bonds is $3n/2$. We will see during this thesis that the pentagons have the leading role for most of the chemical and physical properties of fullerenes. The first example comes with the *Isolated Pentagon Rule* or *IPR*, according

to which the most stable fullerenes are those with no pentagon adjacencies, *i. e.*, each pentagon is isolated and surrounded by hexagonal rings. Experimentally, all the empty fullerenes synthesized so far follow the IPR rule, but the C_{72} . Each C_{2n} can be drawn as much ways as different dispositions of the twelve pentagons exist. Thus, C_{60} has 1812 isomers with one IPR structure; C_{70} , 8149 with one IPR structure as well; C_{80} , 31924 isomers with 7 IPR; etc. The number of isomers both IPR and non-IPR, increases exponentially with the number of atoms of the structure, as shows Table 1.1, so it is noteworthy to mention the huge complexity of the synthesis and characterization processes of these systems. P.W. Fowler y D. E. Manolopoulos presented in their book "An Atlas of Fullerenes" the so-called spiral algorithm in order to sort all the possible isomers by numbering each one according to the relative position of the pentagons.^[11] The IPR isomers appear at the end of the list. This numbering is the one adopted in the scientific community and is the one used in this thesis for naming the cages as $^{\#isomer}C_{2n}$.

Table 1.1. Total number of isomers and IPR structures for C_{2n} families in the range $2n = 60 - 104$.

2n	#Isomers	#IPR	2n	#Isomers	#IPR
60	1,812	1	82	39,718	9
62	2,385	0	84	51,592	24
64	3,465	0	86	63,761	19
66	4,478	0	88	81,738	35
68	6,332	0	90	99,918	46
70	8,149	1	92	126,409	86
72	11,190	1	94	153,493	134
74	14,246	1	96	191,839	187
76	19,151	2	98	231,017	259
78	24,109	5	100	285,913	450
80	31,924	7	104	419,013	823

Both IPR and non-IPR fullerenes have several types of bonds, as shown in Figure 1.3, categorized according to the polyhedra that surround them. Thus, we can distinguish among [6,6] bonds – two hexagons sharing one edge –, [5,6] bonds – between one hexagon and one pentagon –, and [5,5] bonds – two fused pentagons, only present in non-IPR systems. Additionally, each group can be classified in different subgroups according to their neighbor polyhedral figures.

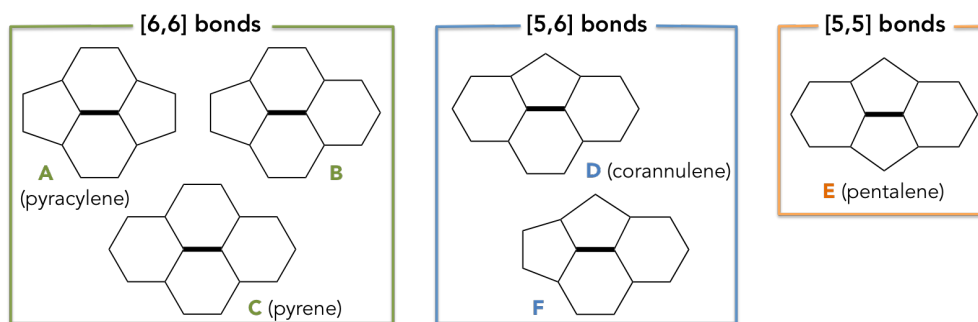


Figure 1.3. Bond types within fullerene structure.

In addition to the common nomenclature used to label each fullerene isomer, a general description of the rings dispositions, and thus the types of bonds present in fullerene net, can be obtained from the Raghavachari numbering. Raghavachari defined the k index as the number of hexagons surrounding one pentagon within the fullerene structure. By assimilation, a new index $p_k = (p_0, p_1, p_2, p_3, p_4, p_5)$ can be defined, where k represents now the number of pentagons surrounding a pentagon. For example, all the IPR isomers are described as $(12, 0, 0, 0, 0, 0)$, with the twelve pentagons surrounded only by hexagons ($k = 0$). Furthermore the Raghavachari number gives us the number of pentagonal fusions, *i. e.*, the number of [5,5] bonds that can be calculated as

$$N_p = \frac{1}{2} \sum_{k=1}^5 (k \cdot p_k) \quad (1.1)$$

The most abundant fullerene I_h-C_{60} presents the highest symmetry in nature, the icosahedral I_h . Its ^{13}C -NMR spectrum shows clearly a single signal. On the other side, the spectrum of the second most abundant fullerene $D_{5h}-C_{70}$ has 5 signals well differentiated. From the first discovery until now, hundreds of fullerenes have been characterized between 28 and 104 carbon atoms, and cages up to 418 carbon atoms have been detected.^[12] The main difference between cages is the relative position of the twelve pentagons. Additionally, the most abundant cages are intimately related: fullerene $D_{5h}-C_{70}$ can be obtained from two halves of I_h-C_{60} plus five C_2 units in the middle of them (Figure 1.4). Similarly, if twenty or thirty atoms are added instead of ten, the synthesized structures $D_{5d}\text{-}^{#1}C_{80}$ and $D_{5h}\text{-}^{#1}C_{90}$ can be obtained, respectively, as shown in Figure 1.4.^[13] Besides, isomers of the same C_{2n} family can be related by Stone-Wales isomerization, where a C_2 unit breaks two of the four bonds, then rotates 90° and links to two new atoms (Figure 1.5).

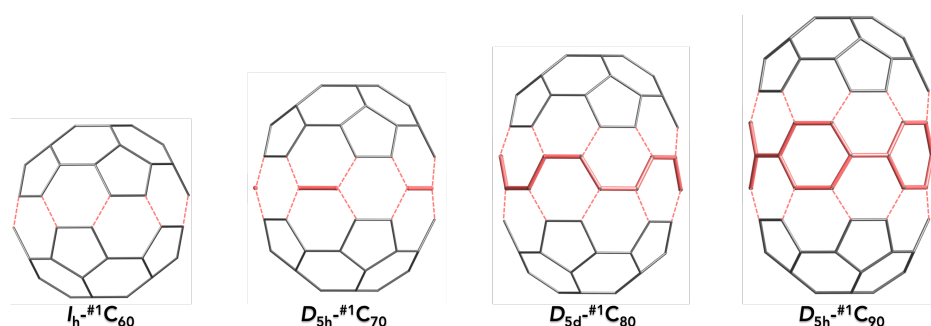


Figure 1.4. Evolution from C_{60} to C_{90} by C_2 addition in the equatorial zone. The bonds where the new atoms are added are represented with broken lines. In red, new atoms and bonds formed.

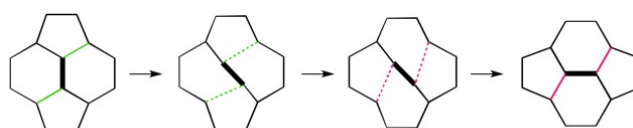


Figure 1.5. Schematic representation of the Stone-Wales isomerization. In green, bonds that are broken; in magenta, bonds that are formed.

1.3. Not all the fullerenes exist

Fullerenes are experimentally synthesized inside the reactor designed by Krätschmer and Huffman; there, graphite is vaporized in an electric arc at low pressure.^[8] During the whole process, the reactor can reach extremely high temperatures, at more than 3000K. For endohedral fullerenes, the graphite bars are filled with the pure metal or its derivate oxide, sulfide, nitride, carbide, etc., depending on the type of cluster of interest. The working conditions can be controlled in order to guide the process to the formation of specific cages. As an example, *arc*ing of scandium nitrides produces mainly C_{60} , C_{70} , $Sc_3N@C_{68}$, $Sc_3N@C_{78}$, $Sc_3N@D_{5h-#6}C_{80}$, and $Sc_3N@I_h-#7C_{80}$. Even so, what is really happening inside the arc is a mystery. Several theories about the formation mechanism of fullerenes have been published; the most significant ones is the growth via C_2 insertion proposed by Kroto,^[14] and Irlle and Morokuma.^[15] Up to date, the formation of fullerenes is one more enigma in this field waiting to be solved by the scientific community.

C_{60} is the only fullerene abundant enough to be commercialized. Since its discovery, Kroto relates its large abundance to its highest I_h symmetry. Regarding fullerene synthesis, it seems that symmetry plays an important role: C_{80} is the most

abundant endohedral cage and has also I_h symmetry; after C_{80} , the following cages with I_h symmetry are C_{180} , C_{240} , C_{320} , C_{500} , C_{540} , etc., and their characterization is expected in a near future. All these I_h fullerenes are known as the *Goldberg series*, and satisfy one of the formulas C_{60k} or C_{60k+20} ($k = 1, 2, 3, \dots$). In all cases, 12 pentagons are placed in the vertices of an icosahedron.

1.3.1. The Isolated Pentagon Rule (IPR)

Hexagons in graphene structures are connected to construct plain structures, although they can roll into tubular structures to form the nanotubes. To achieve the spherical shape of the fullerene cages, it is necessary to introduce curvature with pentagonal rings, thus generating an additional surface tension. In 1987, Kroto suggested that fused pentagons within the fullerene structure increases significantly the cage tension, as well as diminishes its stability.^[16] He explained that the lower the tension produced by pentagons, the larger the stability of the systems. So the IPR rule was defined to explain the stability of all the synthesized fullerenes, which do not contain pentagons sharing bonds since they destabilize significantly the cage.

But, how can the introduction of a pentagon produce tension to a structure formed by hexagons? In a graphene sheet, the carbon atoms have sp^2 hybridization, where π and σ orbitals are perfectly separated. Therefore, π orbitals are oriented perpendicularly to the hexagons sheet and conjugated to induce large delocalization and facile electron movement through it. When such a planarity is altered, the atoms acquire a closer sp^3 hybridization, with a lower overlapping between π orbitals and, consequently, lower electronic movement (Figure 1.6). With all this, the IPR rule can be understood as a search for the lowest tension, *i. e.*, the lower curvature of the cage to reach a structure as similar as possible to a graphene sheet, thus with larger π overlapping and resonance energy.^[17]

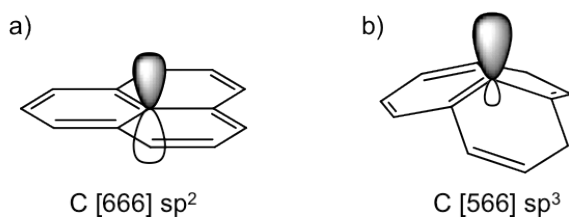


Figure 1.6. Schematic representation of the π orbitals for a) carbon [666] (surrounded by three hexagons) with sp^2 hybridization and b) carbon [566] (surrounded by two hexagons and one pentagon) with closer sp^3 hybridization.

1.3.2. Breaking the Rules: the non-IPR cages

Nowadays, all empty fullerenes discovered are IPR, except the C_{72} : the single IPR isomer D_{6d} - $^{#11190}C_{72}$ is not the most stable one, but the non-IPR C_{2v} - $^{#11188}C_{72}$, determined experimentally as Cl_4C_{72} with the chlorides bonded to the pentalene unit (Figure 1.7).^[18] Below 68 atoms, C_{60} is the only cage with an IPR isomer; as from C_{70} , every fullerene contains at least one IPR isomer.^[11] Each non-IPR fullerene isomer can be classified according to the number of *Adjacent Pentagon Pairs* or APPs present in its structure as APP1, APP2, etc. From the very beginning it was predicted that each fused pentagon pair present in the carbon structure might destabilize the structure around 17-24 kcal·mol⁻¹. Kroto explained that such a destabilization came from the local tension produced by the pentagonal fusion. On the other hand, Schmalz suggested that adjacent pentagons contain an 8π electronic structure that violates the Hückel rule ($4n+2$), hence, does not give resonance stabilization to the system.^[17]



Figure 1.7. Examples of non-IPR fullerenes discovered. *From left to right:* the first empty non-IPR, the first endohedral non-IPR and the smallest fullerene. In orange, the [5,5] pentalene units.

In the year 2000, two groups published simultaneously in the prestigious journal *Nature* the two first non-IPR endohedral structures. On one hand, Shinohara and co-workers synthesized $Sc_2@C_{66}$, with two pairs of fused pentagons,^[19] although the cage isomer is still a dilemma because the first proposal based on maximum-entropy-method (MEM)/Rietveld analyses did not match the computational results. On the other hand, Dorn and co-workers characterized $Sc_3N@C_{68}$, with three pairs of fused pentagons, as shown in Figure 1.7.^[20] From then on, up to 10 non-IPR cages have been obtained between 66 and 84 carbon atoms encapsulating metallic clusters.^[5a] Furthermore, less than 60-atom EMFs have been detected, thus being all of them perforce non-IPR structures. The $Ti@C_{26}$ and $Ti@C_{28}$ (Figure 1.7) are

the smallest fullerenes ever detected, together with the whole family $M@C_{2n}$ ($M=Ti, Zr, Hf, U; 2n = 28-46$).^[21] The encapsulation of non-metallic atoms or small molecules (N_2, H_2, H_2O) does not provide stabilization enough to invert the energies of the non-IPR isomers with respect to the IPR ones.

In summary, there are two ways to violate the IPR rule: (i) external functionalization during the synthesis process using Cl, CF_3 , etc., what guides the formation of non-IPR empty cages; (ii) encapsulation of metallic clusters that stabilize enough the non-IPR cages so as to be preferred in front of the IPR isomers.

1.4. The magic of endohedral fullerenes

Up to date, a large number of endofullerenes have been synthesized. Among them, the leading fullerene in this story is the 80-carbon cage. Not only $Sc_3N@I_h-^{#7}C_{80}$ is the third most abundant fullerene, but also the isomer that captures higher diversity of clusters. The icosahedral is not the unique isomer synthesized of 80-carbon atoms: from the seven possible IPRs, isomers **#1**, **#2** and **#5** have been obtained empty while **#3**, **#5**, **#6** and **#7** were found encapsulating metallic clusters. On the other side, the largest fullerene characterized to date is the IPR $Sm_2@D_{3d}-^{#822}C_{104}$ (Figure 1.8). It is not a coincidence that such structure is formed from two halves of $I_h-^{#7}C_{80}$ plus 24 additional carbon atoms in the middle.^[22] The mono-metallic endohedrals $Tm@C_{3v}-C_{94}$ and $Ca@C_{3v}-C_{94}$ are the second largest structurally characterized endohedral fullerenes.^[23] Anyway, both empty and endohedral fullerenes obtained from the arc are the ones with the lowest energy. Therefore, it is important to take into account the effect of the temperature during the theoretical studies since the relative stability of the cages can change drastically.

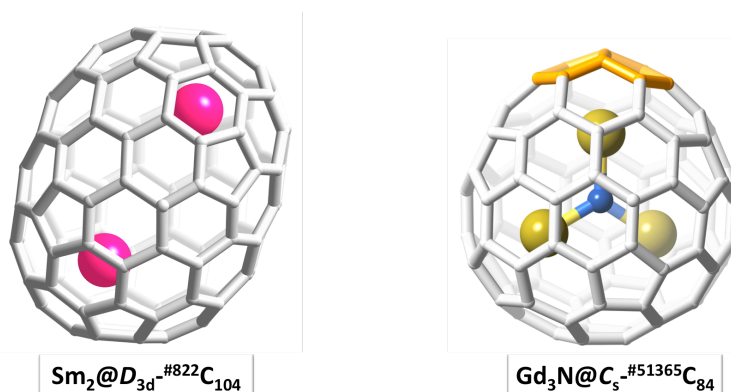


Figure 1.8. The largest IPR and non-IPR fullerenes ever found. In orange, pentagon fusion.

Inside a fullerene, one can expect any kind of atomic or molecular species that fits. From all the possibilities, the most common clusters are the **metallic** ones, and can be divided in (i) mono-, di- and trimetals,^[24] (ii) metal carbides, (iii) metal nitrides,^[25] (iv) metal oxides and (v) metal sulfides.^[5b, 10, 26] All of them are obtained *in situ* from the *arc* by addition of the pure metal or a derivate. The metal atoms are usually alkali or alkaline earth metals, from the groups 3 and 4 (Sc, Y, La, Ti), and lanthanides.^[7, 20, 27] The large list of characterized endofullerenes shows an enormous variety of isomers encapsulating different clusters, even the same host encapsulating distinct clusters or various cages capturing the same guest. The scientists have taken advantage of this fact and used particular clusters as baits to attract specific cages. However, some cages are more favorable than others to catch guests. In Chapter 3 we will consider which are the main requirements of a fullerene cage to accept metallic clusters.

The strain energy is used to determine the relative stability of empty fullerenes and the small ones. Nevertheless, EMFs include other essential factors to describe their own stability, which are (i) the charge transfer from the cluster to the cage, (ii) the electronic properties of the empty cages, (iii) the cluster and cage sizes, and (iv) the interaction between the metal center and the external skeleton, specially in the case of non-IPR cages. These new properties allow the synthesis of new endohedral cages that have never been observed as empty isomers. Examples of this are the non-IPR fullerenes synthesized, since their energies become lower than the related IPR isomers. Among them, those with less than 80 carbon atoms contain 2 or 3 pentagon-fusions, except La@C₇₂. The stabilization of those non-IPR cages is mainly consequence of the charge transfer and the strong coordination between the pentalene unit and the metals. The largest non-IPR cages discovered are APP1 type, C_s-^{#39663}C₈₂ y C_s-^{#51365}C₈₄ (Figure 1.8).^[28]

The *in situ* formation of non-metal endohedral cages is not that common. The synthesis of fullerenes require inert atmosphere inside the reactor, thus it is not difficult to imagine that some of the inert gas molecules or atoms can be trapped inside some cages; the relative abundance of that species is extremely low. For this reason, other techniques have been developed to increase the yield of this kind of endofullerenes: (i) high temperature heating at 3000 atm of the noble gas, (ii) atomic collisions, (iii) ion implantation or (iv) "molecular surgery", where the cage is chemically opened and the gas introduced. The last is the only one that gives macroscopic amounts of the non-metal endofullerene. Furthermore, ion implantation was also used to insert other non-metallic atoms or molecules, such as H, N, O, F, C, P, CO, H₂O, N₂ or HF, into C₆₀. In any case, those non-metallic clusters do not confer special properties from those of the empty classic cages.

1.4.1. Pure metal clusters: M , M_2 and M_3

Soon after the detection of the first endofullerene La@C_{60} , La was also detected inside the larger cages C_{70} , C_{72} , and C_{82} . Since then, lots of systems $M_k@C_{2n}$ ($k=1,2$) have been characterized.^[29] The smallest fullerenes ever known are of the type $M@C_{2n}$ ($M=\text{Ti, Zr, Hf, U; } 2n=26, 28$).^[21, 30] On the other side, the largest cages encapsulating mono- and dimetals are Sm@C_{90} and $\text{La}_2@D_{5h}^{450}\text{C}_{100}$.^[31] One may think that small clusters might be found inside the smallest cages, while large clusters might be destined to the largest cages. This assertion is accomplished for any type of clusters, although the pure metal ones have become a special case. La atom is one of the largest metals of the periodic table (ionic radii=1.30 Å) and is found either in small cages, as La@C_{60} , La@C_{70} , or La@C_{72} , as well as inside the largest ones, such as $\text{La}_2@D_{5h}^{450}\text{C}_{100}$.^[31b] As well, a single Sm atom, which has a similar size as La (ionic radii=1.22 Å), is found in the large cage of 90 atoms in four different IPR isomers, C_{2v}^{40} , C_{2v}^{42} , C_{2v}^{46} , and C_{2v}^{45} , all of them related by Stone-Wales transformations. Moreover, their relative abundance is directly related to their relative stability. On the other side, midsize metal atoms as Dy (radii=1.17 Å) can stabilize the largest cages too: $\text{Dy}_2@C_{100}$, $\text{Dy}_3@C_{98}$.^[32] Notice that the smaller the radii of the metal atom, the higher the number of metals needed to stabilize large cages; otherwise, small cages are stable enough to trap a single metal atom.

The metal-cage interaction, typical when fused pentagons are part of the structure, is what determines the cluster position inside the fullerene. In non-IPR fullerenes, such interaction is strong enough to move the metal cluster off-centered. Otherwise, in IPR isomers these positions are generally placed in the middle of the sphere, and can be predicted with molecular electrostatic potential (MEP) maps of the anionic cages. In the $M_2@C_{2n}$ families, the repulsion between the cluster atoms is the key point to determine their position, so they try to be as much separated as possible. Functionalized fullerenes have an additional interaction between the metal and the addition site, so the metal atoms are normally displaced to the derivatized region.

1.4.2. M_3N Cluster: metallic nitrides

This type of fullerenes was usually known as *Trimetallic Nitride Templates* or *TNT*. This name was given by Dorn when he discovered $\text{Sc}_3\text{N@C}_{80}$ in 1999,^[6] which became the first *TNT* and the most abundant endofullerene until now. Similarly, other endohedral cages between 68 and 96 atoms have been synthesized, among which stands $\text{Sc}_3\text{N@C}_{2v}^{7854}\text{C}_{70}$ as the first non-IPR of 70 carbon atoms.^[33] In order to increase the yield of the *TNT* species in the soot, Dunsch introduced NH_3 as reactive

gas inside the reactor.^[34] In general, endofullerenes are obtained with a relative abundance around 2%, and Sc₃N@C₈₀ among 3-5%.

The cage par excellence with which more endofullerenes have been obtained is I_h-C₈₀. All M₃N clusters inside it remain flat and rotate freely, except Gd₃N that is pyramidalized due to the larger size of the nitrides – note that Gd₂ScN and GdSc₂N clusters do stay flat.^[35] In cages with less than 80 atoms the M₃N rotation can be restricted either because the size of the sphere is too small, as the IPR D_{3h}-^{#5}C₇₈, or because of the structural topology of the non-IPR isomers – the pentalene unit interacts strongly with the metal atoms and confines significantly their movement. The most clear example comes with Sc₃N@D₃-^{#6140}C₆₈ (Figure 1.7): the structure is APP3 with each of the three [5,5] bonds in the vertexes of an equilateral triangle, what fits perfectly with the triangular shape of the cluster; each pentalene is then strongly linked to one Sc atom, so the cluster motion is forbidden.^[20] In addition, this is the smallest cage where a M₃N unit is trapped.

The formation of a specific isomer can be determined by the nature of a cluster: the size of the metal atoms controls the size of the host cage. For instance, Sc₃N is only encapsulated in small and midsize cages as D₃-^{#6140}C₆₈, D_{3h}-^{#5}C₇₈, I_h-^{#1}C₈₀, D_{5h}-^{#6}C₈₀. Otherwise, Gd₃N is the largest cluster found inside C₈₀; together with Nd, Pr and Ce, these clusters are preferentially found inside larger cages between 78 and 88 atoms. Note that D_{3h}-^{#5}C₇₈ has less inner space than C₂-^{#22010}C₇₈, so Sc can be trapped in the first isomer while the second one catches Gd. Finally, the largest M₃N cluster, La₃N, is captured inside the largest fullerene cages, such as C₈₈, C₉₂, and C₉₆.^[36] Besides, the abundance of each endofullerene decreases when the atomic radii of the metal atoms increases. Poblet and co-workers have defined the encapsulation energy or *Binding Energy* (BE) of the systems that correlates with their relative abundance:^[37]

$$BE = E_{EMF} - (E_{M_3N} + E_{C_{2n}}) \quad (1.2)$$

In such a way it is possible to compare the relative stability between endofullerenes of different C_{2n} families and predict which system will be the most abundant one.

1.4.3. Metallic carbides, oxides and sulfides

The carbides are the most difficult endofullerenes to characterize, since the carbon atoms of the cluster can be easily mixed up with the external ones. Most of the carbides found are of the type M_xC₂@C_{2n} (x=2 – 4),^[38] and were initially described

as $M_x@C_{2n+2}$, until X-ray or DFT techniques redefined them.^[29] The most common metals forming the carbides are scandium and yttrium. The first identified carbide was $Sc_2C_2@D_{2d}-C_{84}$, and was initially described as $Sc_2@C_{86}$.^[39] Nowadays, it is common to take into account the carbide option during the characterization process of a new endohedral fullerene.

M_2C_2 clusters usually appear butterfly-shaped and have free rotation inside the cage, such as the metal carbide Gd_2C_2 encapsulated in $D_{3h}-C_{92}$.^[40] Larger carbides clusters present several structures, like Sc_3C_2 , which has been detected in two different conformations: planar and trifoliate.^[41] The most original cluster is the $Sc_4C_2@C_{80}$, described as a Russian doll with free motion where the C_2 unit lays inside the tetrahedron formed by Sc_4 : $C_2@Sc_4@C_{80}$ (Figure 1.9).^[42]

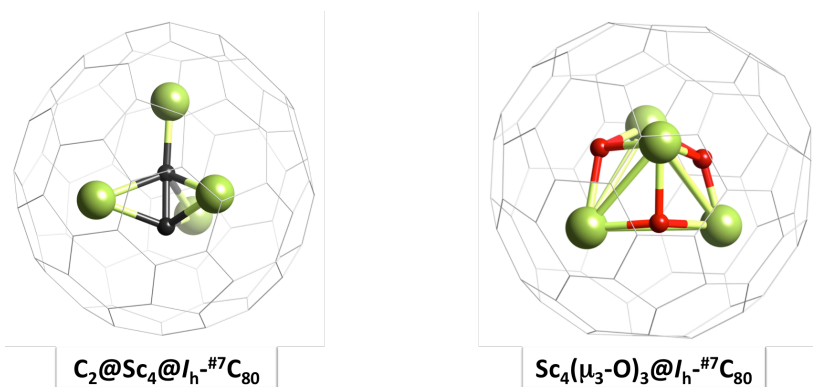


Figure 1.9. Left: carbide endofullerene with a Russian doll cluster. Right: endofullerene containing the largest cluster ever found.

From all the known encapsulated clusters inside fullerene cages, $Sc_4(\mu_3-O)_3@C_{80}$ is the largest one ever found (see Figure 1.9).^[43] Even so, this cluster has unrestricted motion inside the cage, as well as its smaller version $Sc_4(\mu_3-O)_2$.^[44] Any of the two structures are constructed with Sc atoms forming a tetrahedron and the oxygen atoms placed at two or three of its faces. Other oxides found follow the formula $M_2O@C_{82}$.^[45]

Endohedral sulfides are the most recent endofullerenes discovered. The number of isomers and cages of this new family $M_2S@C_{2n}$ increases every day.^[46] Very recently, the compound $Ti_2S@C_{78}$ has been characterized, and it was shown that the cage with the sulfur atom was able to oxidize two Ti-atoms to their highest oxidation state Ti(IV).^[47]

To end with this section, I would like to mention the unique hydrocarbon cluster found $\text{Sc}_3\text{CH@C}_{80}$,^[48] synthesized by the addition of methane gas inside the reactor, and the cyanofullerenes $\text{Sc}_3\text{CN@C}_{80}$ and $\text{Sc}_3\text{CN@C}_{78}$.^[49]

1.5. Reactivity of EMFs

Once the fullerene is obtained, its major limitation is the low solubility, so it is complicated to directly use them in any application. For this reason, exohedral functionalization is a key step to obtain new materials for multiple applications and has been studied from the beginning to take maximum benefit from these novel molecules. In medicine, for instance, water-soluble gadofullerenes are used as powerful contrast agents.^[50] Moreover, derivatization has also become an essential tool to purify and separate fullerene mixtures.^[51] Fullerenes are more reactive than the planar aromatic systems, since the covalent exohedral bond reduces the surface tension produced by pyramidalization of the atoms and gives additional stability to the entire system.^[52] As well, the internal ring network of the EMFs cages is metal-stabilized and, thus, is accessible for external organic reaction chemistry. According to Haddon's analysis, the pyramidalization angle of the carbons of C_{60} is closer to a sp^3 than to a planar sp^2 hybridizations (Figure 1.6);^[53] thus, it is not difficult to imagine that cycloaddition reactions have been important in the development of EMF derivatives,^[54] where the strain is relaxed by the formation of tetrahedral carbon atoms.

Cycloadditions are among the most used methods to form six-membered, heterocyclic five-membered and three-membered rings linked to fullerene surfaces. The first exohedral functionalization of an EMF, a silylation reaction on La@C_{82} , was reported by Akasaka and co-workers in 1993.^[55] Since then, different families of EMFs have been derivatized mainly by means of Diels-Alder reactions, azomethine ylide additions (Prato reaction), cyclopropanations (Bingel-Hirsch reaction), as shown in Figure 1.10, along with photochemical reactions, hydrogenations, reductions, etc.^[26b, 56] However, the small amount of EMF reactant along with the low yields for these reactions lead to almost invisible amounts of products at the sub-milligram level, which are very difficult to characterize in the laboratory. Computational chemistry is therefore essential as a complementary technique for the characterization process.^[10]

It has been demonstrated that the endohedral fullerene structures are less reactive than the empty ones, due to the disposition of the HOMO and LUMO orbitals of the reactants.^[57] Many theoretical works have been devoted to analyze the func-

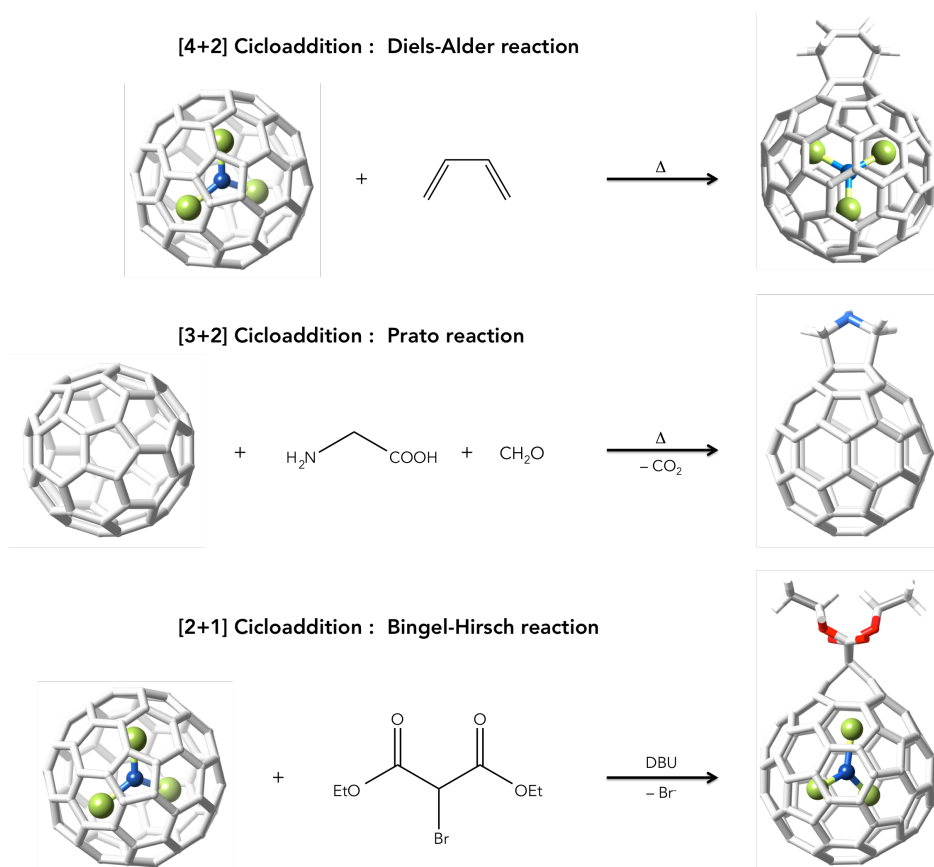


Figure 1.10. Set of significant cycloaddition reactions.

tionalization of EMFs. Although most of them focus on the thermodynamic prediction of the regioselectivity,^[28b, 58] *i.e.*, which bond of the fullerene cage will give the lowest-energy adduct (Figure 1.3), others are devoted to estimate energy barriers.^[54b, 57, 59] Predictions about the regioselectivity of a reaction on a given EMF made from structural or topological parameters of the carbon cage are possible, but an exhaustive analysis of the potential energy surface is required in most cases.^[54b, 60]

The influence of the nature of the metal cluster on the exohedral functionalization for some EMFs has been also considered: on one hand, encapsulation increases the pyramidalization and, thus, the surface tension and the reactivity; on the other, the charge transfer reduces the electronic affinity and, consequently, the reactivity.^[7, 61] It has been concluded that such influence is significant in small cages, where the cluster's mobility is restricted.^[57] Furthermore, it has been discussed about the

regioselectivity depending on the cluster size, having preferential functionalization onto a [5,6] bond when the cluster is small and onto a [6,6] when it is large.^[51b] 1,3-dipolar cycloadditions of N-ethylazomethine ylides (Prato reaction) on $\text{Sc}_3\text{N}@I_h\text{-C}_{80}$ take place regioselectively at a [5,6] bond, but the regioisomer on the [6,6] bond has also been observed in the functionalization of $\text{Y}_3\text{N}@I_h\text{-C}_{80}$.^[62] The [6,6] adduct was found to be the kinetic product from computations as well as from experiments.^[63]

1.6. Potential applications of endofullerenes

Since the first detection of $\text{La}@C_{60}$,^[3] the scientific community had high expectations on EMFs since their novel properties turn them into new materials with potential applications in biomedicine, molecular electronics and material science.^[4, 5b, 50, 64] However, the material was not ready to cross the market line before all their limitations were overcome, in special the low solubility and the bio-incompatibility. For this reason, external derivatization has become an essential field within the fullerene research, in order to improve their natural properties and remove their obstacles. During the past decade, several significant studies have revealed new forms of fullerenes with huge application in medicine and material science. Here some of the most outstanding works are summarized.

Fullerenes are organic molecules composed mainly by carbon atoms; they do not show clear signs of toxicity, so they are great material in medicine. Dorn and co-workers developed the first fullerene-based drug formed with $\text{Gd}_3\text{N}@I_h\text{-}^{#7}\text{C}_{80}$ as contrast agent in Magnetic Resonance Imaging or *MRI* (Figure 1.11).^[65] The three internal Gd metals make the molecule more efficient than the commercial agent, with a single Gd atom. *In vivo* and *in vitro* studies showed that the endofullerene needs a concentration 30 times lower than the commercial *gadodiamide* to provide the same signal intensity.^[65] Recently, the same group of Dorn has synthesized a new EMF $\text{Gd}_3\text{N}@C_{84}(\text{OH})_x$ for magnetic resonance imaging and proved that its intensity signal is even more powerful than the analogous of 80-carbon atoms.^[66]

Among all the properties of the fullerenes, we should now stand out the electronic motion in the most spherical cages and the huge electron affinity of these systems. Thanks to it, endofullerenes found their way in solar cells science – efficiencies up to 7.5% have been reported.^[67] Several published studies show that the new fullerene-based cells are reversible, metastable, and have ultra fast mobility, thus being a good alternative to the current organic solar cells. The solar cells have

been mainly built with C_{60} , because it is the most abundant product, although endofullerenes are expected to give better response.^[68]

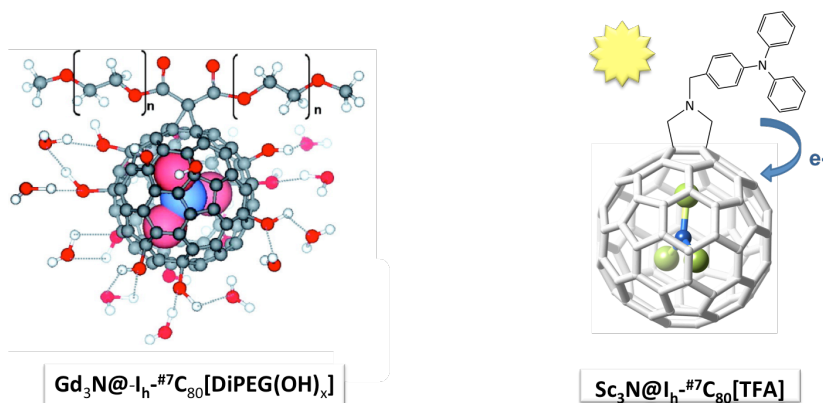


Figure 1.11. *Left:* fullerene-based nanoparticle drug designed as MRI contrast agent. *Right:* functionalized fullerene with application in solar cells.

The endofullerene field is pretty young but in a bit more than a decade the advances achieved have been very productive. Day after day new endohedral or derivatives are synthesized, and with them new unexplored areas for innovative applications are considered. One of the last discoveries moved the scientists to radiochemistry: ${}^7Be@C_{60}$ and ${}^{166}Ho_x@C_{82}$ were synthesized,^[69] thus a window to catch radioactive metals inside fullerenes has been opened. But the scientific imagination always wants more and endofullerenes have been also encapsulated inside nanotubes, changing their properties and walking along a road with unknown destination.^[70] For many specialists, fullerene science has become a game more than a race, where the single rule is being as imaginative and functional as possible.

1.7. Bibliography

- [1] H. W. Kroto, J. R. Heath, S. C. O'Brien, R. F. Curl, R. E. Smalley, *Nature* (1985), 318, 162.
- [2] P. Hienstorfer. Wikimedia Commons. Montreal Biosphère in Montreal, Canada. http://en.wikipedia.org/wiki/Expo_67 (access 27/11/2013).
- [3] J. R. Heath, S. C. O'Brien, Q. Zhang, Y. Liu, R. F. Curl, F. K. Tittel, R. E. Smalley, *J. Am. Chem. Soc.* (1985), 107, 7779.
- [4] T. Akasaka, S. Nagase, *Endofullerenes: a new family of carbon clusters, Vol. 3*, Springer, Dordrecht, The Netherlands, (2002).
- [5] a) Y. Z. Tan, S. Y. Xie, R. B. Huang, L. S. Zheng, *Nature Chem.* (2009), 1, 450; b) M. Chaur, F. Melin, A. Ortiz, L. Echegoyen, *Angew. Chem. Int. Ed.* (2009), 48, 7514.
- [6] S. Stevenson, G. Rice, T. Glass, K. Harich, F. Cromer, M. R. Jordan, J. Craft, E. Hadju, R. Bible, M. M. Olmstead, K. Maitra, A. J. Fisher, A. L. Balch, H. C. Dorn, *Nature* (1999), 401, 55.
- [7] X. Lu, T. Akasaka, S. Nagase, *Chem. Commun.* (2011), 47, 5942.
- [8] W. Kratschmer, L. D. Lamb, K. Fostiropoulos, D. R. Huffman, *Nature* (1990), 347, 354.
- [9] M. Cerón, F. F. Li, L. Echegoyen, *Chem. Eur. J.* (2013), 19, 7410.
- [10] A. Rodríguez-Fortea, A. Balch, J. Poblet, *Chem. Soc. Rev.* (2011), 40, 3551.
- [11] P. W. Fowler, D. E. Manolopoulos, *An Atlas of Fullerenes*, Oxford University Press, Oxford, (1995).
- [12] F. Beer, A. Gugel, K. Martin, J. Rader, K. Mullen, *J. Mater. Chem.* (1997), 7, 1327.
- [13] H. Yang, C. Beavers, Z. Wang, A. Jiang, Z. Liu, H. Jin, B. Mercado, M. Olmstead, A. Balch, *Angew. Chem.* (2010), 49, 886.
- [14] P. Dunk, N. Kaiser, C. Hendrickson, J. Quinn, C. Ewels, Y. Nakanishi, Y. Sasaki, H. Shinohara, A. Marshall, H. Kroto, *Nat. Commun.* (2012), 3, 855.
- [15] S. Irle, G. Zheng, M. Elstner, K. Morokuma, *Nano Lett.* (2003), 3, 1654.
- [16] H. W. Kroto, *Nature* (1987), 329, 529.
- [17] T. G. Schmalz, W. A. Seitz, D. J. Klein, G. E. Hite, *J. Am. Chem. Soc.* (1988), 110.
- [18] Y. Z. Tan, T. Zhou, J. Bao, G. J. Shan, S. Y. Xie, R. B. Huang, L. S. Zheng, *J. Am. Chem. Soc.* (2010), 132, 17102.
- [19] C. Wang, T. Kai, T. Tomiyama, T. Yoshida, Y. Kobayashi, E. Nishibori, M. Takata, M. Sakata, H. Shinohara, *Nature* (2000), 408, 426.

- [20] S. Stevenson, P. W. Fowler, T. Heine, J. C. Duchamp, G. Rice, T. Glass, K. Harich, E. Hajdu, R. Bible, H. C. Dorn, *Nature* (2000), 408, 427.
- [21] P. Dunk, N. Kaiser, M. Mulet-Gas, A. Rodríguez-Forteza, J. Poblet, H. Shinohara, C. Hendrickson, A. Marshall, H. Kroto, *J. Am. Chem. Soc.* (2012), 134, 9380.
- [22] B. Mercado, A. Jiang, H. Yang, Z. Wang, H. Jin, Z. Liu, M. Olmstead, A. Balch, *Angew. Chem. Int. Ed.* (2009), 48, 9114.
- [23] Y. Che, H. Yang, Z. Wang, H. Jin, Z. Liu, C. Lu, T. Zuo, H. C. Dorn, C. M. Beavers, M. M. Olmstead, A. L. Balch, *Inorg. Chem.* (2009), 48, 6004.
- [24] X. Lu, H. Nikawa, T. Nakahodo, T. Tsuchiya, M. O. Ishitsuka, Y. Maeda, T. Akasaka, M. Toki, H. Sawa, Z. Slanina, N. Mizorogi, S. Nagase, *J. Am. Chem. Soc.* (2008), 130, 9129.
- [25] T. M. Zuo, M. M. Olmstead, C. M. Beavers, A. L. Balch, G. B. Wang, G. T. Yee, C. Y. Shu, L. S. Xu, B. Elliott, L. Echegoyen, J. C. Duchamp, H. C. Dorn, *Inorg. Chem.* (2008), 47, 5234.
- [26] a) N. Chen, M. Chaur, C. Moore, J. Pinzón, R. Valencia, A. Rodríguez-Forteza, J. M. Poblet, L. Echegoyen, *Chem. Commun.* (2010), 46, 4818; b) M. N. Chaur, F. Melin, A. L. Ortiz, L. Echegoyen, *Angew. Chem. Int. Ed.* (2009), 48, 7514; c) S. Yang, F. Liu, C. Chen, M. Jiao, T. Wei, *Chem. Commun.* (2011), 47, 11822; d) A. Popov, S. Yang, L. Dunsch, *Chem. Rev.* (2013), 113, 5989.
- [27] M. Chaur, R. Valencia, A. Rodríguez-Forteza, J. Poblet, L. Echegoyen, *Angew. Chem. Int. Ed.* (2009), 48, 1425.
- [28] a) C. M. Beavers, T. Zuo, J. C. Duchamp, K. Harich, H. C. Dorn, M. M. Olmstead, A. L. Balch, *J. Am. Chem. Soc.* (2006), 128, 11352; b) N. Alegret, M. N. Chaur, E. Santos, A. Rodríguez-Forteza, L. Echegoyen, J. M. Poblet, *J. Org. Chem.* (2010), 75, 8299.
- [29] Y. Yamazaki, K. Nakajima, T. Wakahara, T. Tsuchiya, M. Ishitsuka, Y. Maeda, T. Akasaka, M. Waelchli, N. Mizorogi, S. Nagase, *Angew. Chem. Int. Ed.* (2008), 47, 7905.
- [30] T. Guo, M. Diener, Y. Chai, M. Alford, R. Haufler, S. McClure, T. Ohno, J. Weaver, G. Scuseria, R. Smalley, *Science* (1992), 257, 1661.
- [31] a) H. Yang, H. Jin, H. Zhen, Z. Wang, Z. Liu, C. Beavers, B. Mercado, M. Olmstead, A. Balch, *J. Am. Chem. Soc.* (2011), 133, 6299; b) C. Beavers, H. Jin, H. Yang, Z. Wang, X. Wang, H. Ge, Z. Liu, B. Mercado, M. Olmstead, A. Balch, *J. Am. Chem. Soc.* (2011), 133, 15338.
- [32] S. Yang, L. Dunsch, *Angew. Chem. Int. Ed.* (2006), 45, 1299.
- [33] S. Yang, A. A. Popov, L. Dunsch, *Angew. Chem. Int. Ed.* (2007), 46, 1256.
- [34] S. Yang, L. Dunsch, *J. Phys. Chem. B* (2005), 109, 12320.
- [35] S. Stevenson, C. Chancellor, H. Lee, M. Olmstead, A. Balch, *Inorg. Chem.* (2008), 47, 1420.

- [36] F. Melin, M. Chaur, S. Engmann, B. Elliott, A. Kumbhar, A. Athans, L. Echegoyen, *Angew. Chem. Int. Ed.* (2007), *46*, 9032.
- [37] M. N. Chaur, X. Aparicio-Anglès, B. Q. Mercado, B. Elliott, A. Rodríguez-Forteza, A. Clotet, M. M. Olmstead, A. L. Balch, J. M. Poblet, L. Echegoyen, *J. Phys. Chem. C* (2010), *114*, 13003.
- [38] a) C. R. Wang, T. Kai, T. Tomiyama, T. Yoshida, Y. Kobayashi, E. Nishibori, M. Takata, M. Sakata, H. Shinohara, *Angew. Chem. Int. Ed.* (2001), *40*, 397; b) Y. Iiduka, T. Wakahara, K. Nakajima, T. Nakahodo, T. Tsuchiya, Y. Maeda, T. Akasaka, K. Yoza, M. Liu, N. Mizorogi, S. Nagase, *Angew. Chem. Int. Ed.* (2007), *46*, 5562; c) Y. Iiduka, T. Wakahara, T. Nakahodo, T. Tsuchiya, A. Sakuraba, Y. Maeda, T. Akasaka, K. Yoza, E. Horn, T. Kato, M. T. H. Liu, N. Mizorogi, K. Kobayashi, S. Nagase, *J. Am. Chem. Soc.* (2005), *127*, 12500.
- [39] C. R. Wang, T. Kai, T. Tomiyama, T. Yoshida, Y. Kobayashi, E. Nishibori, M. Takata, M. Sakata, H. Shinohara, *Angew. Chem. Int. Ed.* (2001), *40*, 397.
- [40] H. Yang, C. Lu, Z. Liu, H. Jin, Y. Che, M. M. Olmstead, A. L. Balch, *J. Am. Chem. Soc.* (2008), *130*, 17296.
- [41] K. Tan, X. Lu, *J. Phys. Chem. A* (2006), *110*, 1171.
- [42] T. S. Wang, N. Chen, J. F. Xiang, B. Li, J. Y. Wu, W. Xu, L. Jiang, K. Tan, C. Y. Shu, X. Lu, C. R. Wang, *J. Am. Chem. Soc.* (2009), *131*, 16646.
- [43] B. Q. Mercado, M. M. Olmstead, C. M. Beavers, M. L. Easterling, S. Stevenson, M. A. Mackey, C. E. Coumbe, J. D. Phillips, J. P. Phillips, J. M. Poblet, A. L. Balch, *Chem. Commun.* (2010), *46*, 279.
- [44] S. Stevenson, M. A. Mackey, M. A. Stuart, J. P. Phillips, M. L. Easterling, C. J. Chancellor, M. M. Olmstead, A. L. Balch, *J. Am. Chem. Soc.* (2008), *130*, 11844.
- [45] B. Mercado, M. Stuart, M. Mackey, J. Pickens, B. Confait, S. Stevenson, M. Easterling, R. Valencia, A. Rodríguez-Forteza, J. Poblet, M. Olmstead, A. Balch, *J. Am. Chem. Soc.* (2010), *132*, 12098.
- [46] L. Dunsch, S. Yang, L. Zhang, A. Svitova, S. Oswald, A. A. Popov, *J. Am. Chem. Soc.* (2010), *132*, 5413.
- [47] F. F. Li, N. Chen, M. Mulet-Gas, V. Triana, J. Murillo, A. Rodríguez-Forteza, J. M. Poblet, L. Echegoyen, *Chem. Sci.* (2013), *4*.
- [48] M. Krause, F. Ziegls, A. Popov, L. Dunsch, *Chem. Phys. Chem* (2007), *8*, 537.
- [49] a) T. S. Wang, L. Feng, J. Y. Wu, W. Xu, J. F. Xiang, K. Tan, Y. H. Ma, J. P. Zheng, L. Jiang, X. Lu, C. Y. Shu, C. R. Wang, *J. Am. Chem. Soc.* (2010), *132*, 16362; b) W. Jingyi, W. Taishan, M. Yihan, J. Li, S. Chunying, W. Chunru, *J. Phys. Chem. C* (2011), *115*.
- [50] a) K. Braun, L. Dunsch, R. Pipkorn, M. Bock, T. Baeuerle, S. F. Yang, W. Waldeck, M. Wiessler, *Int. J. Med. Sci* (2010), *7*, 136; b) C. Shu, F. D. Corwin, J. Zhang, Z. Chen, J.

- E. Reid, M. Sun, W. Xu, J. H. Sim, C. Wang, P. P. Fatouros, A. R. Esker, H. W. Gibson, H. C. Dorn, *Bioconjugate Chem.* (2009), 20, 1186.
- [51] a) Z. X. Ge, J. C. Duchamp, T. Cai, H. W. Gibson, H. C. Dorn, *J. Am. Chem. Soc.* (2005), 127, 16292; b) N. Chen, E. Y. Zhang, K. Tan, C. R. Wang, X. Lu, *Org. Lett.* (2007), 9, 2011.
- [52] H. Mauser, A. Hirsch, N. J. R. E. Hommes, T. Clark, *J. Mol. Model.* (1997), 3, 415.
- [53] R. C. Haddon, *J. Comput. Chem.* (1998), 19, 139.
- [54] a) M. Rudolf, S. Wolfrum, D. Guldi, L. Feng, T. Tsuchiya, T. Akasaka, L. Echegoyen, *Chem. Eur. J.* (2012), 18, 5136; b) S. Osuna, M. Swart, M. Sola, *Phys. Chem. Chem. Phys.* (2011), 13, 3585.
- [55] T. Akasaka, W. Ando, K. Kobayashi, S. Nagase, *J. Am. Chem. Soc.* (1993), 115, 1605.
- [56] a) M. Yamada, T. Akasaka, S. Nagase, *Acc. Chem. Res.* (2010), 43, 92; b) A. Hirsch, M. Brettreich, *Fullerenes: Chemistry and Reactions*, Wiley-VCH Verlag GmbH&Co. KGaA, Weinheim, Germany, (2005).
- [57] S. Osuna, M. Swart, J. M. Campanera, J. M. Poblet, M. Sola, *J. Am. Chem. Soc.* (2008), 130, 6206.
- [58] a) J. Campanera, C. Bo, J. Poblet, *J. Org. Chem.* (2006), 71, 46; b) O. Lukoyanova, C. M. Cardona, J. Rivera, L. Z. Lugo-Morales, C. J. Chancellor, M. M. Olmstead, A. Rodríguez-Forteza, J. M. Poblet, A. L. Balch, L. Echegoyen, *J. Am. Chem. Soc.* (2007), 129, 10423; c) S. Osuna, A. Rodríguez-Forteza, J. M. Poblet, M. Sola, M. Swart, *Chem. Commun.* (2012), 48, 2486.
- [59] S. Osuna, M. Swart, M. Solà, *J. Am. Chem. Soc.* (2009), 131, 129.
- [60] a) N. Alegret, A. Rodríguez-Forteza, J. Poblet, *Chem. Eur. J.* (2013), 19, 5061; b) A. Rodríguez-Forteza, N. Alegret, A. L. Balch, J. M. Poblet, *Nature Chem.* (2010), 2, 955.
- [61] M. N. Chaur, F. Melin, A. J. Athans, B. Elliott, K. Walker, B. C. Holloway, L. Echegoyen, *Chem. Commun.* (2008), 2665.
- [62] C. M. Cardona, A. Kitaygorodskiy, L. Echegoyen, *J. Am. Chem. Soc.* (2005), 127, 10448.
- [63] a) T. Cai, C. Slebodnick, L. Xu, K. Harich, T. E. Glass, C. Chancellor, J. C. Fettinger, M. M. Olmstead, A. L. Balch, H. W. Gibson, H. C. Dorn, *J. Am. Chem. Soc.* (2006), 128, 6486; b) A. Rodríguez-Forteza, J. M. Campanera, C. M. Cardona, L. Echegoyen, J. M. Poblet, *Angew. Chem. Int. Ed.* (2006), 45, 8176.
- [64] a) E. B. Iezzi, J. C. Duchamp, K. R. Fletcher, T. E. Glass, H. C. Dorn, *Nano Lett.* (2002), 2, 1187; b) R. B. Ross, C. M. Cardona, D. M. Guldi, S. G. Sankaranarayanan, M. O. Reese, N. Kopidakis, J. Peet, B. Walker, G. C. Bazan, E. Van Keuren, B. C. Holloway, M. Drees, *Nature Mater.* (2009), 8, 208; c) L. Dunsch, S. Yang, *Small* (2007), 3, 1298; d) H. Shinohara, *Rep. Prog. Phys.* (2000), 63; e) G. Bottari, G. de la Torre, D. Guldi, T. s. Torres, *Chem. Rev.* (2010), 110, 6768.

- [65] J. Zhang, P. Fatouros, C. Shu, J. Reid, L. Owens, T. Cai, H. Gibson, G. Long, F. Corwin, Z. J. Chen, H. Dorn, *Bioconjugate Chem.* (2010), 21, 610.
- [66] J. Zhang, Y. Ye, Y. Chen, C. Pregot, T. Li, S. Balasubramaniam, D. B. Hobart, Y. Zhang, S. Wi, R. M. Davis, L. A. Madsen, J. R. Morris, S. M. LaConte, G. T. Yee, H. C. Dorn, *J. Am. Chem. Soc.* (2014), DOI: 10.1021/ja412254k.
- [67] M. S. Su, C. Y. Kuo, M. C. Yuan, U. S. Jeng, C. J. Su, K. H. Wei, *Adv. Mater.* (2011), 23, 3315.
- [68] J. Pinzón, D. Gasca, S. Sankaranarayanan, G. Bottari, T. s. Torres, D. Guldi, L. Echegoyen, *J. Am. Chem. Soc.* (2009), 131, 7727.
- [69] a) Ohtsuki, Masumoto, Ohno, Maruyama, Kawazoe, Sueki, Kikuchi, *Phys. Rev. Lett.* (1996), 77, 3522; b) H. J. Huang, S. H. Yang, X. X. Zhang, *J. Phys. Chem. B* (1999), 103, 5928.
- [70] E. Nakamura, *Angew. Chem. Int. Ed.* (2013), 52, 236.



CHAPTER 2

Goals of this Thesis

CHAPTER 2

Goals of this Thesis

Research of fullerenes is a pretty young field, although it is taking giant steps during the last years since computation and experiments are working together in the same direction. This Thesis is part of the story, and we were able to perform it thanks to the collaboration with some of the top experimental groups studying fullerenes. During these years, we aimed to understand and rationalize the structure, the properties and the reactivity of the empty fullerenes and the EMFs, in particular. To achieve that, we have taken advantage of several computational tools, models and strategies as will be reflected throughout this work. Bellow, the specific objectives for each study are described.

Chapter 3. Prediction Models for EMFs

This work has been done in collaboration with Prof. Alan L. Balch (University of California, Davis).

One of the main interests in our group is to understand and rationalize the fullerene behavior inside the arc-discharge reactor in order to be able to unequivocally predict which EMFs would be synthesized. Thus, Poblet has developed a simple rule to predict the most suitable cages that may encapsulate metallic clusters from the orbital gaps in the empty cages. We aimed to:

- × Identify the main physical factors that govern the stability of the endohedral metallofullerene cages and make them suitable to be synthesized in the Krätschmer-Huffmann reactor.
- × Use the abovementioned features to determine a new rule that gives a physical explanation to the orbital rule and is able to explain the already synthesized EMFs and predict new ones.
- × Demonstrate the validity of this physical rule for both the IPR and non-IPR systems.

Chapter 4. Looking for the Identity of the First non-IPR $\text{Sc}_2@C_{66}$

One of the two first non-IPR EMFs was synthesized and characterized by Shinohara and co-workers. However, the cage assignment is still unclear. Computational results performed by Nagase and co-workers proposed an alternative cage different from the one proposed by Shinohara. Therefore, we aimed to:

- × Recover all the works published that could afford clues about the cage assignment in $\text{Sc}_2@C_{66}$ and make the scientific community realize about this unsolved issue.
- × Take advantage of the predicting rules and extensively re-analyze the system to solve the mismatch between the experimental and computational studies.
- × Evaluate whether the EMF could be the carbide $\text{Sc}_2C_2@C_{64}$ instead.
- × Perform additional computational analyses to encourage the experimentalists to re-synthesize this system.

Chapter 5. The Bingel-Hirsch Reaction on Nitride EMFs

This work has been done in collaboration with Prof. Luis Echegoyen (University of Texas at El Paso, El Paso).

The Bingel-Hirsch reaction is commonly used to functionalize fullerenes easily. Echegoyen and co-workers synthesized and derivatized two novel non-IPR cages. However, the low yield of the final products makes the characterization impossible without computational tools. In the background, functionalization of $\text{Sc}_3N@C_{68}$ was published, although experimental and thermodynamic characterization did not

agree. Additionally, no further computational studies about the reaction mechanism were published. Therefore, we aimed to:

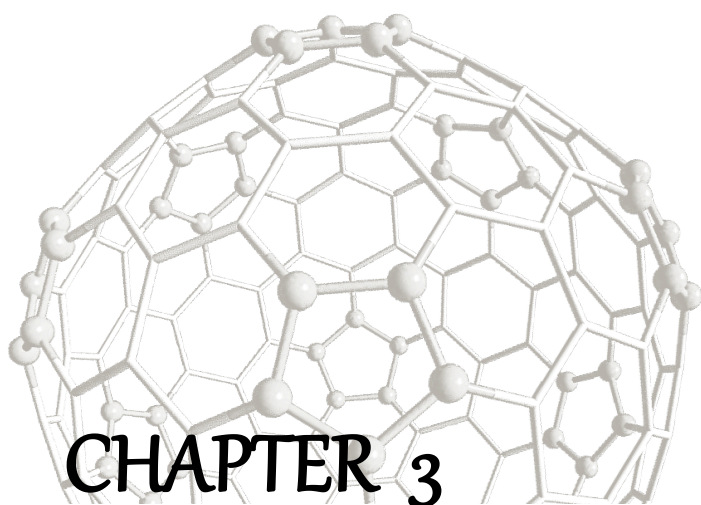
- ✦ Perform an extensive study of the reaction mechanism to clarify whether the reaction undergoes thermodynamically or kinetically controlled.
- ✦ Found a suitable methodology to study the Bingel-Hirsch reaction and use the well-known $\text{Sc}_3\text{N@C}_{80}$ functionalized EMF to validate it.
- ✦ Solve the mismatch between the experimental and computational characterization of the $\text{Sc}_3\text{N@C}_{68}$ Bingel-Hirsch product.
- ✦ Determine the addition bonds where the reaction takes place for the novel functionalized $\text{Gd}_3\text{N@C}_{82}$ and $\text{Gd}_3\text{N@C}_{84}$ EMFs.

Chapter 6. Prato Bisaddition on C_{60}

This work has been done in collaboration and during my stay in the research group of Prof. Luis Echegoyen.

The Prato reaction is also one of the most used reactions to functionalize fullerenes. Due to the simplicity and versatility of this reaction, Prato bisaddition has been successfully performed on C_{60} . During my stay in Prof. Echegoyen's group, we have synthesized three isomers of the C_{60} -bisadducts that have never been observed before. Therefore, we aimed to:

- ✦ Purify and characterize the three bisadducts obtained using the experimental and computational tools.
- ✦ Understand and rationalize the isomerization mechanism observed between two of the three isomers when heated.



Prediction Models for EMFs

Related Publications:

"The maximum pentagon separation rule provides a guideline for the structures of endohedral metallofullerenes." A. Rodríguez-Forteza, N. Alegret, A. L. Balch, J. M. Poblet. *Nature Chem.* (2010), 11, 955

"Electronic structure of IPR and non-IPR endohedral metallofullerenes: Connecting orbital and topological rules." N. Alegret, M. Mulet-Gas, X. Aparicio-Anglès, A. Rodríguez-Forteza, J. M. Poblet. *C. R. Chimie* (2012), 15, 152

CHAPTER 3

Prediction Models for EMFs

Being introduced in the world of fullerenes has been intriguing but has led to lots of questions not easy to answer. During my research lifetime I have learned that only few of those questions can usually be solved, and this chapter collects some of the answers: rules that establish which specific fullerene isomers are able to encapsulate a certain metallic cluster. Maybe that's the reason I have special affection to the IPSI – and a little bit because this work was published on Nature Chemistry! This is not only a theoretical chapter of fullerenes, but also to get computational and experimental chemistry closer. Once again, chemistry let's us understand very easily why things happen the way they happen. Thanks Toni and Poblet for this gift.

3.1. Introduction

From the hundreds of isomers of each C_{2n} family, only few of them have been synthesized. Besides, the endohedral isomers found used to differ from the empty ones. Taking into account the huge similitudes between cage structures, some questions arise: why isomer mixtures of each C_{2n} fullerene are not commonly observed in the *arc-discharge* process? Which characteristic of the experimental cages made them special so they are the ones synthesized? Why do the EMFs isomers differ from the empty ones? Can new isomers not seen yet be expected? To provide suitable answers to all these questions, and many others, theoretical chemis-

try has extensively studied in detail the isomers of several C_{2n} families in order to find out what rules the formation of specific cages, and let the other isomers off-side.

The main difference between the structures with the same number of carbon atoms lays on the disposition of the twelve pentagons. Such disposition is essential to determine the properties of each fullerene. In this chapter we will describe the necessary basis to understand and predict the cage formation of the endohedral metallofullerenes.

3.1.1. The Ionic Model

The stabilization of endohedral metallofullerenes can be easily understood considering an **ionic model** of interaction between the cluster and the cage. There is a formal electronic transfer from the internal cluster to the carbon cage, usually between 2 and 6 electrons. The most common cases are collected in Table 3.1. According to this model, we should take into account the charge separation in endohedral metallofullerenes and describe the systems as $La^{3+}@C_{82}^{3-}$, $Tm^{2+}@C_{82}^{2-}$, $(Sc_3N)^{6+}@C_{80}^{6-}$, and even $(Sc^{3+})_2(Sc^{+2})_2(O^{2-})_2@C_{80}^{6-}$. Such a transfer alters the relative stability of the different isomers and gives extra stability to the cages with "imperfections", as pentagonal fusions, that are unstable when empty.^[1] Yet in 1990 was theoretically predicted that this transfer would cause stabilization on non-IPR cages.^[2] The electron transfer depends mainly on the quantity of electrons that the metals are able to give, so the oxidation state, and the electron affinity of the cages, as we will soon see. The charge transfer changes depending on the type of cluster, and depending on this formal charge transfer the isomer is selected according to its electronic properties.

Table 3.1. Cluster type and their most common charge transfer.

Cluster	Formal charge	Cluster	Formal charge
M	2, 3	M ₂	4,6
M ₃ N	6	M ₂ C ₂	4
M ₂ O	4,6	M ₂ S	4,6

The most efficient procedure to study the huge amount of isomers of the same C_{2n} family is based on an analysis of the relative energies of the empty anionic systems considering the formal charge transfer. Thus, less probable cages, *i. e.*, the most

energetic cages can be rejected. Such analysis is just a first step, and afterwards other factors that may have an important role in the encapsulation process must be taken into account. For example, the analysis of the hexaanionic cages of C_{76} shows that the relative stability of the isomers is **#24109** < **#22010** < **#22107**. Sc_3N is encapsulated inside the most stable isomer, **#24109**, while larger nitrides like Gd_3N need more space inside the cage so they are captured inside **#22010**, where they can be more "comfortable".

3.1.2. Orbital Rule

According to the ionic model, the charge transfer takes place from the HOMOs of the metallic cluster to the LUMOs of the carbon cage. In 2005, Poblet and co-workers proposed a general rule to predict the relative stability of the IPR fullerenes based on the ionic model and the electronic structure of the fullerene cage.^[3] To explain it, we will focus on the metallic nitride clusters, which formally give 6 electrons to the cage. The orbital rule suggests that the most suitable fullerene host to receive the charge must have (i) three low-lying unoccupied molecular orbitals (LUMO, LUMO+1, and LUMO+2), and (ii) sizeable energy gap between the LUMO+2 and the LUMO+3, as shown in Figure 3.1. This reasoning was used to explore the frontier orbitals of all empty IPR isomers between 60 and 100 carbon atoms, concluding that the ones with larger energy gap (LUMO+3 – LUMO+2) match the experimental synthesized fullerenes. When there is a transfer of four

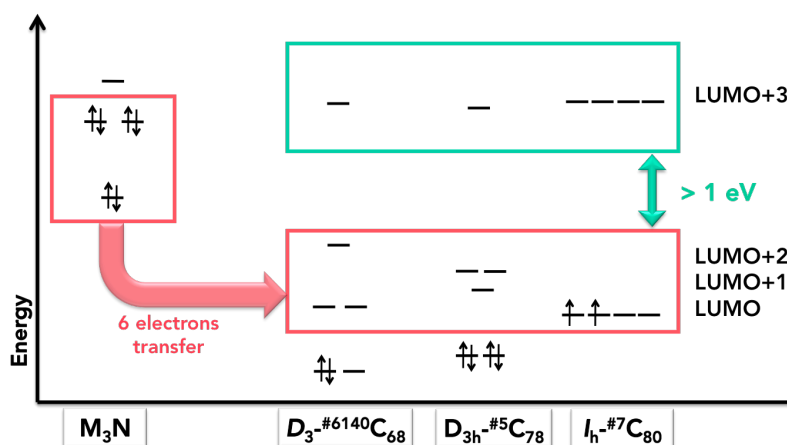


Figure 3.1. Representation of the ionic interaction between the cluster M_3N and several fullerene cages. The 6 electron charge transfer goes from the cluster to the three LUMOs of each cage. In all cases, the energy gap between LUMO+2 and LUMO+3 is large enough to allow the reception, thus encapsulation.

electrons, as in some metal carbides (M_2C_2), metal oxides (Sc_2O) or sulphides (Sc_2S), the orbital gap between the second and third unoccupied orbitals has to be considered (LUMO+2 – LUMO+1).^[4] This rule is valid for any cluster and cage, and thanks to it isomers both IPR and non-IPR have been predicted.^[5]

In summary, each cluster chooses the best cage that better accepts its electronic transfer. The analysis of the orbital gaps for all the IPR isomers between C_{80} and C_{100} leads to the conclusion that the isomers $I_h-^{#7}C_{80}$ and $C_{3v}-^{#8}C_{82}$ are the cages with the most favorable electronic structure to encapsulate clusters when formal transfers of six and four electrons take place, respectively.^[1, 4] As their orbital diagrams shows (Figure 3.2), both structures are intimately related and have more than 1 eV (at the BP86/TZP level of theory) energy gap between the frontier orbitals.

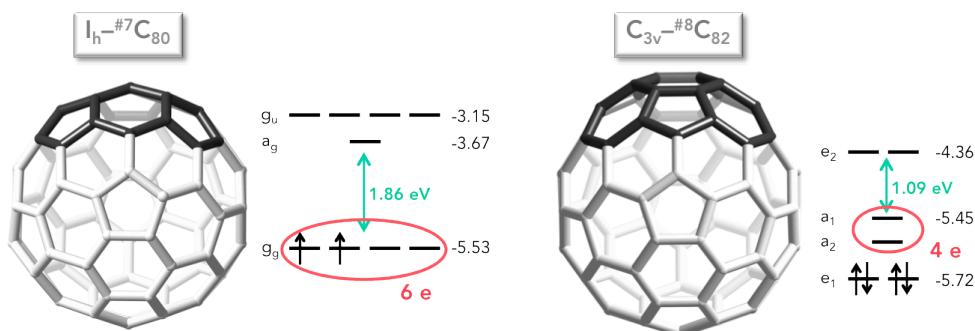


Figure 3.2. Orbital diagram of $C_{3v}-^{#8}C_{82}$ and $I_h-^{#7}C_{80}$ fullerenes. In black, the area that differs between both structures.

Since the three lowest unoccupied molecular orbitals in a carbon cage are rather similar, the simple inspection of their orbital shapes cannot explain the orbital rule. Therefore, a different approach is required.

3.1.3. The Inverse Pentagon Separation Index (IPSI)

In an exhaustive theoretical study of the C_{2n}^{6-} ($2n = 68-98$) empty fullerenes and the corresponding M_3N ($M = Sc$ and Y) metallofullerenes, Popov and Dunsch showed that the isomers of lowest energy always match the structurally characterized M_3N endohedral fullerenes.^[6] The exceptional stabilities of the $I_h-^{#7}C_{80}^{6-}$ and $D_{5h}-^{#6}C_{80}^{6-}$ cages were interpreted to result from the favorable disposition of the pentagons on the surface, which minimizes the steric strain, as the hexagon indices defined by Raghavachari show.^[7]

Alcamí and co-workers analyzed the properties of non-IPR isomers of C_{60} and C_{70} and stated that the relative stability of a charged fullerene is determined by the charge distribution in the carbon cage and the subsequent Coulomb repulsion between the charges of equal signs.^[8] In 2010, we have showed that both terms steric strain and Coulomb repulsion, determine the relative stability of the $C_{2n}^{4-/6-}$ anions. Moreover, this stability is related to the separation among pentagons, which can be measured by the *IPSI* computed by the formula:

$$IPSI = \sum_{i=1}^{12} \sum_{j>i}^{12} \frac{1}{R_{ij}} \quad (3.1)$$

where R_{ij} is the distance between the centroids of pentagons i and j .

The mechanism of non-IPR fullerene stabilization is similar to that proposed for IPR-satisfying fullerenes, but the presence of fused pentagons facilitates the electron transfer and bonding interaction between the internal atoms and the carbon cage. The *IPSI* can also be applied to non-IPR fullerenes with the same number of adjacent pentagon pairs (APPs), which allows us to formulate a simple general rule for IPR and non-IPR anions. The electron transfer from the internal cluster to the fullerene host preferentially adds electrons to the pentagons; therefore, the most suitable carbon cages are those with the largest separations among the 12 pentagons. The maximum separation among pentagons minimizes the electrostatic repulsion induced by the six extra electrons on the carbon cage.

The relative energies of the hexaanions C_{2n}^{6-} also correlate with the number of pyracylene units present in the structure (Figure 1.3).^[9] We also showed that there is a relationship between the energies of the cage orbitals that accept the electrons, the *IPSI* values and the number of pyracylene motifs of the cages. Moreover, these parameters are fundamental to answer questions as, for example, why Sc_3N does not select the most stable empty $D_{5d}^{-\#1}C_{80}$ isomer, which can be seen as the iconic I_h-C_{60} with 20 additional carbon atoms in the equatorial zone, (Figure 1.4), instead of the $I_h^{-\#7}C_{80}$ or $D_{5h}^{-\#6}C_{80}$ cages with few pyracylene motifs (Figure 3.3). Violations of the IPR rule have been observed for several metallofullerenes for small-medium cages ($2n \leq 84$) since the isolation and characterization of $Sc_2@C_{66}$ and $Sc_3N@C_{68}$.^[10] We here will also show why it is so unlikely to find non-IPR fullerenes for large carbon cages ($2n > 84$).

The orbital rule allows the identification of the optimal cage to encapsulate, although it does not give a physical explanation to it. With the *Maximum Pentagon Separation Rule*, which is based on the *IPSI* factor, we have been able to fill the

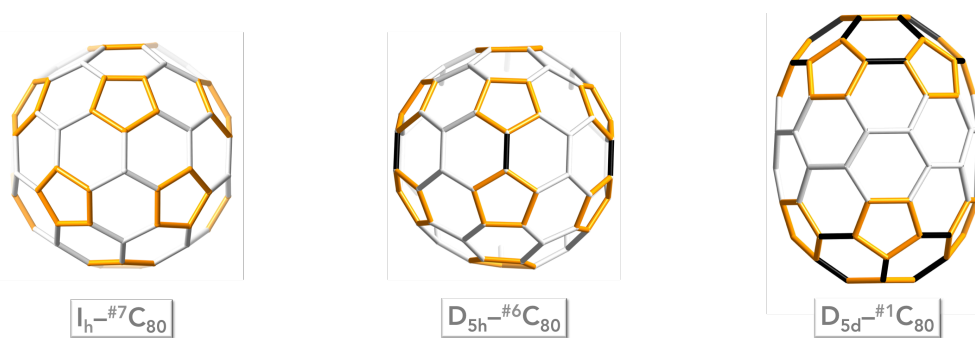


Figure 3.3. Structures of IPR cages D_{5d} -C₈₀, I_h -C₈₀ and D_{5h} -C₈₀. In orange, the 12 pentagons; in black, the [6,6] bonds from pyracylene units.

gap and understand the main points, like why a certain cage encapsulates while the other isomers do not.

Finally, we should not forget about the other factors that may affect the encapsulation of a metallic cluster, such as the size of the internal cavity. For this reason, C₆₀ hardly encapsulates large metallic clusters as M₃N, although the energy gap between the frontier orbitals is large enough. In non-IPR cases an additional factor must be considered: the strong interaction between the pentalene unit and the metal atoms contributes as well in a large stabilization of the whole system, as in Sc₃N@C₆₈.

3.2. Computational Details

Semi-empirical calculations at the AM1 level for the hexaanions, tetraanions and neutral empty cages were performed using the Gaussian03 code.^[11] DFT calculations were carried out using the ADF 2007 program.^[12] The exchange-correlation functionals of Becke^[13] and Perdew^[14] were used. Relativistic corrections were included by means of the zero-order regular approximation. Triple- ζ polarization basis sets were used to describe the valence electrons of the C, N and metal atoms. Frozen cores that consisted of the 1s shell were described by means of single Slater functions. Charges were computed using the Mulliken partition analysis.

IPR and non-IPR cages were identified by their symmetry and by the number assigned according to the spiral algorithm. The truncated numbering system that counts only IPR isomers is used for IPR cages.^[15]

Discussion on atomic charges

All the atomic charges computed through this chapter are based on the Mulliken partition analysis. The charges on pentagons plotted in Figure 3.5 are obtained from electronic structure calculations at semiempirical AM1 level. Semiempirical methods use minimal basis sets (the minimal number of basis functions that are necessary to describe a molecule) to describe the electronic structure of the molecules. We have found that the charges on pentagons computed from the Mulliken partition at DFT level using a basis set of Gaussian functions of double- ζ quality follow the same trend as that shown by semiempirical charges (for the C_{80}^{6-} and C_{88}^{6-} cages). Charges on Table 3.4 are computed following this computational strategy. Since atomic charges computed at DFT level strongly depend on the basis set they are less useful to visualize the electron localization effects. For example, the charges on pentagons computed using a triple- ζ basis set of Slater functions correlate with the energies of the hexaanions for the C_{80}^{6-} systems, but no clear correlation is found for the C_{88}^{6-} cages. However, the molecular electrostatic potentials computed at the same level of theory confirm the localization of the charge on the pentagons as predicted by semiempirical AM1 calculations. So, we observe here that the larger the basis sets the less reliable (more unphysical) Mulliken charges are obtained.

3.3. Maximum Pentagon Separation Rule

3.3.1. Stability and localization of the charge density

The recent characterization of $Sm_2@D_{3d}-^{822}C_{104}$ provides a unique opportunity to evaluate whether the choice of cage isomer in a large endohedral fullerene is determined by the stability of the empty anionic cage, as has been shown for most of the smaller endohedral fullerenes.^[16] Geometry optimizations for the 823 IPR isomers of C_{104} in their neutral and tetraanionic states were carried out at the AM1 level. Isomer **#812** is the most stable neutral cage, but isomer **#822** is the most stable tetraanion, followed by isomer **#821**, which is $8 \text{ kcal}\cdot\text{mol}^{-1}$ higher in energy. To check the validity of these predictions, the five lowest-energy cages were recomputed at the DFT level, which confirmed that cage **#822** is the most stable tetraanion among the 823 IPR isomers of C_{104} . To understand why the tetraanion IPR isomer **#822** is the most stable cage, it is very instructive to represent the relative energy of each isomer with respect to the IPSI defined by equation (3.1). The inverse of the distance ensures the maximum separation among vicinal pentagons

for low values of IPSI. The stability of neutral isomers does not correlate with IPSI. However, the scattering is reduced when the fullerene is negatively charged, as shown in Figure 3.4 for the dianions, tetraanions, and hexaanions of C_{104} IPR isomers. Isomer #822 is one of the IPR cages in which the pentagons are maximally separated.

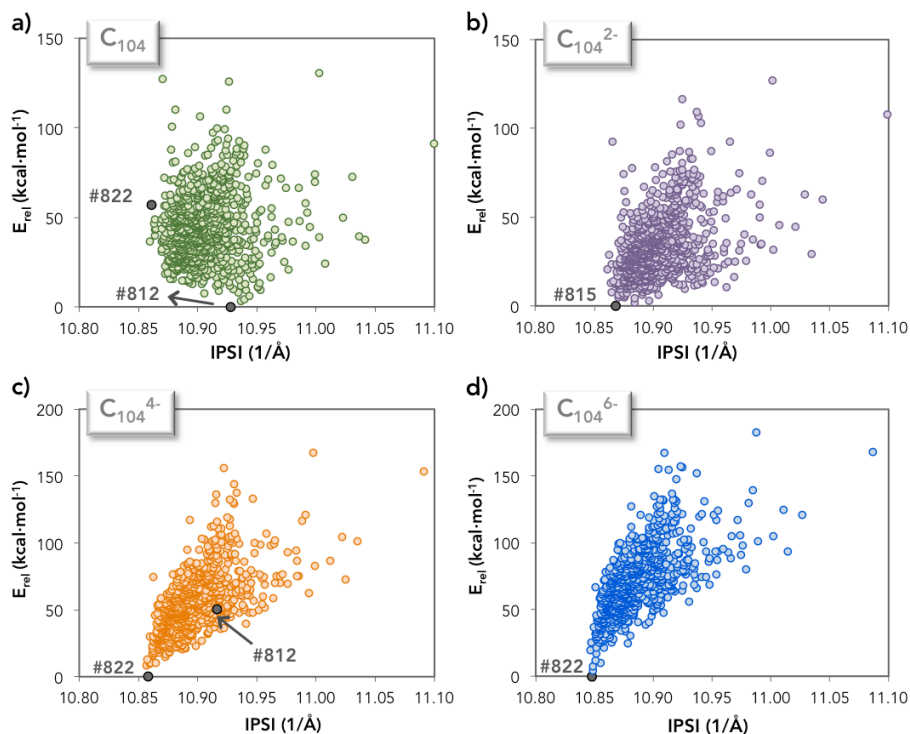


Figure 3.4. Relative stability for the 823 IPR isomers of C_{104} with respect to the inverse pentagon separation index (IPSI) of the a) neutral, b) dianion, c) tetraanion and d) hexaanion.

After a systematic analysis for all IPR isomers of cages that ranged between C_{78} and C_{104} in their hexaanions at the AM1 level, several conclusions emerge: (i) the property that determines the trend observed in Figure 3.4 is the preferential localization of the charge density on the carbon atoms that belong to the pentagonal rings caused by the higher pyramidalization of those C atoms in the [5,6] carbon-carbon bonds. (ii) The correlation between IPSI and relative energies (E_{rel}) decreases with an increase of the cage size. (iii) The electrostatic term is probably the dominant factor that determines the stability of the charged species and, consequently, the stability of many endohedral fullerenes.

Plots of the relative energies with respect to IPSI and the charge localized on the pentagons ($q_{\text{pentagons}}$) are given in Figure 3.5 for C_{80}^{6-} to C_{104}^{6-} . The relative stability also correlates with the total charge localized on pentagons. This is the key point: the negative charge in IPR isomers tends to localize more on carbon atoms that form [5,6]-bonds than on carbon atoms that link two hexagons. Consequently, the Coulomb repulsion decreases when the pentagons are separated maximally.

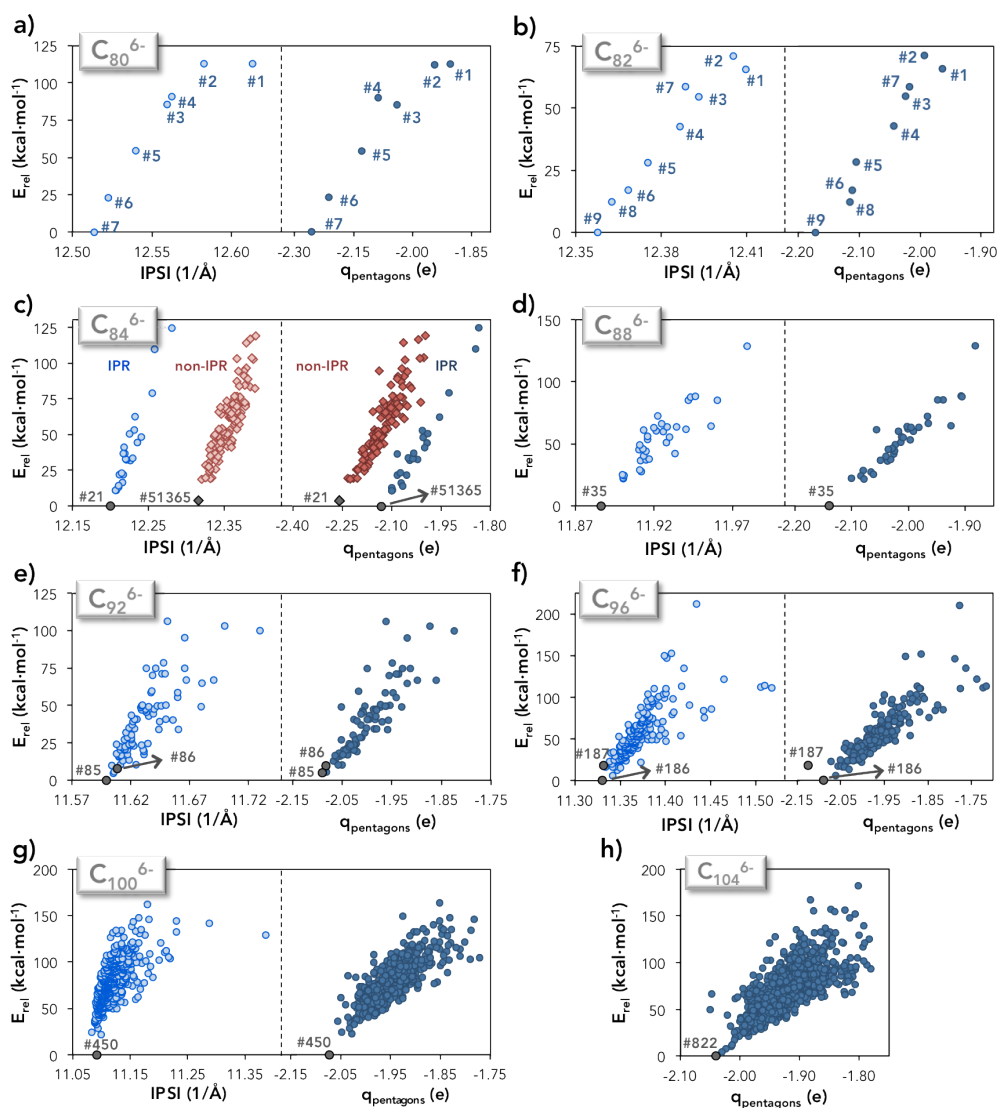


Figure 3.5. Correlation between relative stability of the fullerene anions and atomic charge localized on the pentagons (right) and the inverse pentagon separation index (IPSI, left).

We also carried out DFT calculations on all the IPR isomers for cages C_{80} , C_{84} and C_{88} . The good correlation between E_{rel} and the charge localized on pentagons for the 35 isomers of C_{88} (Figure 3.6d) confirms the hypothesis observed from AM1 calculations. Sometimes, it is useful to separate the different terms that contribute to the total energy of a molecular system. One of the most popular schemes was proposed by Morokuma.^[17] In this formulation, orbital, electrostatic and Pauli repulsion terms are computed separately. Here, the electrostatic term that includes electron–nuclei attraction and electron–electron repulsion contributions appears to be the dominant term. The rather good correlation between the stability of the fullerene and the electrostatic contribution to this stability supports the contention that the electrostatic term must be the dominant factor that governs the relative stability of the fullerene isomers. This behavior was observed for the C_{80} , C_{84} and C_{88} hexaanions (Figure 3.6).

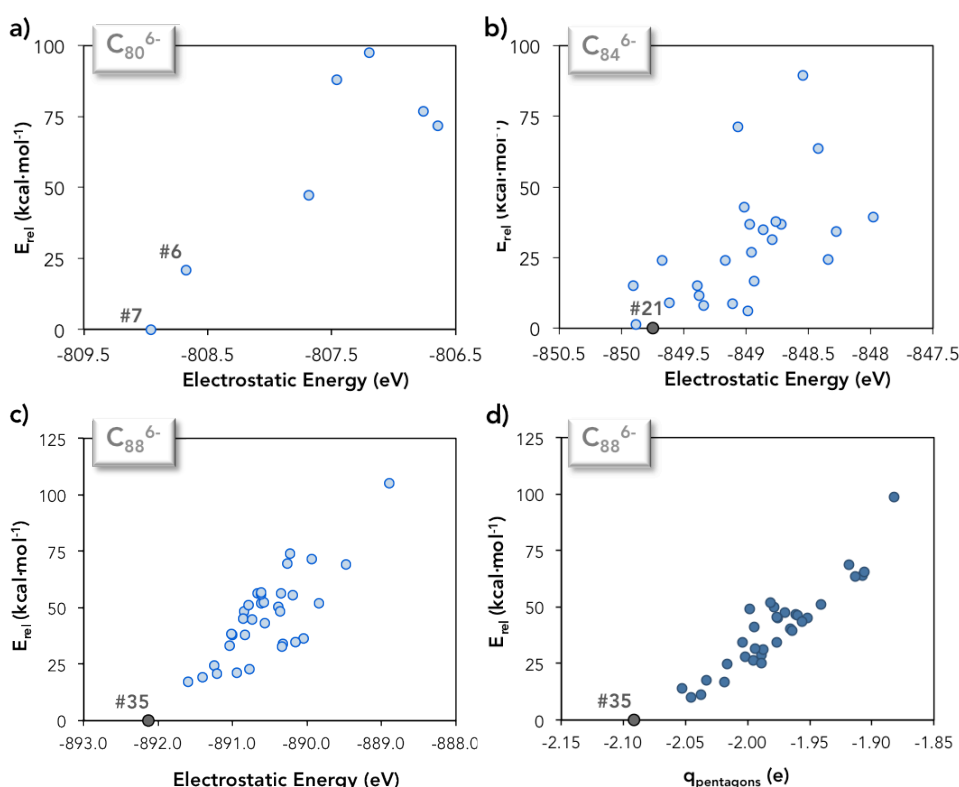


Figure 3.6. DFT relative energies (in kcal·mol⁻¹) with respect to a-c) the electrostatic contribution to the energy (in eV) for C_{80}^{6-} , C_{84}^{6-} and C_{88}^{6-} IPR fullerenes and d) the atomic charge localized on pentagons for C_{88}^{6-} IPR fullerene.

Additional evidence for the charge localization was obtained from the topology of the molecular electrostatic potentials (MEPs), which proved to be useful for detecting the most nucleophilic regions in anions.^[18] Figure 3.7 shows the computed MEPs for the lowest-energy cages for C_{80}^{6-} and C_{104}^{4-} , as well as for the non-IPR C_{84}^{6-} . For the two IPR fullerenes, the red color is somewhat more intense in the vicinity of the [5,6]-bonds, which provides additional evidence of the preferential charge localization on these bonds. For the non-IPR cage, the most intense red zones are in the [5,5]-bonds.

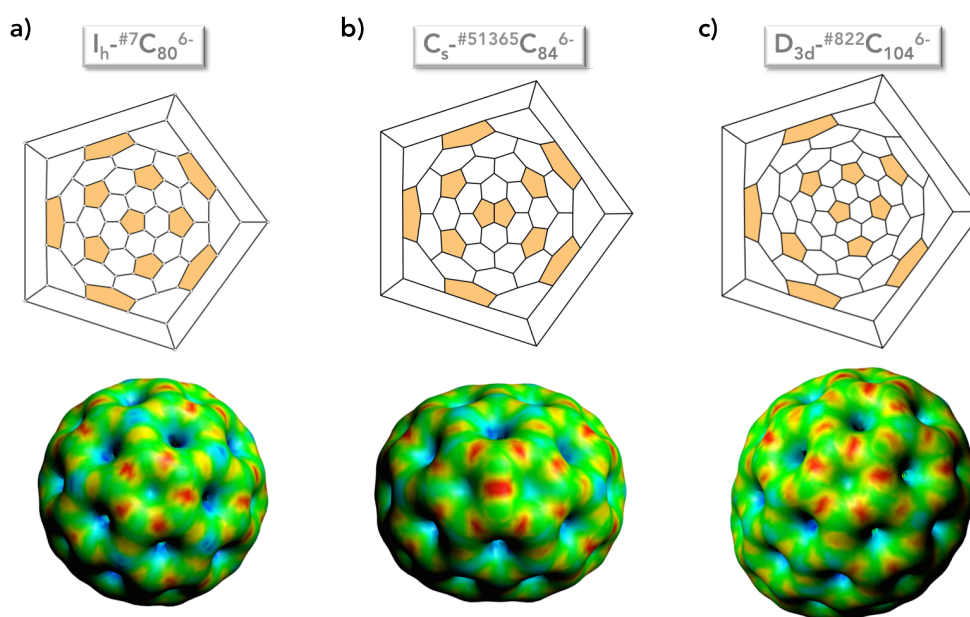


Figure 3.7. Schlegel diagrams and molecular electrostatic potential representations for the hexaanions of a) the I_h -#7 C_{80}^{6-} , b) the non-IPR C_s -#51365 C_{84}^{6-} , and c) the D_{3d} -#822 C_{104}^{6-} cages. Red identifies regions in which the electrostatic potential is more negative (nucleophilic regions) and green identifies less negative potential regions or more electrophilic regions.

It is also interesting that a correlation between the IPSI and the isomer number given by the spiral algorithm should exist, because the two numbers are related to the relative position of the 12 pentagons within the fullerene. Indeed, most of the observed IPR cages in endohedral metallofullerenes correspond to those isomers with the largest numbers according to the nomenclature of Fowler and Manolopoulos (Figure 3.5).^[15]

3.3.2. Non-IPR cages and the pyracylene motif.

In 2008 a paper titled 'Is the IPR merely a suggestion for endohedral fullerenes? The structure of a second egg-shaped endohedral fullerene-Gd₃N@C₅-^{#39663}C₈₂' was published.^[19] Undoubtedly, this title reflects that the origin of the stabilization of non-IPR fullerenes is still not sufficiently understood. A total of thirteen different C_{2n} non-IPR cages have been observed since the characterization of the first non-IPR endohedral metallofullerenes.^[5] All were found for middle-sized fullerenes (66 ≤ 2n ≤ 84) in which the number of IPR isomers is null or relatively small (Table 3.2). For endohedral metallofullerenes with formal transfer of 6 electrons the observed cage is one of the isomers with lowest number of pyracylene motifs within each one of the APPn subsets.

Table 3.2. Selected parameters for observed non-IPR endohedral metallofullerenes.

	Isomer	Formal charge	Pentalenes	Pyracylenes	Ref.
Sc ₂ @C ₆₆	C _{2v} - ^{#4348}	4	2	17	[10a]
Sc ₃ N@C ₆₈	D ₃ - ^{#6140}	6	3	6	[10b]
Sc ₂ C ₂ @C ₆₈	C _{2v} - ^{#6073}	4	2	10	[20]
Sc ₃ N@C ₇₀	C _{2v} - ^{#7854}	6	3	4	[21]
Sc ₂ S@C ₇₀	C ₂ - ^{#7892}	4	2	11	[22]
Sc ₂ S@C ₇₂	C ₅ - ^{#10528}	4	2	6	[23]
La@C ₇₂	C ₂ - ^{#10612}	3	1	15	[24]
M ₂ @C ₇₂ (M=La, Ce)	D ₂ - ^{#10611}	6	2	6	[25]
DySc ₂ N@C ₇₆	C ₅ - ^{#17490}	6	2	3	[26]
M ₃ N@C ₇₈ (M=Y, Gd, Tm, Dy)	C ₂ - ^{#22010}	6	2	2	[27]
Sc ₃ NC@C ₇₈	C ₂ - ^{#22010}	6	2	2	[28]
Gd ₃ N@C ₈₂	C ₅ - ^{#39663}	6	1	4	[19]
M ₃ N@C ₈₄ (M=Gd, Tb, Tm)	C ₅ - ^{#51365}	6	1	2	[29]

Popov and Dunsch demonstrated with DFT calculations that, in many cases, non-IPR endohedral fullerenes are even more stable than IPR ones,^[6] especially for the smallest cages. They concluded that the formation of non-IPR endohedral fullerenes is highly unlikely for larger cages. Experimental data seem to confirm this theoretical prediction by Popov and Dunsch, because the largest non-IPR fullerene

characterized to date is $C_{5-}^{#51365}C_{84}$. The strain energy was invoked to justify why larger non-IPR fullerenes are less favorable. We observed, however, that IPR and non-IPR fullerenes follow similar stabilization mechanisms with a unique, but important, exception: [5,5]-bonds tend to accumulate more negative charge than [5,6]- and [6,6]-bonds. Consequently, non-IPR fullerenes localize the negative charge more on the pentagons than their IPR counterparts. This behavior is clearly perceptible in Figure 3.5c, which shows that in many non-IPR isomers the negative charge localized on the pentagons is larger than that in IPR fullerenes. Hence, the charge computed on pentagons for the most stable non-IPR $C_{84}^{#(51365)}$ is $-2.19 e$, to be compared with $-2.07 e$ that corresponds to the charge localized on the pentagons for the lowest-energy IPR $C_{84}^{#21}$ cage. The charge on pentagons is computed to be $-2.41 e$ for non-IPR $D_{3-}^{#6140}C_{68}$, the smallest cage that encapsulates a metal nitride cluster (Sc_3N). This larger localization of the charge on pentagons involves an electrostatic gain that counterbalances the steric strain caused by the presence of adjacent pentagons, thus making non-IPR isomers suitable cages to encapsulate metal clusters. But, why is cage $C_{5-}^{#51365}C_{84}$ the one that encapsulates metallic nitrides among the other 110 non-IPR isomers with only one APP? And why is it preferred among the 24 IPR isomers? Figure 3.5c answers the first question: the $C_{5-}^{#51365}C_{84}$ cage shows the best distribution of pentagons, that is the lowest IPSI, among the other non-IPR isomers with one pair of adjacent pentagons. So, the maximum pentagon separation rule also holds for non-IPR isomers with the same number of APPs. Regarding the second question, it can be answered from the topology of the cages that encapsulate M_3N or M_2 units: all of them show few pyracylene units. This type of arrangement of pentagons (Figure 3.8b) provides shorter pentagon–pentagon distances compared with those of other non-

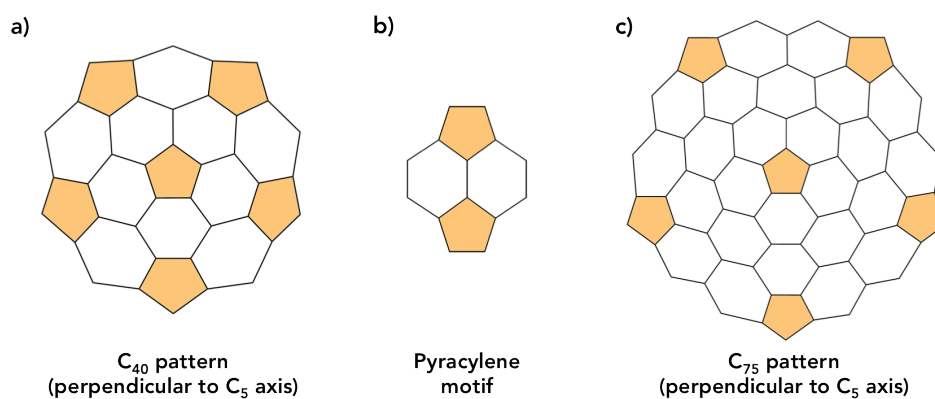


Figure 3.8. Schematic 2D representations of some fullerene fragments: **a)** one-half of the $I_h(7)-C_{80}$ cage bisected by cutting it perpendicular to a five-fold axis; **b)** a pyracylene unit; **c)** the C_{75} unit present in the I_h-C_{180} fullerene is similar to the C_{40} pattern in C_{80} but with two rings of hexagons around each pentagon instead of one.

pyracylene patterns. Therefore, those cages with few pyracylene units show small IPSI values. The relative energies for the seven IPR hexaanions of C_{80} as well as for other larger carbon cages correlate very well with the number of pyracylene motifs present in the fullerene, as shown in Table 3.3 and Figure 3.9.

Table 3.3. Number of pyracylene units, charge localized on pentagons (in e) and relative energies ($\text{kcal}\cdot\text{mol}^{-1}$) for several IPR and non-IPR C_{2n}^{6-} fullerenes.

	C_{80}				C_{84}	C_{88}	C_{92}	C_{96}	C_{100}	
Isomer	#1	#2	#6	#7	#21	#51365	#35	#85	#18	#450
Symmetry	D_{5d}	D_2	D_{5h}	I_h	D_2	C_s	D_2	D_3	D_2	D_5
Pyracylene	20	18	5	0	8	2	4	3	2	0
$q_{\text{pentagons}}$	-1.86	-1.93	-2.14	-2.22	-2.07	-2.19	-2.09	-2.07	-2.07	-2.07
E_{rel}	97.5	88.1	20.8	0.0	0.0	1.4	-	-	-	-

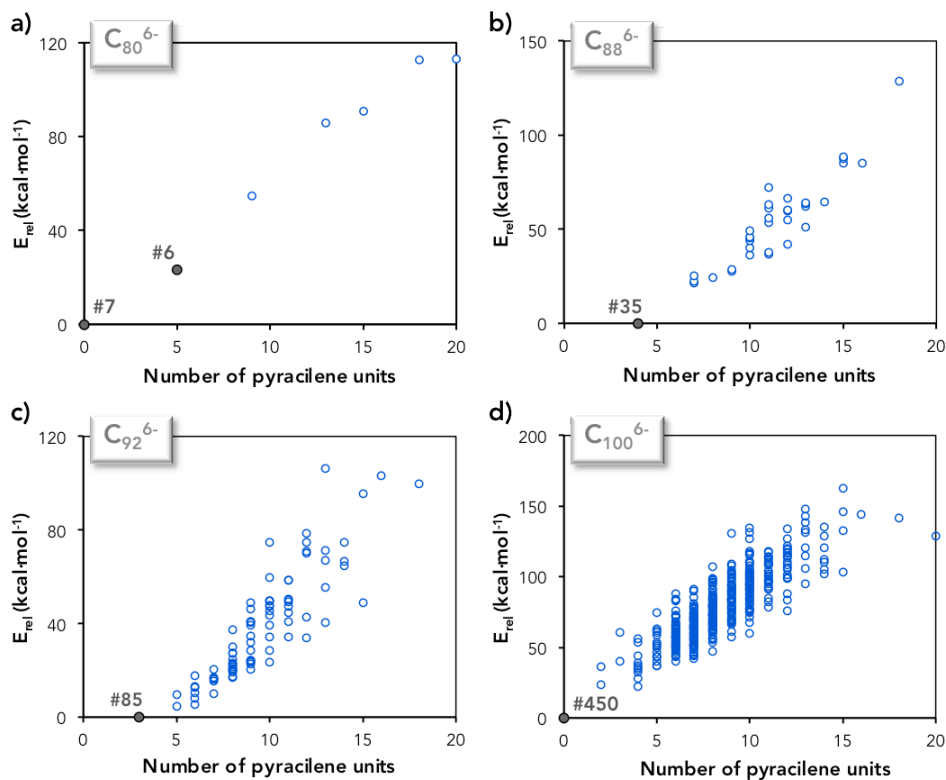


Figure 3.9. AM1 relative energies (in $\text{kcal}\cdot\text{mol}^{-1}$) with respect to the number of pyracylene units for a) C_{80}^{6-} , b) C_{88}^{6-} , c) C_{92}^{6-} and d) C_{100}^{6-} IPR fullerenes.

For example, for C_{80} the most stable neutral fullerene is $D_{5d}\text{-}^{#1}C_{80}$ with 20 pyracylene units; however, the $I_h\text{-}^{#7}C_{80}$ isomer without pyracylene units is the most stable hexaanion. In contrast to Raghavachari indexes,^[7] this criterion allows us to distinguish between isomers $D_{5h}\text{-}^{#6}C_{80}$ and $I_h\text{-}^{#7}C_{80}$. The most stable C_{84} IPR isomer, $D_{2}\text{-}^{#21}C_{84}$, presents eight pyracylene units, the lowest value among the 24 IPR isomers, as opposed to the non-IPR isomer $C_{5}\text{-}^{#51365}C_{84}$, which has only two pyracylene motifs. So, the topology of this latter is more appropriate to accommodate the negative charge than that of the IPR $D_{2}\text{-}^{#21}C_{84}$, being, indeed, the one chosen to encapsulate M_3N units.^[29] Apart from the intrinsic stability of the non-IPR hexaanionic cages, we also have to take into account that coordination of the M_3N cluster to [5,5]-bonds gives extra stabilization to the endohedral fullerene, as pointed out by Popov and Dunsch.^[6, 21] Even though we focus the discussion principally on metal nitride endohedral fullerenes, it can be extended to other families of endohedral metallofullerenes. For example, the cages in non-IPR $La_2@D_{2}\text{-}^{#10611}C_{72}$ ^[25a] and $Sc_2C_2@C_{2v}\text{-}^{#6073}C_{68}$ ^[20] reported by Shinohara and co-workers also show the lowest value of IPSI and the smallest number of pyracylene units within the subset of all fullerenes with two APPs (Figure 3.10).

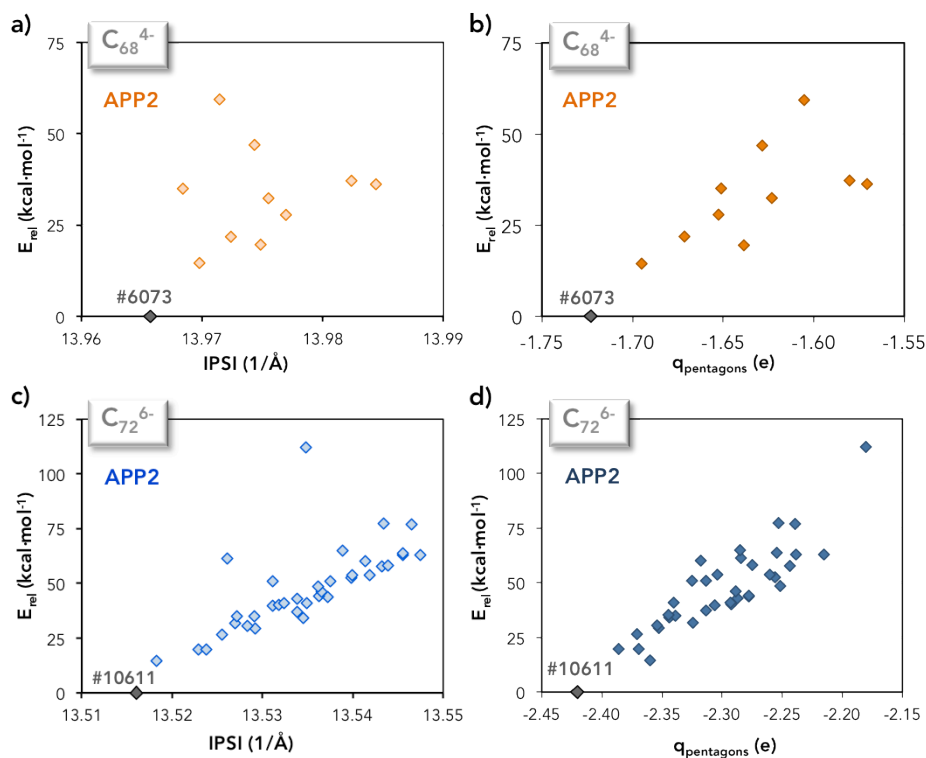


Figure 3.10. AM1 relative energies with respect to IPSI (left) and to the total charge localized on the 12 pentagons (right) for the non-IPR cages with two APPs of C_{68}^{4-} (top) and C_{72}^{6-} (bottom).

Table 3.4. summarizes the observed and theoretically predicted IPR endohedral metallofullerenes with $78 \leq 2n \leq 104$. For all endohedral metallofullerenes with a formal transfer of six electrons, the most abundant observed fullerene or predicted

Table 3.4. Selected parameters for IPR cages between C_{78} and C_{104} .

Endohedral metallofullerene	Charact ^a	Isomer	Formal charge	IPSI order ^b	Pyracylene (order) ^b	Ref.
Sc₃N@C₇₈; La₂@C₇₈	X-ray	#5	6	1	9 (1)	[30]
M₃N@C₈₀ (M=Sc, Y, Gd)	X-ray	#7	6	1	0 (1)	[16, 31]
M₃N@C₈₀ (M=Sc, Lu, Tb)	X-ray	#6	6	2	5 (2)	[32]
M₂@C₈₀ (M=La, Ce)	X-ray	#7	6	1	0 (1)	[30b]
Sc₄(μ-O)_{2/3}@C₈₀	X-ray	#7	6	1	0 (1)	[33]
Er₂@C₈₂	X-ray	#6	4 or 6	3	8 (3)	[34]
	X-ray	#8	4 or 6	2	6 (1)	[34]
	Spectro.	#9	4 or 6	1	6 (1)	[34]
Sc₂C₂@C₈₂	X-ray	#8	4	2	6 (1)	[35]
M@C₈₂ (M=La, Ce)	X-ray	#9	3	1	6 (1)	[30b]
Tb₃N@C₈₆	X-ray	#19	6	1	6 (2)	[36]
Tb₃N@C₈₈	X-ray	#35	6	1	4 (1)	[36]
M₃N@C₉₀	DFT	#43	6	1	4 (1)	[6]
	DFT	#44	6	2	5 (2)	[6]
M₃N@C₉₂ (M=La, Ce)	EC/DFT	#86	6	7	6 (4)	[37]
	DFT	#85	6	1	3 (1)	[6, 37]
Gd₂C₂@C₉₂	X-ray	#85	4	1	3 (1)	[38]
M@C₉₄ (M=Ca, Tm)	X-ray	#134	2	21	6 (7)	[39]
M₃N@C₉₄	DFT	#121	6	4	5 (3)	[1, 6]
M₃N@C₉₆ (M=La, Ce)	EC/DFT	#186	6	1	2 (2)	[37]
La₃N@C₁₀₀; Y₂@C₁₀₀	DFT	#450	6	13	0 (1)	[1]
Sm₂@C₁₀₄	X-ray	#822	4	5	0 (1)	[40]

^a Type of characterization: X-ray crystallography, electrochemical (EC), spectroscopic or DFT. Some of the X-ray structures for $M_k@C_{2n}$ were characterized in their functionalized form.

^b Order in the IPSI and the pyracylene values

cage corresponds to the first or second isomer with the smaller number of pyracylene units. For middle-sized fullerenes, IPSI also discriminates rather well, but for cages with $2n \geq 100$, IPSI obviously becomes less selective. Only isomer 121 of C_{94} , which was predicted from DFT calculations as the most favorable structure for C_{94} , would follow neither the IPSI nor pyracylene number rule, even though both parameters displayed low values. Endohedrals with a small charge transfer, such as $Ca@C_{94}$ and $Tm@C_{94}$, are not expected to fulfill the proposed rule. Finally, we stress that we do not have to explore all the IPR structures to find the most favorable cage for a large fullerene, but only those among the cages without pyracylene units. The combination of IPSI and number of pyracylene units always provides an excellent starting point to characterize the most favorable (thermodynamic) endohedral metallofullerenes.

3.3.3. The icosahedral symmetry: the most favorable charge distribution in an anion.

$Sc_3N@I_h^{-\#7}C_{80}$ is the third most abundant fullerene characterized so far, after C_{60} and C_{70} . A preliminary interpretation to the special stability of $I_h^{-\#7}C_{80}$ was reported by our group through the special configuration of this icosahedral cage: it presents a set of four-fold degenerate low-lying orbitals – with two electrons in the neutral cage – that is filled after the transfer of six electrons from the internal cluster in the M_3N endohedral fullerene.^[3] The ultimate reason, however, is that icosahedral symmetry is the symmetry that best maximizes the separation between 12 pentagons. For the neutral cage, IPR isomer #1 with 20 pyracylene motifs is the most stable carbon cage, but after adding six electrons the icosahedral cage with no pyracylene motifs becomes the most stable isomer. An IPR fullerene with icosahedral symmetry I_h only happens again in the carbon cage with 180 atoms. For this fullerene family, only one of the 4,071,832 IPR isomers has I_h symmetry, with a structure that is characterized by 12 pentagons isolated by two rings of hexagons (Figure 3.8c). It is expected that in large endohedral systems the five pentagons found in the second ring around the central pentagon in the C_{40} motif (Figure 3.8a) will be substituted progressively by hexagons until reaching the C_{75} motif present in the I_h structure of C_{180} (Figure 3.8c). Indeed, all the pentagons in the endohedral fullerene $Sm_2@D_{3d}^{-\#822}C_{104}$ are surrounded by a second ring with four or less pentagons (Figure 3.7c). Superfullerene-like anions with icosahedral symmetry are also reported for some large inorganic anions, as the oxomolybdate $[Mo_{132}O_{372}-(CH_3COO)_{30}(H_2O)_{72}]^{42-}$ ^[41] and, more recently, the uranyl peroxide with 60 uranium atoms.^[42]

3.4. Connecting Orbital and Topological Rules

3.4.1. IPSI: a measure for the size and topology of the cages

The IPSI provides a measure for the separation among the twelve pentagons present in a fullerene cage. It has been shown that IPSI values correlate with the relative stability of charged cages for a given C_{2n} family, especially for tetra- and hexaanions due to the larger ability of pentagons to attract the extra negative charge.^[9] Thus, the larger the separation is, the smaller the Coulomb repulsion and the larger the stabilization are. **Figure 3.11** shows such correlations for the 24 IPR and 110 non-IPR cages with only one pair of adjacent pentagons (APP1) of the C_{84} family. It can be observed that the set of IPR cages group well separated from that of the APP1. The presence of one adjacent pentagon pair makes the IPSI larger for the APP1 set than for the IPR structures. Similarly, isomers with two pairs of adjacent pentagons (APP2) have their IPSI values well separated from those of the APP1 family. Therefore, the IPSI is able to classify the C_{2n} isomers according to their number of adjacent pentagon pairs.

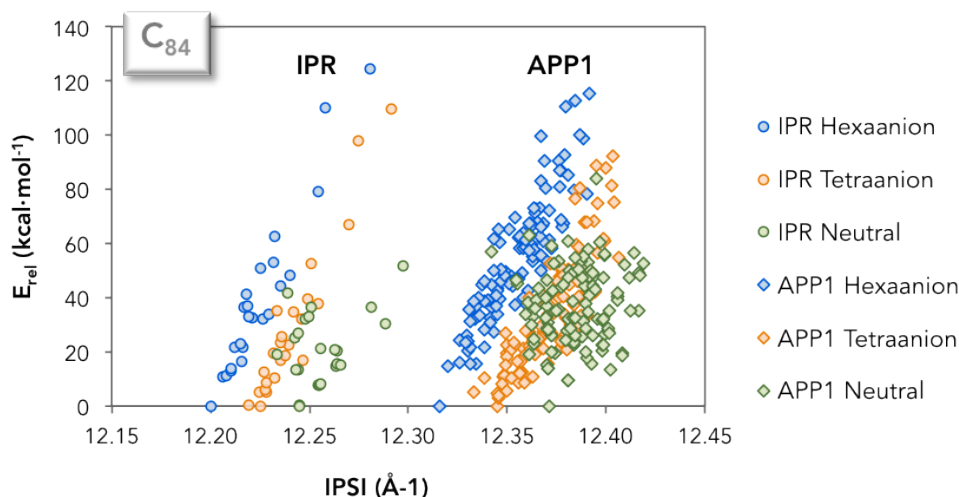


Figure 3.11. Relative stability ($\text{kcal}\cdot\text{mol}^{-1}$) for all the IPR (circles) and APP1 (diamonds) isomers of the C_{84} cage, with respect to the IPSI value. In green, neutral cages; in orange, tetraanionic cages; in blue, hexaanionic cages. The most stable IPR cages are **#23** (neutral and tetraanion) and **#21** (hexaanion); for non-IPR cages, **#51545** (neutral), **#51383** (tetraanion) and **#51365** (hexaanion).

For each of the IPR and APP1 sets, the relative energies of hexaanions and tetraanions correlate with IPSI (Figure 3.11). For neutral cages, a larger dispersion of the

points is observed in both sets since minimization of the steric strain is more important than minimization of the Coulomb repulsion. It is interesting to point out that for each isomer within the IPR or APP1 sets, as the negative charge increases, the IPSI value decreases – compare orange and blue circles for IPR or orange and blue diamonds for APP1 in Figure 3.11. Such increase of charge, which resides preferentially on pentagons, induces a larger separation among them so as to minimize the repulsion and, consequently, a lower value for IPSI. Hence, an increase of the volume of the cage is also reflected in the IPSI parameter.

The correlation between IPSI and the volume of the cage can also be observed in the $M_3N@I_h-C_{80}$ series ($M = Sc, Y, Gd, La$). An increase of the radius of the metal ion entails a larger deformation of the I_h-C_{80} cage, *i.e.* an increase of its volume, and consequently smaller values for IPSI as shown in Table 3.5. The empty cage shows the largest IPSI value. Only the case when $M = Y$, with very similar radius as Gd , does not fit so well into a linear correlation.

Table 3.5. IPSI and ionic radii values for $M_3N@I_h-C_{80}$ ($M = Sc, Lu, Y, Gd, La$).

	M Radii (Å)	IPSI (Å ⁻¹)		M Radii (Å)	IPSI (Å ⁻¹)
Empty	–	12.569	Y₃N	1.16	12.441
Sc₃N	1.01	12.491	Gd₃N	1.19	12.450
Lu₃N	1.12	12.462	La₃N	1.30	12.435

The relative stability of charged fullerenes was shown to be also correlated with the number of pyracylene units.^[9] The pyracylene motif places two pentagons as close together as possible while avoiding direct pentagon-pentagon adjacencies. Hence, the pyracylene motif is not the best disposition to obtain maximal separation between two neighboring pentagons. Thus, those cages with low number of pyracylene units are the most suitable ones to encapsulate metallic clusters. Since both the IPSI and the number of pyracylene units provide information about the separation among pentagons in a given C_{2n} family, these two parameters must be correlated. Figure 3.12 shows that for hexaanionic IPR C_{80} to C_{100} cages such a correlation exists. We have only taken into account hexaanionic cages because they are the most appropriate to be described by the “Maximum Pentagon Separation Rule”. Whereas a clear correlation is observed for the C_{80} family, larger dispersion is found for the largest systems, especially for the highest-energy hexaanionic cages with a large number of pyracylene motifs. This result is in agreement

with the fact that the predictive power of these two parameters decreases when the cage size increases.

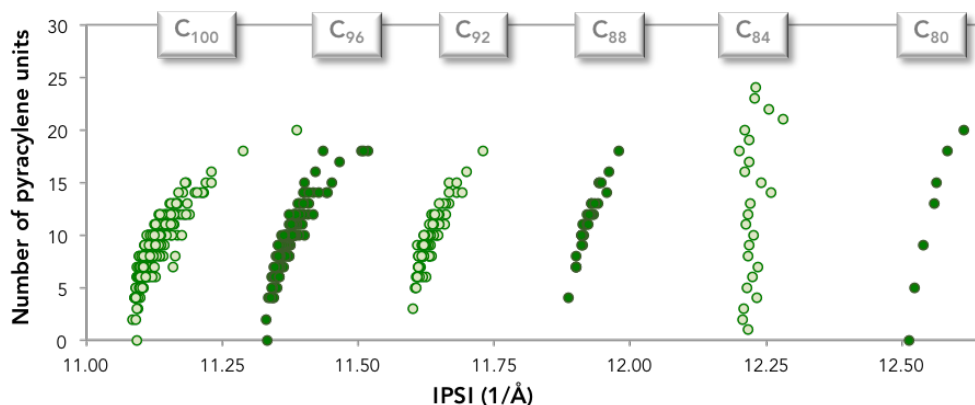


Figure 3.12. Correlation between IPSI and the number of pyracylene units for C_{80} to C_{100} IPR cages.

3.4.2. Orbital and topological rules: is there a connection?

All the nitride EMFs whose structures have been characterized by single crystal X-ray diffraction satisfy the orbital rule so far. Moreover, this rule has successfully predicted the cage isomers in $La_3N@C_{92}$, $La_3N@C_{96}$ and $La_2@C_{100}$, which have been recently characterized by electrochemical measurements^[37] or X-ray crystallography for the latter case.^[43]

It has been observed that the energies of the LUMO orbitals hardly change for different endohedral metallofullerenes or negatively charged empty cages.^[44] On the other hand, significant changes are detected on the three highest-occupied orbitals of the fullerene anions, which are occupied once the transfer of six electrons takes place. These results are in agreement with the changes found in the experimental reduction and oxidation potentials of nitride EMFs.^[44] This evidence shows that the different HOMO-LUMO gaps in such systems are basically affected by the change of the HOMO energies. A plot of the relative energies of the hexaanionic cages for the IPR C_{80} , C_{88} and C_{96} families with respect to the HOMO-LUMO gaps, which are equivalent to the gaps between the LUMO+2 and LUMO+3 in the neutral cages, is depicted in Figure 3.13 left. The plot clearly shows that the cages with the largest HOMO-LUMO gap are among the most stable isomers in all the three families, which is in agreement with the “(LUMO+3) – (LUMO+2) rule”. However, no clear correlation for cages with smaller HOMO-LUMO gaps exists. Since the orbital rule requires three low-lying unoccupied orbitals of

the neutral cage, we have also plotted the relative stabilities of the hexaanions with respect to the average energy of their three highest-occupied orbitals, *i.e.* those that accept the six electrons. Interestingly, much better correlations are observed (Figure 3.13 right). Therefore, the lower the energies of the three HOMOs are, the higher the stabilization of the hexaanion. However, it also happens that the almost-linear trend observed for C_{80} is progressively lost for larger cages. Thus, in terms of thermodynamic stability, the energies of the three orbitals that are to be occupied after the electron transfer are more significant than the HOMO-LUMO gap. Large HOMO-LUMO gaps are consequence of low-energy HOMOs.

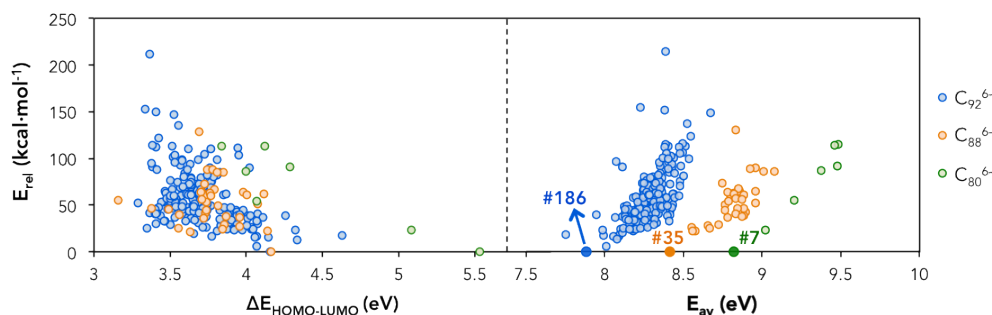


Figure 3.13. Correlation between the relative energies of hexaanions for the C_{80} (green), C_{88} (orange) and C_{96} (blue) families and (a) the orbital HOMO-LUMO gaps; (b) the average of the energies of the three highest-occupied molecular orbitals. The most stable cages are identified by their isomer number.

Finally, we would like to point out the correlation that exists between the IPSI and the average energy of the three HOMOs for the different C_{2n} families analyzed throughout this work (Figure 3.14). As for previous analysis, the correlation is gradually lost as the size of the cage increases. This last correlation links the orbital rule based on energy gaps and the topological rule, which explains the physics of the problem.

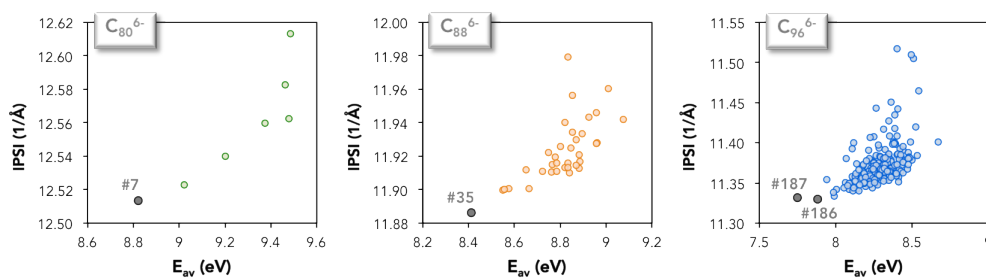


Figure 3.14. Correlation between the average energy of the three HOMOs with IPSI for the C_{80} , C_{88} and C_{96} families. The most stable cages for each family are identified by their isomer number.

3.4.3. IPR versus non-IPR cages: the importance of the charge transfer

The isolated pentagon rule (IPR) and the intimately related pentagon adjacency penalty rule (PAPR) indicate that the presence of adjacent pentagon pairs destabilizes the structure of the fullerene cages due to an increase of the steric strain.^[15] In particular, a destabilization of 19–24 kcal·mol⁻¹ per APP was proposed.^[45] All the neutral and non-functionalized C_{2n} fullerenes (2n ≥ 60) characterized so far present IPR cages, in good agreement with the abovementioned rules. As first seen in 2000 and confirmed during the last decade, endohedral metallofullerenes may show non-IPR cages with a reduced number of APP (up to three).^[16] Moreover, some functionalized fullerenes have been found to present non-IPR cages, such as the chlorinated C₇₂Cl₄, which has a cage with one APP.^[46] All of these non-IPR cages have been found for middle-sized fullerenes (66 < 2n < 84), where the number of IPR isomers is small or even null. As shown previously, the charge transfer from the internal metal cluster to the carbon cage is the main cause for such stabilization. Bonds at pentagon-pentagon junctions, [5,5] bonds, are more electrophilic than [5,6] and [6,6] bonds. Consequently, non-IPR cages localize more negative charge on pentagons than IPR structures do.^[9]

Figure 3.15a shows that most of the 24 neutral IPR structures of C₈₄ present lower energies than the 110 non-IPR structures with a single APP, as predicted by the isolated pentagon rule. The difference between average values for the energies of the two sets is 45 kcal·mol⁻¹ at the semiempirical AM1 level for the neutral cages. For the hexaanions (Figure 3.15c), the energies of the two sets overlap and the difference between their average energies decreases to 19 kcal·mol⁻¹. Apart from this significant reduction on the energy difference, it is important to remark that there is one non-IPR isomer, C_s^{-#51365}C₈₄, which is competitive with the lowest-energy IPR hexaanion, D₂^{-#21}C₈₄ (only 1 kcal·mol⁻¹ higher in energy). This non-IPR cage is ultimately selected due to the extra stabilization gained by the coordination of the M₃N cluster to the pentalene bond. A similar type of analysis was also carried out for the C₉₂ family. Most of the 86 IPR cages are found to be considerably more stable than the 840 non-IPR structures with one APP, with an energy difference between the average values around 31 kcal·mol⁻¹ for the neutral cages (Figure 3.15b). This value, which is somewhat smaller than that found for the C₈₄ family, and the larger overlap observed for the two sets point to a slight reduction of the strain energy in APP1 cages as their sizes increase. For the hexaanions, the average energy difference is also reduced, but only by 6 kcal·mol⁻¹. Now, the points of the two sets do not overlap so much as for the C₈₄ family and the IPR structures clearly show the lowest energies without any competitive non-IPR cage

(Figure 3.15d). With such a sizable number of IPR isomers (86), it is more likely to have some structure with the appropriate topology, i.e. low IPSI and low number of pyracylene motifs, to accept the formal transfer of four or six electrons. Larger cages ($2n > 92$) show a similar behavior because the number of IPR isomers is large enough to have structures with low number or even zero pyracylene motifs – for example, 1 cage for C_{100} and three cages for C_{104} . This is the reason why non-IPR cages have not been observed so far (and most likely will not be observed with the present synthetic procedures) for EMFs with large-size cages.

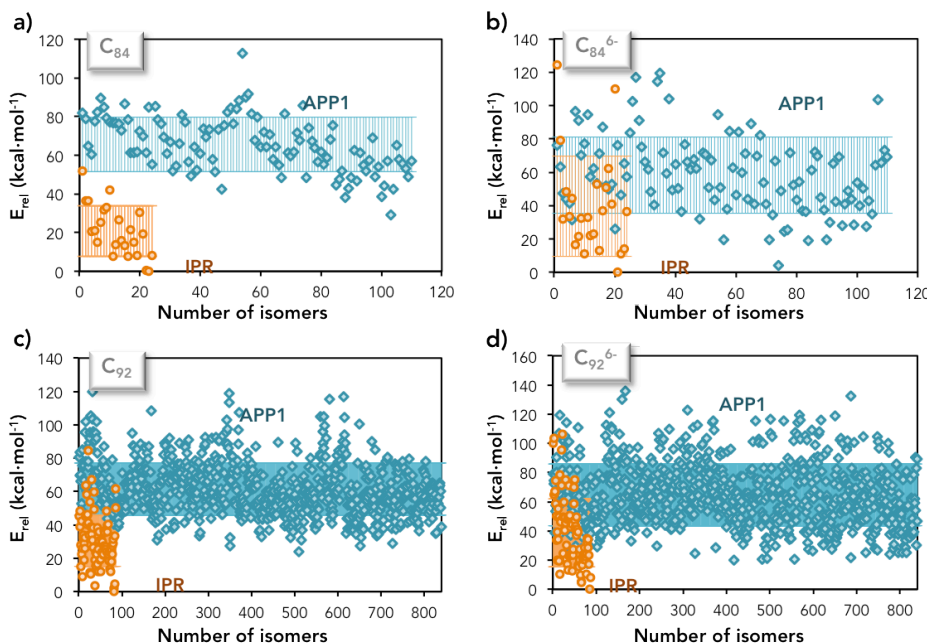


Figure 3.15. AM1 relative energies for IPR and non-IPR structures with one adjacent pentagon pair (APP1) for C_{84} and C_{92} families for the neutral (left) and hexaanionic (right) cages.

3.5. Conclusions

Despite many efforts by experimental and theoretical groups, our understanding as to why a particular IPR or non-IPR fullerene is observed in a given endohedral fullerene is still not completely achieved. To rationalize the factors that govern endohedral fullerene stability, we carried out a systematic study on fullerene hexaanions from C_{78} to C_{104} . The main result is that we have formulated the maximum pentagon separation rule, which describes the physics of fullerene stabilization by

requiring maximal separation among the 12 pentagons. Thanks to the highest pyramidalizations of carbon atoms that belong to pentagons, the negative charge in anionic fullerenes tends to add in the pentagons and favor the stability of cages that have the largest separation among the 12 pentagons. Consequently, the most favorable IPR fullerenes are those with low values of the IPSI or a low number of pyracylene motifs. In this context, fullerenes with icosahedral symmetry show the optimal distribution of 12 pentagons, what explains why endohedral fullerenes based on the I_h - C_{80} cage are the most abundant fullerenes after C_{60} and C_{70} .

It is well established that empty non-IPR fullerenes are, in general, very unstable. Some isomers with a small number of APPs can have relative low energy in their anionic forms thanks to their capacity for accumulating charge density in the adjacent pentagons, especially in the [5,5]-bonds. We predict that violations of the IPR rule will occur only in those C_{2n} fullerenes with IPR isomers that contain large numbers of pyracylene units.

The IPSI, which is a measure of the separation among the twelve pentagons in a fullerene, is able to distinguish between IPR structures and those that show other topologies with one or more pairs of adjacent pentagons. Moreover, it provides an indirect measure of the change in the size or volume of the cage when comparing empty cages with different negative charges or endohedral metallofullerenes with different metal atoms inside. IPSI correlates with the number of pyracylene motifs, since the two parameters give information about the separation among pentagons in a fullerene.

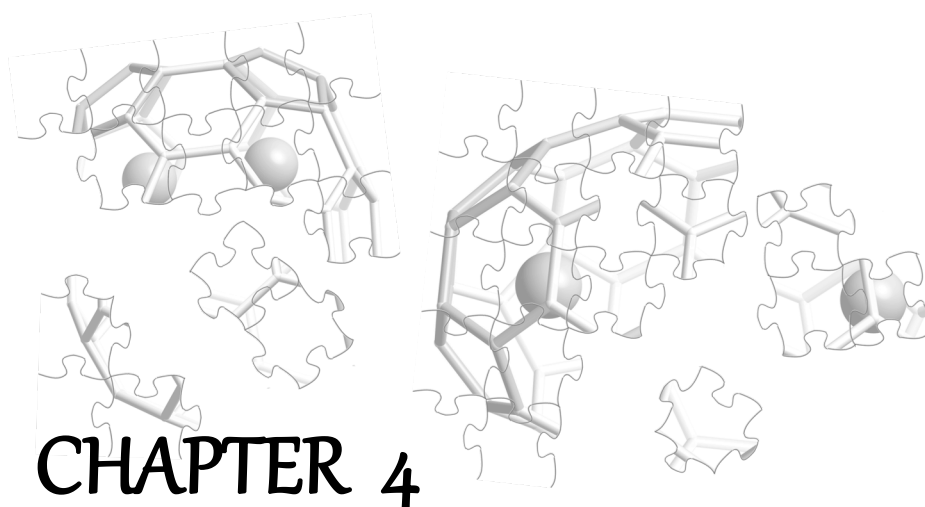
A connection between the orbital and topological rules is found: the more separated the pentagons in the fullerene cage are, the lower the energies of the cage orbitals that accept the electrons. Finally, an explanation for the absence of non-IPR cages in large-size EMFs is also provided. Among the large number of IPR structures in these families, the occurrence of a cage with the appropriate topology to encapsulate a metal cluster is highly probable.

3.6. Bibliography

- [1] R. Valencia, A. Rodríguez-Forteza, J. M. Poblet, *Chem. Commun.* (2007), 4161.
- [2] K. M. Kadish, F. S. Ruoff, *Fullerenes: Chemistry, Physics and Technology*, Wiley-Interscience, (2000).
- [3] J. M. Campanera, C. Bo, J. M. Poblet, *Angew. Chem. Int. Ed.* (2005), 44, 7230.
- [4] R. Valencia, A. Rodríguez-Forteza, J. M. Poblet, *J. Phys. Chem. A* (2008), 112, 4550.
- [5] A. Popov, S. Yang, L. Dunsch, *Chem. Rev.* (2013), 113, 5989.
- [6] A. A. Popov, L. Dunsch, *J. Am. Chem. Soc.* (2007), 129, 11835.
- [7] K. Raghavachari, *Chem. Phys. Lett.* (1992), 190, 397.
- [8] H. Zettergren, M. Alcamí, F. Martín, *Chem. Phys. Chem* (2008), 9, 861.
- [9] A. Rodríguez-Forteza, N. Alegret, A. L. Balch, J. M. Poblet, *Nature Chem.* (2010), 2, 955.
- [10] a) C. Wang, T. Kai, T. Tomiyama, T. Yoshida, Y. Kobayashi, E. Nishibori, M. Takata, M. Sakata, H. Shinohara, *Nature* (2000), 408, 426; b) S. Stevenson, P. W. Fowler, T. Heine, J. C. Duchamp, G. Rice, T. Glass, K. Harich, E. Hajdu, R. Bible, H. C. Dorn, *Nature* (2000), 408, 427.
- [11] *Gaussian 09, Revision A.1*. M. J. Frisch, G. W. Trucks, H. B. Schlegel, G. E. Scuseria, M. A. Robb, J. R. Cheeseman, G. Scalmani, V. Barone, B. Mennucci, G. A. Petersson, H. Nakatsuji, M. Caricato, X. Li, H. P. Hratchian, A. F. Izmaylov, J. Bloino, G. Zheng, J. L. Sonnenberg, M. Hada, M. Ehara, K. Toyota, R. Fukuda, J. Hasegawa, M. Ishida, T. Nakajima, Y. Honda, O. Kitao, H. Nakai, T. Vreven, J. J. A. Montgomery, J. E. Peralta, F. Ogliaro, M. Bearpark, J. J. Heyd, E. Brothers, K. N. Kudin, V. N. Staroverov, R. Kobayashi, J. Normand, K. Raghavachari, A. Rendell, J. C. Burant, S. S. Iyengar, J. Tomasi, M. Cossi, N. Rega, J. M. Millam, M. Klene, J. E. Knox, J. B. Cross, V. Bakken, C. Adamo, J. Jaramillo, R. Gomperts, R. E. Stratmann, O. Yazyev, A. J. Austin, R. Cammi, C. Pomelli, J. W. Ochterski, R. L. Martin, K. Morokuma, V. G. Zakrzewski, G. A. Voth, P. Salvador, J. J. Dannenberg, S. Dapprich, A. D. Daniels, Ö. Farkas, J. B. Foresman, J. V. Ortiz, J. Cioslowski, D. J. Fox, Gaussian, Inc, Wallingford CT, (2009).
- [12] a) E. J. Baerends, D. E. Ellis, P. Ros, *ADF 2007.01, Department of Theoretical Chemistry*, Vrije Universiteit: Amsterdam; b) G. t. Velde, F. M. Bickelhaupt, E. J. Baerends, C. F. Guerra, S. J. A. v. Gisbergen, J. G. Snijders, T. Ziegler, *J. Comput. Chem.* (2001), 22, 932.
- [13] A. D. Becke, *Phys. Rev. A* (1988), 38, 3098.
- [14] J. P. Perdew, *Phys. Rev. B* (1986), 33, 8822.
- [15] P. W. Fowler, D. E. Manolopoulos, *An Atlas of Fullerenes*, Oxford University Press, Oxford, (1995).

- [16] Y. Z. Tan, S. Y. Xie, R. B. Huang, L. S. Zheng, *Nature Chem.* (2009), 1, 450.
- [17] K. Morokuma, *J. Chem. Phys.* (1971), 55, 1236.
- [18] J. M. Poblet, X. Lopez, C. Bo, *Chem. Soc. Rev.* (2003), 32, 297.
- [19] B. Q. Mercado, C. M. Beavers, M. M. Olmstead, M. N. Chaur, K. Walker, B. C. Holloway, L. Echegoyen, A. L. Balch, *J. Am. Chem. Soc.* (2008), 130, 7854.
- [20] Z. Q. Shi, X. Wu, C. R. Wang, X. Lu, H. Shinohara, *Angew. Chem. Int. Ed.* (2006), 45, 2107.
- [21] S. Yang, A. A. Popov, L. Dunsch, *Angew. Chem. Int. Ed.* (2007), 46, 1256.
- [22] N. Chen, M. Mulet-Gas, Y. Y. Li, R. E. Stene, C. W. Atherton, A. Rodriguez-Forteza, J. M. Poblet, L. Echegoyen, *Chem. Sci.* (2013), 4, 180.
- [23] N. Chen, C. Beavers, M. Mulet-Gas, A. Rodríguez-Forteza, E. Munoz, Y. Y. Li, M. Olmstead, A. Balch, J. M. Poblet, L. Echegoyen, *J. Am. Chem. Soc.* (2012), 134, 7851.
- [24] T. Wakahara, H. Nikawa, T. Kikuchi, T. Nakahodo, G. Rahman, T. Tsuchiya, Y. Maeda, T. Akasaka, K. Yoza, E. Horn, K. Yamamoto, N. Mizorogi, Z. Slanina, S. Nagase, *J. Am. Chem. Soc.* (2006), 128, 14228.
- [25] a) H. Kato, A. Taninaka, T. Sugai, H. Shinohara, *J. Am. Chem. Soc.* (2003), 125, 7782; b) M. Yamada, T. Wakahara, T. Tsuchiya, Y. Maeda, T. Akasaka, N. Mizorogi, S. Nagase, *J. Phys. Chem. A* (2008), 112, 7627.
- [26] S. Yang, A. Popov, L. Dunsch, *J. Phys. Chem. B* (2007), 111, 13659.
- [27] a) C. Beavers, M. Chaur, M. Olmstead, L. Echegoyen, A. Balch, *J. Am. Chem. Soc.* (2009), 131, 11519; b) A. Popov, M. Krause, S. Yang, J. Wong, L. Dunsch, *J. Phys. Chem. B* (2007), 111, 3363; c) Y. Ma, T. Wang, J. Wu, Y. Feng, W. Xu, L. Jiang, J. Zheng, C. Shu, C. Wang, *Nanoscale* (2011), 3, 4955.
- [28] W. Jingyi, W. Taishan, M. Yihan, J. Li, S. Chunying, W. Chunru, *J. Phys. Chem. C* (2011), 115, 23755.
- [29] C. M. Beavers, T. Zuo, J. C. Duchamp, K. Harich, H. C. Dorn, M. M. Olmstead, A. L. Balch, *J. Am. Chem. Soc.* (2006), 128, 11352.
- [30] a) M. M. Olmstead, A. de Bettencourt-Dias, J. C. Duchamp, S. Stevenson, D. Marciu, H. C. Dorn, A. L. Balch, *Angew. Chem. Int. Ed.* (2001), 40, 1223; b) M. Yamada, T. Akasaka, S. Nagase, *Acc. Chem. Res.* (2010), 43, 92.
- [31] S. Stevenson, G. Rice, T. Glass, K. Harich, F. Cromer, M. R. Jordan, J. Craft, E. Hadju, R. Bible, M. M. Olmstead, K. Maitra, A. J. Fisher, A. L. Balch, H. C. Dorn, *Nature* (1999), 401, 55.
- [32] T. Cai, L. Xu, M. R. Anderson, Z. Ge, T. Zuo, X. Wang, M. M. Olmstead, A. L. Balch, H. W. Gibson, H. C. Dorn, *J. Am. Chem. Soc.* (2006), 128, 8581.

- [33] a) S. Stevenson, M. A. Mackey, M. A. Stuart, J. P. Phillips, M. L. Easterling, C. J. Chancellor, M. M. Olmstead, A. L. Balch, *J. Am. Chem. Soc.* (2008), *130*, 11844; b) B. Q. Mercado, M. M. Olmstead, C. M. Beavers, M. L. Easterling, S. Stevenson, M. A. Mackey, C. E. Coumbe, J. D. Phillips, J. P. Phillips, J. M. Poblet, A. L. Balch, *Chem. Commun.* (2010), *46*, 279.
- [34] M. M. Olmstead, A. de Bettencourt-Dias, S. Stevenson, H. C. Dorn, A. L. Balch, *J. Am. Chem. Soc.* (2002), *124*, 4172.
- [35] Y. Iiduka, T. Wakahara, K. Nakajima, T. Nakahodo, T. Tsuchiya, Y. Maeda, T. Akasaka, K. Yoza, M. Liu, N. Mizorogi, S. Nagase, *Angew. Chem. Int. Ed.* (2007), *46*, 5562.
- [36] T. Zuo, C. M. Beavers, J. C. Duchamp, A. Campbell, H. C. Dorn, M. M. Olmstead, A. L. Balch, *J. Am. Chem. Soc.* (2007), *129*, 2035.
- [37] M. Chaur, R. Valencia, A. Rodríguez-Forteza, J. Poblet, L. Echegoyen, *Angew. Chem. Int. Ed.* (2009), *48*, 1425.
- [38] H. Yang, C. Lu, Z. Liu, H. Jin, Y. Che, M. M. Olmstead, A. L. Balch, *J. Am. Chem. Soc.* (2008), *130*, 17296.
- [39] Y. Che, H. Yang, Z. Wang, H. Jin, Z. Liu, C. Lu, T. Zuo, H. C. Dorn, C. M. Beavers, M. M. Olmstead, A. L. Balch, *Inorg. Chem.* (2009), *48*, 6004.
- [40] B. Mercado, A. Jiang, H. Yang, Z. Wang, H. Jin, Z. Liu, M. Olmstead, A. Balch, *Angew. Chem. Int. Ed.* (2009), *48*, 9114.
- [41] A. Müller, E. Krickemeyer, H. Bögge, M. Schmidtman, F. Peters, *Angew. Chem. Int. Ed.* (1998), *37*, 3359.
- [42] G. Sigmon, D. Unruh, J. Ling, B. Weaver, M. Ward, L. Pressprich, A. Simonetti, P. Burns, *Angew. Chem. Int. Ed.* (2009), *48*, 2737.
- [43] C. Beavers, H. Jin, H. Yang, Z. Wang, X. Wang, H. Ge, Z. Liu, B. Mercado, M. Olmstead, A. Balch, *J. Am. Chem. Soc.* (2011), *133*, 15338.
- [44] R. Valencia, A. Rodríguez-Forteza, A. Clotet, C. de Graaf, M. Chaur, L. Echegoyen, J. M. Poblet, *Chem. Eur. J.* (2009), *15*, 10997.
- [45] E. Albertazzi, C. Domene, P. W. Fowler, T. Heine, G. Seifert, C. Van Alsenoy, F. Zerbetto, *Phys. Chem. Chem. Phys.* (1999), *1*, 2913.
- [46] a) Y. Z. Tan, T. Zhou, J. Bao, G. J. Shan, S. Y. Xie, R. B. Huang, L. S. Zheng, *J. Am. Chem. Soc.* (2010), *132*, 17102; b) K. Ziegler, A. Mueller, K. Amsharov, M. Jansen, *J. Am. Chem. Soc.* (2010), *132*, 17099.



*Looking for the identity of the
first non-IPR $\text{Sc}_2@C_{66}$*

CHAPTER 4

Looking for the identity of the first non-IPR $\text{Sc}_2@C_{66}$

The path to understand the EMFs and find a computational methodology to accurately predict them has been complicated and not trivial in the beginnings. Luckily, the initial studies of EMFs was very fruitful, quite important advances were performed, and it seems that the synthesized cages could be predicted without major complications. And I used to feel like that until I faced the $\text{Sc}_2@C_{66}$ system. This chapter has history in my scientific life. I began it at 2010, and although it was not a hot topic in fullerenes research, some experimentalists found it really interesting when I presented it in the ISI congress at Puerto Rico. This is not the typical novel cage discovery, but the first non-IPR isomer, who had never had a clear ID number. Experiments and calculations don't match this time, and both of them fail in some aspects. During the last years we have been trying to unravel the discrepancies that appear, we really wished to find the solution, and realized that this is an impossible dream without the help of more experiments. Now, at the end of my PhD, it's time to me to release it. Our last wish about this never-ending story is to convince any experimentalist to synthesize again the cage and, hopefully, get a good crystal.

4.1. Discrepancies in the cage assignments

We have already seen that the difficulties working with fullerenes mainly come from the low yield obtained from the arc, which in the case of EMFs is usually in the order of the milligrams. In addition, such a small yield is not composed of a

single cage, but of lots of different empty and endofullerenes. Thus, the purification and characterization processes are arduous, and sometimes even impossible. A good example is one of the two firsts non-IPR cages discovered, $\text{Sc}_2@C_{66}$. In 2000, Shinohara and co-workers recovered only 2 mg of $\text{Sc}_2@C_{66}$ material from the 800 g of soot obtained from the arc-discharge reactor. Even so, ^{13}C -NMR and synchrotron X-ray powder diffraction analyses were carried out, and the cage assignment for this first non-IPR structure was the isomer $\text{C}_{2v}\text{-}\#4348$.^[1] This proposed cage has the two Sc atoms inside the carbon structure and close to the two-pentylene fusions, as shown in Figure 4.1.

Two years later, Nagase and co-workers published a computational study of this system. Surprisingly, the proposed structure by Shinohara appeared not to be an energy minimum.^[2] After an extensive analysis of several orientations of the metal cluster and other possible candidates, they concluded that the most probable cage to encapsulate Sc_2 is the isomer $\text{C}_{2v}\text{-}\#4059$ (Figure 4.1), which completely agrees with the experimental ^{13}C -NMR spectrum. This new structure allows a larger separation between the two metal atoms, thus reducing their inherent repulsion present in the first proposal. However, the MEM/Rietveld analysis from the X-ray powder diffraction data performed by Shinohara didn't match Nagase's choice.^[3]

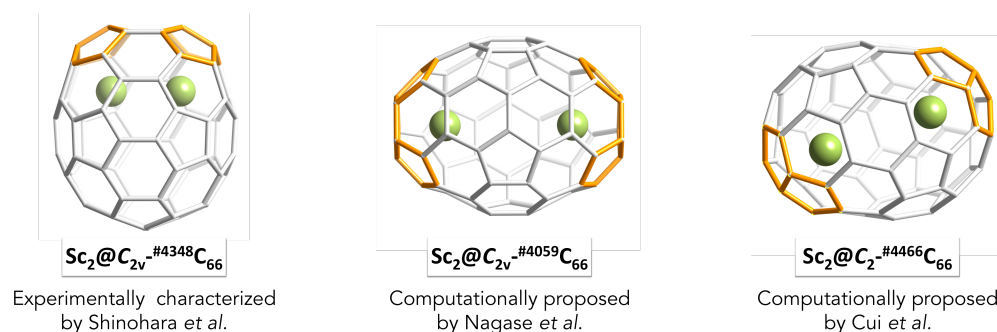


Figure 4.1. The different experimental and computational cage isomer assignments for $\text{Sc}_2@C_{66}$ since its discovery in 2000. In orange, the [5,5] pentylene bonds.

Not only the structure of the cage was under discussion between the two groups, but also the charge transfer present from the metal cluster to the cage. Shinohara, based on *ab initio* calculations, observed a formal charge transfer of two electrons, and defined the system as $\text{Sc}_2^{2+}@C_{66}^{2-}$.^[1] On the other side, Nagase guaranteed that such systems are formally described as $\text{Sc}_2^{6+}@C_{66}^{6-}$. Even more, in his calculations of the empty anionic systems, he didn't consider the C_{66}^{2-} isomers.^[2]

The cage mismatch was forgotten for several years, and the experimental assignment was usually assumed. However, in 2009 Cui *et al.* reopened the case and, based on theoretical calculations, proposed a third isomer $C_{2-}^{\#4466}$ to capture Sc_2 .^[4] As shown in Figure 4.1, this new cage has two pairs of adjacent pentagons, as the experimental cage, although its C_2 symmetry did satisfy neither the experimental ^{13}C -NMR spectra nor the diffraction results.

Since its birth, the structure of $Sc_2@C_{66}$ has become a matter of discrepancy and, up to date, no final and definitive conclusion is undeniable yet. Therefore, experiments and computations do not agree in the characterization of this pristine EMF, although someone may have misunderstood some parts of the discussion and assures that both Nagase and Shinohara's conclusions lead to the same **#4348** isomer.^[5] With this project we have tried to understand and collect all the pieces of the puzzle to make the scientific community realize about the problem. As well, we provide new computational analyses and data to encourage the experimentalists working with fullerene production to reconsider the problem and re-synthesize and elucidate the $Sc_2@C_{66}$ metallofullerene.

4.2. Computational Details

All calculations have been performed with the combined use of Gaussian-09, TurboMole-6.3 and ADF 2009. Optimizations of all the empty anionic cages were performed using semi-empirical AM1 calculations with the Gaussian-09 code.^[6] The most stable cages were recomputed as anions and EMFs with the hybrid functional B3LYP and the Ahlrichs def-TZVP basis set,^[7] using the TurboMole-6.3 program.^[8]

In order to determine the formal charge transfer of the EMFs, orbital analyses were carried out with the TurboMole-6.3 package. Additionally, the results obtained were confirmed by fragment calculations carried out with the ADF 2009 code at the B3LYP/TZP level of theory.^[9] We have defined two fragments: the cluster – Sc_2 or Sc_2C_2 – and the empty cage – C_{66} or C_{64} . This fragment option in ADF allows us to tell the program which atoms belongs to each fragment and, therefore, obtain the contribution of each fragment to the molecular orbitals of the whole system.

The vibrational frequencies and the corresponding normal modes were calculated using the harmonic approach. Relative abundances along the range of temperatures were obtained from the rigid rotor and harmonic oscillator (RRHO) and the related free-encapsulating model (FEM). In the FEM model we consider that if at high temperature the cluster rotates freely inside the cage, its contribution to the

partition function will be similar for the different cages and will cancel out. The predicted IR spectra were plotted with the Lorentzian distribution function using a line width of 20 cm^{-1} .

4.3. Looking for the empty anionic cage

4.3.1. The 4478 isomers of C_{66}^{6-}

There are no IPR structures among the 4478 isomers of C_{66}^{6-} .^[10] In particular, none of them is APP1-type ($N_p=1$), and the lowest number of pentagon adjacencies found is two. There are three APP2 ($N_p=2$) isomers, two of which are the **#4348** and the **#4466** isomers, proposed by Shinohara and Cui, respectively. Then, 26 APP3 ($N_p=3$) and 176 APP4 ($N_p=4$) isomers can be formed – a complete list of the number of isomers of each APP can be found in Table A1.

We have first evaluated the 4478 isomers of C_{66}^{6-} by AM1 optimizations. The plot of these results is presented in Figure 4.2, and a complete list of values and some structural parameters can be found in Table A1. According to the ionic model, we have chosen the hexaanionic charge since Sc clusters have been predicted to transfer usually 3 electrons per metal (*vide infra*).^[11] The plot in Figure 4.2 shows a rough decrease of the energy while the isomer numbering increases. Isomer **#4059** – proposed by Nagase – lies out this trend and becomes the most stable hexaanion, followed by the last in the list isomers at more than $4 \text{ kcal}\cdot\text{mol}^{-1}$ (see

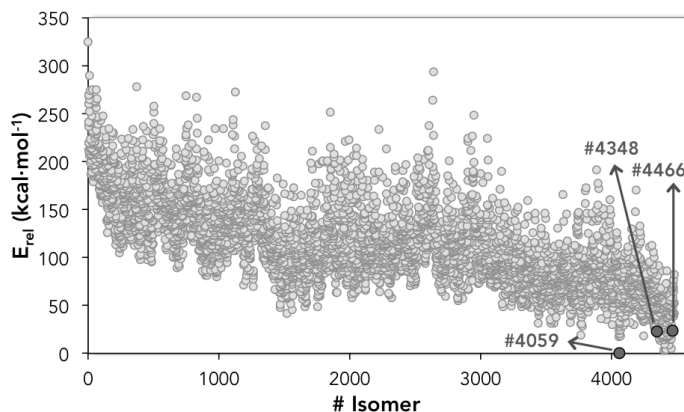


Figure 4.2. Relative stability for 4478 isomers of C_{66}^{6-} , at the AM1 level of theory. The most stable and most relevant isomers are highlighted in dark grey.

Table A2). Cages **#4348** and **#4466** lie among the 30 most stable isomers, with relative energies of 22.5 and 23.7 kcal·mol⁻¹, respectively.

We have observed a correlation between the relative energy and the number of adjacent pentagon pairs (APP), the N_p number defined by Ragavachari (see section 1.1 and Table A2). Figure 4.3 shows that as the N_p number is increased, the hexaanions become unstable. Nevertheless, cages within the APP3 and the APP4 groups appear as the most stable ones, being the APP2 the third less energetic group. In addition, the IPSI value also correlates with the relative energy of the isomers, as shown in Figure 4.3, in good agreement with the Maximum Pentagon Separation Rule (see Chapter 3).

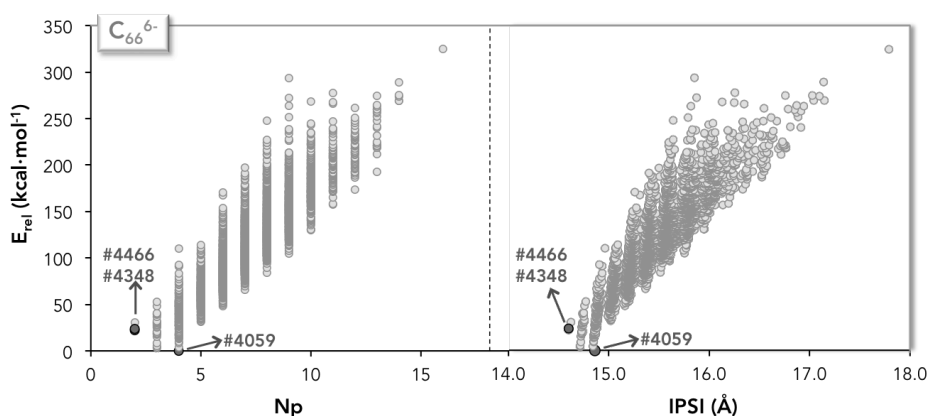


Figure 4.3. Relative stability of 4478 isomers of C_{66}^{6-} with respect the number of fused pentagons N_p (left, Raghavachari number, see section 1.1) and the IPSI (right).

The most stable cages at the AM1 level, as well as those under discussion, have been recomputed using a more accurate methodology at the B3LYP/def-TZVP level. Results are collected in Table 4.1, together with the energies obtained at the AM1 level. The relative energies of the isomers are essentially maintained with respect the AM1 results. The cage **#4059** is also the most stable one, in good agreement with Nagase's results, and isoenergetic to isomer **#4417**. The latter has never been studied in the previous works. Isomers proposed by Shinohara and Cui, **#4348** and **#4466**, respectively, are found at more than 20 kcal·mol⁻¹. So, we can confirm that AM1 calculations are, once again, reliable enough for a qualitative study of the empty pristine fullerene hexaanions.^[12]

Table 4.1. Relative energies (in kcal·mol⁻¹), computed at the B3LYP/def-TZVP, and several structural properties for the most stable isomers of C_{66}^{6-} according to the AM1 calculations (**Figure 4.2**).

Isomer	Proposed by	Symmetry	IPSI	N _p	AM1	B3LYP/TZVP
#4417		C ₂	14.85	4	4.0	0.0
#4059	Nagase ^[2]	C _{2v}	14.86	4	0.0	0.1
#4454		C ₂	14.72	3	5.2	2.8
#4437		C ₂	14.85	4	8.7	3.0
#4398		C ₁	14.71	3	3.3	3.9
#4410		C _s	14.71	3	4.0	4.6
#4407		C ₂	14.85	4	9.6	6.1
#4348	Shinohara ^[1]	C _{2v}	14.60	2	22.5	21.7
#4466	Cui ^[4]	C ₂	14.60	2	23.7	24.1
#4169		C _s	14.62	2	30.2	31.9

4.3.1. The carbide option: evaluation of C_{64}^{4-}

We have also considered the option that the experimental endofullerene could be the carbide $Sc_2C_2@C_{64}$, since several studies have demonstrated that in many cases what initially was described as an endofullerene with a dimetallic cluster inside was really a carbide EMF, and the two carbons of the cluster were mixed-up with the carbon skeleton during the characterization process.^[13] As with the larger system, we have first evaluated all the 3465 isomers of C_{64} . In this case, since scandium carbides transfer 4 electrons to the cage according to the ionic model, we have computed the tetraanionic species. As C_{66} , the C_{64} fullerene does not contain any IPR or single-fused pentagon bond isomer in its list. A complete classification according to the N_p number is collected in Table A1.

Our results, considering the tetraanionic cages, are plotted in Figure 4.4 – a complete data list can be found in Table A2. The most stable isomer is **#2983**, followed by **#3414** and **#3451** at 2.7 and 3.8 kcal·mol⁻¹, respectively (see Table A2).

The computational study of all the possible neutral C_{64} isomers has been previously performed by Cui and co-workers.^[14] They predicted that the isomer **#3451** is the most suitable to capture the scandium carbide. However, they didn't take into account the ionic model to evaluate the 3465 isomers – they do not consider the effect of the charge transfer –, so their final conclusions may not be reliable at all. It

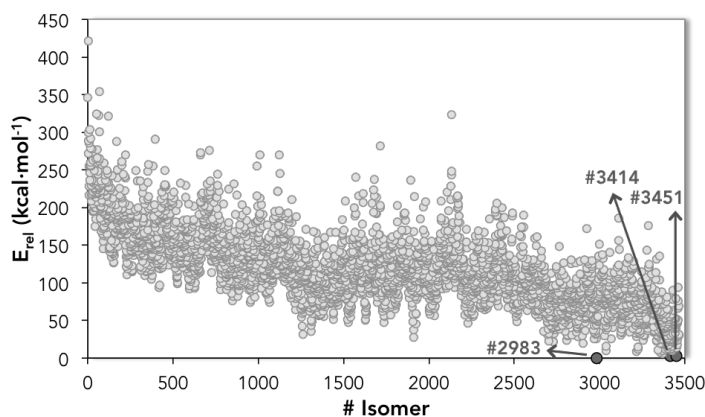


Figure 4.4. Relative stability for 3465 isomers of C_{64}^{4-} , at the AM1 level of theory. The most stable isomers are highlighted in dark grey.

is noteworthy to point out that this first set of results do not match the ones obtained by Cui and co-workers, meaning that the consideration of the ionic model in this kind of calculations is essential.

As with the C_{66} system, we have also observed that both the IPSI and the Raghavachari N_p factor correlate with the relative energy of the anions, as shown in Figure 4.5 (see section 1.2 and Chapter 3). Again, the most stable cages present the lowest number of adjacent pentagons – low N_p number – and the maximum separation among pentagons – low IPSI. This time, the three first APP groups (APP2, APP3 and APP4) are the most stable ones, within the same range of energy.

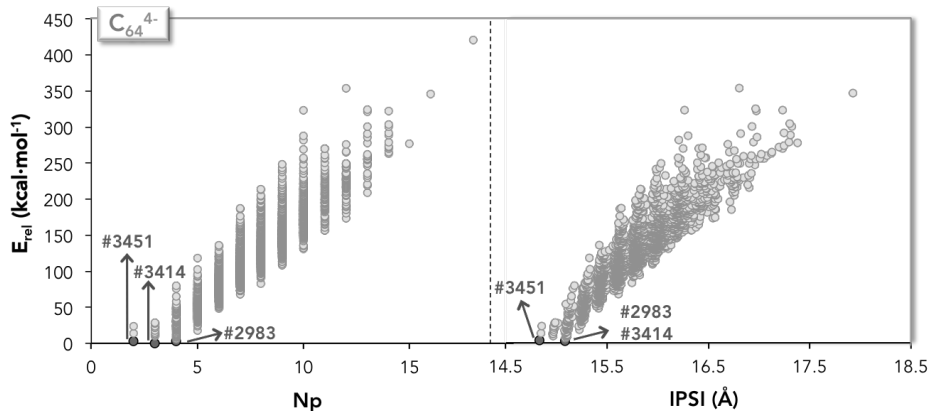


Figure 4.5. Relative stability of 3465 isomers of C_{64}^{4-} with respect the number of fused pentagons N_p (left, Raghavachari number, see section 1.1) and the IPSI value (right).

Finally, the most stable tetraanionic isomers were recomputed with a more accurate methodology by means of B3LYP/def-TZP. Results are collected in Table 4.2. It can be clearly seen that the energetic order of the cages is maintained with respect the AM1 calculations. The isomers **#3414** and **#2983** appear almost isoenergetic, with an energy difference of 1.5 kcal·mol⁻¹. Above, isomer **#3451** lays at 2.7 kcal·mol⁻¹. The remaining cages appear at more than 4 kcal·mol⁻¹.

Table 4.2. Relative energies (in kcal·mol⁻¹), computed at the B3LYP/def-TZVP, and several structural properties for the most stable isomers of C_{64}^{4-} according to the AM1 calculations (**Figure 4.4**).

Isomer	Symmetry	IPSI	Np	AM1	B3LYP/TZVP
#3414	D_{2d}	15.08	4	2.7	0.0
#2983	C_s	14.97	3	0.0	1.5
#3451	D_2	14.84	2	3.3	2.7
#3356	C_1	15.10	4	7.6	4.3
#3367	C_2	15.09	4	6.1	4.4
#3425	C_1	14.97	3	9.5	6.0
#3368	C_1	15.10	4	9.3	7.0
#3216	C_1	15.11	4	9.1	7.1
#3037	C_1	15.10	4	10.2	7.6
#3423	C_s	14.96	3	12.7	9.2
#3452	C_s	14.85	2	13.4	9.3
#3424	C_2	14.96	3	12.1	9.6

4.4. The endohedral fullerene

4.4.1. Relative stabilities and electronic structures of the lowest-energy EMFs

Since the non-IPR systems are stabilized by metal-pentalene interactions,^[11b] we have computed the endohedral species for the most stable empty C_{66} hexaanionic cages and the ones under discussion. Additionally, we have taken into account the carbide option and have therefore evaluated the carbide system $Sc_2C_2@C_{64}$ for the most stable C_{64} tetraanionic cages.

At first glance, we have performed MEP analyses to predict the metal position inside the fullerene cages. The MEPs were calculated from the empty anionic systems, and are drawn in Figure 4.6. Clearly, the most negative region inside the fullerenes is located in the center of the cage. Note that the red surface is polarized toward the [5,5] bonds. Hence, we have placed the metal atoms near the pentalene junctions and as much separated as possible between them.

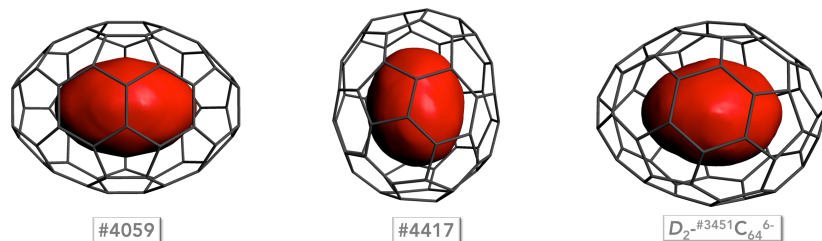


Figure 4.6. MEPs of the empty anionic systems.

Results collected in Table 4.3 show that the encapsulation of the cluster produces higher energy differences between isomers due to differential metal-pentalene interaction for the different isomers. For the $\text{Sc}_2@\text{C}_{66}$ species, the isomer **#4059** is the most stable one, in good agreement with Nagase's results. Then, isomer **#4417**, which was isoenergetic to the previous one without the dimetallic cluster,

Table 4.3. Relative energies (in $\text{kcal}\cdot\text{mol}^{-1}$), computed at the B3LYP/def-TZVP, and several properties for specific $\text{Sc}_2@\text{C}_{66}$ and $\text{Sc}_2\text{C}_2@\text{C}_{64}$ fullerene isomers.

Isomer	Proposed by	Symm	E_{rel}	Formal transfer	$d_{\text{Sc-Sc}}$ (Å)
$\text{Sc}_2@\text{C}_{66}$					
#4059	Nagase	C_{2v}	0.0	6 –	4.89
#4417		C_2	27.8	6 –	3.80
#4348 (vertical)		C_{2v}	39.9	6 –	3.90
#4466	Cui	C_2	44.0	6 –	3.99
#4348	Shinohara	C_{2v}	87.8	4 –	2.68
$\text{Sc}_2\text{C}_2@\text{C}_{64}$					
#2983		C_s	70.5	4 –	4.12
#3425		C_1	84.1	4 –	3.85
#3451	Cui	D_2	85.1	4 –	4.04

is found at nearly $28 \text{ kcal}\cdot\text{mol}^{-1}$. The proposed cage by Cui and co-workers **#4466** appears quite far in energy, at $44 \text{ kcal}\cdot\text{mol}^{-1}$, while the experimental characterized **#4348** cage lies almost at $88 \text{ kcal}\cdot\text{mol}^{-1}$. Regarding the $\text{Sc}_2\text{C}_2@C_{64}$ systems, the most stable carbide **#2983** appears at $71 \text{ kcal}\cdot\text{mol}^{-1}$ with respect the most stable $\text{Sc}_2@C_{2v}\text{-}\#4059C_{66}$ EMF. The remaining carbides, including the one proposed by Cui **#3451**, lay at more than $84 \text{ kcal}\cdot\text{mol}^{-1}$. Therefore, we can confirm that the carbide option for the Sc_2C_{66} system can be excluded since it is not competitive with the $\text{Sc}_2@C_{66}$ possibility. All the optimized structures are represented in Figure 4.7.

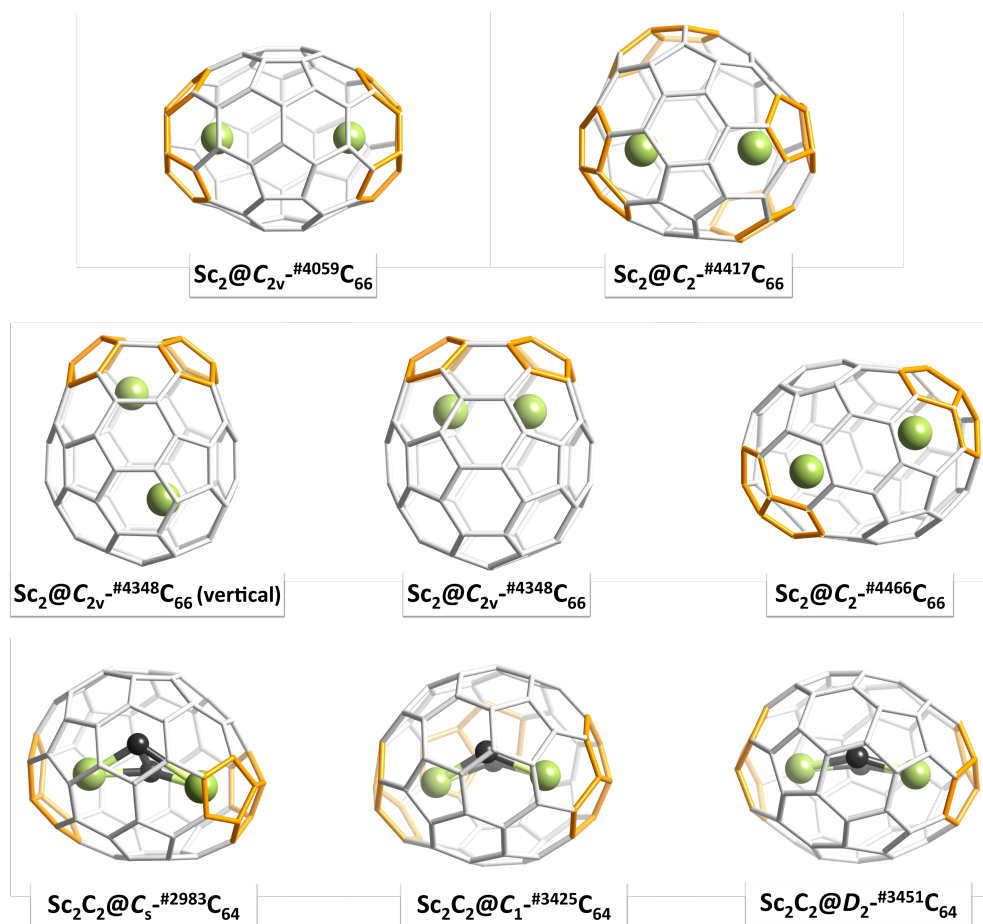


Figure 4.7. Optimized structures of the computed $\text{Sc}_2@C_{66}$ and $\text{Sc}_2C_2@C_{64}$ systems in Table 4.3.

According to Nagase,^[2] isomer **#4348** as described by Shinohara and drawn in Figure 4.1 does not appear as a minimum in the potential energy surface, since the repulsion between the two Sc atoms is too high – the distance between Sc atoms

is about 2.7 Å in the experimental cage, while it increases up to 4.89 Å in the **#4059** isomer. He also analyzed other conformations of the scandium cluster inside the **#4348** cage and concluded that a rotation of 90° of the Sc₂ results in an energy minimum. This orientation is labeled in Table 4.3 and Figure 4.7 as the isomer **#4348 (vertical)**. According to our results, which agree completely with those obtained by Nagase, such a simple rotation decreases the energy of the endofullerene by 50 kcal·mol⁻¹, due to the increase of the distance between the metal atoms to 3.9 Å, thus the repulsion is lower. Even though, this decrease is not enough to invert energies with the most stable cage **#4059**. In addition, the rotation of the metallic cluster decreases the symmetry level to C₁, what would mismatch with the experimental ¹³C-NMR spectrum.

In general words, we have observed that the higher the repulsion between the Sc atoms, *i.e.*, the shorter the Sc–Sc distance, the lower the stability of the whole system. Since the metal atoms carry considerable positive charge, the repulsive electrostatic interactions between them are much more stronger than the covalent bonding. This fact was already pointed out by Nagase in his previous studies on the Sc₂@C₆₆,^[2] and also seen in other works with dimetallic clusters, such as La₂@D_{2h}-C₈₀.^[15]

The charge transfer was determined by means of orbitals analyses and fragment calculations. The orbital diagrams with the contribution of each fragment obtained for **#4348** and **#4059** structures are represented in Figure 4.8. As well, the energies of the HOMO and the LUMO and the gap between them are collected in Table 4.4, along with the orbital energies for the Sc₃N@I_h-C₈₀. The orbital diagram of the Sc₂@C_{2v}-^{#4059}C₆₆ EMF clearly shows that the 3 HOMOs of the Sc₂ fragment (green in Figure 4.8) transfer their 6 electrons to the three lowest unoccupied orbitals of the cage (orange in Figure 4.8). Thus, the three LUMOs of the C₆₆ become the three HOMOs of the EMF system (orange arrows in Figure 4.8), while the HOMO-1 of the metal fragment becomes the LUMO of the EMF, as shown with dashed lines in Figure 4.8. Similar results were obtained for the **#4417**, **#4466** isomers, as well as for the **#4348** isomer with the cluster in vertical position. On the other hand, the orbital diagram for the experimental Sc₂@C_{2v}-^{#4348}C₆₆ reveals that the Sc₂ cluster transfers only 4 electrons to the carbon cage: the HOMO-1 of the metal fragment remains as the HOMO-1 orbital of the EMF, and the two LUMOs of the cage become the HOMO and the HOMO-2 of the EMF. These facts correlate with the Sc-Sc distances: the shorter the distance, the stronger the covalent Sc-Sc bond and, therefore, the lower the number of transferred electrons. So it is not surprising that the experimental **#4348** isomer with the shortest Sc-Sc distance of 2.7 Å transfers only 4 electrons, even though the usual transfer for Sc clusters is 3 electrons per metal. In good agreement with previous studies, the metal carbide

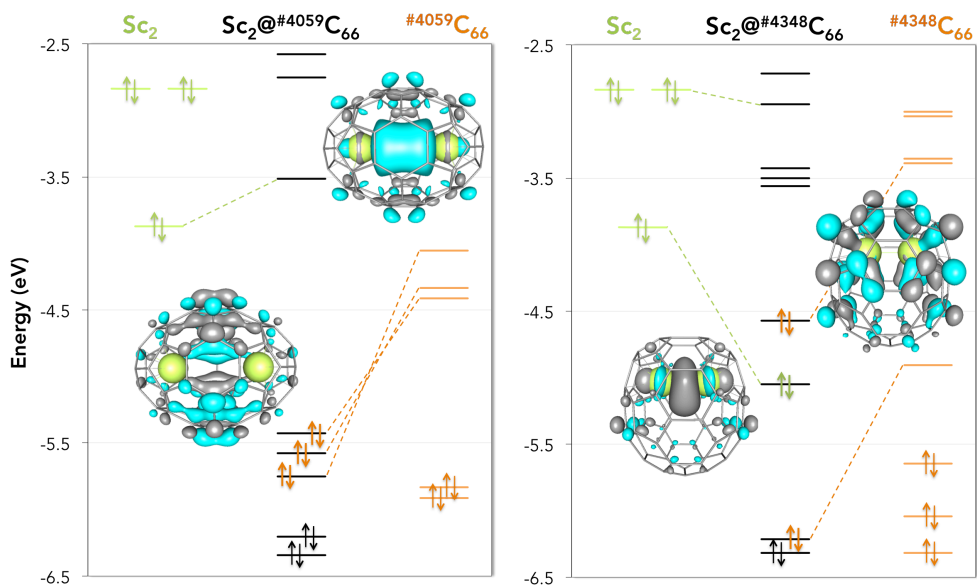


Figure 4.8. Representation of the orbitals and the electronic transfer for the $Sc_2@C_{2v}\text{-}\#4059C_{66}$ (left) and $Sc_2@C_{2v}\text{-}\#4348C_{66}$ (right) EMFs. In green, the Sc_2 orbitals; in orange, the C_{66} fragment; in black, the $Sc_2@C_{66}$ orbitals.

Table 4.4. Energies of the HOMO, LUMO and the HOMO-LUMO gap for the computed $Sc_2@C_{66}$ and $Sc_2C_2@C_{64}$ systems in Table 4.3 and the $Sc_3N@C_{80}$.

Isomer	HOMO (eV)	LUMO (eV)	HOMO-LUMO gap (eV)
$Sc_3N@I_h\text{-}C_{80}$	-5.693	-3.195	2.498
$Sc_2@C_{66}$			
#4059	-5.427	-3.514	1.914
#4417	-5.129	-4.131	0.998
#4348 (vertical)	-4.726	-3.562	1.164
#4466	-4.560	-3.691	0.869
#4348	-4.573	-3.560	1.012
$Sc_2C_2@C_{64}$			
#2983	-4.969	-3.766	1.203
#3425	-5.120	-3.702	1.418
#3451	-5.041	-4.076	0.965

clusters transfer 4 electrons to the carbon cage in the $\text{Sc}_2\text{C}_2@\text{C}_{64}$ EMFs (see Annex A).^[16] Each metal atom remains at the highest oxidation state Sc(III), while the C_2 unit is formally 2-.

4.4.2. The effect of the temperature

The molar fractions of the lowest-energy EMF isomers as a function of the temperature were also evaluated using the rigid rotor and harmonic oscillator (RRHO) approximation and the related free-encapsulating model (FEM) proposed by Slaniņa.^[17] For both FEM and RRHO approximations, the $\text{Sc}_2@\text{C}_{2v}\text{-}^{\#4059}\text{C}_{66}$ system is the most abundant isomer in whole range of temperatures, up to 4000K. In general, the FEM approximation is more suitable for the IPR clusterfullerenes, since the rotation of the metal clusters is usually completely allowed, if there is enough space for it. All of our systems are at least APP2, thus it is not so clear that the cluster rotates inside the cages since the interaction of the Sc ions with the pentalene motifs is significant and there is not a lot of space to rotate inside such small cages. So, real systems are in between these two models. In any case, the two FEM and RRHO approximations lead to the same conclusion: clearly the most abundant isomer produced at high-energy temperature inside the arc is the one predicted initially by Nagase, $\text{Sc}_2@\text{C}_{2v}\text{-}^{\#4059}\text{C}_{66}$.

4.4.3. Computational clues: predicted IR and ⁴⁵Sc-NMR

Up to now, all the computational results point to the isomer **#4059** as the most appropriate to capture the Sc_2 cluster inside, in agreement with Nagase's conclusions.^[2] Compared to the experimental **#4348** assignment, the computational isomer not only is the most stable by more than 80 kcal·mol⁻¹, but also fits perfectly with the experimental ¹³C-NMR spectrum. However, it does not match the experimental X-ray powder diffraction experiments. In order to unravel this tangle, we have performed computed the ⁴⁵Sc-NMR and IR spectra.

The intensities of the IR spectrum for the $\text{Sc}_2@\text{C}_{2v}\text{-}^{\#4059}\text{C}_{66}$ and the $\text{Sc}_2@\text{C}_{2v}\text{-}^{\#4348}\text{C}_{66}$ systems are plotted in Figure 4.9. The two spectra are completely different: while large peaks are observed for **#4059** between 300 and 900 cm⁻¹, no significant peaks are observed for **#4348** in the whole range between 150 and 1600 cm⁻¹. The Sc-Sc vibration is found around 250 cm⁻¹, although it is not visible in the IR spectra.

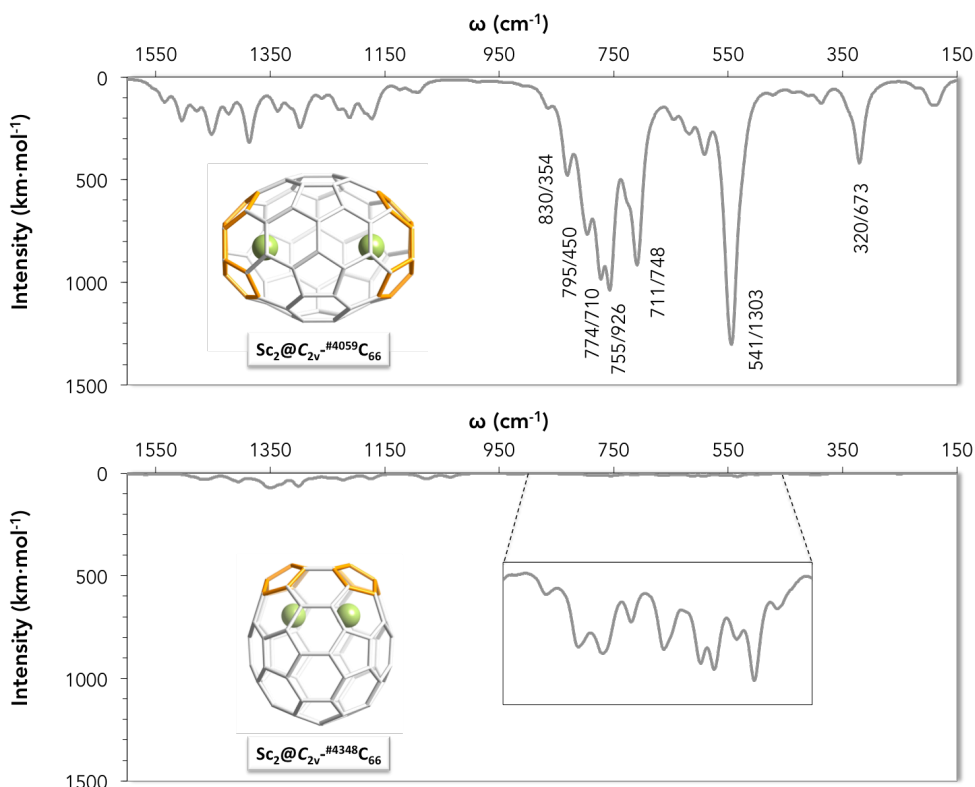


Figure 4.9. Computed IR spectrum for the $\text{Sc}_2@C_{2v}-\#4059C_{66}$ (top) and the $\text{Sc}_2@C_{2v}-\#4348C_{66}$ (bottom).

Although is not routine, ^{45}Sc -NMR spectroscopy is a very sensitive technique not only to help in the determination of the carbon cage, but also on the internal structure of the metal cluster.^[18] In 2012 Akasaka and co-workers carried out the first ^{45}Sc -NMR for a dimetal cluster EMF, $\text{Sc}_2@C_{3v}-\#8C_{82}$.^[19] The predicted ^{45}Sc -NMR chemical shifts for the isomers $\text{Sc}_2@C_{66}$ discussed along the chapter and the most suitable carbide are collected in Table 4.5. All signals are related to the computed value of the experimental $\text{Sc}_3(\text{NO}_3)_3$ as external reference. This methodology has been validated with the experimental spectrum of $\text{Sc}_3\text{N}@I_h-C_{80}$.^[20] We obtained an estimation error of 20 ppm, which is insignificant in the working range of the chemical shifts. Interestingly, each endofullerene shows distinctive spectrum. Both the **#4059** and the **#4348** isomers present a single signal, although separated by almost 700 ppm. We have already seen that if the rotation of the metal cluster in **#4348** leads to a non-symmetric species, what is also reflected in the NMR spectra: the single signal in **#4348 (vertical)** is split in two, one near 600 ppm and the other around 400 ppm. Finally, the two signals for the lowest-energy carbide EMF are shifted near 1000 ppm and separated by 60 ppm.

Table 4.5. Predicted ^{45}Sc -NMR chemical shifts, with respect the $\text{Sc}_3(\text{NO}_3)_3$ reference.

Isomer	Chemical shift (ppm)
$\text{Sc}_3\text{N}@I_h\text{-C}_{80}$ ^a	218.5
$\text{Sc}_2@\text{C}_{2v}\text{-}\#4059\text{C}_{66}$	1.7
$\text{Sc}_2@\text{C}_{2v}\text{-}\#4348\text{C}_{66}$	682.0
$\text{Sc}_2@\text{C}_{2v}\text{-}\#4348\text{C}_{66}$ (vertical)	623.0 / 382.0
$\text{Sc}_2\text{C}_2@\text{C}_s\text{-}\#2983\text{C}_{64}$	979.1 / 1037.2

^a Experimental chemical shift: 196.6 ppm. Obtained from ref.^[20]

4.5. Conclusions

The $\text{Sc}_2@\text{C}_{66}$ was one of the two firsts non-IPR fullerenes discovered in the year 2000. However, there is no unambiguous evidence on the cage assignation. Shinohara proposed by experimental analyses isomer **#4348**; afterwards, Nagase, on one hand, and Cui, on the other, proposed from their computational analysis the cages **#4059** and **#4466**, respectively.

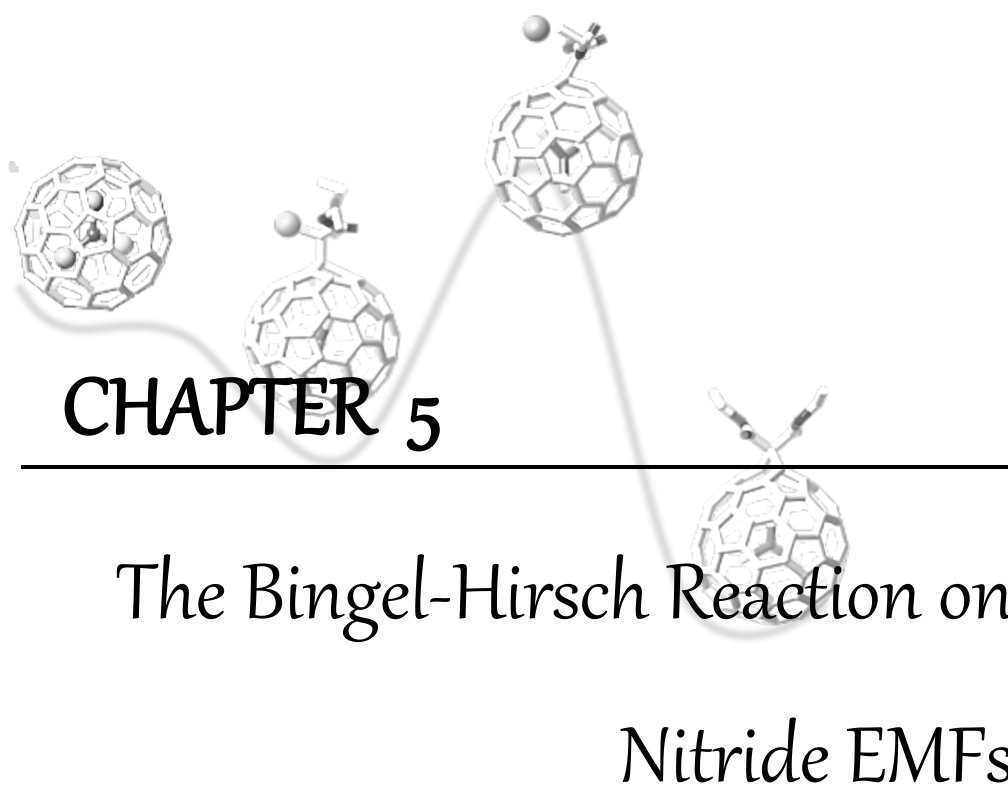
We have re-analyzed the $\text{Sc}_2@\text{C}_{66}$ system and confirmed that the cage suggested by Nagase **#4059** is the best candidate to encapsulate Sc_2 , with a formal charge transfer of 6 electrons. The proposed isomers **#4348** and **#4466** from experiments and previous computations, respectively, are not among the most suitable. The melon-shape structure of **#4059** allows $\text{Sc}\cdots\text{Sc}$ separation and, thus, an increase of the stabilization due to a minimization of the electrostatic repulsion. Additionally, we have demonstrated that the carbide $\text{Sc}_2\text{C}_2@\text{C}_{64}$ is not a competitive option for the first non-IPR EMF synthesized. We have also considered the effect of the temperature, which corroborate the results obtained at OK.

In summary, the discussion moves between the experimental proposal, which is neither an energy minimum nor the most stable EMF, and the computed suggestion, which does not match the experimental X-ray powder diffraction data. We encourage the experimental scientific community to reconsider this unsolved problem and explore one more time this Sc_2C_{66} species to finally solve this puzzle and find out which the experimental or the computed predicted cage is the encapsulating isomer. Thus, we present the predicted IR and ^{45}Sc -NMR spectra to support the experimental characterization and help in the assignment.

4.6. Bibliography

- [1] C. Wang, T. Kai, T. Tomiyama, T. Yoshida, Y. Kobayashi, E. Nishibori, M. Takata, M. Sakata, H. Shinohara, *Nature* (2000), 408, 426.
- [2] K. Kobayashi, S. Nagase, *Chem. Phys. Lett.* (2002), 362, 373.
- [3] T. Masaki, E. Nishibori, M. Sakata, C. R. Wang, H. Shinohara, *Chem. Phys. Lett.* (2003), 372, 512.
- [4] Y. H. Cui, W. Q. Tian, J. K. Feng, D. L. Chen, *J. Nanopart. Res.* (2009), 12, 429.
- [5] A. R. Khamatgalimov, V. I. Kovalenko, *Russ. J. Phys. Chem. A* (2008), 82, 1164.
- [6] *Gaussian 09, Revision A.1*. M. J. Frisch, G. W. Trucks, H. B. Schlegel, G. E. Scuseria, M. A. Robb, J. R. Cheeseman, G. Scalmani, V. Barone, B. Mennucci, G. A. Petersson, H. Nakatsuji, M. Caricato, X. Li, H. P. Hratchian, A. F. Izmaylov, J. Bloino, G. Zheng, J. L. Sonnenberg, M. Hada, M. Ehara, K. Toyota, R. Fukuda, J. Hasegawa, M. Ishida, T. Nakajima, Y. Honda, O. Kitao, H. Nakai, T. Vreven, J. J. A. Montgomery, J. E. Peralta, F. Ogliaro, M. Bearpark, J. J. Heyd, E. Brothers, K. N. Kudin, V. N. Staroverov, R. Kobayashi, J. Normand, K. Raghavachari, A. Rendell, J. C. Burant, S. S. Iyengar, J. Tomasi, M. Cossi, N. Rega, J. M. Millam, M. Klene, J. E. Knox, J. B. Cross, V. Bakken, C. Adamo, J. Jaramillo, R. Gomperts, R. E. Stratmann, O. Yazyev, A. J. Austin, R. Cammi, C. Pomelli, J. W. Ochterski, R. L. Martin, K. Morokuma, V. G. Zakrzewski, G. A. Voth, P. Salvador, J. J. Dannenberg, S. Dapprich, A. D. Daniels, Ö. Farkas, J. B. Foresman, J. V. Ortiz, J. Cioslowski, D. J. Fox, Gaussian, Inc, Wallingford CT, (2009).
- [7] a) A. Schäfer, C. Huber, R. Ahlrichs, *J. Chem. Phys.* (1994), 100, 5829; b) P. J. Stephens, F. J. Devlin, C. F. Chabalowski, M. J. Frisch, *J. Phys. Chem.* (1994), 98, 11624.
- [8] a) R. Ahlrichs, M. Bär, M. Häser, H. Horn, C. Kölmel, *Chem. Phys. Lett.* (1989), 162, 165; b) O. Treutler, R. Ahlrichs, *J. Chem. Phys.* (1995), 102, 346.
- [9] a) E. J. Baerends, D. E. Ellis, P. Ros, *ADF 2009.01, Department of Theoretical Chemistry, Vrije Universiteit: Amsterdam*; b) G. t. Velde, F. M. Bickelhaupt, E. J. Baerends, C. F. Guerra, S. J. A. v. Gisbergen, J. G. Snijders, T. Ziegler, *J. Comput. Chem.* (2001), 22, 932.
- [10] P. W. Fowler, D. E. Manolopoulos, *An Atlas of Fullerenes*, Oxford University Press, Oxford, (1995).
- [11] a) B. Mercado, M. Stuart, M. Mackey, J. Pickens, B. Confait, S. Stevenson, M. Easterling, R. n. Valencia, A. Rodríguez-Forteza, J. Poblet, M. Olmstead, A. Balch, *J. Am. Chem. Soc.* (2010), 132, 12098; b) Y. Z. Tan, S. Y. Xie, R. B. Huang, L. S. Zheng, *Nature Chem.* (2009), 1, 450.
- [12] A. Rodríguez-Forteza, N. Alegret, A. Balch, J. Poblet, *Nature Chem.* (2010), 2, 955.

- [13] a) X. Lu, K. Nakajima, Y. Iiduka, H. Nikawa, T. Tsuchiya, N. Mizorogi, Z. Slanina, S. Nagase, T. Akasaka, *Angew. Chem., Int. Ed.* (2012), 51, 5889; b) Y. Iiduka, T. Wakahara, T. Nakahodo, T. Tsuchiya, A. Sakuraba, Y. Maeda, T. Akasaka, K. Yoza, E. Horn, T. Kato, M. T. H. Liu, N. Mizorogi, K. Kobayashi, S. Nagase, *J. Am. Chem. Soc.* (2005), 127, 12500.
- [14] Y. H. Cui, W. Tian, J. K. Feng, D. L. Chen, *J. Comput. Chem.* (2008), 29, 2623.
- [15] A. A. Popov, L. Dunsch, *Chem. Eur. J.* (2009), 15, 9707.
- [16] R. Valencia, A. Rodríguez-Fortea, J. Poblet, *J. Phys. Chem. A* (2008), 112, 4550.
- [17] a) Z. Slanina, S. Nagase, *Chem. Phys. Chem.* (2005), 6, 2060; b) Z. Slanina, S. L. Lee, F. Uhlík, L. Adamowicz, S. Nagase, *Theor. Chem. Acc.* (2006), 117, 315.
- [18] A. Popov, S. Yang, L. Dunsch, *Chem. Rev.* (2013), 113, 5989.
- [19] H. Kurihara, X. Lu, Y. Iiduka, N. Mizorogi, Z. Slanina, T. Tsuchiya, S. Nagase, T. Akasaka, *Chem. Commun.* (2012), 48, 1290.
- [20] W. Fu, X. Wang, H. Azuremendi, J. Zhang, H. Dorn, *Chem. Commun.* (2011), 47, 3858.



CHAPTER 5

The Bingel-Hirsch Reaction on
Nitride EMFs

Related Publications:

"Bingel-Hirsch reactions on non-IPR $Gd_3N@C_{2n}$ ($2n=82$ and 84)." N. Alegret, M.N. Chaur, E. Santos, A. Rodríguez-Forteza, L. Echegoyen, J. M. Poblet. *J. Org. Chem.* (2010), 75, 8299

"Bingel-Hirsch addition on endohedral metallofullerenes: kinetic versus thermodynamic control." N. Alegret, A. Rodríguez-Forteza, J. M. Poblet. *Chem. Eur. J.* (2013), 19, 5061

"Bingel-Hirsch addition on non-isolated-pentagon-rule $Gd_3N@C_{2n}$ ($2n=82$ and 84) metallofullerenes: products under kinetic control." N. Alegret, P. Salvadó, A. Rodríguez-Forteza, J. M. Poblet. *J. Org. Chem.* (2013), 78, 9986

CHAPTER 5

The Bingel-Hirsch Reaction on Nitride EMFs

My first assignment as a computational chemist was a thermodynamic study of the Bingel-Hirsch products on two fullerenes: the non-IPRs $Gd_3N@C_{82}$ and $Gd_3N@C_{84}$. The request came from Echegoyen's lab; they synthesized the cages, made the reaction but couldn't characterize the final products. And that's how my bosses and I got close to the Bingel-Hirsch reaction. After that first study, we were encouraged to solve another problem related to the Bingel-Hirsch reaction, this time with the first isolated non-IPR metallofullerene $Sc_3N@D_3^{-\#6140}C_{68}$. Again, no crystal data was published and the only characterization made was a comparative experimental and computational study of ^{13}C -NMR. The peculiarity was that the proposed product was not the one with the lowest energy – it lies at more than 11 kcal·mol⁻¹ with respect to the thermodynamic product. We were then facing another kind of problem: what if the Bingel-Hirsch addition undergoes under kinetic control? To prove it, we used the well-known and prototypical system: $Sc_3N@I_h-C_{80}$. The monoaddition on the most abundant endofullerene was published to take place indistinctively only on the [6,6] bond, what agrees completely with our study of the reaction path. Then, we used the same methodology to analyze the case of $Sc_3N@C_{68}$, and again we found that the kinetic product was the one that matches the ^{13}C -NMR! Finally, to end up the work, we went back to our first Bingel-Hirsch task and performed a complete study on the reaction path for the two $Gd_3N@C_{82}$ and $Gd_3N@C_{84}$. Up to date, no further experimental information about the Bingel-Hirsch reaction for those two systems has been published, although from our experience we proposed the kinetic products as the ones formed in the reaction. We are looking forward to see our predictions being confirmed.

5.1. A cyclopropanation reaction

The Bingel-Hirsch reaction is a type of nucleophilic [2+1] cycloaddition where a bromomalonate reacts with a fullerene cage.^[1] To perform it, the presence of a strong base in a standard organic media of *o*-dichlorobenzene (*o*-DCB from now on) is required to ionize the malonate. According to Hirsch, the reaction takes place in two separate steps (Figure 5.1).^[1] Initially, an intermediate with the bromomalonate bonded to a C atom of the fullerene is formed through an almost barrierless process, becoming the whole system negatively charged. After that, a bromide anion is released while a second bond between the C atom of the malonate and the fullerene is formed. The Bingel-Hirsch reaction has been defined as a very simple and efficient reaction because of the accessibility of the malonic acid derivatives.^[2] Although multiadducts are commonly formed, the major product is in all cases the monoadduct, reaching yields up to 40%.^[3]

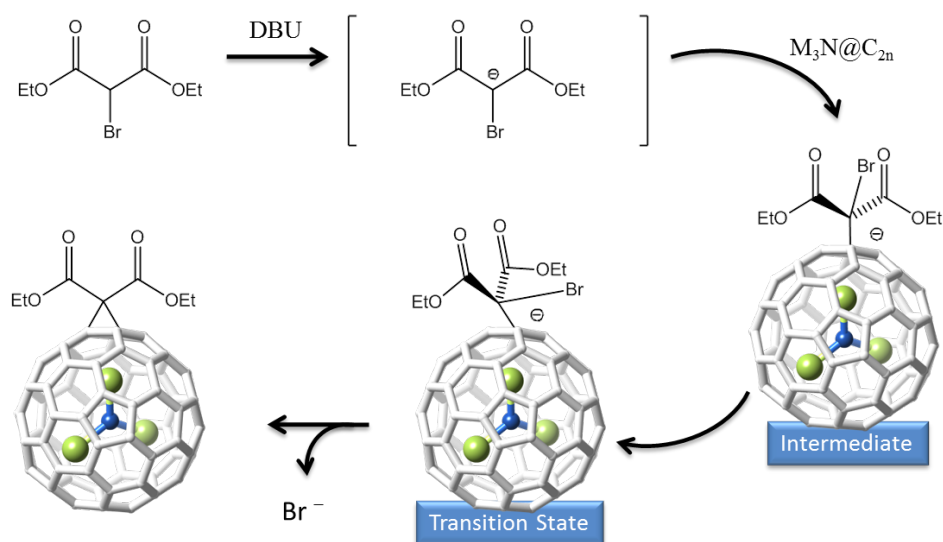


Figure 5.1. General mechanism of the Bingel-Hirsch reaction.

The first Bingel-Hirsch derivative of an EMF was synthesized in 2003 from $Gd@C_{60}$, giving $Gd@C_{60}[C(COOH)_2]_{10}$ multiadducts on [6,6] bonds.^[4] After that, functionalizations of $M_3N@I_h-C_{80}$ with $M=Y, Lu$ and Er gave stable monoadducts regioselectively on a [6,6] bond.^[5] Currently, Bingel-Hirsch adducts of other nitride EMFs such as

$\text{Sc}_3\text{N}@I_h\text{-C}_{80}$,^[2] $\text{Gd}_3\text{N}@C_{2n}$ ($2n=80, 82, 84, 88$),^{[6],[7]} $\text{Sc}_3\text{N}@C_{78}$,^[8] and $\text{Sc}_3\text{N}@C_{68}$,^[9] are also known. Even adducts of the heterofullerene $\text{Gd}_2@C_{79}\text{N}$ have been reported.^[10] It should be remarked that in most of these systems the addition yields open-cage fullerooids.

In order to advance in the understanding of the reactivity properties of IPR and non-IPR fullerenes we have performed an exhaustive computational study of the thermodynamics and the kinetics of the Bingel-Hirsch addition on the prototypical $\text{Sc}_3\text{N}@I_h\text{-C}_{80}$ and the non-IPR systems $\text{Sc}_3\text{N}@D_{3h}\text{-}^{6140}\text{C}_{68}$ and $\text{Gd}_3\text{N}@C_{2n}$ ($2n=82, 84$).

5.1.1. Insights into the stationary points of the reaction

This chapter includes the study of the reaction path of the Bingel-Hirsch reaction on several fullerene systems. Thus, different intermediates and transition states (TS) have been computed. In both structures, the malonate group is bonded to one C atom of the cage, named from now C_α , as shown in Figure 5.2a. To form the final product, the malonate must bond a second C atom of the carbon cage, labeled as C_β , which is also bonded to C_α in the non-functionalized fullerene. Since each C_α atom of the fullerene is bonded to three C_β atoms, there are three possible products, through three different TSs, that can be obtained from one intermediate if rotation around the $C_\alpha\text{-C}_{\text{mal}}$ bond is allowed (Figure 5.2a) – C_{mal} stands for the central C atom of the malonate group. The proper conformation of the bromomalonate in the intermediate to yield a given TS is that in which the Br leaving group is in the plane defined by the atoms C_{mal} , C_α and C_β and forming a dihedral angle of 180° , as shown in Figure 5.2b.

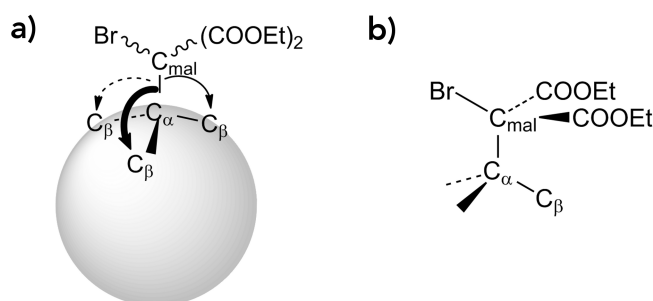


Figure 5.2. a) Paths that each intermediate can follow in its way to form the product through different TSs. The three possible paths are shown with thin, dotted and bold arrows. b) Orientation of the bromomalonate in the intermediate to form the monoadduct on the $C_\alpha\text{-C}_\beta$ bond.

5.2. Computational Details

The theoretical study of the Bingel-Hirsch reaction has been performed by means of DFT methodology with the combined use of the ADF and Gaussian09 codes.^[11] All the stationary points were first calculated using the ADF 2009 code – ADF2007 version for the first thermodynamic study of $Gd_3N@C_{2n}$ ($2n=82, 84$).^[12] Geometry optimizations of saddle points were first performed with the QUILD (QUantum-regions Interconnected by Local Descriptions) program, which functions as a wrapper around the ADF program.^[13] Transition states were characterized, by computing the analytical vibrational frequencies, to have only one imaginary frequency corresponding to the release of bromine and formation of the product molecules. The exchange-correlation GGA density functionals of Becke and Perdew (BP86) were used.^[14] Relativistic corrections were included by means of the ZORA (Zero-Order Regular Approximation) formalism. Triple- ζ polarization basis sets (TZP) of Slater type were employed to describe the valence electrons of C, N, O, H, Sc, Y and Gd. Frozen cores consisting of: i) the 1s shell for C, N, O; ii) the 1s to 2p shells for Sc; iii) the 1s to 3d shells for Y; and iv) the 1s to 4d shells for Gd were described by means of single Slater functions.

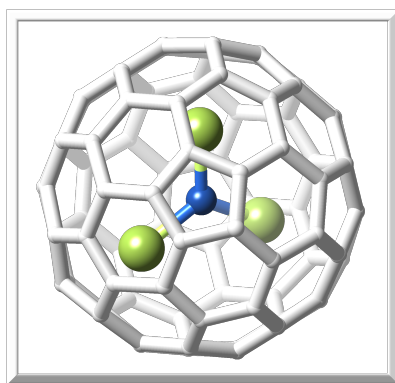
In a second step, the minima (reactants, intermediates and products) as well as the transition states obtained at BP86/TZP level with the ADF code were used as starting geometries and recomputed using the M06 functional,^[15] which is more adequate to compute energy barriers, within the Gaussian09 code^[11c]. The $Sc_3N@C_{2n}$ ($2n=68$ and 80) calculations were performed at M06/6-311G** level^[16] (TZV from Ahlrichs for Sc)^[17] – named as “M06/TZP” from now on. The $Gd_3N@C_{2n}$ ($2n=82, 84$) systems were recomputed at the M06/6-31G** level (LANL2DZ pseudopotential for Y) – named as “M06/DZP” from now on. On the optimized geometries, solvent effects were included by single point energy calculations using the polarizable continuum model (PCM)^[18] to simulate the effects of *o*-DCB at the M06/6-311G** level (TZV from Ahlrichs for Sc and dhf-TZVP pseudopotential for Y)^[19] – named as “pcm/M06/TZP” from now. We have checked that the computational methodology, optimizing stationary points at M06/DZP level and then performing a single-point calculation of the energy at pcm/M06/TZP level, provides a correct description of the relative energies of minima and TSs as compared to the more demanding optimization at M06/TZP level (see Section 5.4.5).

We have labeled the different bonds for each of the EMFs analyzed here using consecutive lowercase bold letters: **a-b** for $Sc_3N@I_h-C_{80}$; **c-t** for $Sc_3N@D_{3h}^{#6140}C_{68}$; **a'-k'** for $Y_3N@C_{82}$; **l'-t'** for $Y_3N@C_{84}$. In previous works, lowercase letters were used for [5,6] bonds and numbers for [6,6] bonds. Here, we use numbers to label the C

atoms of the structures. Products are, therefore, characterized by the functionalized bond. Intermediates are named by the number of the attacked carbon followed by the lowercase letter that identifies the product that is formed from the intermediate. Hence, for example, intermediate **22o** denotes that the malonate is attached to C₂₂ and that the intermediate yields product **o**. The same nomenclature has been used for the corresponding transition states. Intermediate (TS) **22d** has the malonate also attached to atom 22, but oriented to yield adduct **d**.

For the study of Sc₃N@D₃-^{#6140}C₆₈ and Gd₃N@C_{2n} (2n=82, 84), the reaction products were first optimized using the methylmalonate model instead of the experimental ethylmalonate. Then the most stable regioisomers were recalculated using the ethylmalonate group.

5.3. Addition on Sc₃N@I_h-C₈₀



In 1999, Dorn and co-workers reported the synthesis, isolation and characterization of Sc₃N@I_h-C₈₀, the prototype of the family of nitride EMFs and the most abundant fullerene after C₆₀ and C₇₀.^[20] Its functionalization became somehow particular. Previous attempts to prepare Bingel-Hirsch derivatives on this EMF using the standard conditions failed, which was attributed to the nature of the encapsulated metal cluster – note that the reaction was successfully performed on Y₃N@C₈₀ using the

standard conditions.^[5a] In 2010, Echegoyen and co-workers, using a different base and in the presence of DMF, synthesized successfully the first Bingel-Hirsch monoadduct of Sc₃N@C₈₀, which was characterized as a [6,6] addition product by means of electrochemical measurements.^[2]

5.3.1. Description of the system

The highly symmetrical I_h-C₈₀ cage shows only two types of C atoms, those at pentagon-hexagon-hexagon junctions (the so-called 566 atoms, **1** in Figure 5.3) and those at hexagon-hexagon-hexagon junctions (the so-called 666 atoms, **2** in Figure 5.3). Consequently, only two types of C–C bonds exist, the [5,6] bond between a pentagon and a hexagon (corannulene, type D, bond **a** from now on) and the [6,6]

bond between two hexagons (type B, bond **b** from now on) – see Figure 1.3 and Figure 5.3. It is worth mentioning here that the [6,6] bond in the I_h -C₈₀ cage is different from the [6,6] bond present in the prototypical I_h -C₆₀ buckminsterfullerene (pyracylene, type A, see Figure 1.3 and Figure 5.3) with the subsequent different reactivity.

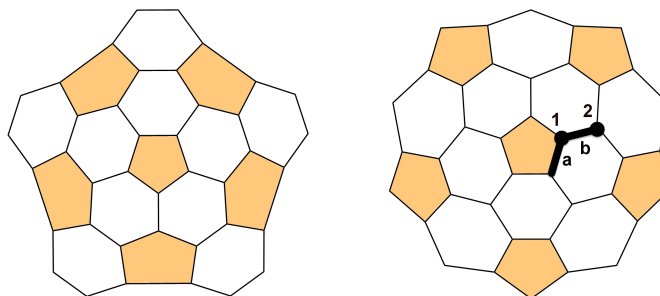


Figure 5.3. Schematic representation of the structural motifs present in I_h -C₆₀ (left) and I_h -C₈₀ (right) with the pentagons highlighted in orange. The labels for the two different C atoms (**1** and **2**) and bonds (**a** and **b**) in I_h -C₈₀ are also shown (see the main text for details).

5.3.2. Thermodynamics: rotation of the Sc₃N cluster in products

The presence of the encapsulated Sc₃N cluster inside the carbon cage would lead to a symmetry descent in Sc₃N@ I_h -C₈₀, but at NMR time scale the original high symmetry of the cage is preserved.^[20] Computational studies have confirmed that the Sc₃N unit rotates freely inside the I_h -C₈₀ cage at ambient temperature.^[21] Therefore, only two different regioisomers can be formed when an addition reaction takes place on I_h -C₈₀. The computational study of such an addition reaction on Sc₃N@ I_h -C₈₀ is, however, not so straightforward because for each regioisomer several orientations of the internal cluster must be considered.

Previous studies of the Bingel-Hirsch reaction and other cycloadditions on M₃N@ I_h -C₈₀ show that the rotation of the cluster inside the functionalized cage is more hindered than in the pristine metallofullerene.^[5b, 22] In particular, when bromoethylmalonate reacts with Y₃N@ I_h -C₈₀ the cluster is located with one Y atom pointing to the functionalized bond and only rotation of the Y₃N unit around the N–Y–C_{mal} axis is allowed.^[5b] Thus, several orientations of the Sc₃N unit have been taken into consideration for products (see Figure 5.4). A complete list of all the orientations for each regioisomer is collected in Table 5.1. We find a restricted rotation of the internal cluster as happens with Y₃N, although Sc is smaller than Y.

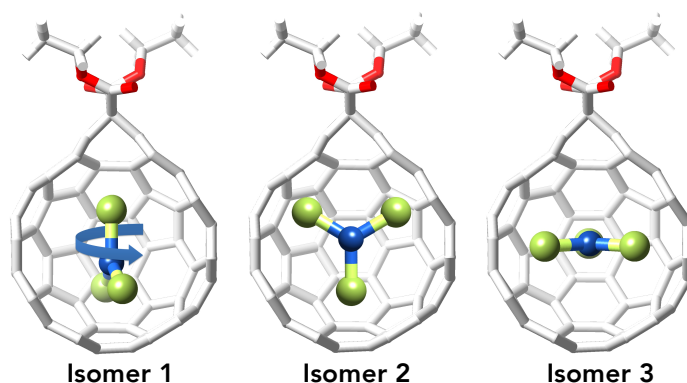


Figure 5.4. Representation of the relative position of the nitride unit with respect to the position of the external functionalization for the different orientational isomers computed in this work. The blue arrow in orientational isomer **1** denotes that only rotation around the N–Sc–C_{mal} axis is allowed

Table 5.1. Reaction energies and relative stabilities (in parenthesis) for the different computed orientational isomers of ethylmalonate monoadducts of $Sc_3N@I_h-C_{80}$ in gas phase.

Monoadduct a				Monoadduct b			
# ^a	Rotation ^b	E _{reaction}	(E _{rel}) ^c	# ^a	Rotation ^b	E _{reaction}	(E _{rel}) ^c
1	90°	-91.9	(0.0)	1	90°	-90.6	(0.0)
1	45°	-90.9	(1.0)	1	45°	-90.7	(0.0)
1	0°	-90.0	(1.9)	1	0°	-88.3	(2.4)
2	0° Bent	-84.0	(7.9)	3		-81.8	(8.8)
3		-82.6	(9.3)	2	0°	-81.3	(9.3)
2	0°	-82.6	(9.3)	2	0° Bent	-80.6	(10.0)
2	25°	-81.1	(10.8)	2	45°	-80.4	(10.3)
2	90° Bent	-80.5	(11.4)	2	90°	-79.1	(11.5)
2	115°	-80.5	(11.4)	2	115°	-79.0	(11.6)

^a Orientational isomer numbering according to **Figure 5.4**.

^b Angle of the cluster plane with respect to the addition bond.

^c Energies in kcal·mol⁻¹, computed with ADF2009 at the BP86/TZP level.

Our results show that the lowest-energy orientational isomer for the adducts on $Sc_3N@I_h-C_{80}$ is isomer **1** (Figure 5.4), where one Sc atom is pointing to the functionalized bond, which has been broken yielding open fulleroid cages, as observed previously for $Y_3N@I_h-C_{80}$.^[5b] Rotation around the N–Sc–C_{mal} axis is allowed in both [5,6] and [6,6] regioisomers, but much more restricted around other directions (see Table 5.1). The two regioisomers are predicted to be isoenergetic – adduct on the

[5,6] bond is only $1.3 \text{ kcal}\cdot\text{mol}^{-1}$ more stable than that on the [6,6] bond. According to these results, if the reaction was under thermodynamic control, a mixture of the [6,6] and [5,6] adducts would be observed. However, NMR and electrochemical experiments by Pinzon *et al.* confirmed that the Bingel-Hirsch reaction on $\text{Sc}_3\text{N}@I_h\text{-C}_{80}$ takes place uniquely on the [6,6] bond.^[2]

5.3.3. Step 1: intermediates formation

To unravel this apparent controversy, we have also investigated the kinetic aspects of the process computing the different stationary points in the reaction path. In the first step, the intermediates are formed by the addition of the malonate anion onto the fullerene surface. Those intermediates (and TSs in the next section) are named as **1a**, **1b** and **2b**, where the number indicates the C atom (C_α) that reacts with the malonate to yield the intermediate and the letter denotes the addition bond (see Figure 5.2). For the intermediate in which the ligand is linked to a 666 C atom, **2b**, the three possible reaction paths are equivalent and yield the [6,6] adduct (**b**). However, the intermediates on 566 C atoms, **1a** and **1b**, can yield indistinctively the [5,6] (**a**) or [6,6] (**b**) adducts (Figure 5.5).

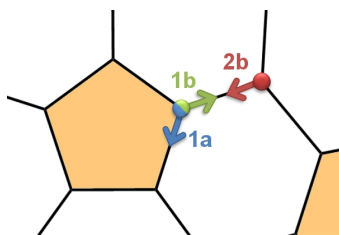


Figure 5.5. Schematic two-dimensional representation of a $I_h\text{-C}_{80}$ portion with the two independent atoms labeled according their surrounding rings as 566 (atom **1**, blue and green) and 666 (atom **2**, red). The colored arrows represent the possible reaction paths to form the [5,6] (blue) or the [6,6] monoadduct (green and red).

We have evaluated the probability of rotation of the cluster inside the intermediate structure, using the same orientations of the cluster as for the products (Figure 5.4). The results are collected in Table 5.2. Rotation of the internal cluster was found for the intermediates not so hindered as in the products. Interestingly, the orientation of the Sc_3N unit in the lowest-energy intermediate is different – orientational **isomer 2** in Figure 5.4 – as that found for the products – **isomer 1**.

Table 5.2. Reaction energies (in kcal·mol⁻¹) and relative stabilities (in parenthesis) for the different computed orientational isomers of ethylmalonate intermediates of $Sc_3N@I_h-C_{80}$ in the gas phase.

Intermediate 1a				Intermediate 1b				Intermediate 2b			
# ^a	Rot. ^b	$E_{reaction}$	(E_{rel}) ^c	# ^a	Rot. ^b	$E_{reaction}$	(E_{rel}) ^c	# ^a	Rot. ^b	$E_{reaction}$	(E_{rel}) ^c
2*	45°	-26.5	(0.0)	2*	90°	-26.1	(0.0)	2	80°	-25.6	(0.0)
2	45°	-25.3	(1.3)	2	90°	-26.0	(0.1)	2	30°	-22.3	(3.3)
2	6°	-19.2	(7.3)	2	115°	-19.0	(7.1)	2	40°	-22.3	(3.3)
1	165°	-15.0	(11.5)	1	45°	-13.0	(13.1)	2	145°	-22.2	(3.4)
1	110°	-12.7	(13.9)	1	110°	-15.6	(10.6)	2*	25°	-22.1	(3.5)
3		-15.2	(11.4)	2	20°	-15.7	(10.5)	1	50°	-19.9	(5.6)
1	16°	-13.6	(13.0)	2*	20°	-14.4	(11.8)	1	0°	-20.1	(5.5)
1	70°	-12.7	(13.8)	1	6°	-13.5	(12.6)	1	140°	-19.7	(5.9)

* Different conformation of the malonate groups.

^a Orientational isomer numbering according to Figure 5.4.

^b Dihedral angle of the cluster plane with respect to the addition bond.

^c Energies in kcal·mol⁻¹, computed with ADF2009 at the BP86/TZP level.

In order to complete the analysis of the first step of the Bingel-Hirsch reaction, we have confirmed that the formation of the intermediate is a barrierless process, as suggested previously for the same type of reaction on the hollow C_{60} (see Figure 5.6). A scan of the potential energy surface (PES) along the reaction coordinate was performed for the lowest-energy intermediate **2b** along the reaction coordinate $C_{mal}-C_{\alpha}$, and no energy barrier along such a coordinate has been detected.

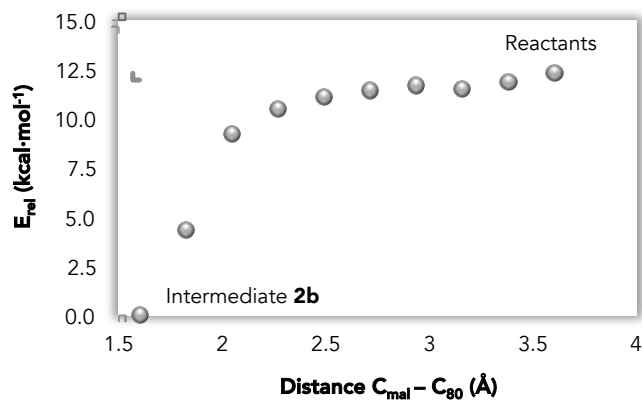


Figure 5.6. Scan along the addition coordinate from the intermediate **2b** to the reactants, computed with ADF2009 at the BP86/TZP level in the gas phase. See also Table B1 for a detailed list.

5.3.4. Step 2: going through a TS

The second step of the Bingel-Hirsch reaction is an activated process; therefore, a more accurate methodology is required, *i. e.*, taking into account solvent and dispersion effects, as well as a more appropriate density functional (M06, see Section 5.2). Since rotation of the internal cluster is partially hindered in the intermediate and given that the reaction is exothermic – according to the Hammond postulate, in this case the TS will be more similar to the intermediate than to the product –, we have computed the TSs with the same cluster orientation than in the corresponding intermediate. The general features of the final structures of both intermediates and TSs are drawn in Figure 5.7.

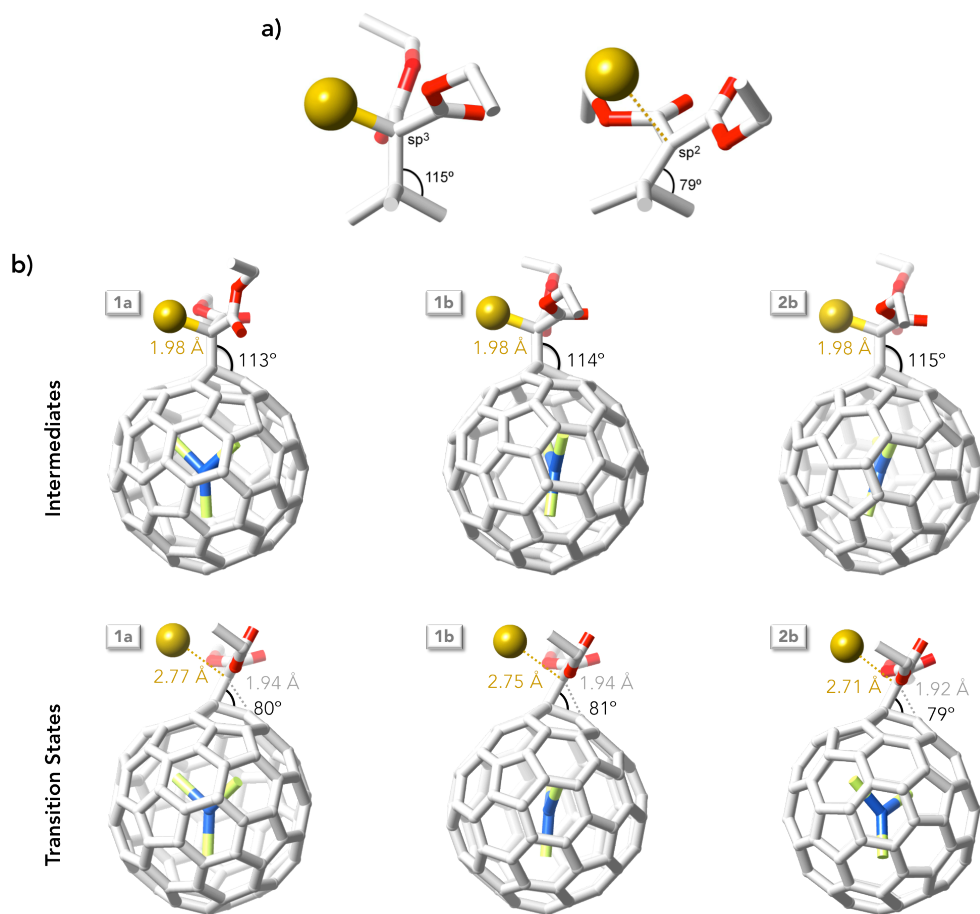


Figure 5.7. a) Fragments of the optimized intermediate (left) and TS (right) structures. H atoms are omitted for clarity. b) Optimized structures of the intermediates and TS. In yellow, the Br-C_{mal} distance; in grey, the C_β-C_{mal} distance; in black, the C_{mal}-C_α-C_β angle (Figure 5.2).

It can be clearly seen that the distance between the central C_{mal} and Br is larger in the TS structure than in the intermediate, indicating the release of the bromide anion. Furthermore, the distance between that central C_{mal} atom of the malonate and the second C atom of the fullerene C_β is reduced in the TS, which confirms the formation of the expected second bond. Additionally, it is important to note the change in the hybridization of the central C_{mal} atom of the malonate group, from sp³ in the intermediate to sp² in the TS, as well as the different C_{mal}-C_α-C_β angle in the two structures (see Figure 5.7). Notice also the different relative conformations of the two malonate groups in each of the two structures: in the intermediate, the two COO planes are nearly perpendicular, while in the TS they are almost parallel.

Table 5.3 summarizes the data collected from the optimized structures along the Bingel-Hirsch path. Results show that the three intermediates span in an energy range of less than 3 kcal·mol⁻¹. The intermediate on the 666 C atom, **2b**, is the one with the lowest energy. When the reactant attacks a 566 C atom with the bromomalonate oriented to lead the [6,6] adduct, the intermediate formed, **1b**, is 2.6 kcal·mol⁻¹ higher in energy. The same intermediate with the bromomalonate oriented to form the [5,6] adduct, **1a**, is found at 1.7 kcal·mol⁻¹ with respect to the lowest-energy **2b**. Note that intermediates **1a** and **1b** are related by a 120° rotation around the C_α-C_{mal} axis (see Figure 5.5)

Table 5.3. Relative energies with respect to reactants for the different computed intermediates, transition states and products of the Bingel-Hirsch cyclopropanation of Sc₃N@I_h-C₈₀ including the solvent effects (*o*-DCB).

Product	Bond type	Inter. ^a	C _α type	E _{rel} Inter. ^b		E _{rel} TS ^b		E _{rel} Product ^b	
b	[6,6]-B	2b	666	-18.3	(0.0)	0.2	(18.5)	-24.3	(0.0)
b	[6,6]-B	1b	566	-15.7	(2.6)	5.2	(20.9)	-24.3	(0.0)
a	[5,6] Coran.	1a	566	-16.6	(1.7)	7.4	(24.0)	-23.7	(0.6)

^aLabels for intermediates (see Figure 5.5). Note that the labels for the intermediates are also applicable to the TSs.

^bRelative energies with respect to reactants (in kcal·mol⁻¹); in parenthesis, relative stabilities with respect to the most stable intermediate/product (for intermediates/products) or the corresponding intermediate (for TS).

The TS derived from intermediate **2b** is the one with the lowest energy. All the other TSs lay more than 5 kcal·mol⁻¹ higher in energy (Table 5.3 and Figure 5.8). Thus assuming that the rate-determining step of the Bingel-Hirsch addition is the conversion of intermediates to products – the formation of intermediates is a barrierless process –, the most favored product from a kinetic point of view would be that with the lowest-energy TS, *i.e.* the [6,6] adduct, which is the only regioisomer observed in experiments.^[2] The TS **1a** that leads to the isoenergetic [5,6] regioisomer is found at more than 7 kcal·mol⁻¹ higher in energy. Therefore, our results

clearly show that the formation of the [6,6] Bingel-Hirsch adduct on $\text{Sc}_3\text{N}@I_h\text{-C}_{80}$ takes place under kinetic control.

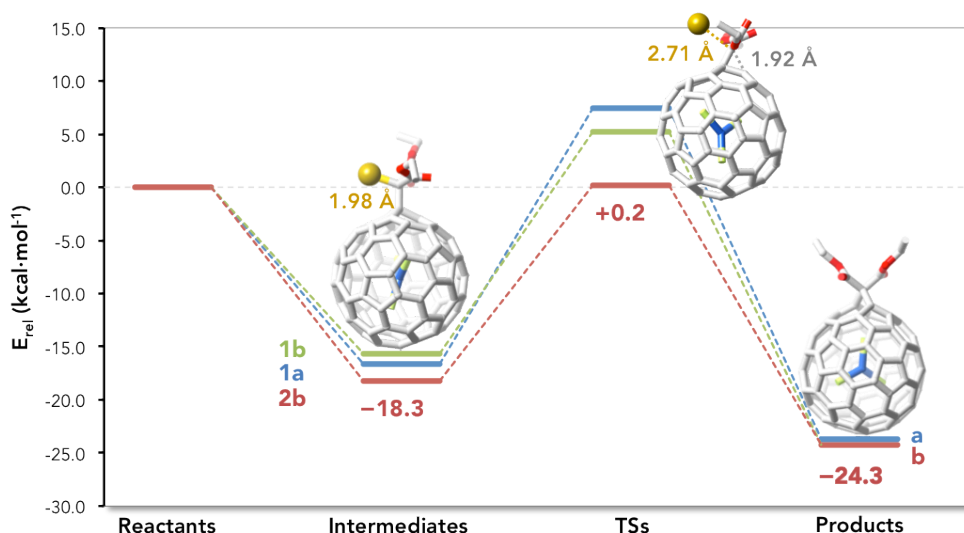
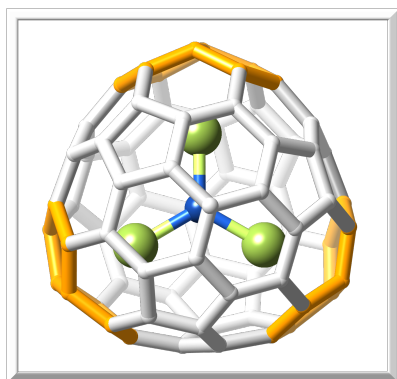


Figure 5.8. Energy profiles for the Bingel-Hirsch addition on $\text{Sc}_3\text{N}@I_h\text{-C}_{80}$, considering solvent effects (*o*-DCB). The bond Br-C_{mal} increases from 1.92 Å and 1.98 Å in the reactants and intermediates, respectively, to 2.71 Å in the TS.

5.4. Addition on $\text{Sc}_3\text{N}@D_3\text{-}^{#6140}\text{C}_{68}$



The first two EMFs with non-IPR cages discovered were $\text{Sc}_2@\text{C}_{66}$ and $\text{Sc}_3@\text{C}_{68}$, with two and three adjacent pentagon pairs (APP), respectively. Dorn, Gibson and co-workers reported in 2008 the first study of functionalization of non-IPR metallofullerenes using the Bingel-Hirsch reaction.^[9] They isolated and characterized the monoadduct of the reaction between $\text{Sc}_3\text{N}@D_3\text{-}^{#6140}\text{C}_{68}$ and diethylbromomalonate and proposed an addition site among the different bonds of the non-IPR fullerene with the help of

theoretical calculations. Those authors found that the adduct with the predicted ^{13}C -NMR spectrum that best matches the experimental data is not the lowest-energy adduct. According to these results, it seems that the Bingel-Hirsch reaction

on $Sc_3N@D_3^{-\#6140}C_{68}$ does not take place under thermodynamic control. However, no crystallographic data has been published so far, therefore one could claim that no clear and definitive structure of the final monoadduct is known yet. Particularly, if one takes into account the high number of distinct bonds in the $D_3^{-\#6140}C_{68}$ cage.

5.4.1. Description of the system

The non-IPR cage $D_3^{-\#6140}C_{68}$ presents three pentalene units orthogonal to the C_3 axis and in the vertexes of an equilateral triangle.^[23] Furthermore, each Sc atom of the cluster is pointing to one of the three-pentalene bonds. In contrast to the highly symmetrical I_h-C_{80} cage, the $D_3^{-\#6140}C_{68}$ cage exhibits 12 independent atoms and 18 distinct bonds (**c** to **t**) that would eventually lead to a large number of regioisomers when the fullerene is attacked by diethylbromomalonate or other reactants (see Figure 5.9). Another significant difference in comparison with $Sc_3N@I_h-C_{80}$ is that the internal cluster is not able to rotate in $Sc_3N@D_3^{-\#6140}C_{68}$ because (i) the C_{68} cage is smaller than C_{80} and (ii) the structure of $D_3^{-\#6140}C_{68}$, with three pairs of fused pentagons forming a perfect equilateral triangle, is optimal to establish three $Sc^{3+}\cdots$ pentalene interactions that stabilize the system. Consequently, a single orientation of the Sc_3N cluster has been considered in the present study

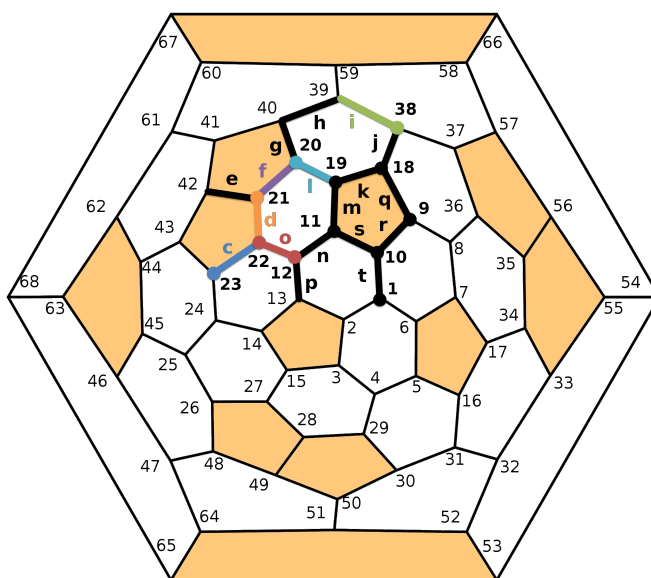


Figure 5.9. Schlegel diagram for $D_3^{-\#6140}C_{68}$. The asymmetric unit (12 atoms and 18 bonds) is highlighted in bold. Bonds for which the potential energy surface has been studied in detail are remarked in color (**c**: blue; **d**: orange; **f**: purple; **i**: green; **l**: cyan; **o**: red).

5.4.2. Thermodynamics: analysis of products

The 18 possible monoadducts have been calculated in a first approximation. For a general analysis, the methylmalonate products have been considered. The monoadducts on short bonds with small pyramidalization angles show the largest relative energies (see Table 5.4). Moreover, in all the eighteen regioisomers the functionalized bond is broken, *i.e.*, open-cage fullerooids are formed. Relative product energies agree in general with those reported in ref. [9] predicting the [6,6] adduct on the **i** bond as the main product under thermodynamic control, without discarding some amount of the adduct on the **c** bond of [5,6] type.

Table 5.4. Reaction energies (in kcal·mol⁻¹) and relative stabilities (in parenthesis) for the different computed methylmalonate monoadducts of Sc₃N@D₃-^{#6140}C₆₈ in the gas phase.

Product	Bond ^a	Bond type	Bond distance (Å)	Angle (°) ^b	E _{reaction}	(E _{rel})	Final bond ^c
i	38-39	(6,6) – C	1.462	9.01	-67.3	(0.0)	Open
c	22-23	(5,6) – D	1.467	11.37	-67.2	(0.2)	Open
d	21-22	(5,6) – F	1.445	14.59	-65.6	(1.7)	Open
g	20-40	(5,6) – D	1.451	11.42	-63.2	(4.1)	Open
j	18-38	(6,6) – B	1.437	9.95	-59.1	(8.3)	Open
n	11-12	(6,6) – B	1.443	9.75	-58.7	(8.7)	Open
m	11-19	(5,6) – D	1.449	10.64	-57.6	(9.8)	Open
f	20-21	(5,6) – F	1.446	14.64	-56.8	(10.6)	Open
e	21-42	(5,5) – E	1.444	16.61	-55.5	(11.9)	Open
o	12-22	(6,6) – B	1.445	10.60	-55.2	(12.2)	Open
q	9-18	(5,6) – D	1.449	10.54	-54.0	(13.4)	Open
r	9-10	(5,6) – D	1.439	10.32	-52.6	(14.8)	Open
t	1-10	(6,6) – B	1.432	9.51	-47.3	(20.1)	Open
h	39-40	(6,6) – B	1.454	9.58	-46.8	(20.6)	Open
l	19-20	(6,6) – A	1.416	11.53	-46.2	(21.1)	Open
s	10-11	(5,6) – D	1.439	10.66	-44.9	(22.5)	Open
k	18-19	(5,6) – D	1.436	10.64	-43.5	(23.9)	Open
p	12-13	(6,6) – B	1.430	9.41	-41.4	(26.0)	Open

^a The bond which the malonate reacts with.

^b Average of the pyramidalization angle of the two atoms that form the bond.

^c Defines whether the C–C bond where the reaction occurs is broken (open) or not (closed).

5.4.3. Step 1: intermediates formation

As for $Sc_3N@I_h-C_{80}$, intermediates and TSs are named by the number of the attacked carbon (C_α in Figure 5.2) followed by the lowercase letter that identifies the product that is formed, according to the Schlegel diagram in Figure 5.9. For example, intermediate **22o** denotes that the malonate is attached to C-22 and that the intermediate leads to product **o**. We have also analyzed all the different intermediates for $Sc_3N@D_3^{-#6140}C_{68}$. The criteria followed to select them was the following: (i) at least one intermediate per independent atom; (ii) all the neighbor bonds of the [5,5] motif were computed; (iii) the [5,5] motif was not chosen due to its low reactivity observed in other additions; (iv) for the remaining atoms, intermediates leading to [6,6] monoadducts were preferred against the ones leading to a [5,6] product.

Table 5.5. Reaction energies (in kcal·mol⁻¹) and relative stabilities (in parenthesis) for the different computed methylmalonate monoadducts of $Sc_3N@D_3^{-#6140}C_{68}$ in the gas phase.

Intermediate ^a	Atom type	E _{rel} (kcal·mol ⁻¹)	Intermediate ^a	Atom type	E _{rel} (kcal·mol ⁻¹)
22c	566	0.0	19l	566	6.9
20l	566	0.3	18j	566	7.2
22d	566	0.5	1t	666	8.8
20f	566	1.5	21d	556	9.9
22o	666	1.7	11n	566	11.1
20g	566	2.4	23c	566	15.4
38i	666	3.2	9q	566	16.2
39i	666	3.2	10t	566	22.0
12o	666	3.9			

^a Label according to **Figure 5.9**.

The results show that all the intermediates around the pentalene unit are almost isoenergetic – with less than 2.5 kcal·mol⁻¹ difference. Then, the three 666 intermediates near the pentagon fusion lie at 3.2 and 3.9 kcal·mol⁻¹. The rest of the intermediates far from the [5,5] junction are found further at more than 7 kcal·mol⁻¹. As with the case of $Sc_3N@C_{80}$, we have here evaluated the energy path of the formation of the intermediates as well. Figure 5.10 shows that this first step of the Bingel-Hirsch reaction undergoes through an almost imperceptible energy barrier, thus the process can be considered barrierless.

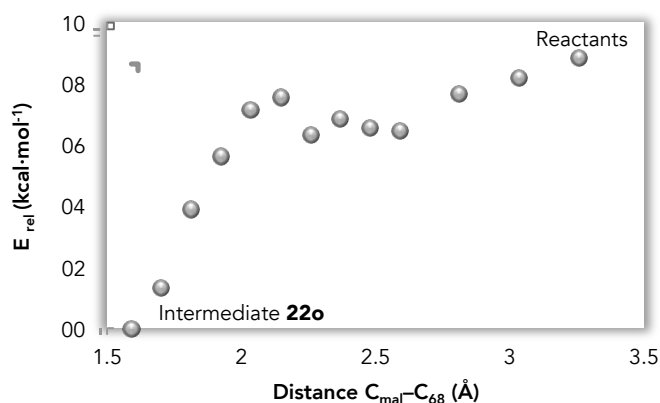


Figure 5.10. Plot of the relative energy of the scan of the PES along the addition coordinate from the intermediate **22o** to the reactants of the Bingel-Hirsch reaction on $\text{Sc}_3\text{N@C}_{68}$, in the gas phase See Table B2 for more details.

5.4.4. Step 2: going through a TS

The results obtained for the lowest-energy adducts, intermediates and TS are collected in Table 5.6 – as for $\text{Sc}_3\text{N@C}_{80}$, a more accurate methodology pcm/M06/TZP was also used here (see section 5.2). Regarding the monoadducts, three regioisomers are found to have similar energies, within 2 kcal·mol⁻¹, in the gas phase. The relative energies become somewhat larger in *o*-DCB (see Tables 5.4 and 5.6). Functionalization of the [6,6] pyrene-type **i** bond yields the lowest-energy adduct. Products derived from the functionalization of [5,6] corannulene-type **c** bond and of the type-F **d** bond are found at +2.7 and +5.4 kcal·mol⁻¹, respectively (Figure 5.9). Other regioisomers lay at higher energies. It is worth noting that the most stable isomers are near or within the pentalene unit.

Intermediates with the bromomalonate attached to atom **22** appear as the most stable ones. As previously commented, the malonate is able to rotate around the bond that forms with the fullerene with a rotation barrier of 7 kcal·mol⁻¹ (see Figure 5.11 and Figure 5.12), which is clearly accessible at ambient temperature. Depending on the orientation of the bromomalonate in this intermediate three different products can be formed: adducts on the **o**, **c** and **d** bonds. Intermediates **22c** and **22d** appear degenerated with energies of -21.3 kcal·mol⁻¹; the alternative orientation (intermediate **22o**), which functionalizes bond **o**, lays 2.1 kcal·mol⁻¹ higher. The same three adducts could be formed via attack of the ligand to atoms 12, 21 and 23. However the corresponding intermediates (**12o**, **21d** and **23c**) appear higher in energy (3.3, 9.6 and 15.0 kcal·mol⁻¹, respectively, see Table 5.6). Atom 22 shows a

larger pyramidalization angle compared to atoms 12 or 23; but atom 21, which is at a pentagon-pentagon-hexagon junction (556), shows the largest pyramidalization. Intermediate **20l** that yields adduct on the unique [6,6] pyracylene bond (**l**) appears almost degenerated to the lowest-energy intermediates **22c** and **22d**. Intermediate **20f** is only 1.3 kcal·mol⁻¹ above. The two intermediates that lead to the adduct on the [6,6] pyrene-type **i** bond, **38i** and **39i**, are degenerate at 3.2 kcal·mol⁻¹ with respect to **22d** in line with their identical pyramidalization angle due to their symmetry equivalence. Therefore, yet being some correlation, the stability of the intermediates does not only depend on this structural parameter.

Table 5.6. Relative energies with respect to reactants for the different computed intermediates, transition states and products of the Bingel-Hirsch addition on $Sc_3N@D_3^{-#6140}C_{68}$, including the solvent effects (o-DCB).

Product	Bond type	Inter. ^a	C _α type	E _{rel} Inter. ^b		E _{rel} TS ^b		E _{rel} Product ^b	
o	[6,6]-B	22o	566	-19.2	(2.1)	-2.3	(16.9)	-27.1	(13.6)
l	[6,6] Pyracylene	20l	566	-21.1	(0.2)	-1.3	(19.8)	-21.8	(18.8)
i	[6,6] Pyrene	38i	666	-18.1	(3.2)	-0.4	(17.7)	-40.7	(0.0)
i	[6,6] Pyrene	39i	666	-18.1	(3.2)	-0.4	(17.7)	-40.7	(0.0)
d	[5,6]-F	21d	566	-11.8	(9.6)	1.2	(13.0)	-35.3	(5.4)
d	[5,6]-F	22d	566	-21.3	(0.0)	1.3	(22.6)	-35.3	(5.4)
f	[5,6]-F	20f	566	-20.0	(1.3)	2.3	(22.3)	-26.7	(14.0)
c	[5,6] Coran.	22c	566	-21.3	(0.0)	4.6	(25.9)	-38.0	(2.7)
o	[6,6]-B	12o	666	-18.0	(3.3)	5.8	(23.8)	-27.1	(13.6)
c	[5,6] Coran.	23c	566	-6.3	(15.0)	11.2	(17.5)	-38.0	(2.7)

^a Labels for intermediates (see Figure 5.9). Note that the labels for the intermediates are also applicable to the TSs.

^b Relative energies with respect to reactants (in kcal·mol⁻¹); in parenthesis, relative stabilities with respect to the most stable intermediate/product (for intermediates/products) or the corresponding intermediate (for TS).

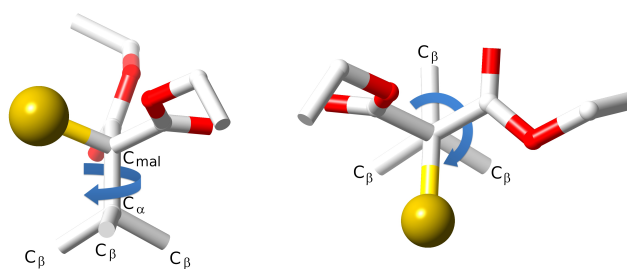


Figure 5.11. Schematic representation of the rotation of the bromomalonate group around the C_α-C_{mal} bond, front view (left) and top view (right). H atoms have been omitted for clarity.

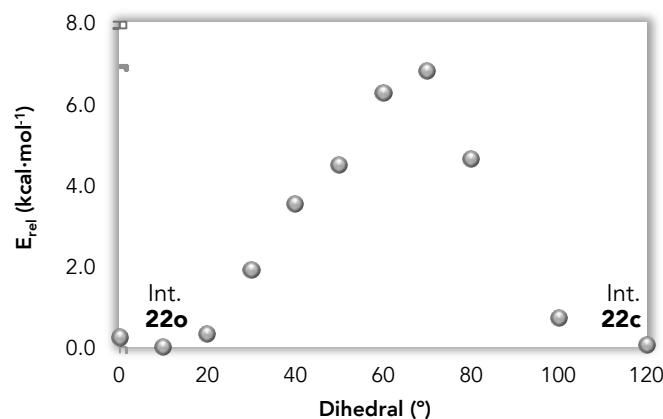


Figure 5.12. Plot of the relative energy for the intermediate **22o** with respect the dihedral angle (Figure 5.11). The dihedral angle changes from the intermediate **22o** (0°) to the intermediate **22c** (120°). See Table B3 for more details.

TSs for the lowest-energy intermediates have been computed. From intermediate **22o**, the formation of the monoadduct on bond **o** must overcome a TS (**22o**) with an activation energy barrier of 16.9 kcal·mol⁻¹ (-2.3 kcal·mol⁻¹ is the energy with respect to the reactants, Table 5.6 and Figure 5.13). The other two intermediates obtained from the rotation of the malonate group around the C_{mal}-C_α axis, **22d** and **22c**, lead to TSs with energies 3.6 and 6.9 kcal·mol⁻¹ higher, respectively. Therefore, upon coordination on the most favorable site **22** the formation of adduct **o** is expected as the main product. Intermediate **20l** yields a TS that is 1 kcal·mol⁻¹ higher in energy. The TSs obtained from intermediates **21d** and **23c** present low activation barriers with respect to the energy of their intermediates, but energies that are around 3.5 and 13.5 kcal·mol⁻¹ larger than the lowest-energy TS (Table 5.6). The degenerate **38i** and **39i** intermediates yield degenerate TSs, which lay around 2 kcal·mol⁻¹ higher than the lowest TS **22o**. Finally, TS **12o** is also around 8 kcal·mol⁻¹ higher than TS **22o**.

In agreement with the Sc₃N@I_h-C₈₀ system the lowest-energy intermediates lead to the lowest-energy TSs. Assuming that the conversion of intermediates to products is the rate-determining step of the Bingel-Hirsch addition, the product under kinetic control will be that with the lowest-energy TS, *i.e.* the adduct on type-B [6,6] bond **o**. Therefore, if this kinetic control is present, our results can fully explain the experiments performed by Gibson, Dorn and co-workers who proposed the regioisomer on bond **o** to be the product of the Bingel-Hirsch addition on Sc₃N@D₃-^{#6140}C₆₈.

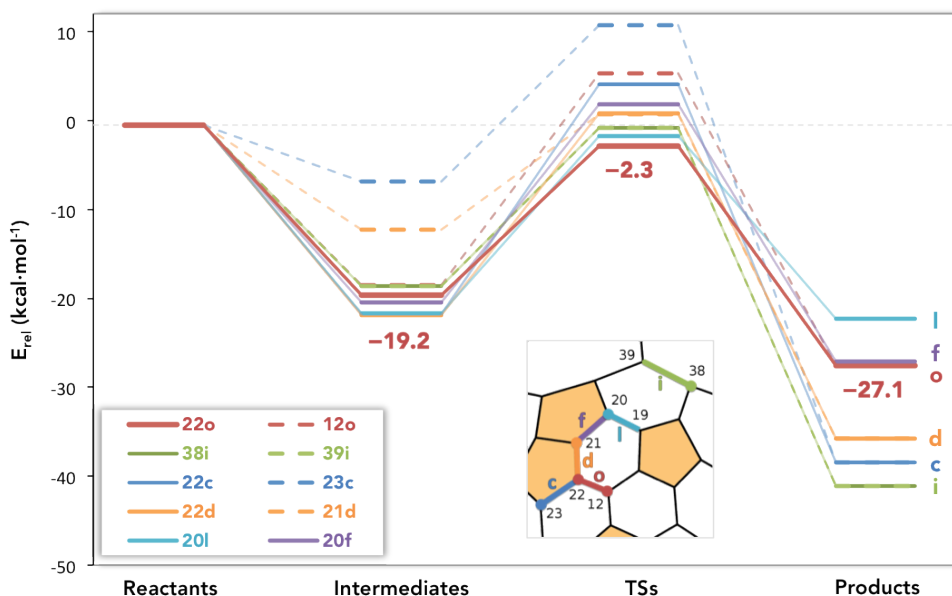


Figure 5.13. Plot of the different reaction paths studied in this work for the Bingel-Hirsch addition on $\text{Sc}_3\text{N}@D_3^{-\#6140}\text{C}_{68}$, considering solvent effects (o-DCB).

In general terms, our results show that the energetic profiles for the Bingel-Hirsch addition of bromomalonate on endohedral metallofullerenes with IPR and non-IPR cages are parallel: the lowest-energy intermediate is found around $-20 \text{ kcal}\cdot\text{mol}^{-1}$ with respect to reactants, and activation energies that appear about $17\text{-}19 \text{ kcal}\cdot\text{mol}^{-1}$ above intermediates. Moreover, in both cases the reaction takes place under kinetic control through the lowest-energy TS.

5.4.5. Looking for a "cheaper" methodology: test study for the Bingel-Hirsch reaction on $\text{Sc}_3\text{N}@C_{68}$

In the two already presented works of the Bingel-Hirsch addition on $\text{Sc}_3\text{N}@C_{80}$ and $\text{Sc}_3\text{N}@C_{68}$, a rather high-level computational methodology has been used – optimization using a TZP basis set, see section 5.2 – that has successfully explained the experimental results. To face new problems regarding the same reaction in other systems, we have found a somewhat "cheaper" methodology that saves computation time. We have first optimized the products, intermediates and TSs at different computational strategies in the gas phase (BP86/TZP, M06/DZP and M06/TZP); then, solvent effects (COSMO, PCM or SMD models) were included by single-point energy calculations at the pcm/M06/TZP, smd/M06/TZP or cosmo/BP86/TZP lev-

els. Final results are displayed in Figure 5.14, and the abbreviations used are found in Annex B.

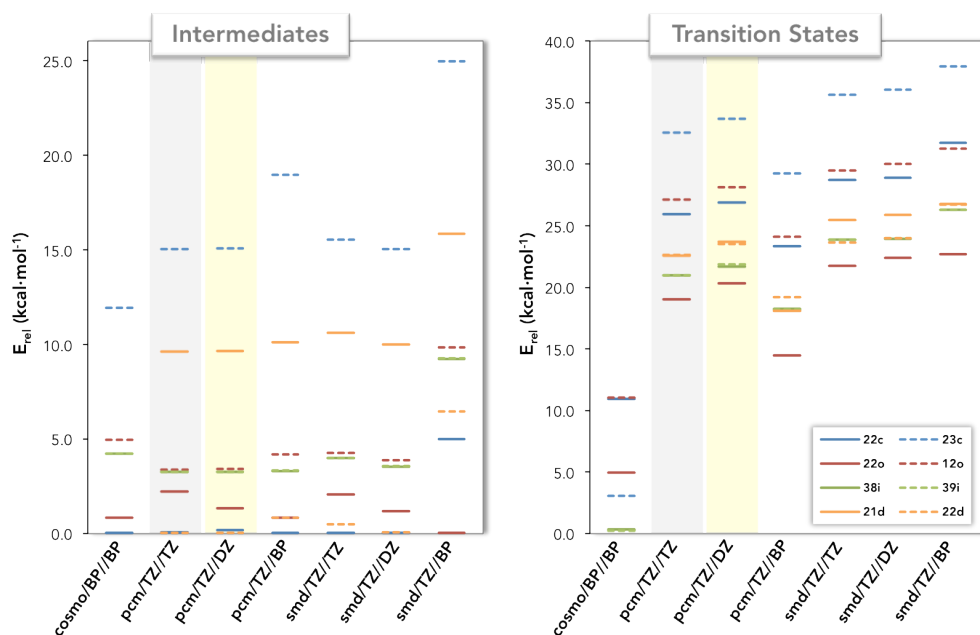


Figure 5.14. Comparison of the relative energies for the computed intermediates and TSs of the Bingel-Hirsch reaction on $\text{Sc}_3\text{N@C}_{68}$ using different computational strategies. Energies (in $\text{kcal}\cdot\text{mol}^{-1}$) include the solvent effects (o-DCB). See Tables B4 and B5 for a detailed list of values.

A general overview of the results shows that any of the methodologies gives qualitatively almost the same energy order than the first high-level methodology (colored in grey in Figure 5.14). The main differences are observed when optimization is performed at BP86/TZP level: energy differences are increased when SMD is used to include solvent effects, while they decrease when COSMO model is chosen. However, the most significant data is found for the TS computed at the cosmo/BP//BP (BP86/TZP//BP86/TZP including solvent effects with COSMO), where energy barriers respect the intermediates appear too short or even inexistent.

We checked that for the Bingel-Hirsch addition on $\text{Sc}_3\text{N@C}_{68}$ the methodology pcm/TZ//DZ (colored in yellow) gives almost identical results to the first high-level method and leads to the same conclusions. The unique difference is the optimization step, calculated using a DZP basis set instead of TZP. Thus, we have chosen the "cheaper" pcm/M06/TZP//M06/DZP strategy (see section 5.2) for the study of the endohedral metallofullerenes $\text{Y}_3\text{N@C}_{82}$ and $\text{Y}_3\text{N@C}_{84}$ in the next section.

5.5. Addition on $Gd_3N@C_{2n}$ ($2n=82$ and 84)

As of today, several reactions have been reported for trimetallic nitrides endohedral metallofullerenes (EMFs) of general formula $M_3N@C_{80}$.^[24] In the case of larger cages, Echegoyen and co-workers reported a reactivity study of gadolinium nitride EMFs ($Gd_3N@C_{2n}$; $2n=80, 84$ and 88) towards the cyclopropanation reaction, the Bingel-Hirsch reaction.^[7] The authors reported that the reactivity of the EMF is highly influenced on the fullerene size. Therefore $Gd_3N@C_{88}$ is the least reactive while $Gd_3N@C_{80}$ reacts readily with diethylbromomalonate in the presence of DBU to afford multiple additions if the reaction is not quenched. On the other hand, it was observed that non-IPR $Gd_3N@C_{s-}^{#51365}C_{84}$ afforded a monoadduct that was characterized by HPLC, UV-vis-NIR, MALDI-TOF MS and electrochemistry.

Similarly to $Gd_3N@C_{84}$, only monoaddition is obtained on non-IPR $Gd_3N@C_{s-}^{#39663}C_{82}$ when reacted with diethylbromomalonate under the same conditions. No signs of further additions to the fullerene cage were observed, as observed in the mass spectrum of the reaction mixture after 20 minutes of reaction (see Figure 5.15). The reaction mixture was subjected to purification by HPLC, being required a multistage separation with the Buckyprep-M and Buckyprep columns, isolating three monoadducts with relative amounts of 90%, 7% and 3%, as calculated from the HPLC trace (see Figure 5.15).

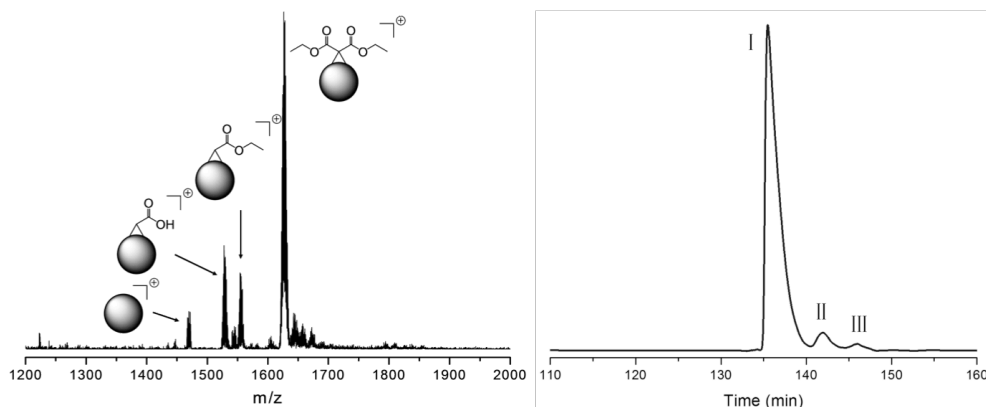


Figure 5.15. a) MALDI-TOF mass spectrum of the reaction mixture of $Gd_3N@C_{82}$, diethylbromomalonate and DBU in *o*-DCB. b) HPLC trace of the mixture of $Gd_3N@C_{82}$ monoadducts (I, II and III) when passed throughout a linear combination of Buckyprep and Buckyprep-M columns. The three fractions were identified by MALDI-TOF MS. Attempts to obtain suitable crystals of isomer I for X-ray analysis have been unsuccessful so far. Solvent: Toluene; Flow rate: 2.0 mL/min; Detection: 370 nm.

In 2010, an extensive computational study based on relative stabilities of the reaction products was also done to rationalize the regioselectivity observed in these two non-IPR EMFs.^[6] The results along this chapter, however, showed that the Bingel-Hirsch addition on EMFs does not take place under thermodynamic control, but under kinetic control,^[25] as the first available fullerene oxides $C_{60}O$ and $C_{60}O_2$.^[26] Based on that, we have performed here a thorough exploration of the reaction profiles for the Bingel-Hirsch addition on $Gd_3N@C_s\text{-}\#39663C_{82}$ and $Gd_3N@C_s\text{-}\#51365C_{84}$ that complements our previous studies. Products that should be observed under kinetic control are proposed.

Since calculations with metals that have unfilled the 4f shell such as Gd^{3+} ion (f^7) are not yet a routine task, the model replacing Gd^{3+} by Y^{3+} , $Y_3N@C_{84}$ and $Y_3N@C_{82}$, is used. Such an approximation has been proposed earlier for modeling properties of $M_3N@C_{2n}$ (M =lanthanide).^[21b, 27] Moreover, instead of the ethylmalonate we have used the methylmalonate as computational model.

5.5.1. Description of the systems

X-ray diffraction studies have shown that Gd_3N is encapsulated, among others, in the egg-shaped non-IPR $C_s\text{-}\#39663C_{82}$ and $C_s\text{-}\#51365C_{84}$ fullerenes.^[28] These two cages are pretty similar, as shown in Figure 5.17. Apart from the adjacent pentagon pair (APP, orange colored), the two structures have a large common part (grey colored). Structure $C_s\text{-}\#39663C_{82}$ can be obtained from $C_s\text{-}\#51365C_{84}$ after the Stone-Wales isomerization of two bonds and subsequent C_2 extrusion (see Figure 5.16). It is not coincidence that both cages show low number of pyracylene units (Figure 1.3), just four and two for C_{82} and C_{84} , respectively. As shown in Chapter 3, structures with a low number of pyracylenes are found among the most suitable cages to encapsulate metallic clusters.^[29]

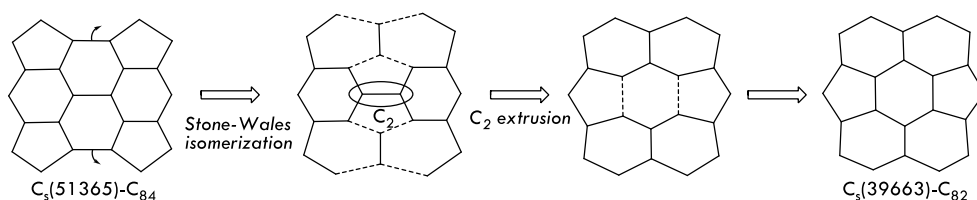


Figure 5.16. Isomerization path from $C_s\text{-}\#51365C_{84}$ to $C_s\text{-}\#39663C_{82}$.

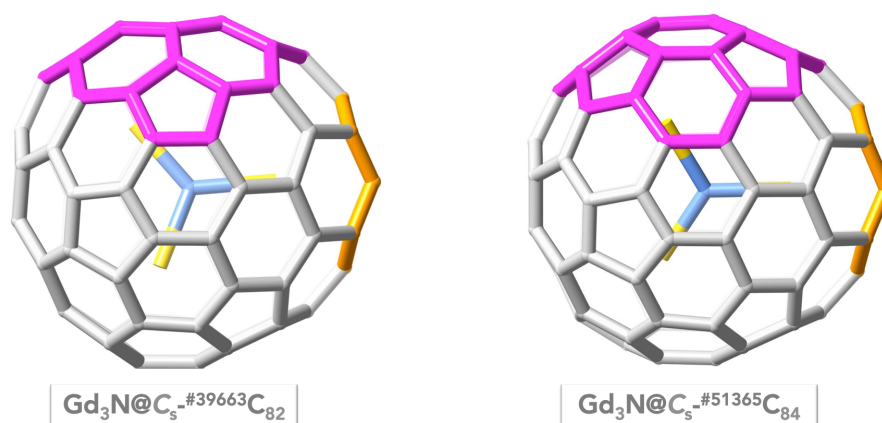


Figure 5.17. Representation of fullerene structures for $Gd_3N@C_{82}$ (left) and $Gd_3N@C_{84}$ (right). The adjacent pentagon pair is highlighted in orange. The difference between the two structures is shown in magenta.

Due to the low symmetry of the carbon cages (C_s), a large number of different C–C bonds exist – 67 for C_{84} and 66 for C_{82} . The symmetry of the trimetallic nitride EMF is reduced to C_1 when the X-ray structure is considered – 126 bonds for C_{84} and 123 for C_{82} –, but pseudo- C_s symmetry can be considered, since the plane of the cluster is near to the σ_h plane that relates the two halves of the C_{2n} cages. We have checked that this approximation is valid as well. Additionally, the $C_s\text{-}\#51365C_{84}$ shows pseudo- C_{2v} symmetry in the area around the pentalene motif, thus reducing considerably the number of independent bonds to be analyzed (Figure 5.18).

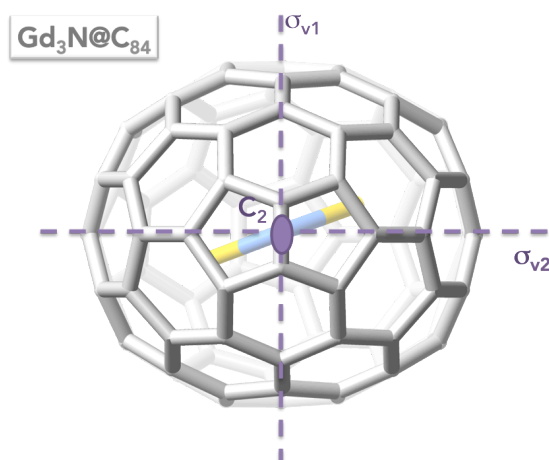


Figure 5.18. Local pseudo- C_{2v} symmetry around the pentalene motif in $Gd_3N@C_{84}$. The C_2 axis is represented as an ellipse, and the vertical planes as dotted lines.

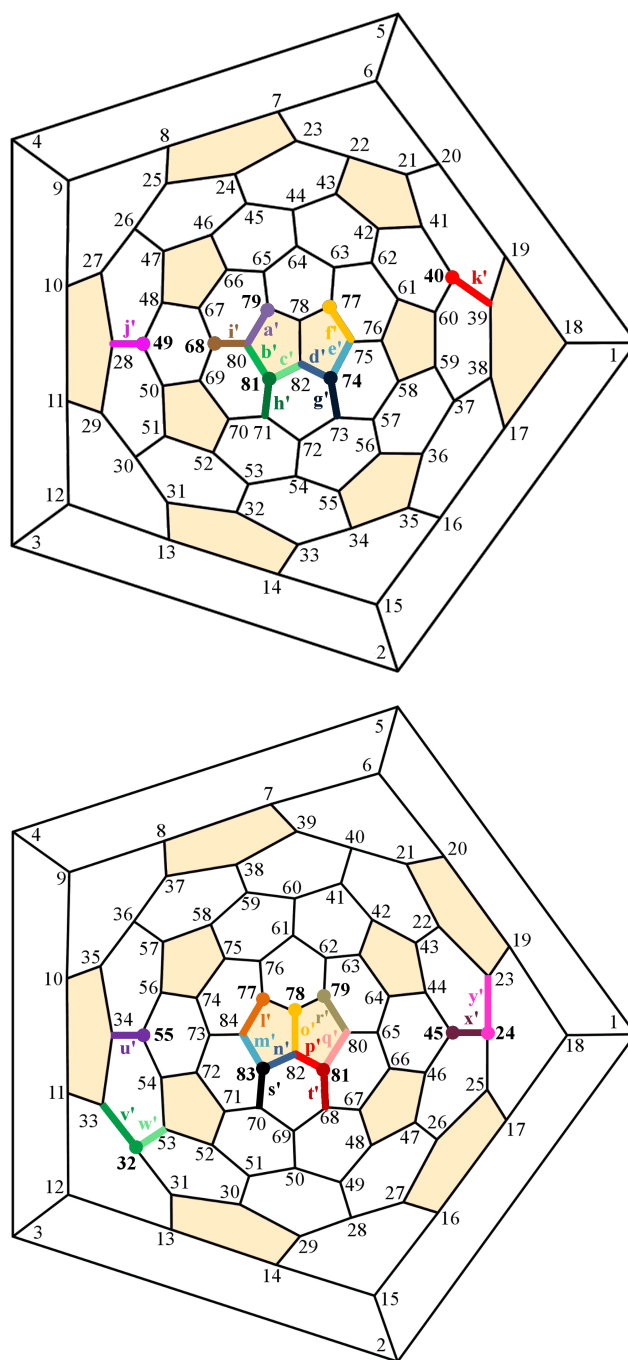


Figure 5.19. Schlegel diagrams for $C_{82}^{\#39663}$ (top) and $C_{84}^{\#51365}$ (bottom). The 12 pentagons are colored in orange. The bonds for which the potential energy surface has been studied in detail are highlighted in bold. The colour code is also used in Figure 5.22 and 5.24.

5.5.2. Thermodynamics: Rotation of the Gd_3N cluster in products

First of all, we have analyzed the possibility of rotating the cluster inside the carbon cage, around the three axis showed in Figure 5.20. The results obtained in Table 5.7 show that the cluster is able to rotate only around the axis N–Y–centroid of the [5,5] bond, called from now “y axis”, due to the egg-shaped framework of the $C_{5-}^{#51365}C_{84}$ and $C_{5-}^{#39663}C_{82}$ cages. Only 2 kcal·mol⁻¹ are necessary to rotate the cluster 45° around the y axis in the two EMFs. One important difference between the two cages is that the Y_3N cluster is able to freely rotate around the y axis in $C_{5-}^{#39663}C_{82}$, but free rotation around this axis is hindered in the $C_{5-}^{#51365}C_{84}$ cage (the energy rises up to 23 kcal·mol⁻¹ when the cluster rotates 90°). Moreover, the cluster does not fit so well in any of the two egg-shaped cages when it is rotated around the other two perpendicular axes, so rotation around them is not feasible.

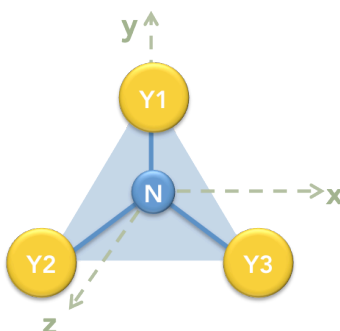


Figure 5.20. Schematic representation of the planar Y_3N cluster and its orientation in a Cartesian reference system. Orientational isomers obtained from rotation of Y_3N around these three axis (x, y, and z) are analyzed in **Table 5.7**.

Table 5.7. Relative energies (kcal·mol⁻¹) for different orientational isomers of $Y_3N@C_{2n}$ ($2n=84$ and 82)

Axis	Rotation ^a	C_{82} E_{rel} (kcal·mol ⁻¹)	C_{84} E_{rel} (kcal·mol ⁻¹)
x	90 °	27.3	16.4
x	180 °	–	14.0
y	0 °	0.0	0.0
y	22 °	0.2	2.1
y	45 °	2.5	2.3
y	90 °	4.1	23.1
z	60 °	13.3	–

^a Rotation angle with respect the initial position drawn in Figure 5.20.

In Table 5.8 we show the structural parameters of 23 C–C bonds in $Y_3N@C_{84}$ and 29 C–C bonds in $Y_3N@C_{82}$ (C–C distance and average pyramidalization angle of the two carbon atoms), for which we have computed the Bingel-Hirsch reaction along with the reaction energies of the resulting monoadducts. The labels of the C atoms as well as the bond type for each of the C–C bond are also displayed (see Schlegel diagram in Figure 5.19). Apart from the [5,5] bond, there are different types of [5,6] and [6,6] bonds that are designed according to the typical notation in Figure 1.3.

As a general conclusion, we find that the most stable adducts are those that have reacted on C–C bonds whose distance is larger than the average C–C distance and whose pyramidalization angle is larger than the average angle. Accordingly, bonds with short C–C distances and small pyramidalization angles are related to unstable adducts. This dependence can be nicely observed when the relative energy of the different monoadducts is plotted against these two variables (see Figure 5.21). There is a region of low energy for large C–C distances and large pyramidalization angles. It is important to note that for most of the monoadducts (16 out of 21 for $Y_3N@C_{84}$ and 24 out of 29 for $Y_3N@C_{82}$), the C–C bond where the addition takes place is broken, as experimentally observed in $Y_3N@C_{80}$ ^[5b] and $Sc_3N@C_{68}$ ^[9] and in contrast what is found for $Sc_3N@C_{78}$.^[8] Interestingly, adducts with closed C–C bonds are within the most unstable structures. This opening is mainly caused by the presence of the M_3N cluster since most of the predicted adducts on the empty C_{84} and C_{82} cages feature closed C–C bonds.

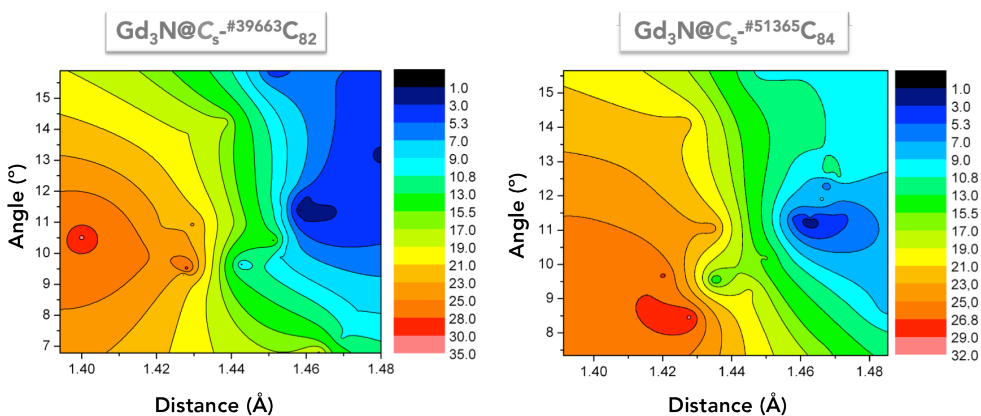


Figure 5.21. 2D plots of the relative energy ($\text{kcal}\cdot\text{mol}^{-1}$) of the computed monoadducts with respect to the C–C distances and the pyramidalization angles for a) $C_5\text{-}\#39663C_{82}$ and b) $C_5\text{-}\#51365C_{84}$.

Table 5.8. Reaction energies (in kcal·mol⁻¹) and relative stabilities (in parenthesis) for the different computed monoadducts and most significant structural parameters of pristine $Y_3N@C_{84}$ and $Y_3N@C_{82}$.

Product	Bond ^a	Bond type	Bond distance (Å)	Angle (°) ^b	E_{reaction}	(E_{rel}) ^c	Final bond ^d
$Y_3N@C_{5-39663}C_{82}$							
	38-39	[5,6]-D	1.459	11.39	-68.9	(0.0)	Open
f'	75-77	[5,6]-D	1.461	11.75	-68.4	(0.5)	Open
e'	74-75	[5,6]-D	1.461	11.69	-67.3	(1.6)	Open
	28-29	[5,6]-D	1.480	13.22	-66.7	(2.2)	Open
	29-30	[6,6]-B	1.466	11.32	-66.7	(2.2)	Open
a'	79-80	[5,6]-D	1.459	10.97	-66.1	(2.8)	Open
	78-82	[5,5]-E	1.451	15.89	-65.8	(3.1)	Open
j'	28-49	[6,6]-B	1.465	11.75	-65.2	(3.7)	Open
b'	80-81	[5,6]-D	1.459	10.98	-64.9	(4.0)	Open
	19-39	[5,6]-D	1.462	11.77	-63.2	(5.7)	Open
g'	73-74	[6,6]-B	1.456	10.19	-61.2	(7.7)	Open
	57-58	[6,6]-B	1.443	9.141	-60.9	(8.0)	Open
	18-19	[5,6]-D	1.456	12.24	-60.4	(8.5)	Open
k'	39-40	[6,6]-B	1.453	9.87	-60.2	(8.7)	Open
	15-16	[6,6]-C	1.474	8.15	-60.0	(8.9)	Open
	11-29	[5,6]-D	1.453	11.43	-59.1	(9.8)	Open
	44-45	[6,6]-C	1.470	7.29	-58.8	(10.1)	Open
	24-25	[5,6]-D	1.451	10.42	-52.3	(16.6)	Open
	60-61	[5,6]-D	1.442	10.98	-52.3	(16.6)	Open
d'	74-82	[5,6]-F	1.438	14.25	-50.6	(18.3)	Open
c'	81-82	[5,6]-F	1.428	13.83	-49.7	(19.2)	Closed
	54-72	[6,6]-C	1.463	6.78	-48.7	(20.2)	Open
	32-53	[6,6]-B	1.427	9.30	-48.6	(20.3)	Open
	58-76	[5,6]-D	1.427	10.497	-46.7	(22.2)	Closed
	18-1	[6,6]-A	1.422	10.94	-46.6	(22.3)	Open
	14-33	[5,6]-D	1.430	10.94	-45.3	(23.6)	Open
	22-23	[6,6]-A	1.394	10.66	-42.1	(26.8)	Closed
i'	68-80	[6,6]-B	1.428	9.52	-38.2	(30.7)	Closed
	75-76	[6,6]-A	1.400	10.51	-37.7	(31.2)	Closed

Table 5.8. Cont.

Product	Bond ^a	Bond type	Bond distance (Å)	Angle (°) ^b	E _{reaction}	(E _{rel}) ^c	Final bond ^d
Y₃N@C_s-^{#51365}C₈₄							
l'	77-84	(6,5) – D	1.461	11.28	-71.4	(0.0)	Open
m'	83-84	(6,5) – D	1.464	11.26	-71.2	(0.2)	Open
q'	80-81	(6,5) – D	1.458	11.34	-67.0	(4.4)	Open
y'	23-24	(6,6) – B	1.472	11.37	-66.9	(4.5)	Open
v'	32-33	(6,6) – B	1.468	12.30	-66.7	(4.7)	Open
r'	79-80	(6,5) – D	1.463	11.40	-63.9	(7.5)	Open
x'	24-45	(6,6) – C	1.485	8.75	-63.7	(7.6)	Open
o'	78-82	(5,5) – E	1.449	12.55	-62.4	(9.0)	Open
	22-23	(6,5) – D	1.461	12.85	-62.0	(9.4)	Open
	33-34	(6,5) – D	1.466	11.90	-61.2	(10.2)	Open
	17-25	(6,5) – D	1.457	10.03	-60.0	(11.4)	Open
	19-23	(6,5) – D	1.471	12.58	-59.9	(11.5)	Open
	11-33	(6,5) – D	1.468	12.73	-59.5	(11.9)	Open
	10-35	(6,5) – D	1.435	9.55	-59.2	(12.2)	Open
	13-31	(6,5) – D	1.450	10.14	-57.6	(13.8)	Open
	40-41	(6,6) – C	1.466	7.35	-54.7	(16.7)	Open
	35-36	(6,6) – B	1.445	9.20	-51.4	(20.0)	Open
p'	81-82	(6,5) – F	1.427	14.12	-48.9	(22.5)	Closed
	56-74	(6,5) – D	1.435	11.05	-46.4	(24.9)	Closed
	26-47	(6,6) – A	1.391	10.69	-45.3	(26.1)	Closed
	15-16	(6,6) – B	1.420	9.69	-44.0	(27.4)	Closed
	30-51	(6,6) – B	1.428	8.46	-41.0	(30.4)	Closed

^a The bond which the malonate reacts with.

^b Average pyramidalization angle of the C atoms of the reacting bond.

^c Computed at the BP86/TZP level in the gas phase.

^d Defines whether the C–C bond where the reaction occurs is broken (open) or not (closed).

The origin of the stability of those adducts with large C–C distances and large pyramidalization angles can be: (1) a topological effect, *i.e.* the type of C–C bond ([5,5], [5,6], etc.); or (2) the presence of a nearby M atom from the encapsulated M₃N cluster. Therefore, some bonds are intrinsically reactive as a consequence of the release of bond strain (as for example bond 77-84 in Y₃N@C₈₄ and 72-74 in

$Y_3N@C_{82}$) whereas other bonds are activated by the presence of the M_3N cluster (as for example bond 23-24 in $Y_3N@C_{84}$ and 31-32 in $Y_3N@C_{82}$, compare Table 5.8 and Table 5.9). This can be clearly seen in Table 5.9 where the reaction (and relative) energies of different products of the Bingel-Hirsch reaction on the pristine C_{84} and C_{82} cages are displayed.

Table 5.9. Reaction energies of some adducts without the internal M_3N cluster for the C_{2n} cage. Only the most stable adducts in Table 5.8 are calculated.

Product	Bond ^a	Bond type	Bond distance (Å)	Angle (°) ^b	E_{reaction}	(E_{rel})	Final bond ^c
$C_{5-}^{\#39663}C_{82}$							
f'	75-77	[5,6]-D	1.468	11.48	-67.6	(0.0)	Open
	19-39	[5,6]-D	1.418	10.64	-63.9	(3.7)	Open
	78-82	[5,5]-E	1.399	15.31	-57.8	(9.8)	Closed
a'	79-80	[6,6]-B	1.459	11.60	-52.1	(15.6)	Closed
	28-29	[6,6]-B	1.436	10.79	-53.0	(14.6)	Closed
	29-30	[6,6]-C	1.421	9.68	-52.2	(15.4)	Closed
g'	73-74	[5,6]-D	1.436	9.85	-52.0	(15.7)	Closed
	28-49	[6,6]-C	1.429	9.72	-49.6	(18.0)	Closed
	38-39	[5,6]-D	1.467	10.45	-42.9	(24.8)	Closed
$C_{5-}^{\#51365}C_{84}$							
l'	77-84	[5,6]-D	1.457	11.31	-66.8	(0.0)	Open
m'	83-84	[5,6]-D	1.455	11.32	-66.1	(0.7)	Open
q'	80-81	[5,6]-D	1.455	11.33	-62.2	(4.6)	Closed
r'	79-80	[5,6]-D	1.452	11.34	-62.2	(4.6)	Closed
x'	24-45	[6,6]-C	1.474	8.79	-56.7	(10.1)	Open
y'	23-24	[6,6]-B	1.472	9.87	-54.1	(12.3)	Closed
v'	32-33	[6,6]-B	1.427	9.97	-54.5	(12.7)	Closed
o'	78-82	[5,5]-E	1.448	16,116			

^a The bond which the malonate reacts with.

^b Average pyramidalization angle of the C atoms of the reacting bond.

^c Defines whether the C-C bond where the reaction occurs is broken (open) or not (closed).

There are five adducts of $Y_3N@C_{84}$ which show relative energies within 5 kcal·mol⁻¹ (Table 5.8). The two most stable adducts correspond to the intrinsically reactive [5,6]-D bonds 77-84 and 83-84, see Figure 5.19. Nonetheless, the [5,5] bond 78-82

is not found to be between the most stable adducts (relative energy around 9 kcal·mol⁻¹). Other bonds with larger C–C distances seem to give more stable adducts than the [5,5] bond. On the other hand, for Y₃N@C₈₂, up to nine adducts show relative energies within 5 kcal·mol⁻¹. The two most stable adducts correspond to one activated bond (31-32) and to one intrinsically reactive bond (72-74), see Figure 5.19. The other low-energy adducts are also on intrinsically reactive (71-72) and activated bonds (20-21). The [5,5] bond 75-80 is found within the most reactive bonds, but it does not lead to the most stable adduct (relative energy of around 3 kcal·mol⁻¹). The [5,6]–D bonds with large C–C distances (72-74, 71-72, 76-78) yield more stable adducts than the [5,5] bond. So, the internal cluster clearly activates the 31-32 bond in Y₃N@C₈₂ that otherwise would yield to a very unstable adduct (see Table 5.9). However, the effect of the metal cluster is not so critical in Y₃N@C₈₄, being the 77-84 bond the most reactive either for the empty cage or the endohedral metallofullerene (see Table 5.8). It is important noticing that those intrinsically reactive bonds that give rise to the most stable adducts for the two non-IPR EMF considered here are bonds of [5,6]–D type that are placed in the APP-pentalene unit (see Schlegel diagrams in Figure 5.19). So, the release of strain in the fullerene cages due to functionalization must be at the origin of such stable adducts.

Comparison of the reaction energies on “symmetric” bonds (77-84 vs 83-84 and 79-80 vs 80-81 in Y₃N@C₈₄; and bonds 72-74 vs 71-72 and 76-78 vs 78-79 in Y₃N@C₈₂, see Table 5.8) corroborates that the error due to considering pseudo-C_s symmetry is acceptable (within few kcal·mol⁻¹).

As shown in Table 5.9, the bond that leads to the most stable adduct in Y₃N@C₈₂ (31-32) is clearly activated by the presence of the internal cluster (it would be very unstable without the encapsulation of the M₃N cluster). However, the nitride does not affect the most stable adduct of Y₃N@C₈₄ (in both cases the most stable product is on the 77-84 bond).

Finally, we have checked the validity of Y₃N@C_{2n} as computational model for Gd₃N@C_{2n}. We have computed a total of five adducts of different types for both fullerenes. The reaction (and relative) energies for the computed adducts are displayed in Table 5.10. The most important difference in the reaction energies with respect to the results obtained with our model Y₃N@C_{2n} are, in Gd₃N@C₈₄ and Gd₃N@C₈₂, only 1.5 kcal·mol⁻¹ (for the bond 23-24) and 1.6 kcal·mol⁻¹ (for bond 21-23), respectively, which confirms the validity of our analysis.

Interestingly, for Gd₃N@C₈₂, the adduct on the [5,6]–D type 72-74 bond is now somewhat more stable than the activated [5,6]–D type 31-32 bond. Since the en-

ergy differences between the most stable adducts are so small, the modeling by $Y_3N@C_{82}$ changes the relative stability of the two most stable isomers. The important point is, however, that the two most stable isomers show very similar energies.

Table 5.10. Reaction energies and relative stabilities for five computed monoadducts and structural parameters of the parent $Gd_3N@C_{84}$ and $Gd_3N@C_{82}$

Product	Bond ^a	Bond type	Bond distance (Å)	Angle (°) ^b	E_{reaction}	(E_{rel})	Final bond ^c
$Gd_3N@C_s(39663)-C_{82}$							
	38-39	[5,6]-D	1.459	11.46	-69.6	(0.0)	Open
f'	75-77	[5,6]-D	1.461	11.81	-69.8	(-0.2)	Open
	29-30	[6,6]-B	1.466	11.32	-68.3	(1.3)	Open
	78-82	[5,5]-E	1.452	15.88	-65.3	(4.3)	Open
	75-76	[6,6]-A	1.401	10.52	-37.2	(32.4)	Closed
$Gd_3N@C_s(51365)-C_{84}$							
l'	77-84	[5,6]-D	1,462	11,28	-71.6	(0.0)	Open
m'	83-84	[5,6]-D	1,464	11,26	-71.5	(0.1)	Open
y'	23-24	[6,6]-B	1,472	11,37	-68.4	(3.2)	Open
v'	32-33	[6,6]-B	1,468	12,30	-67.9	(3.7)	Open
o'	78-82	[5,5]-E	1,449	15,65	-61.6	(10.0)	Open

^a The bond which the malonate reacts with.

^b Average pyramidalization angle of the C atoms of the reacting bond.

^c Defines whether the C-C bond where the reaction occurs is broken (open) or not (closed).

To conclude, it is important to keep in mind that the rotation of the metal cluster around the N-Gd-centroid [5,5] bond in $Gd_3N@C_{82}$ can activate other bonds that would yield other adducts as stable as the ones that we have found. At the same time, bonds that are activated by the cluster (as for example 31-32) would become less reactive due to this internal rotation. On the other hand, other bonds, as for example bond 72-74, will remain reactive regardless of the internal rotation. So, the prediction of the most abundant adduct (90%) of $Gd_3N@C_{82}$ is not a trivial task since a synergy between the addition process and the internal rotation of the cluster could exist. On the contrary, only two regioisomers are found to be the most stable when the Bingel-Hirsch reaction takes place on $Gd_3N@C_{84}$: adducts on bonds 77-84 and 83-84 (more than 3 kcal·mol⁻¹ more stable than the other regioisomers). These two bonds, which are equivalent in the absence of the metal cluster (C_s symmetry), become equivalent due to the possible rotation of the Gd_3N cluster

around the y axis (up to 45 degrees). So, our computations predict that only one regioisomer is much more stable than the rest if the reaction took place under thermodynamic control.

5.5.3. Steps 1 & 2: analysis of reaction path study

Rotation of the internal cluster is another important issue that has to be considered in this type of analysis. Only those orientations with one Y^{3+} ion directed to the pentalene unit have been selected for each regioisomer and intermediate due to the limited rotation of the Y_3N cluster in these cages (Table 5.7).^[6] The products under kinetic control for the Bingel-Hirsch reaction on $Sc_3N@C_{2n}$ ($2n=80$ and 68) are adducts on [6,6] B-type bonds near the pentalene unit (Figure 1.3).^[25] For the IPR C_{80} cage the intermediate was formed on a 666 atom, *i.e.* atom surrounded by three hexagons, while for the non-IPR C_{68} cage it was formed in one of the 566 atoms of the pentalene unit. Based on those results, in this study we have analyzed (i) all the different bonds around the pentalene region; and (ii) all the B-type bonds near to the metal atoms, taking into account the restricted rotation of the internal cluster. Only for those intermediates with the lowest energies, which are highlighted in bold in Figure 5.19, we have computed the associated transition states (TSs). Notice that bonds are named with letters while atoms are labeled with numbers. Thus, for example, we can identify the intermediate/TS **74g'** of the $Y_3N@C_{82}$ cage as the one in which the malonate is bonded to atom 74 and oriented to form the product **g'**.

5.5.3.1. Addition on $Y_3N@C_s^{#39663}C_{82}$

The results related to the analysis of the reaction path on $Y_3N@C_{82}$ are collected in Table 5.11 (a complete list of all the results is presented in Table B1, Annex B). Four products are almost isoenergetic within the error of the methodology: **b'**, **f'**, **a'**, and **e'**, with relative energies of 0.0, 0.3, 0.5 and 0.7 kcal·mol⁻¹, respectively. Note that all these four adducts are on corannulene-type bonds located around the pentalene motif (Figure 5.19). Moreover, the four bonds show very similar structural parameters according to their symmetry equivalence. Due to the reduced rotation of the nitride around the N–Y–pentalene axis, we have only considered the adducts on bonds **j'** and **k'**, among the bonds that are far from the pentalene unit (Figure 5.19). Products **j'** and **k'** appear 5.2 and 6.4 kcal·mol⁻¹ higher in energy than **b'**, respectively. Product **g'** is close in energy to them, at 6.1 kcal·mol⁻¹. The energy difference between this first set of monoadducts and the rest of possible regioisomers is more than 11 kcal·mol⁻¹ (see Table 5.11 and B1).

Results are analogous to those already found using different computational settings (see Table 5.8).^[6]

Table 5.11. Energies with respect to reactants for the different computed intermediates, TS and products of the Bingel-Hirsch addition on $Y_3N@C_{82}$ including solvent effects (*o*-DCB).

Product	Bond type	Inter. ^a	C _α type	E _{rel} Inter. ^b	E _{rel} TS ^b	E _{rel} Product ^b
$Y_3N@C_s(39663)-C_{82}$						
g'	[6,6]-B	74g'	566	-15.7 (1.1)	-2.1 (13.7)	-32.3 (6.1)
h'	[6,6]-B	81h'	566	-14.5 (2.4)	2.4 (19.2)	-20.6 (17.8)
j'	[6,6]-B	49j'	666	-14.6 (2.2)	3.6 (18.2)	-33.2 (5.2)
c'	[5,6]-F	81c'	566	-16.1 (0.7)	3.9 (20.7)	-20.2 (18.2)
i'	[6,6]-B	68i'	666	-14.4 (2.4)	4.1 (18.5)	-12.6 (25.8)
e'	[5,6] coran.	74e'	566	-12.8 (4.0)	6.3 (22.0)	-37.7 (0.7)
a'	[5,6] coran.	79a'	566	-14.3 (2.5)	6.8 (21.0)	-37.9 (0.5)
d'	[5,6]-F	74d'	566	-14.9 (1.9)	6.9 (22.6)	-19.9 (18.5)
b'	[5,6] coran.	81b'	566	-16.8 (0.0)	8.0 (24.8)	-38.4 (0.0)
k'	[6,6]-B	40k'	666	-15.7 (1.2)	8.7 (24.4)	-32.0 (6.4)
f'	[5,6] coran.	77f'	566	-14.8 (2.0)	8.8 (23.6)	-38.1 (0.3)

^a Labels for intermediates: **74g'** stands for intermediate on atom 74 that leads to adduct on bond **g** (see Figure 5.19). Note that the labels for the intermediates are also applicable to the TSs.

^b Relative energies with respect to reactants (in kcal·mol⁻¹); in parenthesis, relative stabilities with respect to the most stable intermediate/product (for intermediates/products) or the corresponding intermediate (for TS).

We have analyzed the different intermediates that lead to these products (Table 5.11). The most stable intermediate **81b'** is the one that leads to the most stable product. Intermediates **81c'** and **81h'**, which are directly related to **81b'** by 120-degree rotation around the formed C_{fuller}-C_{malonate} axis, appear at 0.7 and 2.4 kcal·mol⁻¹ above (see Figure 5.11). Intermediates **74g'** and **40k'** are found at 1.1 and 1.2 kcal·mol⁻¹ with respect to **81b'**. Finally, we found a set of different type of intermediates in the range between 1.9 and 2.5 kcal·mol⁻¹. Note that the energy differences within the intermediates are not as significant as those found among products (see Table 5.11).

The TSs for the lowest-energy intermediates have been also computed (Table 5.11). From intermediate **74g'**, the formation of product on bond **g'** requires to overcome an activation barrier of 13.7 kcal·mol⁻¹ (the energy of the TS is -2.1 kcal·mol⁻¹ relative to reactants, Table 5.11 and Figure 5.22). The second lowest-energy TS, **81h'**, was found 4.5 kcal·mol⁻¹ above. TSs **49j'**, **81c'** and **68i'** are locat-

ed within $6 \text{ kcal}\cdot\text{mol}^{-1}$ with respect to **74g'**. The rest of computed TSs lie at more than $6 \text{ kcal}\cdot\text{mol}^{-1}$. The lowest-energy TSs are, in general, those that lead to [6,6] B-type products. Furthermore, near the pentalene unit, the TSs formed on 566 atoms are favored, while far from the pentalene, those formed on 666 atoms are preferred. We can explain these results because addition onto a 566 atom near the [5,5] region releases more surface strain than addition onto a 666 atom as found for other EMFs.^[25, 30] Thus, if the Bingel-Hirsch reaction were to happen under kinetic control on $\text{Y}_3\text{N}@C_{5^{-}\#39663}C_{82}$, we propose that the most abundant monoadduct should be product **g'**, which shows the lowest-energy TS (Figure 5.22). For the second most abundant monoadduct, with yields of 7%, we propose product **h'**. Finally, three candidates are proposed for the third abundant monoadduct: products **j'**, **c'**, and **l'**.

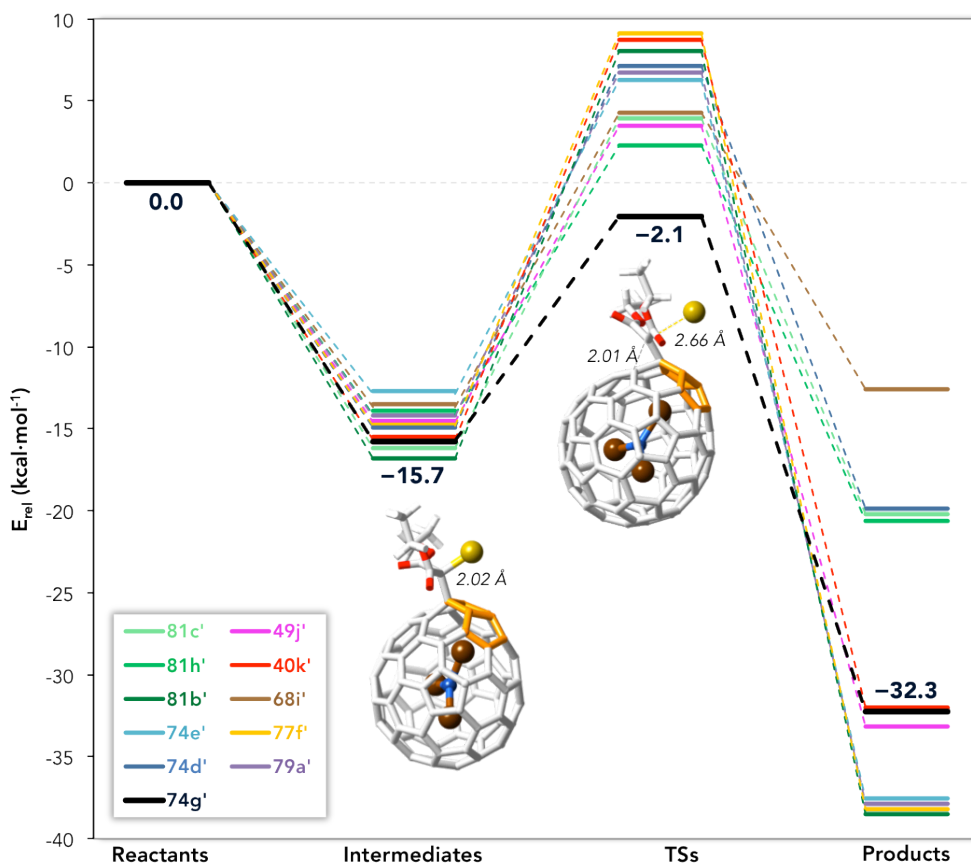


Figure 5.22. Plot of the relative energies of the different intermediates and transition states studied in this work for the Bingel-Hirsch addition on $\text{Y}_3\text{N}@C_{5^{-}\#39663}C_{82}$, considering solvent effects (*o*-DCB). Part of the structures of the lowest-energy intermediate and TS are also depicted.

5.5.3.2. Addition on $Y_3N@C_s\text{-}\#51365C_{84}$

The same analysis has been performed for $Y_3N@C_s\text{-}\#51365C_{84}$ (see Table 5.12). Now, the number of possible [6,6] B-type bonds far from the pentalene unit that can be activated due to interaction with the internal metal atoms is larger. We found the products on bonds **l'** and **m'**, with relative energies of 0.0 and 0.7 kcal·mol⁻¹, as the lowest-energy monoadducts. These two so similar values are in good agreement with the fact that the two bonds are related by symmetry in the empty $C_s\text{-}\#51365C_{84}$ cage. Above, at 2.3 and 5.0 kcal·mol⁻¹, we found products **r'** and **q'**, respectively. Notice that also now the lowest-energy products correspond to adducts on the four [5,6] corannulene bonds around the pentalene motif. Monoadducts on [6,6] bonds **y'**, **v'** and **x'**, which are far from the pentalene, but activated by the metal atoms, show energies around 4.7–6 kcal·mol⁻¹ higher than adduct **l'**. Other products show energies above 12 kcal·mol⁻¹ (Table 5.12).

Table 5.12. Energies with respect to reactants for the different computed intermediates, TS and products of the Bingel-Hirsch addition on $Y_3N@C_{84}$ including solvent effects (o-DCB).

Product	Bond type	Inter. ^a	C _α type	E _{rel} Inter. ^b	E _{rel} TS ^b	E _{rel} Product ^b
$Y_3N@C_s(51365)-C_{84}$						
s'	[6,6]-B	83s'	566	-16.6 (0.2)	0.7 (17.3)	-29.6 (12.7)
t'	[6,6]-B	81t'	566	-15.8 (0.9)	2.9 (18.7)	-25.9 (16.4)
n'	[5,6]-F	83n'	566	-14.4 (2.4)	3.4 (20.1)	-23.3 (19.0)
y'	[6,6]-B	24y'	666	-15.0 (1.7)	4.6 (19.6)	-37.6 (4.7)
m'	[5,6] coran.	83m'	566	-15.1 (1.7)	4.9 (21.5)	-41.6 (0.7)
q'	[5,6] coran.	81q'	566	-15.4 (1.4)	5.1 (20.5)	-37.3 (5.0)
u'	[6,6]-B	55u'	566	-15.2 (1.6)	5.1 (20.3)	-25.0 (17.3)
l'	[5,6] coran.	77l'	566	-14.6 (2.1)	5.5 (20.2)	-42.3 (0.0)
r'	[5,6] coran.	79r'	566	-16.8 (0.0)	5.8 (22.6)	-40.0 (2.3)
p'	[5,6]-F	81p'	566	-14.3 (2.5)	5.9 (21.3)	-20.4 (21.9)
w'	[6,6]-B	32w'	566	-14.6 (2.2)	6.3 (20.7)	-20.0 (22.3)
v'	[6,6]-B	32v'	666	-14.4 (2.4)	6.5 (20.8)	-36.5 (5.8)
x'	[6,6] pyrene	24x'	666	-14.5 (2.3)	7.5 (22.5)	-36.4 (5.9)
o'	[5,5]-E	78o'	556	-10.7 (6.0)	9.2 (19.9)	-30.4 (11.9)
x'	[6,6] pyrene	45x'	666	-12.5 (4.3)	10.0 (22.5)	-36.4 (5.9)

^a Labels for intermediates: **83s'** stands for intermediate on atom 83 that leads to adduct on bond **s** (see Figure 5.19). Note that the labels for the intermediates are also applicable to the TSs.

^b Relative energies with respect to reactants (in kcal·mol⁻¹); in parenthesis, relative stabilities with respect to the most stable intermediate/product (for intermediates/products) or the corresponding intermediate (for TS).

Intermediates **79r'**, **83s'** and **81t'**, which are essentially isoenergetic within the error of the methodology, show the lowest energies. A large group of intermediates with energies between 1.4 and 2.5 kcal·mol⁻¹ is observed: **81q'**, **55u'**, **83m'**, **24y'**, **77l'**, **32w'**, **24x'**, **32v'**, **83n'** and **81p'**. Intermediates on the [6,6] pyrene- and [5,5] pentalene-type bonds, **45x'** and **78o'**, respectively, appear at higher energies (Table 5.12). As for C_s-^{#39663}C₈₂, intermediates on 566 atoms are favored near the pentalene unit, while intermediates on 666 atoms are preferred far from the pentalene (see Figure 5.23). Again, energy differences within the intermediates are not as significant as in products. As far as the TSs are concerned, **83s'** is that with the lowest energy (0.7 kcal·mol⁻¹ with respect to reactants) and the lowest barrier (17.3 kcal·mol⁻¹). TS **81t'** is found more than 2 kcal·mol⁻¹ above. Other TSs show much larger energies and barriers (Table 5.12). Therefore, monoadduct on bond **s'** is proposed to be the single regioisomer observed in experiment, if the Bingel-Hirsch reaction on Y₃N@C_s-^{#51365}C₈₄ takes place under kinetic control.

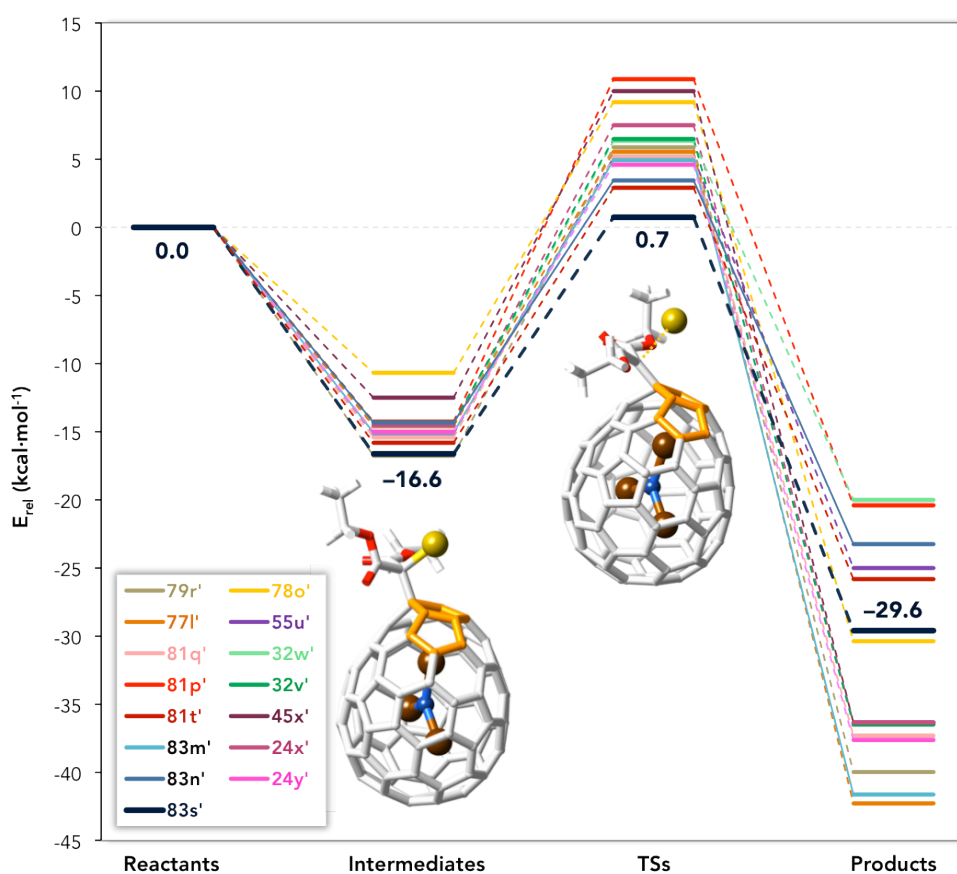


Figure 5.23. Plot of the different intermediates and transition states studied in this work for the Bingel-Hirsch addition on Y₃N@C_s-^{#51365}C₈₄, considering solvent effects (o-DCB).

5.6. Conclusions

A detailed study of the Bingel-Hirsch addition of bromomalonate on metal (M=Sc, Y, Gd) nitride EMFs has been performed. Four different systems are analyzed: the prototypical and most abundant $\text{Sc}_3\text{N}@I_h\text{-C}_{80}$, with an IPR structure, the first isolated and characterized non-IPR nitride EMF, $\text{Sc}_3\text{N}@D_{3h}\text{-}^{6140}\text{C}_{68}$; and the two largest non-IPR $\text{Gd}_3\text{N}@C_{5h}\text{-}^{39663}\text{C}_{82}$ and $\text{Gd}_3\text{N}@C_{5h}\text{-}^{51365}\text{C}_{84}$. We here not only characterize the products of the reaction (thermodynamic study), but also the intermediates and the TSs (kinetic study).

We have first analyzed the IPR $\text{Sc}_3\text{N}@I_h\text{-C}_{80}$ EMF, which is experimentally well characterized. The icosahedral C_{80} cage shows only two different C–C bonds: a type-B [6,6] bond and a corannulene-type [5,6] bond. However, the free rotation of the Sc_3N inside the cage makes the analysis not so straightforward and several orientations of the cluster for each product and each intermediate have to be considered. Rotation of the cluster is more hindered when the adduct is formed, with one Sc atom pointing to the functionalized bond that has been broken yielding an open fulleroid structure. Rotation of the cluster in the intermediates is not so hindered as in products. The two regioisomers are predicted to be isoenergetic, within the error of the methodology. The reaction takes place in two main steps: formation of an intermediate and its evolution to a transition state to give the final monoadducts. The intermediate and the TS that yield the [6,6] regioisomer show lower energies than those corresponding to the [5,6] one. Since experiments clearly show the formation of only the [6,6] regioisomer we conclude that the Bingel-Hirsch reaction on $\text{Sc}_3\text{N}@I_h\text{-C}_{80}$ must take place under kinetic control.

For the non-IPR $\text{Sc}_3\text{N}@D_{3h}\text{-}^{6140}\text{C}_{68}$, we have computed the products on the different eighteen bonds of the fullerene. No rotation of the cluster is possible inside this carbon cage. Bonds that are near the pentalene units are predicted to give the most stable regioisomers. The product under kinetic control is not the same as the product under thermodynamic control. Like the ^{13}C NMR experiments by Gibson, Dorn and co-workers, which point to a non-thermodynamic product, present calculations indicate that the reaction takes place under kinetic control confirming the adduct proposed from NMR experiments. Furthermore, the energetic profiles for the IPR and non-IPR systems are rather similar. Other common feature is that all the products show open-fulleroid structure with the functionalized C–C bond broken.

Regarding the non-IPR $\text{Y}_3\text{N}@C_{2n}$ ($2n=82, 84$) fullerenes, we have assumed that the reaction takes place under kinetic control as observed for similar nitride EMFs. The

two egg-shaped non-IPR cages in these EMFs are rather similar and intimately related. Besides, the nitride cluster has limited rotation around the N–M–pentalene axis. So, similar behavior for the two EMFs is expected. All the regioisomers analyzed show open-fulleroid structures where the functionalized C–C bond is broken. The energy differences between intermediates are much smaller than between final products. The predicted products, which come from the lowest-energy intermediates and TSs, are monoadducts on [6,6] B-type bonds placed near the pentalene motif, as also found for the non-IPR $\text{Sc}_3\text{N}@D_{3h}\text{-}^{6140}\text{C}_{68}$. Thus, we have shown that the Bingel-Hirsch addition presents analogous reaction paths on different non-IPR nitride EMFs.

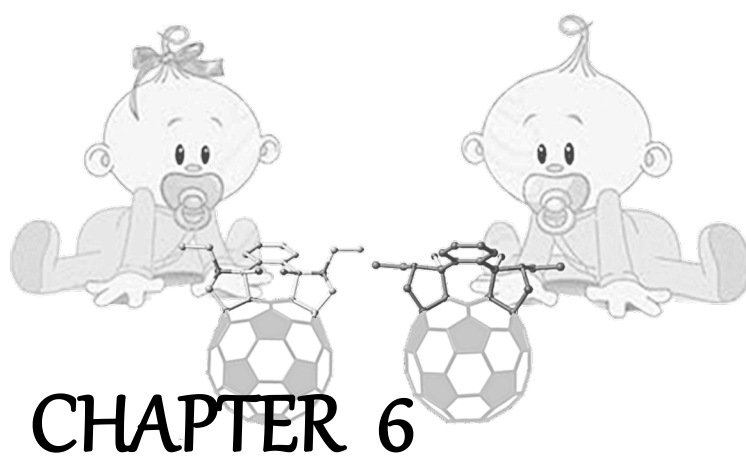
To sum up, the Bingel-Hirsch reaction has shown analogous reaction paths for IPR and non-IPR EMFs despite the different rotation freedom of the internal cluster. In all cages, the reaction leads to a [6,6] monoaddition under kinetic control. The presence of the [5,5] bonds in the non-IPR cage with high pyramidalized carbon atoms is not determinant for the addition, although it takes place around these C atoms. Present results show that predicting the reactivity of endohedral fullerenes is not straightforward and often an accurate analysis of the potential energy surface is required.

5.7. Bibliography

- [1] A. Hirsch, M. Brettreich, *Fullerenes: Chemistry and Reactions*, Wiley-VCH Verlag GmbH&Co. KGaA, Weinheim, Germany, (2005).
- [2] J. R. Pinzón, T. Zuo, L. Echegoyen, *Chem. Eur. J.* (2010), *16*, 4864.
- [3] L. Feng, T. Nakahodo, T. Wakahara, T. Tsuchiya, Y. Maeda, T. Akasaka, T. Kato, E. Horn, K. Yoza, N. Mizorogi, S. Nagase, *J. Am. Chem. Soc.* (2005), *127*, 17136.
- [4] R. D. Bolskar, A. F. Benedetto, L. O. Husebo, R. E. Price, E. F. Jackson, S. Wallace, L. J. Wilson, J. M. Alford, *J. Am. Chem. Soc.* (2003), *125*, 5471.
- [5] a) C. M. Cardona, A. Kitaygorodskiy, L. Echegoyen, *J. Am. Chem. Soc.* (2005), *127*, 10448; b) O. Lukyanova, C. M. Cardona, J. Rivera, L. Z. Lugo-Morales, C. J. Chancellor, M. M. Olmstead, A. Rodríguez-Fortea, J. M. Poblet, A. L. Balch, L. Echegoyen, *J. Am. Chem. Soc.* (2007), *129*, 10423.
- [6] N. Alegret, M. N. Chaur, E. Santos, A. Rodríguez-Fortea, L. Echegoyen, J. M. Poblet, *J. Org. Chem.* (2010), *75*, 8299.
- [7] M. N. Chaur, F. Melin, A. J. Athans, B. Elliott, K. Walker, B. C. Holloway, L. Echegoyen, *Chem. Commun.* (2008), 2665.
- [8] T. Cai, L. Xu, C. Shu, H. Champion, J. Reid, C. Anklin, M. Anderson, H. Gibson, H. Dorn, *J. Am. Chem. Soc.* (2008), *130*, 2136.
- [9] T. Cai, L. Xu, C. Shu, J. E. Reid, H. W. Gibson, H. C. Dorn, *J. Phys. Chem. C* (2008), *112*, 19203.
- [10] W. J. Fu, J. Y. Zhang, T. Fuhrer, H. Champion, K. Furukawa, T. Kato, J. E. Mahaney, B. G. Burke, K. A. Williams, K. Walker, C. Dixon, J. C. Ge, C. Y. Shu, K. Harich, H. C. Dorn, *J. Am. Chem. Soc.* (2011), *133*, 9741.
- [11] a) E. J. Baerends, D. E. Ellis, P. Ros, *ADF 2009.01, Department of Theoretical Chemistry*, Vrije Universiteit: Amsterdam; b) G. te Velde, F. M. Bickelhaupt, E. J. Baerends, C. F. Guerra, S. J. A. v. Gisbergen, J. G. Snijders, T. Ziegler, *J. Comput. Chem.* (2001), *22*, 931; c) *Gaussian 09, Revision A.1*. M. J. Frisch, G. W. Trucks, H. B. Schlegel, G. E. Scuseria, M. A. Robb, J. R. Cheeseman, G. Scalmani, V. Barone, B. Mennucci, G. A. Petersson, H. Nakatsuji, M. Caricato, X. Li, H. P. Hratchian, A. F. Izmaylov, J. Bloino, G. Zheng, J. L. Sonnenberg, M. Hada, M. Ehara, K. Toyota, R. Fukuda, J. Hasegawa, M. Ishida, T. Nakajima, Y. Honda, O. Kitao, H. Nakai, T. Vreven, J. J. A. Montgomery, J. E. Peralta, F. Ogliaro, M. Bearpark, J. J. Heyd, E. Brothers, K. N. Kudin, V. N. Staroverov, R. Kobayashi, J. Normand, K. Raghavachari, A. Rendell, J. C. Burant, S. S. Iyengar, J. Tomasi, M. Cossi, N. Rega, J. M. Millam, M. Klene, J. E. Knox, J. B. Cross, V. Bakken, C. Adamo, J. Jaramillo, R. Gomperts, R. E. Stratmann, O. Yazyev, A. J. Austin, R. Cammi, C. Pomelli, J. W. Ochterski, R. L. Martin, K. Morokuma, V. G. Zakrzewski, G. A. Voth, P. Salvador, J. J. Dannenberg, S. Dapprich, A. D. Daniels,

- Ö. Farkas, J. B. Foresman, J. V. Ortiz, J. Cioslowski, D. J. Fox, Gaussian, Inc, Wallingford CT, (2009).
- [12] E. J. Baerends, D. E. Ellis, P. Ros, *ADF 2007.01, Department of Theoretical Chemistry, Vrije Universiteit: Amsterdam*.
- [13] a) M. Swart, F. M. Bickelhaupt, *J. Comput. Chem.* (2008), 29, 724; b) M. Swart, F. M. Bickelhaupt, *Int. J. Quantum Chem.* (2006), 106, 2536.
- [14] a) A. D. Becke, *Phys. Rev. A* (1988), 38, 3098; b) J. P. Perdew, *Phys. Rev. B.* (1986), 33, 8822.
- [15] Y. Zhao, D. Truhlar, *Theor. Chem. Acc.* (2008), 120, 215.
- [16] R. Krishnan, J. S. Binkley, R. Seeger, J. A. Pople, *J. Chem. Phys.* (1980), 72, 650.
- [17] A. Schafer, C. Huber, R. Ahlrichs, *J. Chem. Phys.* (1994), 100, 5829.
- [18] J. Tomasi, B. Mennucci, R. Cammi, *Chem. Rev.* (2005), 105, 2999.
- [19] K. Peterson, D. Figgen, M. Dolg, H. Stoll, *J. Chem. Phys.* (2007), 126, 124101.
- [20] S. Stevenson, G. Rice, T. Glass, K. Harich, F. Cromer, M. R. Jordan, J. Craft, E. Hadju, R. Bible, M. M. Olmstead, K. Maitra, A. J. Fisher, A. L. Balch, H. C. Dorn, *Nature* (1999), 401, 55.
- [21] a) A. Popov, L. Dunsch, *J. Am. Chem. Soc.* (2008), 130, 17726; b) R. Valencia, A. Rodríguez-Forteza, A. Clotet, C. de Graaf, M. N. Chaur, L. Echegoyen, J. M. Poblet, *Chem. Eur. J.* (2009), 15, 10997.
- [22] A. Rodríguez-Forteza, J. M. Campanera, C. M. Cardona, L. Echegoyen, J. M. Poblet, *Angew. Chem. Int. Ed.* (2006), 45, 8176.
- [23] S. Stevenson, P. W. Fowler, T. Heine, J. C. Duchamp, G. Rice, T. Glass, K. Harich, E. Hajdu, R. Bible, H. C. Dorn, *Nature* (2000), 408, 427.
- [24] a) N. Martín, *Chem. Commun.* (2006), 2093; b) M. N. Chaur, F. Melin, A. L. Ortiz, L. Echegoyen, *Angew. Chem. Int. Ed.* (2009), 48, 7514.
- [25] N. Alegret, A. Rodríguez-Forteza, J. Poblet, *Chem. Eur. J.* (2013), 19, 5061.
- [26] Z. Slanina, L. Stobinski, P. Tomasik, H.-M. Lin, L. Adamowicz, *J. Nanosci. Nanotechnol.* (2003), 3, 193.
- [27] A. Popov, *J. Comput. Theor. Nanosci* (2009), 6, 292.
- [28] a) T. Zuo, K. Walker, M. Olmstead, F. Melin, B. Holloway, L. Echegoyen, H. Dorn, M. Chaur, C. Chancellor, C. Beavers, A. Balch, A. Athans, *Chem. Commun.* (2008), 1067; b) B. Mercado, C. Beavers, M. Olmstead, M. Chaur, K. Walker, B. Holloway, L. Echegoyen, A. Balch, *J. Am. Chem. Soc.* (2008), 130, 7854.
- [29] A. Rodríguez-Forteza, N. Alegret, A. L. Balch, J. M. Poblet, *Nature Chem.* (2010), 2, 955.

- [30] M. R.-N. Danisha, R. P. n. Julio, S. Steven, A. E. Luis, *J. Phys. Org. Chem.* (2013), 26, 194.



CHAPTER 6

Prato Bisaddition on C_{60}

Related Publications:

“Unexpected Isomerism in *cis*-2 Bis(pyrrolidino)[60]Fullerene Diastereomers.”
M. Izquierdo, M. R. Cerón, N. Alegret, A. J. Metta-Magaña, A. Rodríguez-Forteza,
J. M. Poblet, L. Echegoyen. *Angew. Chem. Int. Ed.* (2013), 52, 12928.

CHAPTER 6

Prato Bisaddition on C₆₀

This topic began after all my work with the Bingel-Hirsch reaction and, like the Bingel on C₈₂ and C₈₄, it came from the UTEP lab. Initially, it seemed an easy project, and I felt brave enough to do all the work in few weeks: the Prato mechanism was previously studied computationally and it appears thermodynamically controlled, so no big deal. How wrong I was! Experimentally, three bisadducts were obtained, with relative yields of 26%, 9% and 8%; however, thermodynamic products don't match the experimental abundances. There began the nightmare. So, unlike a typical Prato reaction, the bisaddition may be kinetically controlled? A work that should have lasted few weeks was extended months. Even so, I have special affection to this study because it was my first direct contact to the experimental manipulation with fullerenes. I can't write a word of this chapter without thinking on Marta and Mayra (co-authors of this project), all you taught me, and all the headaches we share together in the lab. I owe you this one.

6.1. Introduction

Fullerene functionalization has been studied extensively since they became available in macroscopic quantities in 1990.^[1] Because of its versatility, utility, and ease of implementation, the 1,3-dipolar cycloaddition reaction of azomethine ylides is probably the most frequently used method for the synthesis of fullerene deriva-

tives.^[2] The asymmetric version of this reaction has also been recently reported by Martín *et al.*, thus giving rise to enantiomerically pure fullerenes.^[3]

Bisfunctionalization of fullerenes is challenging because of the many isomeric products that are typically obtained. Since C₆₀ has 30 reactive double bonds, eight bisadducts can be obtained when the two addends are identical (*cis-1*, *cis-2*, *cis-3*, *equatorial*, *trans-1*, *trans-2*, *trans-3*, and *trans-4*, as shown in Figure 6.1). Prato and co-workers found that when monoaldehydes are used as reactants, the main bisaddition products are the *trans-3* and *equatorial* isomers,^[4] although others have reported that the *cis-3* bisadduct is the most abundant one.^[5] Bisadducts *cis-1* and *cis-2* are hardly ever observed because of the steric congestion.^[6]

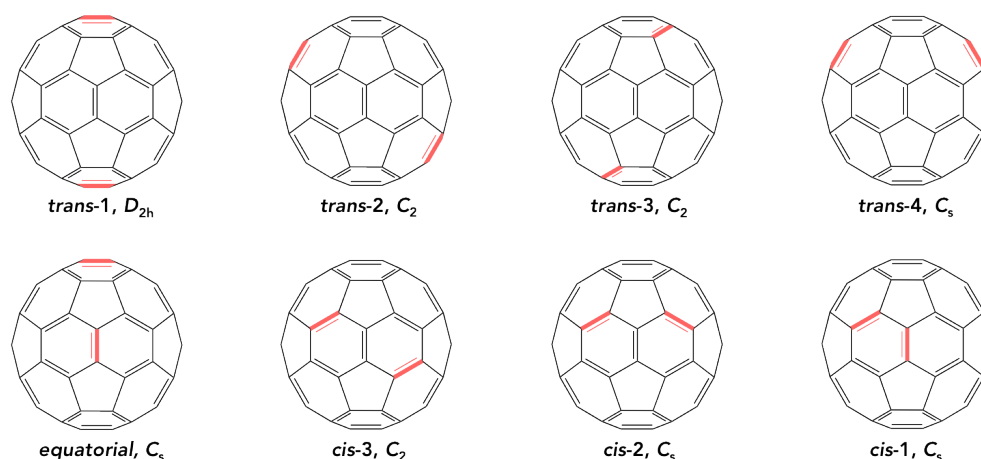


Figure 6.1. Addition patterns and symmetries of the eight possible bisadducts on C₆₀ for a symmetrical addend.

Controlled multifunctionalization of C₆₀ is crucial to improve the yield of specific bisadduct isomers and to avoid tedious HPLC chromatographic separations.^[7] One approach to achieve controlled bisfunctionalization is the tether-directed remote method,^[8] which was introduced by Diederich and co-workers in 1994.^[9] This method was used to conduct bis-1,3-dipolar cycloadditions to C₆₀ by D'Souza *et al.* and Zhou *et al.*^[10]

Examples of regioselective syntheses of bisadducts with a *cis-1* addition pattern were reported by Martín *et al.*, who used an intramolecular Pauson–Khand reaction, a thermal [2+2] cycloaddition,^[11] and nucleophilic addition.^[12] Also, selective

tether-controlled tandem additions of nitrile oxides and azomethine ylides to yield *cis*-1 bisadducts were reported by Prato *et al.*^[13]

Herein we report the one-step synthesis and characterization of three pure C₆₀ fullerene bisadducts, including the X-ray crystal structure of two *cis*-2 bisadducts (**1** and **2**; see Scheme 1 for structures), which are individual *meso* forms. Although there are multiple reports of chirality for fullerene derivatives,^[3, 14] the isomerism reported here is unprecedented. These *meso* bisadducts, easily isolable by silica gel chromatography, show a unique isomerization and the proposed mechanism is supported by computational studies.

6.2. Methods

6.2.1. Experimental strategy

All chemicals were of reagent grade, purchased from Sigma Aldrich. HPLC was performed on an LC-9130NEXT apparatus (Japan Analytical Industry Co. Ltd.) monitored using a UV detector at 320 nm. A Buckyprep column (ϕ = 10 ID x 250 mm) was used for analytical HPLC with toluene as eluent. Silica gel (Redisep silica, 40-60 μ , 60 Å) was used to purify the products. MALDI-TOF mass spectrometry was conducted on a Bruker Microflex LRF mass spectrometer. NMR spectra were recorded using a JEOL 600 MHz spectrometer. The UV-vis-NIR spectra were taken using a Cary 5000 UV-vis-NIR spectrophotometer. Cyclic voltammetry was carried out in a one-compartment cell using a BAS 100 B workstation in a solution of *o*-DCB containing 0.1 M n-Bu₄NPF₆. A 2 mm diameter glassy carbon disk was used as the working electrode. Ferrocene was added to the solution at the end of each experiment as an internal potential standard. The X-ray intensity data were measured on a Bruker SMART APEX CCD system equipped with a graphite monochromator and a MoK α fine-focus tube (λ = 0.71073 Å).

6.2.1.1. Synthesis of compounds **1**, **2** and **3**

A mixture of 155 mg of C₆₀ (0.21 mmol), 25 mg of *o*-phthalaldehyde (OPA) (0.18 mmol) and 153 mg of N-ethylglycine (1.49 mmol) in 60 ml of toluene were refluxed for 1 day. After cooling to room temperature, the solvent was removed in vacuum and the crude product was purified by silica gel column using initially hexane/CS₂ 6:4 as eluent (to separate the unreacted fullerene) and then, CS₂ to obtain compound **1** (9% yield), **2** (26%) and **3** (8% yield) in order of polarity.

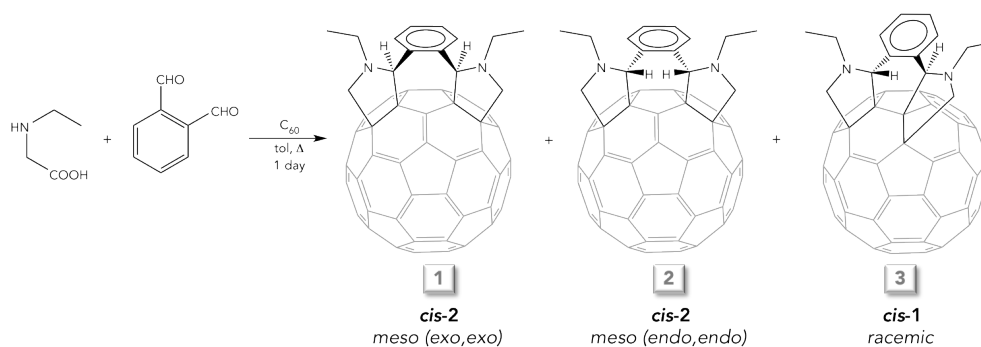
6.2.2. Computational details

The calculations were performed by means of DFT methodology with the combined use of the ADF-2011 and Gaussian-09 codes.^[15] Geometry optimizations of the transition states were first performed with the Quantum-regions Interconnected by Local Descriptions (QUILD) program, which act as a wrapper around the ADF program.^[16] All the minima and TS were characterized, by computing the analytical vibrational frequencies, to have none and one imaginary frequency, respectively, being the latter related to the reaction coordinate of the system. The exchange-correlation GGA density functionals of Becke and Perdew (BP86)^[17] were employed to calculate all the minima and the TS optimized geometries with ADF-2011. Relativistic corrections were included by means of the ZORA (Zero-Order Regular Approximation) formalism. Dispersion corrections were also incorporated (D3 method by Grimme).^[18] Triple- ζ polarization basis sets (TZP) of Slater type were used to describe the valence electrons of the atoms. Frozen cores consisting of the 1s shell were described by means of single Slater functions. At the optimized geometries (BP86-D3/TZP), the energies of reactants, intermediates and products, as well as the transition states were recomputed by using the M06 functional,^[19] which is more adequate to compute energy barriers, at the M06/6-311G** level with the Gaussian-09 code. Solvent effects were also included by using the polarizable continuum model (PCM) to simulate the effects of toluene.

6.3. Synthesis and characterization

6.3.1. Experimental section

Three pure bisadducts, **1**, **2**, and **3**, were prepared by the 1,3-dipolar cycloaddition of an ylide, resulting from OPA and N-ethylglycine, in the presence of C₆₀ by using the procedure reported by Prato et al., drawn in Scheme 6.1.^[2a, 20] To prevent the formation of monoadducts, an excess of N-ethylglycine was added. The purification of the crude reaction mixture by silica gel column chromatography (CS₂) gave rise, in order of elution, to unreacted C₆₀, the three compounds denoted **1**, **2**, and **3**, and finally the polyadducts. The major product of the reaction was the bisadduct **2**, which was isolated in 26% yield, followed by **1** and **3** in 9% and 8% yield, respectively.



Scheme 6.1. Synthesis of **1** (*cis-2*), **2** (*cis-2*) and **3** (*cis-1*).

OPA has the formyl groups in the *ortho* positions, therefore after the first 1,3-cycloaddition occurs, the most accessible double bonds on C_{60} for a second cycloaddition are the *cis-1* and *cis-2*. Three diastereomers could in principle be formed for each regioisomer (*cis-1* and *cis-2*) depending on the orientation of the hydrogen atoms at the stereogenic centers, so a total of six isomers are possible (Figure 6.2).

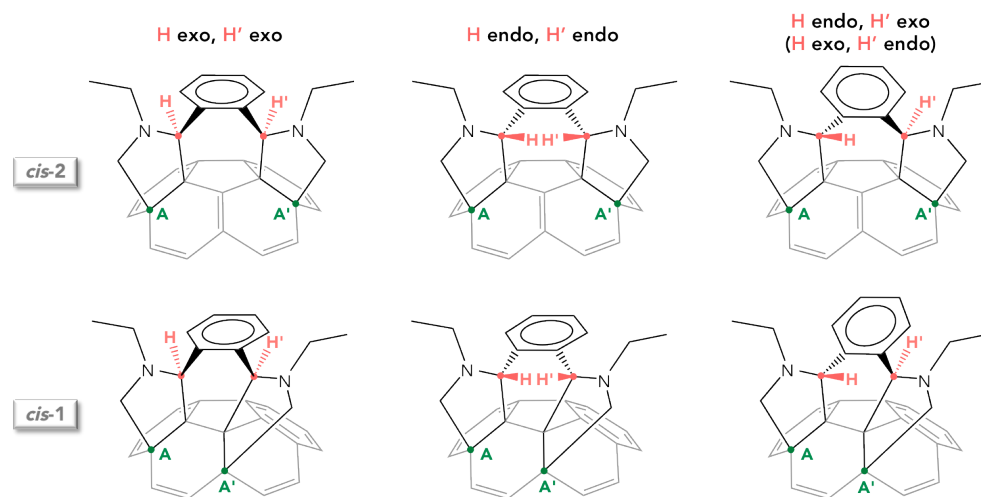


Figure 6.2. Structures of the six possible bisadducts that can be formed from the 1,3-dipolar cycloaddition to C_{60} of the ylide resulting from OPA and N-ethylglycine. If the hydrogens in the stereogenic centers (in red) are pointing away from the direction of A and A', they are "exo" type and if they are in the direction towards A and A' they are "endo" type.

The compounds **1** and **2** were characterized by UV/Vis and NMR spectroscopy, mass spectrometry, and X-ray crystallography (see Figures C1 to C8). They have almost identical UV/Vis spectra, with a λ_{max} characteristic of *cis*-2 isomers (see Figure C13). These assignments are based on the unique UV/Vis absorption patterns for each [60]fullerene bisadducts in the $\lambda=400\text{--}750$ nm region, reported for the first time by Hirsch *et al.*^[4, 6] After the first cycloaddition, the *cis*-1 bond should be more reactive than the *cis*-2 for the second addition, however the former leads to a more sterically strained compound, and is thus disfavored.^[6, 21]

The ¹H-NMR spectra of **1** and **2** showed half of the possible number of signals, thus evidencing the presence of a plane of symmetry for both compounds.^[22] The most pronounced difference between **1** and **2** corresponds to the protons of the methylene groups of the pyrrolidine ring, the signals for which appear as two doublets centered at $\delta=4.65$ and 4.55 ppm for **1** and at $\delta=4.81$ and 3.81 ppm for **2** (Figure 6.3). The singlet for the CH proton of the pyrrolidine ring appears at $\delta=5.63$ ppm for **1** and at $\delta=4.73$ ppm for **2** (shifted 0.92 ppm). The methylene signals of the ethyl group are diastereotopic, thus showing two multiplets centered at $\delta=3.63$ and 3.53 ppm ($\Delta\delta=0.1$ ppm) for **1** and at $\delta=3.63$ and 2.53 ppm ($\Delta\delta=1.1$ ppm) for **2**.

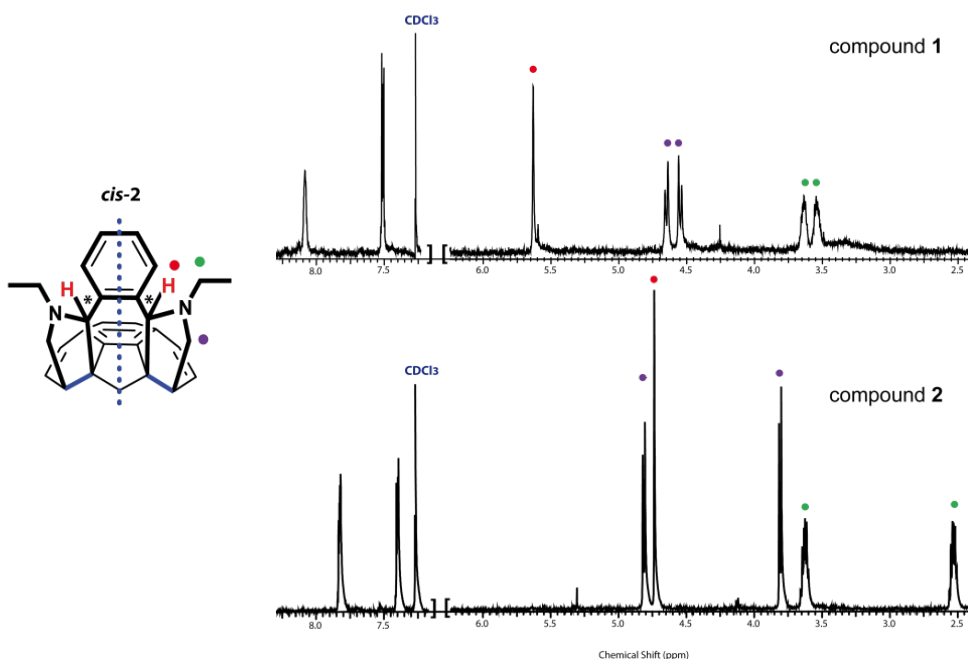


Figure 6.3. Representation of compounds **1** and **2** without stereochemical information and the corresponding ¹H-NMR (600 MHz, CDCl₃, 298K).

Both **1** and **2** have a symmetry plane, and the presence of the two stereogenic centers establishes that these are non-chiral and correspond to two diastereoisomers, each in a different *meso* form. It is not common to have two *meso* isomeric forms of one compound.^[23] The *cis*-2 compounds reported here have two stereogenic centers, thus suggesting, at most, four configurational isomers: *RR*, *SS*, *RS*, and *SR*. In this case, *RR* and *SS* are the enantiomeric pair, which is not observed because they are only possible if the molecule is not symmetric. Usually the *RS* and *SR* are the same, thus a single *meso* compound is observed,^[24] but in this case they are two different and isolable *meso* forms (**1** and **2**). This peculiar result is due to the three dimensionality of the molecule, and, to the best of our knowledge, this phenomenon has never been reported for fullerene compounds.

Surprisingly, these two diastereomeric bisadducts having the same *cis*-2 addition pattern also differ in electronic and redox properties (Table C1), polarity, and specially solubility (in CS₂: 0.695 mg·ml⁻¹ for **1** and 11.26 mg·ml⁻¹ for **2**). Stereochemical assignments were possible by X-ray crystallography.

Compound **3** was characterized by spectroscopic techniques and mass spectrometry (see Figures C9 to C12). NMR and UV/Vis experiments on **3** were sufficient to establish its structure. The UV/Vis spectrum of **3** is typical for a *cis*-1 addition pattern (Figure C14). The compound **3** does not possess a symmetry plane as evidenced by the ¹H and ¹³C-NMR spectra, which exhibit unsymmetrical pyrrolidines (Figure 6.4).

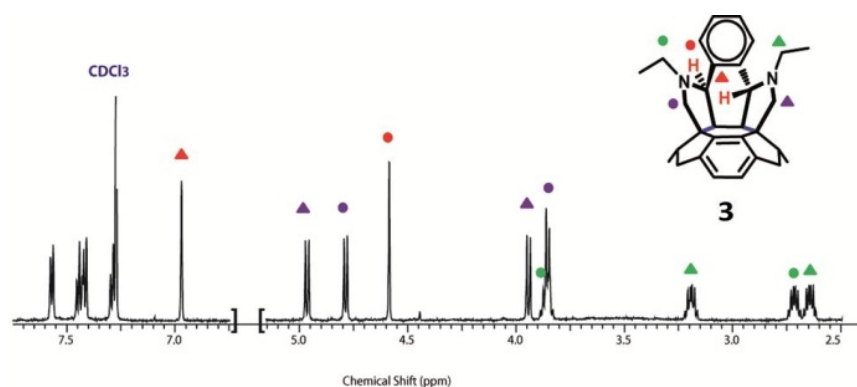


Figure 6.4. ¹H-NMR (600 MHz) compound **3** in CDCl₃ at room temperature.

Bisaddition at the *cis*-1 positions leads to an inherently symmetric pattern. However, the ¹H and ¹³C-NMR spectra clearly show that the molecule is unsymmetrical. The lack of symmetry must arise from the relative orientation of the hydrogen at-

oms in an opposite arrangement (*exo,endo* or *endo,exo*) at the stereogenic centers, thus **3** is a racemic mixture.

6.3.1.1. Crystallographic information for compounds **1** and **2**

Single crystals of **1** and **2** were grown from CS₂/toluene. The bond distances and bond angles are comparable to those of similar compounds in the literature.^[9a] Analysis of the crystal structures showed the configuration at the chiral centers (**1**: *S,R* and **2**: *R,S* from left to right based on the arbitrary orientations introduced in Figure 6.2). The restricted motion of the N-Et groups in the crystal of **1** reduces the symmetry in the solid state to the P2₁/c spatial group. **2** has symmetric N-Et groups making it a *meso* compound with spatial group Pnm. Both compounds exhibit the same symmetry in solution because of the free rotation of the ethyl groups. Changing the chirality of the two stereogenic centers results in the two possible diastereoisomers (Figure 6.5).

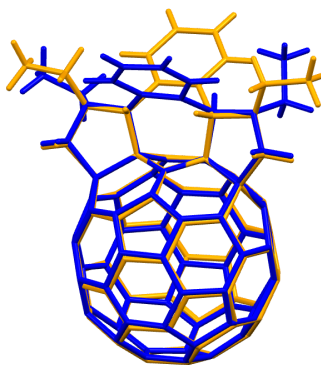


Figure 6.5. Superimposition of the crystal structures of **1** (blue) and **2** (orange) showing the difference in orientation of the phenylene group between both compounds and the asymmetry of the N-Et groups for **1**.

6.3.2. Thermodynamic and kinetic aspects

The Prato cycloaddition is known to take place in two steps where first an ylide is formed – this process consumes a large amount of energy – and then it is added onto a fullerene surface. Previous computational studies about the reaction path mechanism showed that this second step is almost barrierless.^[25] Thus, we have first studied the relative stabilities of the three experimental products (see Table 6.1). A complete list of the computed conformations is collected in Table C2. In agreement with previous studies, the lowest-energy isomer is the *cis*-1, product **3**.

The most abundant isomer **2** lies at 2.0 kcal·mol⁻¹ higher, followed by product **1**, at 6.4 kcal·mol⁻¹. We have confirmed these results using different computational strategies (Table C3). The optimized geometries for products **1** and **2** are in very good agreement with observed X-ray crystallographic data, as shown in Figure 6.6.

Table 6.1. Relative energies (in kcal·mol⁻¹) with respect the most stable intermediate computed for intermediates, TSs and bisadducts of the Prato reaction on C₆₀ in toluene.

Isomer	Addition	Intermediate	TS	Product ^a
1	<i>cis</i> -2	5.4	8.9	-32.1 (6.4)
2	<i>cis</i> -2	0.0	6.9	-36.5 (2.0)
3	<i>cis</i> -1	1.9	13.3	-38.5 (0.0)

^a In parenthesis, relative energy of the bisadducts.

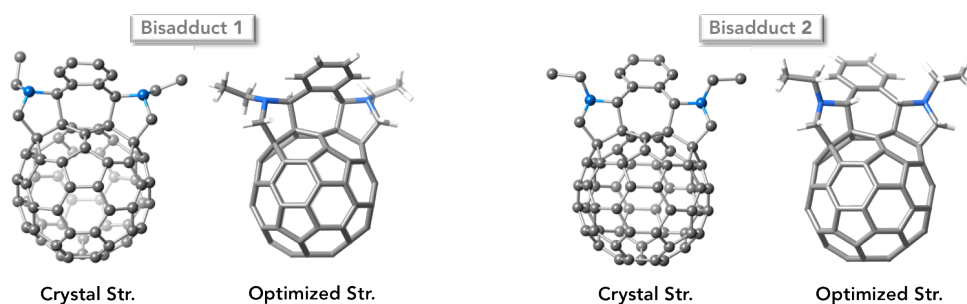


Figure 6.6. Crystallographic and optimized structures of the bisadducts **1** and **2**. Hydrogens atoms in the crystallographic structures are omitted.

According to these results, isomer **3** should be the most abundant product if the bisaddition reaction takes place under thermodynamic control. Nevertheless, the relative abundances of the three products do not match with the relative energies observed. Therefore, we have moved a step forward and deeply analyzed the reaction mechanism to understand the regioselectivity in this bisaddition reaction. We have considered that once the mono-ylide of the *o*-phthalaldehyde is formed, it immediately reacts with C₆₀ since it is an extremely reactive species, leading to a pyrrolidino-aldehyde species, named from now simply aldehyde (Figure 6.7). After this first Prato addition, the second ylide is formed via a pyrrolidino-ylide species, which is proposed to be an intermediate of the reaction. From then on, the second Prato addition takes place through a low energy transition state (TS) to give rise finally the bisadduct product.

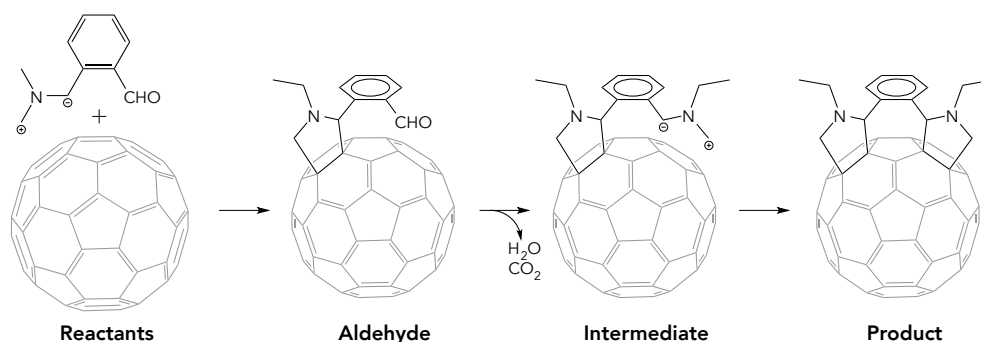


Figure 6.7. Schematic representation of the non-concerted Prato bisaddition.

The first addition step is identical for each of the products, so we have analyzed the process from the intermediate to the final bisadduct for **1**, **2**, and **3**. The results, collected in Table 6.1 and represented in Figure 6.8, appear in good agreement with previous studies about the mechanism of the Prato reaction.^[25c] Product **2** is predicted to be formed rather easily, with the lowest-energy intermediate (**Int-2**) and the lowest-energy TS (**TS-2**, at 6.9 kcal·mol⁻¹). This coincides with the fact that it is the most abundant bisadduct obtained – 26% yield. Product **3** is formed via an intermediate (**Int-3**) that is only 1.9 kcal·mol⁻¹ higher than **Int-2**, but showed the highest TS (**TS-3**), at 13.3 kcal·mol⁻¹. Since the reaction took place at 120 °C, this **TS-3** is accessible enough to observe the formation of bisadduct **3**. Intermedi-

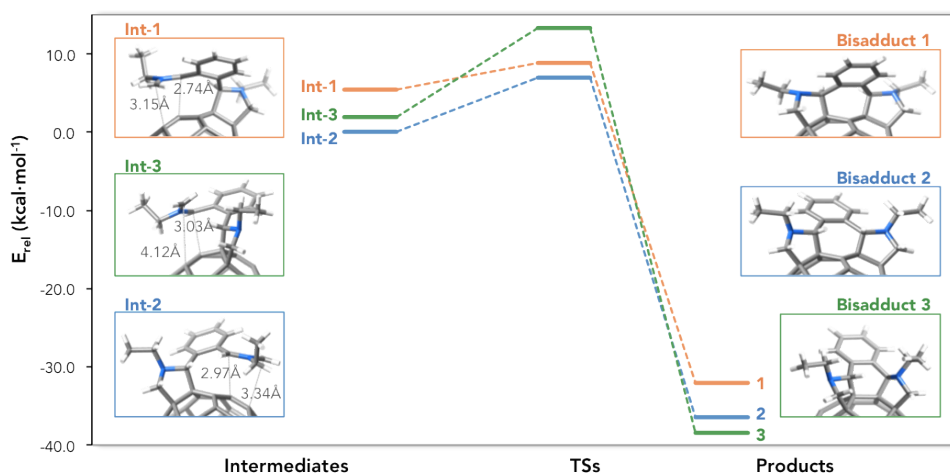


Figure 6.8. Computed energy profile and optimized structures for the intermediates (**Int-1**, **Int-2** and **Int-3**) and products for the addition mechanism of the second ylide to form the bispyrrolidino adducts on C₆₀.

ate **Int-1** appeared at $5.4 \text{ kcal}\cdot\text{mol}^{-1}$ with respect to **Int-2**, but the corresponding TS (**TS-1**) lies at 8.9, only $2 \text{ kcal}\cdot\text{mol}^{-1}$ higher than **TS-2**. The abundances of products **1** and **3** (9 and 8%, respectively) can be rationalized, only qualitatively, from the relative energies of their TSs. Product **1** should be appreciably more abundant than product **3**. However, we should keep in mind that **1** is easily isomerized to **2**, as will be discussed below, and probably some of **1** formed during the process was converted to **2**.

At this point, we would like to focus on the geometries of intermediates, which are rather important to understand the isomerization process that we explain in detail in the next section. As done with the products, we have analyzed several conformations of the intermediates (see Table C4). Taking into account that the order of formation of the first or the second pyrrolidine is irrelevant, analysis of the intermediate structures reveals that the three geometries are rather similar. Intermediate **Int-3** is related to intermediate **Int-2** by a 180° rotation of the free ylide with respect to the $\text{C}_{\text{ylide}}\text{-C}_{\text{benzene}}$ bond (see Figure 6.9). Intermediate **Int-1** is also intimately related to intermediate **Int-2** by a conformational change of the attached pyrrolidine (*vide infra*).

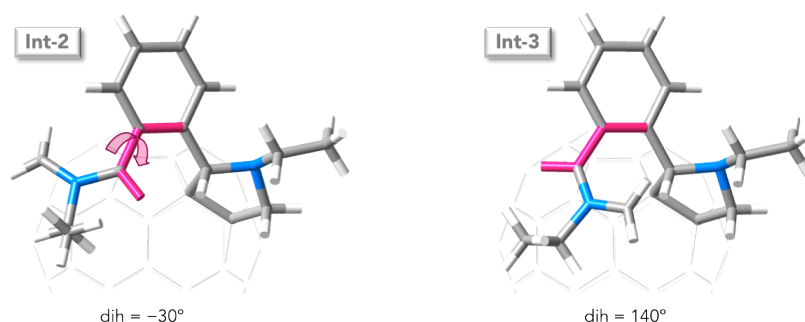


Figure 6.9. Optimized geometries of the intermediates **Int-2** and **Int-3**. The difference between them is the dihedral angle (*dih*, in magenta), formed by $\text{C}_{\text{benzene}}\text{-C}_{\text{benzene}}\text{-C}_{\text{ylide}}\text{-H}$. By an approximate 180° rotation of this angle (magenta arrow), **Int-2** can be transformed into **Int-3**.

In general words, when the two H atoms bonded to the stereogenic centers are placed in a *cis* position, the resultant intermediate is quite linear, so the ylide lies on top of the *cis*-2 addition site and leads to symmetric products (see Figure 6.10). Otherwise, when the relative position of the two H atoms is *trans*, the intermediate structure is more angular and the *cis*-1 addition was favored, since the ylide lied onto the *cis*-1 bond (Figure 6.10). With this simple analysis of the intermediates, we can explain why the symmetric products obtained – with the two H in *cis* – are

the two possible *cis*-2 symmetric bis-(adducts); while the non-symmetric product – with *trans* H – is the only possible non-symmetric *cis*-1 bisadduct.

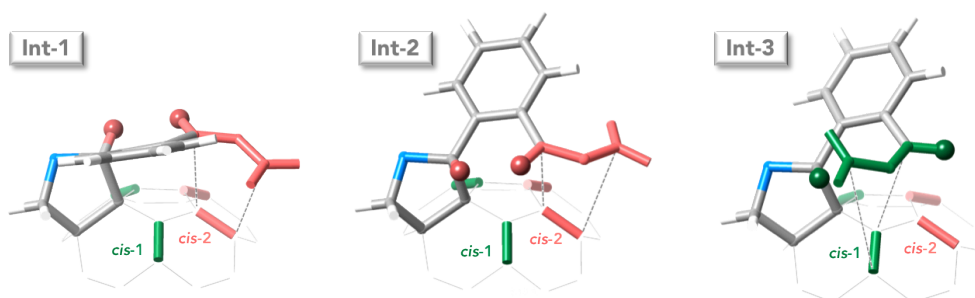


Figure 6.10. Ball-and-stick representation for the computed retro-1,3-dipolar-cycloaddition intermediates. The bonds for *cis*-2 and *cis*-1 additions are represented in red and green, respectively. When the hydrogens of the stereogenic centers are in a *endo,endo* or *exo,exo* arrangement (red balls), the favored addition site is the *cis*-2 bond (compounds **1** and **2**). When the hydrogens of the stereogenic centers are in a *exo,endo* or *endo,exo* arrangement (green balls) the favored addition site is the *cis*-1 bond (compound **3**).

6.4. Isomerization from **1** to **2**

The compound **1** was heated at 180°C (*o*-dichlorobenzene reflux) for two days, and was found to almost quantitatively convert into **2** by TLC and HPLC (Figure 6.11); as well, some of the pristine C₆₀ was detected. Thermalization of **2** at 180°C does not lead to **1**, but results in a small amount of pure C₆₀, so most of the compound remains unchanged. Heating **3** under the same conditions gave rise to C₆₀ and some uncharacterized insoluble compounds. No isomerization to other compounds was observed. These data suggests that retro-1,3-dipolar cycloadditions are involved in the interconversion processes – such reactions have received considerable attention recently since their discovery in 2006.^[25a, 26]

We now aim to provide a plausible explanation of the reaction mechanism that takes place in this isomerization process. According to the structure determination shown in Figure 6.6, the main differences between the two *cis*-2 isomers lie on i) the orientation of the H bonded to the stereogenic carbon atoms – *exo* for **1** and *endo* for **2**; ii) the bent direction of the benzyl group – *endo* for **1** and *exo* for **2**; and iii) the conformation of the ethyl group attached to the N atom of the pyrrolidines – axial for **1** and equatorial for **2**.

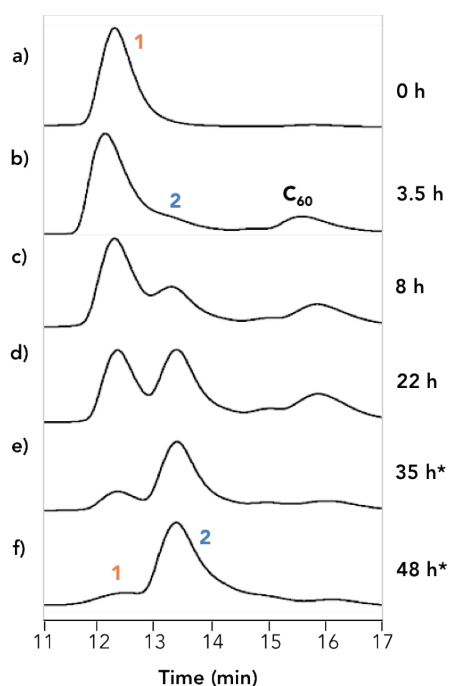


Figure 6.11. HPLC profile of compound **1** (Buckyprep column, ϕ : 10x250 nm, toluene, flow rate 2 ml·min⁻¹, room temperature). a) original sample (t=0), b) after heating 3.5 h at 180°C, c) after heating 8 h at 180°C, d) after heating 22 h at 180°C, e) after heating 35 h at 180°C, f) after heating 48 h at 180°C. * Although the amount of C₆₀ increased with the time (observed by TLC), it is not evidenced in the HPLC profile due to solubility issues. Samples a-d were dissolved in a mixture of toluene:CS₂ in a ratio 1:1 to be injected due to the low solubility of isomer **1**. Samples e-f were injected in toluene because isomer **2** was soluble enough.

Several mechanisms have been considered. At first glance, flipping the H of the stereogenic centers to the other side of the molecule would seem one of the most reasonable paths for the isomerization process; however, the energy required for this turn is too high (see sections 6.4.1 and 6.4.2 in Annex C) so other alternatives were explored.

Once the retro-cycloaddition occurs for one of the pyrrolidines, the ylide can link again to any of the three additional double bonds as well as the original one (reverse reaction): two *cis*-1 bonds and another *cis*-2 bond (green and red in Figure 6.12). The only migration observed was the one towards the non-original *cis*-2 bond to obtain **2** exclusively (Figure 6.12), without any H flipping required. It is remarkable that shifting the attachment position of one pyrrolidine from a *cis*-2 bond to the other very proximal *cis*-2 bond results in a totally different compound with drastically different properties.

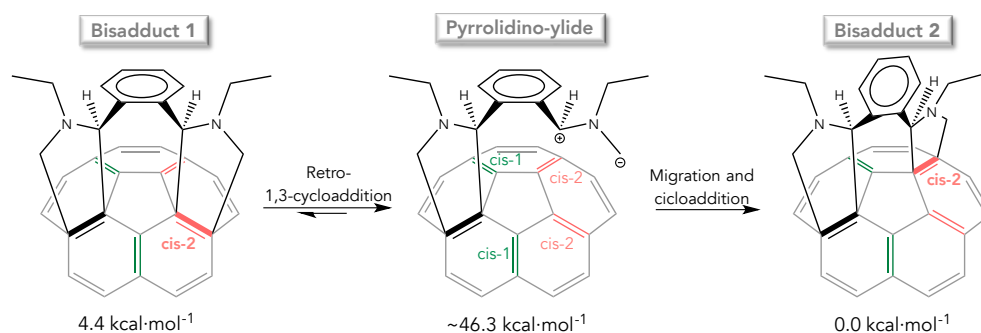


Figure 6.12. Isomerization of **1** into **2**. One of the two pyrrolidines undergoes a retro-1,3-dipolar-cycloaddition, migrates, and reacts preferentially with the other available *cis*-2 bond to obtain a totally different isolable compound.

Two intermediates and three transition states were identified for the transformation from **1** to **2** (Figure 6.13). The highest-energy point in the profile, at 41 kcal·mol⁻¹ with respect to **1**, is easily achieved at 180°C.

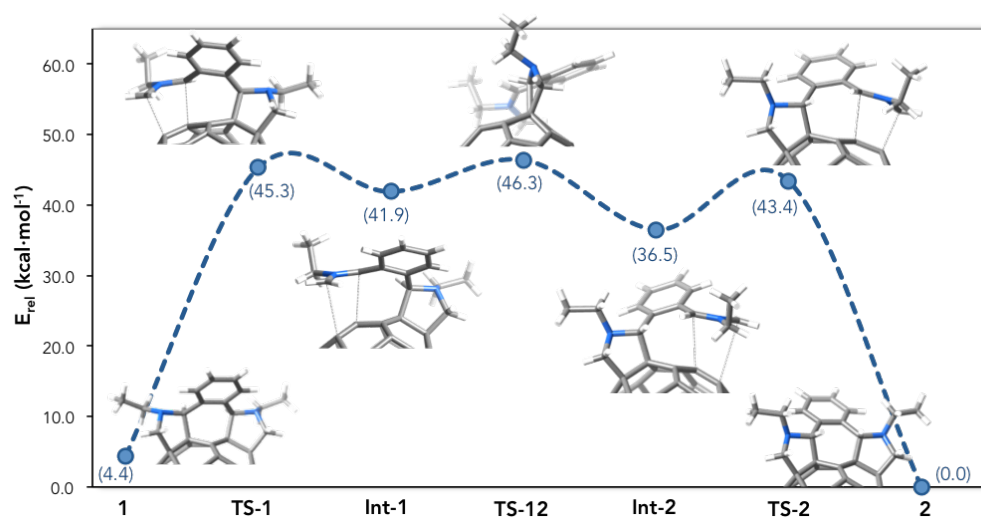


Figure 6.13. Computed energy profile and optimized structures for the isomerization mechanism of **1** to **2**. Retro-cycloaddition of one pyrrolidine followed by migration and a conformational change of the pyrrolidino-ylide intermediate.

To achieve the migration, retrosynthesis of the second Prato addition is needed. So, the key point of the process lies on the conversion of **Int-1** to **Int-2**: the main difference between the intermediates is the conformation of the pyrrolidine-ethyl group in axial position for **Int-1** and equatorial for **Int-2**. The optimized geometries

and their relative energies for the conversion are given in Figure 6.14. **Int-1**, with the ethyl group (orange) of the pyrrolidine in axial position (left side of Figure 6.14), needs only 4.5 kcal·mol⁻¹ to achieve the transition state to reach **Int-2**, with the ethyl group in equatorial (right side of Figure 6.14). The conformational change of the pyrrolidine reorganizes the entire molecule, so the ylide (pink), which is on top of a *cis*-2 site in **Int-1**, moves on top of the neighbor and equivalent *cis*-2 bond. Note that the benzyl group (in grey) does not move appreciably with respect to the pyrrolidine. In conclusion, migration is just a consequence of a conformational change of the pyrrolidino-ylide intermediate.

The small amount of pure C₆₀ observed corresponds to the unlikely, but not impossible, bis-retro-1,3-dipolar cycloaddition occurring almost simultaneously. Although the stereogenic carbon centers do not rotate during the isomerization, and thus retain their intrinsic stereochemistry, upon reattachment at the other *cis*-2 position the absolute stereochemistry is inverted (from *SR* to *RS*, Figure 6.6). Another mechanistic possibility were analyzed and found more unlikely based on their computed energy profiles (see section 6.4.3 in Annex C).

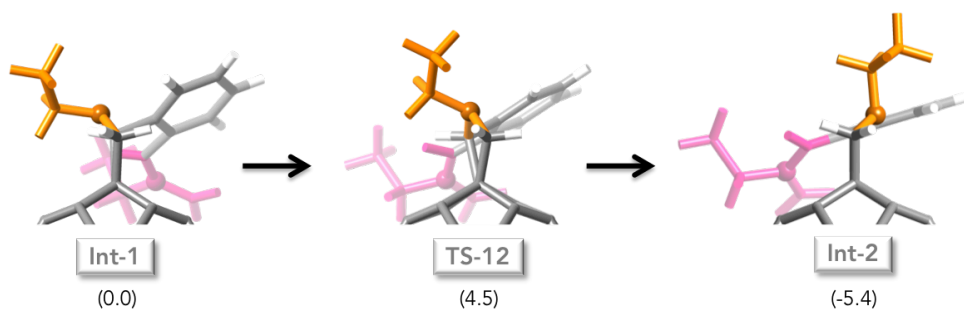


Figure 6.14. Optimized structures of the migration mechanism. The pyrrolidine of **Int-1** turns on the other side, through a **TS-12**, and reaches **Int-2**. The ethyl group, the ylide and the benzyl group are accommodated with this conformational change.

6.5. Conclusions

In conclusion, we successfully prepared, isolated, and characterized three pure [60]fullerene bisadducts, from a double 1,3-dipolar cycloaddition, without using HPLC techniques. This reaction exhibits regio- and diastereoselectivity towards *cis*-1 and *cis*-2 bisadducts. The compounds **1** and **2** are two independent *meso* forms confirmed by X-ray crystallography, which have never been isolated before. Alt-

though **1** and **2** are very similar structurally, they exhibit very different chemical, physical, and electrochemical properties. Our computations show that the bisaddition seems to take place under kinetic control, unlike the common Prato monoaddition. Interestingly, an analysis of the conformation of the intermediates allows us for a qualitative explanation of the observed regioisomers.

We also observed a unique isomerization of **1** to **2**, which can be accounted for as a consequence of a retro-cycloaddition of one pyrrolidine with subsequent migration and a conformational change of the pyrrolidine ylide intermediate. We have given a plausible explanation for this isomerization process from product **1** to **2**. Retrosynthesis of **1** is the most costly step, since a barrier of 40 kcal·mol⁻¹ must be overcome. However, the key point lies on the conversion of the **Int-1** to **Int-2** by a simple conformational change of the pyrrolidine, which requires a rather low energy barrier. From then on, the molecule follows the lowest-energy path to form the bisadduct. Taking into account that the process is performed during two days at 180°, the retrosynthetic energy barrier can be considered reachable enough.

6.6. Bibliography

- [1] a) W. Krätschmer, D. L. Lowell, K. Fostiropoulos, R. H. Donald, *Nature* (1990), 347, 354; b) A. Hirsch, in *The Chemistry of the Fullerenes* (Ed.: A. Hirsch), Wiley-VCH, Weinheim, (2002); c) S. R. Wilson, D. I. Schuster, B. Nuber, M. S. Meier, M. Maggini, M. Prato, R. Talor, in *Fullerenes: Chemistry, Physics, and Technology* (Eds.: K. M. Kadish, R. Ruoff), Wiley, New York, (2000).
- [2] a) M. Maggini, G. Scorrano, M. Prato, *J. Am. Chem. Soc.* (1993), 115, 9798; b) M. A. Yurovskaya, A. A. Ovcharenko, *Chem. Heterocycl. Compd.* (1998), 34, 261; c) A. Mateo-Alonso, C. Sooambar, M. Prato, *Org. Biomol. Chem.* (2006), 4, 1629.
- [3] S. Filippone, E. E. Maroto, Á. Martín-Domenech, M. Suarez, N. Martín, *Nature Chem.* (2009), 1, 578.
- [4] K. Kordatos, S. Bosi, T. Da Ros, A. Zambon, V. Lucchini, M. Prato, *J. Org. Chem.* (2001), 66, 2802.
- [5] Q. Lu, D. Schuster, S. Wilson, *J. Org. Chem.* (1996), 61, 4764.
- [6] F. Djojo, A. Herzog, I. Lamparth, F. Hampel, A. Hirsch, *Chem. Eur. J.* (1996), 2, 1537.
- [7] a) F. Diederich, R. Kessinger, *Acc. Chem. Res.* (1999), 32, 537; b) M. Carano, T. Da Ros, M. Fantì, K. Kordatos, M. Marcaccio, F. Paolucci, M. Prato, S. Roffia, F. Zerbetto, *J. Am. Chem. Soc.* (2003), 125, 7139; c) Z. Zhou, S. Wilson, *Curr. Org. Chem.* (2005), 9, 789; d) S. Kitaura, K. Kurotobi, M. Sato, Y. Takano, T. Umeyama, H. Imahori, *Chem. Commun.* (2012), 48, 8550.
- [8] a) G. Rotas, N. Tagmatarchis, *Tetrahedron Lett.* (2009), 50, 398; b) M. Sander, T. Jarrosson, S.-C. Chuang, S. Khan, Y. Rubin, *J. Org. Chem.* (2007), 72, 2724; c) M. Tzirakis, M. Alberti, M. Orfanopoulos, *Org. Lett.* (2011), 13, 3364; d) T. Nishimura, K. Tsuchiya, S. Ohsawa, K. Maeda, E. Yashima, Y. Nakamura, J. Nishimura, *J. Am. Chem. Soc.* (2004), 126, 11711; e) D. Sigwalt, M. Holler, J.-F. Nierengarten, *Tetrahedron Lett.* (2013), 54.
- [9] a) J.-F. Nierengarten, V. Gramlich, C. Francesc, F. Diederich, *Angew. Chem.* (1996), 108, 2242; b) L. Isaacs, R. F. Haldimann, F. Diederich, *Angew. Chem.* (1994), 33, 2339.
- [10] a) P. Smith, A. McCarty, N. Nguyen, M. Zandler, F. D'Souza, *Chem. Commun.* (2003), 1754; b) Z. Zhou, D. Schuster, S. Wilson, *J. Org. Chem.* (2006), 71, 1545.
- [11] a) N. Martín, M. Altable, S. Filippone, A. Martín-Domenech, *Chem. Commun.* (2004), 1338; b) N. Martín, M. Altable, S. Filippone, A. Martín-Domenech, A. Poater, M. Solà, *Chem. Eur. J.* (2005), 11, 2716; c) N. Martín, M. Altable, S. Filippone, A. Martín-Domenech, M. Güell, M. Solà, *Angew. Chem.* (2006), 118, 1467.
- [12] a) M. Izquierdo, S. Osuna, S. Filippone, A. Martín-Domenech, M. Solà, N. Martín, *J. Org. Chem.* (2009), 74, 6253; b) M. Izquierdo, S. Osuna, S. Filippone, A. Martín-Domenech, M. Solà, N. Martín, *Eur. J. Org. Chem.* (2009), 6231; c) M. Izquierdo, S.

- Osuna, S. Filippone, A. Martín-Domenech, M. Solà, N. Martín, *J. Org. Chem.* (2009), 74, 1480.
- [13] T. Da Ros, M. Prato, V. Lucchini, *J. Org. Chem.* (2000), 65, 4289.
- [14] C. Thilgen, F. Diederich, *C. R. Chim.* (2006), 9, 868.
- [15] a) E. J. Baerends, D. E. Ellis, P. Ros, *ADF 2011.01, Department of Theoretical Chemistry, Vrije Universiteit: Amsterdam*; b) G. t. Velde, F. M. Bickelhaupt, E. J. Baerends, C. F. Guerra, S. J. A. v. Gisbergen, J. G. Snijders, T. Ziegler, *J. Comput. Chem.* (2001), 22; c) *Gaussian 09, Revision A.1.* M. J. Frisch, G. W. Trucks, H. B. Schlegel, G. E. Scuseria, M. A. Robb, J. R. Cheeseman, G. Scalmani, V. Barone, B. Mennucci, G. A. Petersson, H. Nakatsuji, M. Caricato, X. Li, H. P. Hratchian, A. F. Izmaylov, J. Bloino, G. Zheng, J. L. Sonnenberg, M. Hada, M. Ehara, K. Toyota, R. Fukuda, J. Hasegawa, M. Ishida, T. Nakajima, Y. Honda, O. Kitao, H. Nakai, T. Vreven, J. J. A. Montgomery, J. E. Peralta, F. Ogliaro, M. Bearpark, J. J. Heyd, E. Brothers, K. N. Kudin, V. N. Staroverov, R. Kobayashi, J. Normand, K. Raghavachari, A. Rendell, J. C. Burant, S. S. Iyengar, J. Tomasi, M. Cossi, N. Rega, J. M. Millam, M. Klene, J. E. Knox, J. B. Cross, V. Bakken, C. Adamo, J. Jaramillo, R. Gomperts, R. E. Stratmann, O. Yazyev, A. J. Austin, R. Cammi, C. Pomelli, J. W. Ochterski, R. L. Martin, K. Morokuma, V. G. Zakrzewski, G. A. Voth, P. Salvador, J. J. Dannenberg, S. Dapprich, A. D. Daniels, Ö. Farkas, J. B. Foresman, J. V. Ortiz, J. Cioslowski, D. J. Fox, Gaussian, Inc, Wallingford CT, (2009).
- [16] a) M. Swart, F. M. Bickelhaupt, *J. Comput. Chem.* (2008), 29, 724; b) M. Swart, F. M. Bickelhaupt, *Int. J. Quantum Chem.* (2006), 106, 2536.
- [17] a) A. D. Becke, *Phys. Rev. A* (1988), 38, 3098; b) J. P. Perdew, *Phys. Rev. B* (1986), 33, 8822.
- [18] S. Grimme, J. Antony, S. Ehrlich, H. Krieg, *J. Chem. Phys.* (2010), 132, 154104.
- [19] Y. Zhao, D. Truhlar, *Theor. Chem. Acc.* (2008), 120, 215.
- [20] L. Pasimeni, A. Hirsch, I. Lamparth, A. Herzog, M. Maggini, M. Prato, C. Corvaja, G. Scorrano, *J. Am. Chem. Soc.* (1997), 119, 12896.
- [21] A. Hirsch, in *Fullerenes and Related Structures, Vol. 199* (Ed.: A. Hirsch), Springer, Berlin, (1999).
- [22] A. L. Balch, D. A. Costa, B. C. Noll, M. M. Olmstead, *J. Am. Chem. Soc.* (1995), 117, 8926.
- [23] M. Jokic, V. Caplar, T. Portada, J. Makarevic, V. Natasa Sijakovic, M. Zinic, *Tetrahedron Lett.* (2009), 50, 509.
- [24] G.-W. Wang, C.-Z. Wang, S.-E. Zhu, Y. Murata, *Chem. Commun.* (2011), 47, 6111.
- [25] a) S. Filippone, M. Barroso, A. Martín-Domenech, S. Osuna, M. Solà, N. Martín, *Chem. Eur. J.* (2008), 14, 5198; b) A. Alvarez, E. Ochoa, Y. Verdecia, M. Suárez, M. Solà, N. Martín, *J. Org. Chem.* (2005), 70, 3256; c) A. Rodríguez-Fortea, J. M. Campanera, C.

- M. Cardona, L. Echegoyen, J. M. Poblet, *Angew. Chem. Int. Ed.* (2006), 45, 8176; d) S. Osuna, A. Rodriguez-Fortea, J. M. Poblet, M. Sola, M. Swart, *Chem. Commun.* (2012), 48, 2486.
- [26] a) N. Martín, M. Altable, S. Filippone, A. Martín-Domenech, *Synlett* (2007), 3077; b) N. Martín, M. Altable, S. Filippone, A. Martín-Domenech, L. Echegoyen, C. M. Cardona, *Angew. Chem.* (2006), 118, 116; c) O. Lukyanova, C. Cardona, M. Altable, S. Filippone, A. Martín Domenech, N. Martín, L. Echegoyen, *Angew. Chem.* (2006), 118, 7590.



CHAPTER 7

Final Conclusions

CHAPTER 7

Final Conclusions

This chapter is the last step of this project. It summarizes the most important achievements and conclusions presented along this thesis and my years of PhD research. In general words, we have succeeded in most of the projects we have faced and our computational studies resulted in suitable and simple explanations that were in agreement with experiments.

Chapter 3. Prediction Models for EMFs

Following our main objective in understanding why a particular endofullerene is observed, we have performed systematic analyses on fullerene hexaanions from C_{78} to C_{104} to determine the essence of the EMF stability. We have formulated the Maximum Pentagon Separation Rule that is based on separation among pentagons, measured with the IPSI, to explain the observed stability. It can be summarized as follows:

- ✦ The charge is mainly localized on the pentagons. To minimize the generated repulsion, maximal separation among the 12 pentagons of a fullerene cage is required for the stabilization of EMF, *i.e.*, the structures with the lowest IPSI values.
- ✦ For the largest cages, the main factor governing the stability of the cages is the number of pyracylene bonds, which is the motif that brings as closer as possible two pentagons in an IPR structure. Thus, cages with low number of pyraclenes are preferred.

- × In non-IPR systems, the charge accumulated on the [5,5] bonds is larger. Their formation can be understood for those C_{2n} families with IPR isomers that show a large number of pyracylene motifs.
- × The IPSI not only is a measure of the separation between pentagons, but also an indirect measure of the volume of the cages.
- × A correlation was found with the orbital rule: more separation among pentagons results in lower LUMO of the empty cages.

Chapter 4. Looking for the Identity of the First non-IPR $Sc_2@C_{66}$

We have reopened the case of the cage assignment of one of the two first non-IPR systems and collected all the published works on this topic and the mismatches between them. As well, we have performed our own computational study of the $Sc_2@C_{66}$ system taking into account the previous proposals, which leads to the following deductions:

- × In agreement with Nagase, computational results showed that the most suitable isomer to encapsulate the dimetal Sc_2 cluster is $C_{2v}^{-\#4059}$. It matches the experimental ^{13}C -NMR spectrum, but not the synchrotron X-ray powder diffraction analyses.
- × According to Shinohara, isomer $C_{2v}^{-\#4348}$ was the one that fit the experimental characterization. However, computationally, this proposed EMF is not a minimum and, at more than $80 \text{ kcal}\cdot\text{mol}^{-1}$, is far from being the most stable $Sc_2@C_{66}$ among all the possible isomers.
- × In agreement with Nagase, a rotation of the metal cluster inside the $C_{2v}^{-\#4348}$ cage leads to an energy minimum, although still $40 \text{ kcal}\cdot\text{mol}^{-1}$ above the most stable $Sc_2@C_{66}$ isomer.
- × The carbide $Sc_2C_2@C_{64}$ was dismissed as a competitive option.
- × We were not able to find the crossroads between the experiments and the computations. Additional experiments are required to unravel the controversy. In order to help in the characterization, we computed ^{45}Sc -NMR and IR spectra for the different possibilities.

Chapter 5. The Bingel-Hirsch Reaction

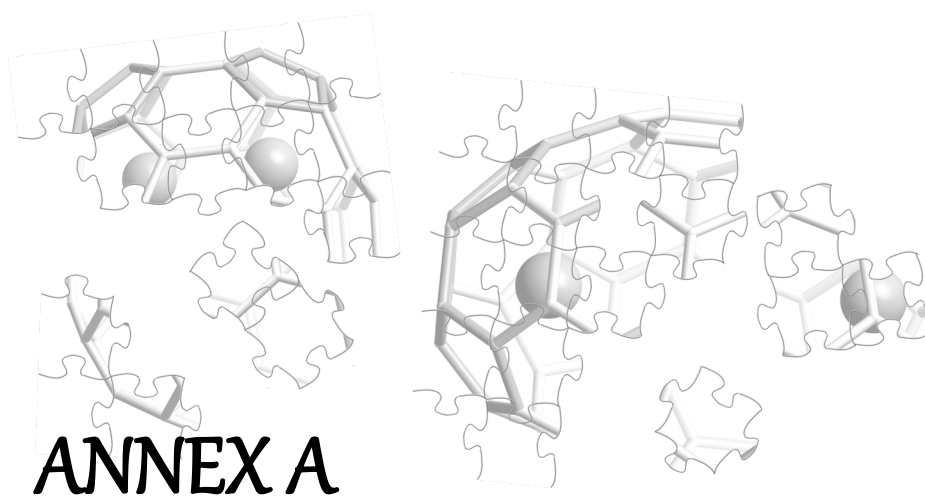
We reported the first reaction mechanism study of the Bingel-Hirsch reaction on EMFs. We have performed an extensive study of this reaction on four different systems: $\text{Sc}_3\text{N@C}_{80}$, $\text{Sc}_3\text{N@C}_{68}$, $\text{Gd}_3\text{N@C}_{82}$ and $\text{Gd}_3\text{N@C}_{84}$, from which several conclusions emerged:

- ✦ The $\text{Sc}_3\text{N@C}_{80}$ has been tested out to confirm that the Bingel-Hirsch reaction undergoes under kinetic control, thus being necessary complete analyses of the TS and intermediates involved.
- ✦ Solvent (PCM model) and dispersion effects (M06 functional) are key points and must be considered. This methodology has been validated and confirmed to be suitable for the studies on this reaction.
- ✦ We have solved the discrepancies between computational and experimental analyses of the Bingel-Hirsch reaction on $\text{Sc}_3\text{N@C}_{68}$.
- ✦ We have proposed one candidate for $\text{Gd}_3\text{N@C}_{84}$ and three for $\text{Gd}_3\text{N@C}_{82}$, as the observed monoadducts in experiments.
- ✦ Both IPR and non-IPR EMFs have analogous Bingel-Hirsch paths, leading to [6,6] monoaddition. Besides, in non-IPR systems the [6,6] bond is as nearest as possible to the pentalene motif.

Chapter 6. Prato Bisaddition on C_{60}

The Prato bisaddition on C_{60} has been studied from the two experimental and computational sides. As a result:

- ✦ Three main products were purified without using HPLC techniques, and successfully characterized, two of which by X-ray diffraction techniques.
- ✦ Two bisadducts are two *meso* forms on *cis-2* positions while the third one appears as a *cis-1* bisadduct.
- ✦ Computations showed that the bisaddition is kinetically controlled.
- ✦ We have determined that a migration mechanism takes place during the isomerization process between the two *cis-2* isomers.



4. Looking for the identity of the
first non-IPR $\text{Sc}_2@C_{66}$

ANNEX A

4. Looking for the identity of the first non-IPR $Sc_2@C_{66}$

4.2. Looking for the empty anionic cage

Table A1. Number of C_{66} and C_{64} isomers for each N_p value.

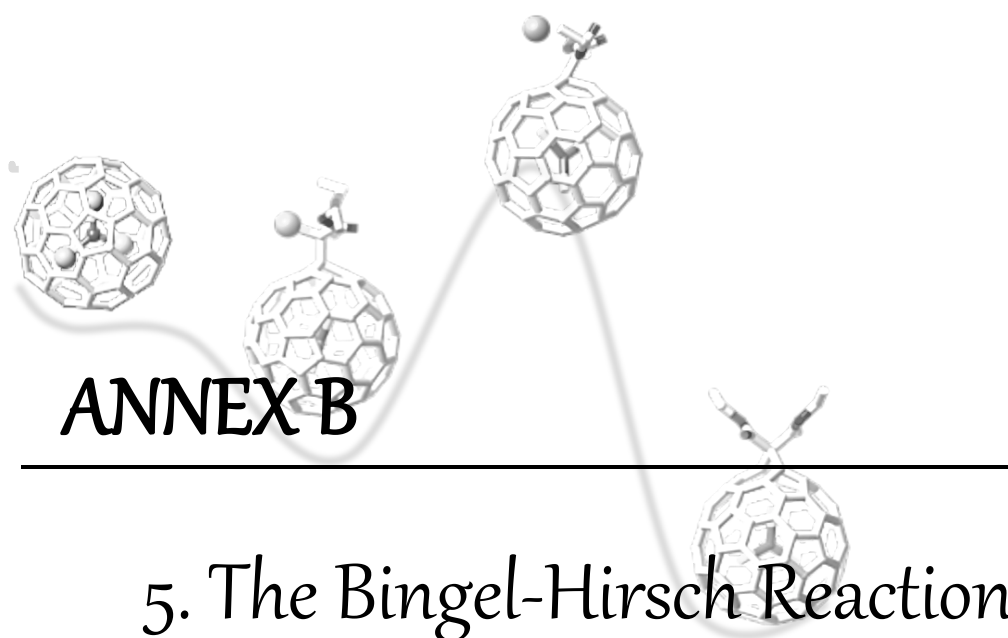
N_p	Number of C_{66} isomers	Number of C_{64} isomers
0	0	0
1	0	0
2	3	3
3	26	12
4	176	89
5	504	310
6	955	639
7	980	777
8	857	678
9	524	479
10	283	270
11	88	104
12	54	65
13	22	25
14	5	11
15	0	1
16	1	1
18	0	1
TOTAL ISOMERS	4478	3465

Table A2. Relative energies (in kcal·mol⁻¹) and structural parameters of the most stable isomers of C₆₆⁶⁻, computed at the AM1 level of theory.

Isomer	N _p	IPSI	E _{rel}	Isomer	N _p	IPSI	E _{rel}	Isomer	N _p	IPSI	E _{rel}
4059	4	14.86	0.0	4064	4	14.87	20.5	4433	4	14.86	29.5
4398	3	14.71	3.3	4060	3	14.74	20.6	4404	4	14.87	29.7
4410	3	14.71	4.0	4462	3	14.73	20.6	4455	3	14.74	29.8
4417	4	14.85	4.0	4415	4	14.86	22.1	4349	4	14.87	30.1
4454	3	14.72	5.2	4348	2	14.60	22.5	4007	3	14.75	30.1
4439	3	14.72	8.5	4466	2	14.60	23.7	4169	2	14.62	30.3
4437	4	14.85	8.7	4057	4	14.89	23.9	3765	3	14.75	30.6
4407	4	14.85	9.6	4400	4	14.86	24.1	4070	4	14.89	30.6
4371	4	14.85	13.4	4413	4	14.86	24.1	3769	4	14.87	30.9
4453	4	14.86	13.9	4068	4	14.88	24.3	3560	4	14.88	31.1
4405	4	14.86	14.1	4434	3	14.73	25.1	3538	3	14.76	31.2
4399	4	14.85	14.6	4411	4	14.86	25.8	4426	4	14.87	31.4
4456	3	14.73	15.4	4447	3	14.74	26.3	4326	4	14.88	31.6
4367	4	14.86	15.6	4452	4	14.87	26.7	3441	4	14.90	31.6
4386	4	14.86	16.4	4393	4	14.87	26.8	4066	5	15.02	31.7
4412	4	14.85	16.5	4430	4	14.86	27.2	4389	4	14.87	32.0
4381	4	14.86	17.0	4366	4	14.87	27.4	3687	4	14.88	32.1
4058	4	14.87	17.2	4331	3	14.74	27.4	4382	4	14.87	32.2
4409	3	14.73	17.3	4362	4	14.87	27.6	4414	4	14.88	32.2
4435	4	14.86	17.5	4327	4	14.87	27.6	4141	3	14.76	32.3
4445	4	14.86	17.8	4401	4	14.87	27.7	4110	5	15.02	32.4
4408	4	14.86	17.9	4332	4	14.87	27.7	4246	5	15.03	33.3
4069	4	14.87	18.4	4065	4	14.88	27.8	4061	4	14.88	33.4
4244	4	14.87	18.4	4425	4	14.87	27.9	3540	4	14.89	33.4
3764	3	14.74	18.7	4448	4	14.87	27.9	4370	4	14.87	33.7
4369	3	14.73	19.0	4458	3	14.74	28.5	4440	4	14.87	33.8
4406	4	14.86	19.1	3774	4	14.88	28.7	4296	4	14.89	34.2
4444	3	14.73	19.1	4092	4	14.88	28.8	4313	4	14.88	34.5
4379	4	14.86	19.9	4438	4	14.87	28.9	4241	5	15.01	34.8

Table A3. Relative energies (in kcal·mol⁻¹) and structural parameters of the most stable isomers of C_{64}^{4+} , computed at the AM1 level of theory.

Isomer	N_p	IPSI	E_{rel}	Isomer	N_p	IPSI	E_{rel}	Isomer	N_p	IPSI	E_{rel}
2983	3	14.97	0.0	3435	4	15.10	20.9	3217	5	15.24	29.0
3414	4	15.08	2.7	2730	3	14.99	21.4	3029	5	15.25	29.2
3451	2	14.84	3.3	2729	4	15.11	21.4	3463	4	15.10	29.2
3367	4	15.09	6.1	3428	3	14.98	21.4	2897	5	15.26	29.3
3356	4	15.10	7.6	3415	4	15.10	21.8	3387	5	15.24	29.4
3216	4	15.11	9.1	3334	4	15.10	22.8	3264	4	15.13	29.5
3368	4	15.10	9.3	2702	4	15.12	23.1	2810	4	15.12	29.6
3425	3	14.97	9.5	3257	4	15.11	23.1	3393	4	15.11	29.6
3037	4	15.10	10.2	3416	3	14.97	23.4	3427	4	15.11	29.8
3344	4	15.11	11.2	3457	2	14.85	23.4	3124	5	15.24	30.4
3386	4	15.09	11.8	3408	5	15.22	23.7	3340	4	15.11	30.8
3224	4	15.11	11.8	3412	4	15.10	23.7	2811	4	15.13	30.8
3424	3	14.96	12.1	2805	4	15.13	23.9	3262	4	15.12	30.9
3423	3	14.96	12.7	3333	4	15.11	23.9	3418	4	15.11	30.9
3399	4	15.09	13.2	3410	4	15.09	24.0	2836	4	15.13	30.9
3452	2	14.85	13.4	3443	4	15.11	24.3	2977	5	15.25	31.2
3223	4	15.09	14.3	3361	4	15.11	24.4	1261	5	15.27	31.8
3402	3	14.97	15.3	3372	4	15.11	24.6	3464	4	15.12	31.9
3038	4	15.11	15.6	3406	4	15.10	24.8	2695	4	15.12	32.0
3426	4	15.10	15.7	3421	4	15.11	25.3	2731	4	15.12	32.0
3401	4	15.08	17.8	3070	5	15.25	25.4	3355	5	15.24	32.1
3407	4	15.10	18.0	2981	4	15.11	25.4	3431	4	15.11	32.2
3455	3	14.98	18.1	2969	4	15.12	25.4	3222	5	15.25	32.7
3365	5	15.23	18.2	3400	4	15.09	26.5	3236	5	15.25	32.7
3373	4	15.10	18.7	3438	3	14.98	27.3	2701	4	15.12	32.8
3371	4	15.10	19.4	1911	3	15.02	27.4	2976	5	15.26	33.0
2901	4	15.12	19.5	2872	4	15.13	28.5	3357	5	15.24	33.4
3354	4	15.10	19.8	3341	4	15.12	28.5	3364	5	15.24	33.5
3392	4	15.10	20.4	3454	3	14.99	28.6	3132	4	15.13	33.6



ANNEX B

5. The Bingel-Hirsch Reaction

5.3. Addition on $\text{Sc}_3\text{N}@I_h\text{-C}_{80}$

Table B1. Relative energies (in kcal mol⁻¹) of the scan along the addition coordinate from the intermediate to the reactants of the Bingel-Hirsch reaction on $\text{Sc}_3\text{N}@C_{80}$, in the gas phase. The initial intermediate is the one labeled as **2b** in Figure 5.5. Graphical plot is represented in Figure 5.6.

Distance C_{80} – malonate (Å)	E_{rel} (kcal·mol ⁻¹)
1.600	0.0
1.822	4.3
2.044	9.2
2.267	10.5
2.489	11.1
2.711	11.4
2.933	11.7
3.156	11.5
3.378	11.9
3.600	12.3

5.4. Addition on $\text{Sc}_3\text{N}@D_3\text{-}^{6140}\text{C}_{68}$.

Table B2. Relative energies (in kcal mol⁻¹) of the scan along the addition coordinate from the intermediate to the reactants of the Bingel-Hirsch reaction on $\text{Sc}_3\text{N}@C_{68}$, in the gas phase. The initial intermediate is the one labeled as **22o** in Figure 5.9. Graphical plot is represented in Figure 5.12.

Distance C ₆₈ – malonate (Å)	E _{rel} (kcal·mol ⁻¹)
1.590	0.0
1.701	1.3
1.812	3.9
1.923	5.6
2.034	7.1
2.146	7.6
2.257	6.3
2.368	6.9
2.479	6.5
2.590	6.5
2.812	7.7
3.034	8.2
3.257	8.9

Table B3. Solvent-phase relative energies (at M06/6-311G and the SMD model, in kcal·mol⁻¹) of the different computed malonate rotational isomers of Sc₃N@C₆₈. The dihedral angle changes from the intermediate **22o** (0°) to the intermediate **22c** (120°). Graphical plot is represented in Figure 5.11.

Intermediate	Dihedral (°) ^a	E _{rel} (kcal mol ⁻¹)
22o	0	0.2
	10	0.0
	20	0.3
	30	1.9
	40	3.5
Eclipsed 22d	50	4.5
	60	6.2
	70	6.8
	80	4.6
	100	0.7
22c	120	0.0

^a Rotation angle with respect to the initial **22o** intermediate.

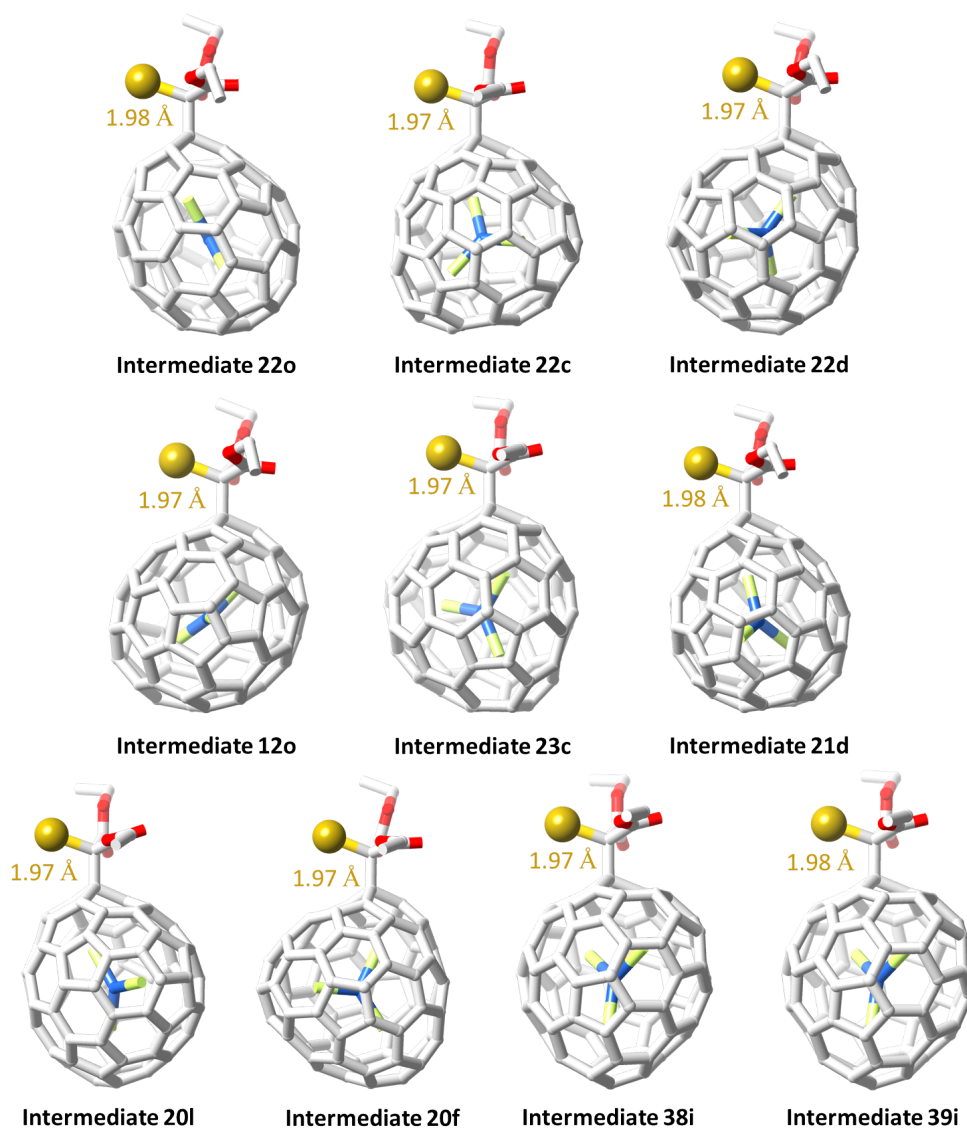


Figure A.1. Optimized structures of the intermediates for the Bingel-Hirsch addition onto $\text{Sc}_3\text{N}@C_{68}$. In yellow, the Br - C_{mal} distance.

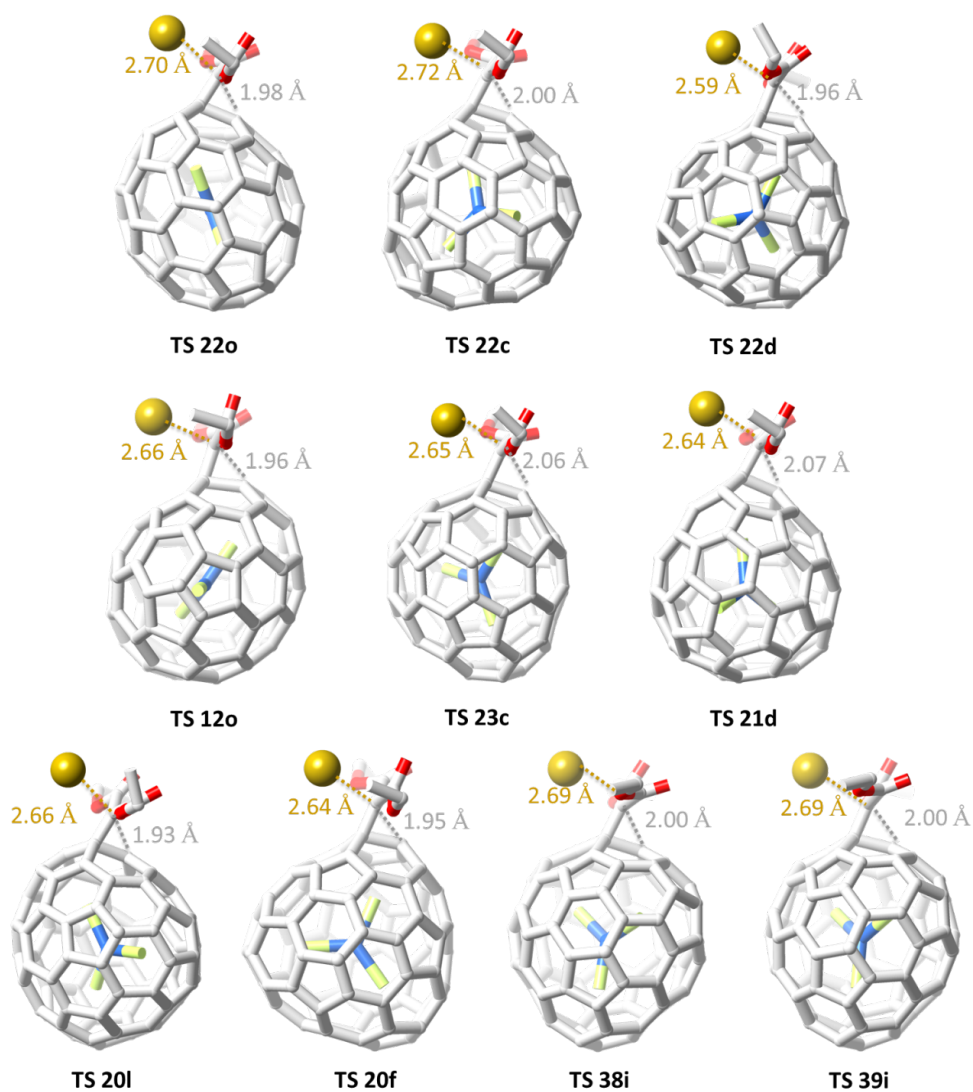


Figure A.2. Optimized structures of the transition states (TS) for the Bingel-Hirsch addition onto $\text{Sc}_3\text{N}@C_{68}$. In yellow, the Br - C_{mal} distance; in grey, the C_{β} - C_{mal} distance.

Looking for a “cheaper” methodology: test study for the Bingel-Hirsch reaction on $\text{Sc}_3\text{N@C}_{68}$

Abbreviations used in Figure 5.14 and **Table B5**:

- * **cosmo/BP//BP**: BP86/TZP//BP86/TZP including solvent effects with COSMO by single point energy calculation, computed with ADF2009
- * **pcm/TZ//TZ**: pcm/M06/TZP // M06/TZP
- * **pcm/TZ//DZ**: pcm/M06/TZP // M06/DZP
- * **pcm/TZ//BP**: single point energy calculation at the pcm/M06/TZP level (computed with Gaussian09) from an optimized geometry at the BP86/TZP level (computed with ADF2009)
- * **smd/TZ//TZ**: M06/TZP//M06/TZP including solvent effects with SMD
- * **smd/TZ//DZ**: M06/TZP//M06/DZP including solvent effects with SMD
- * **smd/TZ//BP**: single point energy calculation at the M06/TZP level including solvent effects with SMD (computed with Gaussian09) from an optimized geometry at the BP86/TZP level (computed with ADF2009)

Table B4. Relative energies (in kcal·mol⁻¹) for the different computed intermediates of the Bingel-Hirsch reaction on Sc₃N@C₆₈ using different computational strategies. Solvent effects (o-DCB) were included by use of the PCM or the SMD model. Abbreviations^{s-g}. Graphical representation in Figure 5.14

Atom	E _{rel} Intermediates						
	cosmo BP//BP	pcm TZ//TZ	pcm TZ//DZ	pcm TZ//BP	smd TZ//TZ	smd TZ//DZ	smd TZ//BP
22o	0.8	2.2	1.3	0.8	2.0	1.2	0.0
38i	4.2	3.2	3.2	3.3	4.0	3.5	9.2
39i	4.2	3.2	3.2	3.3	4.0	3.5	9.2
21d	–	9.6	9.6	0.8	10.6	10.0	6.4
22d	–	0.0	0.0	10.1	0.5	0.0	15.8
22c	0.0	0.0	0.2	0.0	0.0	0.0	5.0
12o	4.9	3.3	3.4	4.2	4.2	3.8	9.8
23c	11.9	15.0	15.0	18.9	15.5	15.0	24.9

Table B5. Relative energies (in kcal·mol⁻¹) for the different computed TSs of the Bingel-Hirsch reaction on Sc₃N@C₆₈ using different computational strategies. Solvent effects (o-DCB) were included by use of the PCM or the SMD model. Abbreviations^{s-g}. Graphical representation in Figure 5.14

Atom	E _{rel} TSs						
	cosmo BP//BP	pcm TZ//TZ	pcm TZ//DZ	pcm TZ//BP	smd TZ//TZ	smd TZ//DZ	smd TZ//BP
22o	4.9	19.0	20.3	14.5	21.7	18.5	22.6
38i	0.3	21.0	21.6	18.2	23.8	20.0	26.3
39i	0.2	21.0	21.9	18.2	23.8	20.1	26.2
21d	–	22.5	23.7	19.2	25.5	22.0	26.7
22d	–	22.6	23.5	18.0	23.6	20.1	26.8
22c	10.9	25.9	26.8	23.3	28.7	25.0	31.7
12o	11.0	27.1	28.1	24.1	29.5	26.1	31.2
23c	3.0	32.5	33.7	29.2	35.6	32.2	37.9

5.5. Addition on $Gd_3N@C_{2n}$ ($2n = 82$ and 84)

Study on $Y_3N@C_{s^{-39663}}C_{82}$

Table B6. Relative stabilities for the different computed monoadducts of $Y_3N@C_{82}$ in the gas phase at BP86/TZP level of theory, computed with ADF2009.

Interm.	E_{rel} Gas BP86	Interm.	E_{rel} Gas BP86	Interm.	E_{rel} Gas BP86
81b	0.0	16 ₃₅	7.0	76 ₅₈	11.9
74g	0.8	15 ₁₆	8.9	11 ₂₉	12.1
77f	1.3	51 ₅₂	9.3	45 ₄₄	12.4
81c	1.4	18 ₁₉	10.0	76 ₇₅	12.8
40k	1.8	19 ₁₈	10.2	14 ₃₃	13.0
79a	2.1	18 ₁	10.3	80b	13.2
49j	2.2	19 ₃₉	10.4	80i	13.3
74d	2.4	28j	10.5	73g	13.3
74e	3.4	39k	10.5	1 ₁₈	13.4
68i	3.5	75f	10.8	80a	13.7
52 ₅₁	5.4	29 ₁₁	10.8	32 ₅₃	14.4
58 ₅₇	5.4	29 ₂₈	11.0	24 ₂₅	14.5
30 ₂₉	5.4	53 ₃₂	11.0	25 ₂₄	14.7
58 ₇₆	5.6	75e	11.1	23 ₂₂	15.0
82d	6.2	39 ₃₈	11.2	33 ₁₄	15.6
82c	6.5	28 ₂₉	11.2	22 ₂₃	16.8
78 ₈₂	6.6	39 ₁₉	11.2	72 ₅₄	19.6
57 ₅₈	6.6	38 ₃₉	11.3	54 ₇₂	21.3
78 ₈₂	6.7	75 ₇₆	11.4	44 ₄₅	22.1
16 ₁₅	6.9	29 ₃₀	11.4		

Table B7. Relative stabilities and activation barriers for the different computed monoadducts of $Y_3N@C_{82}$ in the gas phase and solvent (o-DCB) at different levels of theory. To include solvent effects, single-point energy calculations are performed on geometries optimized in the gas phase. The intermediates have been chosen among the most stable ones shown in **Table B6**.

Interm.	E_{rel} intermediate				E_a TS			
	Gas BP86 ^a	o-DCB BP86 ^b	Gas M06 ^c	o-DCB M06 ^d	Gas BP86 ^a	o-DCB BP86 ^b	Gas M06 ^c	o-DCB M06 ^d
81b	0.0	0.0	0.0	0.0	30.7	18.6	34.4	24.8
74g	0.8	1.7	1.5	1.1	19.0	7.0	22.4	13.7
77f	1.3	2.2	1.4	2.0	28.9	21.4	33.9	23.6
81c	1.4	1.0	2.4	0.7	21.7	14.5	28.0	20.7
40k	1.8	1.4	2.0	1.2	24.4	23.4	32.5	24.4
79a	2.1	2.8	3.8	2.5	27.7	15.2	29.5	21.0
49j	2.2	2.5	2.9	2.2	22.1	12.8	24.7	18.2
74d	2.4	2.6	2.9	1.9	21.7	16.8	29.4	22.6
74e	3.4	3.9	5.6	4.0	24.9	13.8	31.9	22.0
68i	3.5	3.4	3.3	2.4	28.6	14.0	24.7	18.5
81h	–	–	3.7	2.4	–	–	29.1	19.2
52₅₁	5.4	7.7	–	–	–	–	–	–
58₅₇	5.4	7.6	–	–	–	–	–	–
30₂₉	5.4	5.6	–	–	–	–	–	–
16₃₅	7.0	6.2	–	–	–	–	–	–

^a opt BP86/TZP. Values of the intermediates energies taken from **Table B6**.

^b sp BP86/TZP on opt BP86/TZP

^c M06/6-31G**

^d sp M06/6-311G** on opt M06/6-31G**

Study on $Y_3N@C_{59}^{#51365}C_{84}$

Table B8. Relative stabilities and activation barriers for the different computed monoadducts of $Y_3N@C_{82}$ in the gas phase and solvent (o-DCB) at different levels of theory. To include solvent effects, single-point energy calculations are performed on geometries optimized in the gas phase.

Interm.	E_{rel} intermediate				E_a TS			
	Gas BP86 ^a	o-DCB BP86 ^b	Gas M06 ^c	o-DCB M06 ^d	Gas BP86 ^a	o-DCB BP86 ^b	Gas M06 ^c	o-DCB M06 ^d
83n	2.1	0.0	3.5	2.4	25.1	13.8	29.1	20.1
79r	0.0	0.1	0.2	0.0	28.9	16.8	31.1	22.6
28₂₇	10.8	0.4	11.0	10.3	24.4	18.9	26.8	18.5
81q	0.5	0.9	0.8	1.4	26.6	14.2	30.7	20.5
55t	3.0	1.1	2.4	1.6	24.6	15.6	27.1	20.3
24w	4.5	1.4	2.9	2.3	26.9	19.1	29.9	22.5
83m	1.4	1.5	1.4	1.7	28.1	17.0	31.1	21.5
32u	4.1	1.8	3.4	2.4	25.3	16.1	27.1	21.0
24x	4.6	1.8	3.6	1.7	24.3	16.2	26.0	19.6
77l	2.8	2.1	2.7	2.1	24.7	15.5	29.3	20.2
32v	4.3	2.1	3.6	2.2	26.5	16.0	28.8	20.9
83s	0.6	2.4	0.0	0.2	24.2	17.1	28.2	17.3
81p	2.0	2.5	2.9	2.5	–	–	32.8	21.3
81₆₈	–	–	-0.2	0.9	–	–	29.2	18.7
32₃₁	4.2	2.6	–	–	26.2	16.0	–	–
12₁₃	4.9	2.6	–	–	–	–	–	–
12₁₁	5.0	3.1	–	–	–	–	–	–
18₁₇	6.6	3.4	–	–	–	–	–	–
45w	5.3	4.1	5.4	4.3	28.1	19.5	30.2	22.5
78o	2.9	5.6	6.5	6.0	24.6	19.4	27.3	19.9
82p	3.7	7.2	–	–	18.4	–	–	–
82n	3.8	7.4	–	–	18.5	–	–	–
70s	10.3	7.9	–	–	42.9	–	–	–
82o	4.1	8.5	–	–	30.7	–	–	–

^a opt BP86/TZP.

^b sp BP86/TZP on opt BP86/TZP

^c M06/6-31G**)

^d sp M06/6-311G** on opt M06/6-31G**

Table B8. Cont.

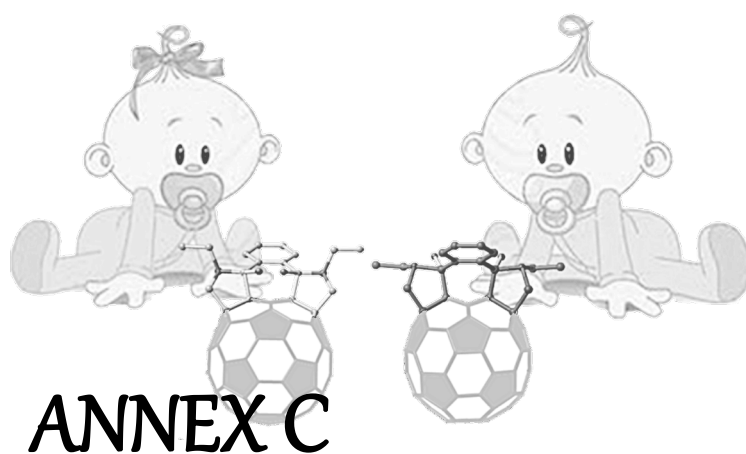
Interm.	E_{rel} intermediate				E_a TS			
	Gas BP86 ^a	<i>o</i> -DCB BP86 ^b	Gas M06 ^c	<i>o</i> -DCB M06 ^d	Gas BP86 ^a	<i>o</i> -DCB BP86 ^b	Gas M06 ^c	<i>o</i> -DCB M06 ^d
80r	8.4	8.8	–	–	24.0	–	–	–
80q	8.6	9.1	–	–	22.2	–	–	–
33u	11.1	11.1	–	–	17.1	–	–	–
84l	10.5	11.7	–	–	21.5	–	–	–
84m	10.5	12.2	–	–	23.3	–	–	–
23x	11.1	12.2	–	–	18.7	6.2	–	–
47₂₆	14.7	14.3	–	–	–	–	–	–
26₄₇	16.4	16.4	–	–	–	–	–	–

^a opt BP86/TZP.

^b sp BP86/TZP on opt BP86/TZP

^c M06/6-31G**)

^d sp M06/6-311G** on opt M06/6-31G**



6. Prato Bisaddition on C_{60}

ANNEX C

6. Prato Bisaddition on C₆₀

6.3. Synthesis and characterization

6.3.1. Experimental section

MALDI-TOF and NMR spectra for Compound 1

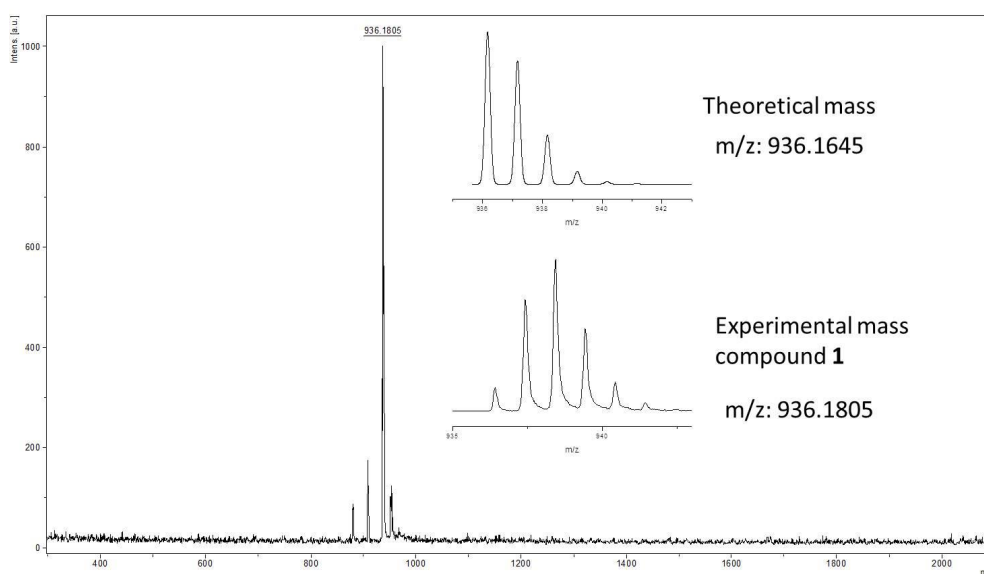


Figure C1. MALDI-TOF spectrum of compound 1.

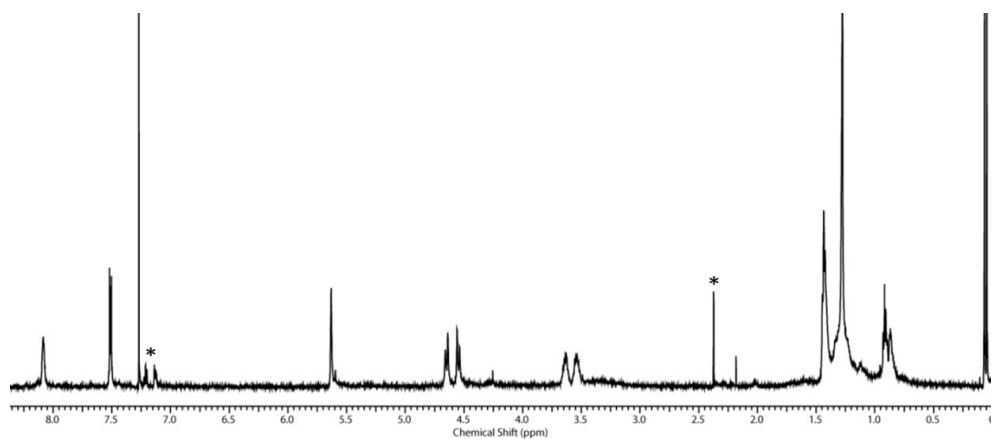


Figure C2. $^1\text{H-NMR}$ (600 MHz; $\text{CDCl}_3/\text{CS}_2$ (3/7), 298 K); Compound **1**: δ 8.13 (m, 1H_{Ar}), 7.51 (m, 1H_{Ar}), 5.63 (s, 1H, N-CH), 4.65 (d, 1H, N- $\text{CH}_2\text{-C}_{60}$, $J=13.06$ Hz), 4.55 (d, 1H, N- $\text{CH}_2\text{-C}_{60}$, $J=13.06$ Hz), 3.63 (m, 1H, N- $\text{CH}_2\text{-CH}_3$), 3.53 (m, 1H, N- $\text{CH}_2\text{-CH}_3$), 1.43 (m, 3H, CH_3) ppm. * Residual toluene

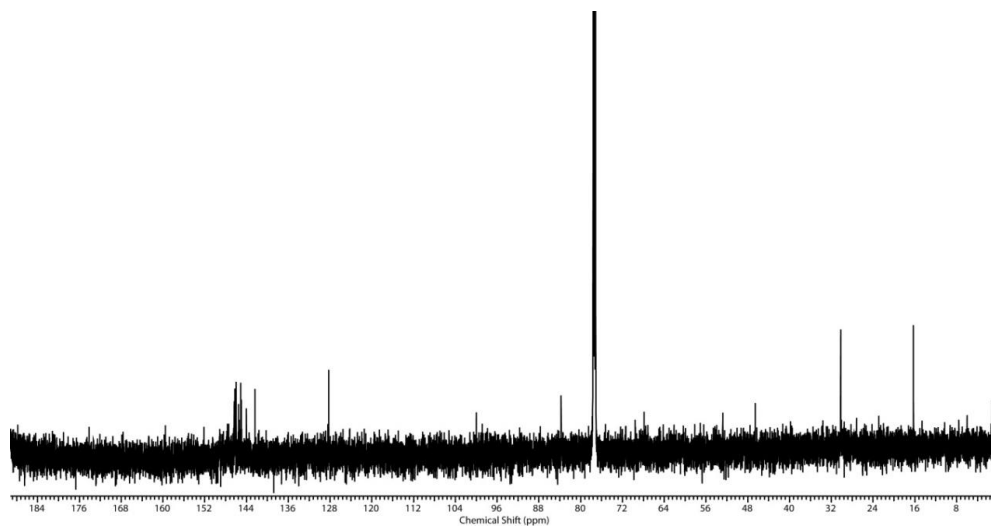


Figure C3. $^{13}\text{C-NMR}$ (150 MHz; $\text{CDCl}_3/\text{CS}_2$ (3/7), 298 K) Compound **1**: the resolution of the spectrum was not satisfactory due to the low solubility of compound **1**.

MALDI-TOF and NMR spectra for Compound 2

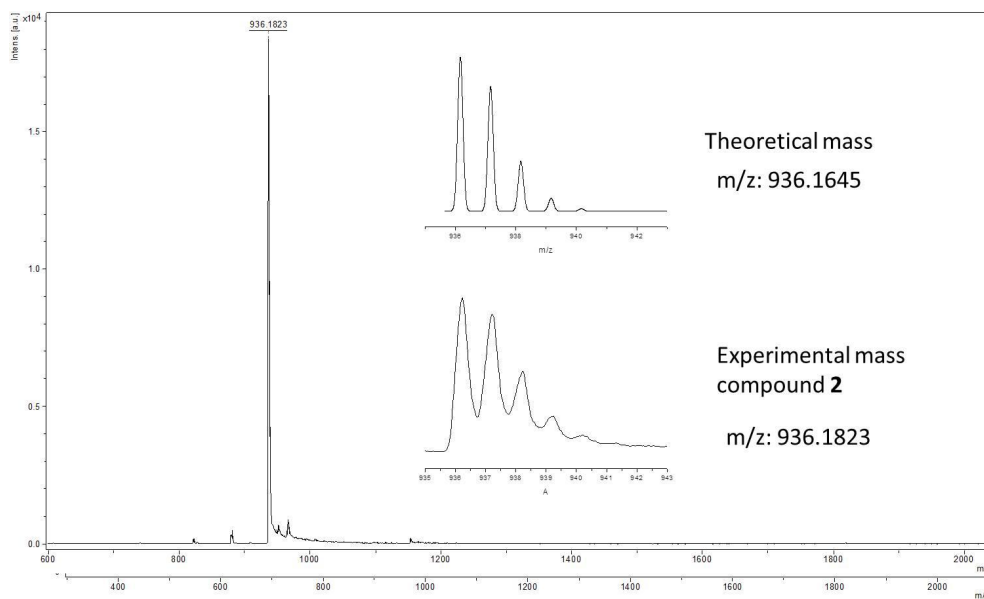


Figure C4. MALDI-TOF spectrum of compound 2.

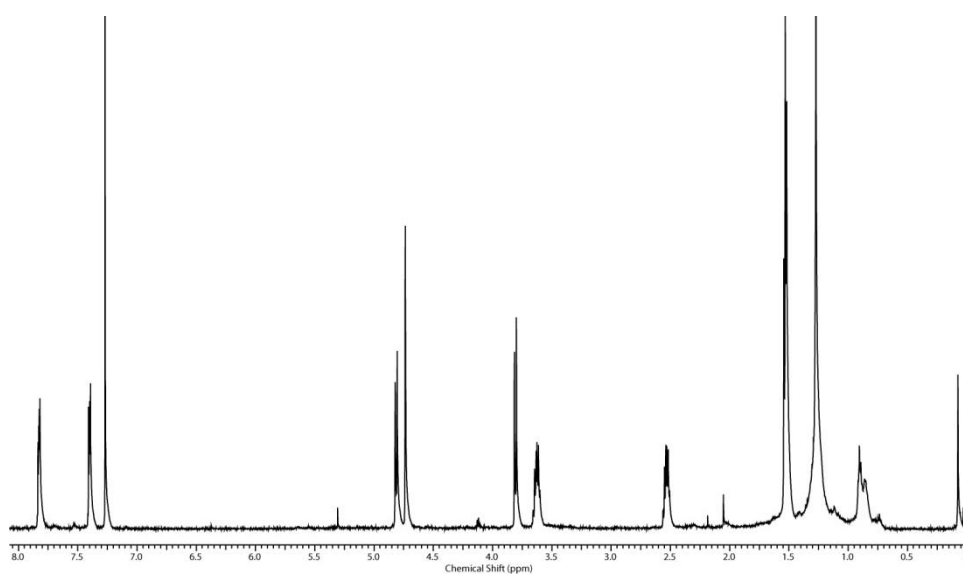


Figure C5. ¹H-NMR (600 MHz; CDCl₃/CS₂ (8/2), 298 K); Compound 2: δ 7.82 (m, 1H_A), 7.40 (m, 1H_A), 4.73 (s, 1H, N-CH), 4.81 (d, 1H, N-CH₂-C₆₀, J=13.06 Hz), 3.81 (d, 1H, N-CH₂-C₆₀, J=13.06 Hz), 3.63 (m, 1H, N-CH₂-CH₃), 2.53 (m, 1H, N-CH₂-CH₃), 1.52 (m, 3H, CH₃) ppm.

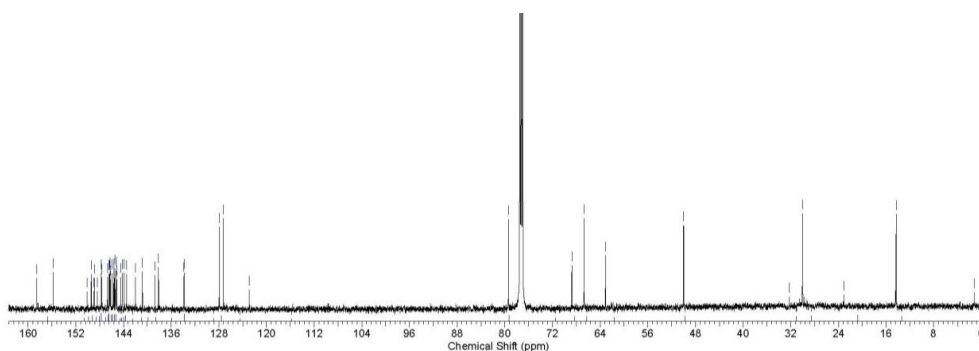


Figure C6. ^{13}C -NMR (150 MHz; $\text{CDCl}_3/\text{CS}_2$ (8/2), 298 K); Compound **2**: δ 158.54, 155.75, 150.11, 149.42, 148.91, 147.74, 147.65, 146.69, 146.44, 146.35, 146.27, 146.18, 145.94, 145.65, 145.55, 145.40, 145.20, 145.11, 144.42, 144.21, 143.88, 143.49, 141.96, 140.80, 138.71, 138.12, 133.87, 133.77, 127.92, 127.22, 122.88, 79.39, 68.76, 66.68, 63.07, 49.98, 14.33 ppm.

MALDI-TOF and NMR spectra for Compound **3**

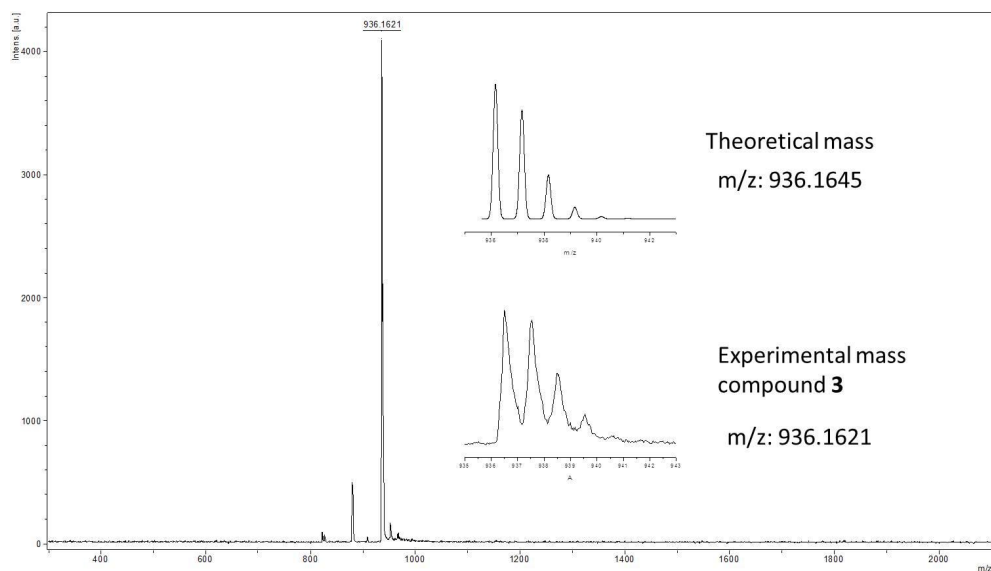


Figure C7. MALDI TOF spectrum of compound **3**.

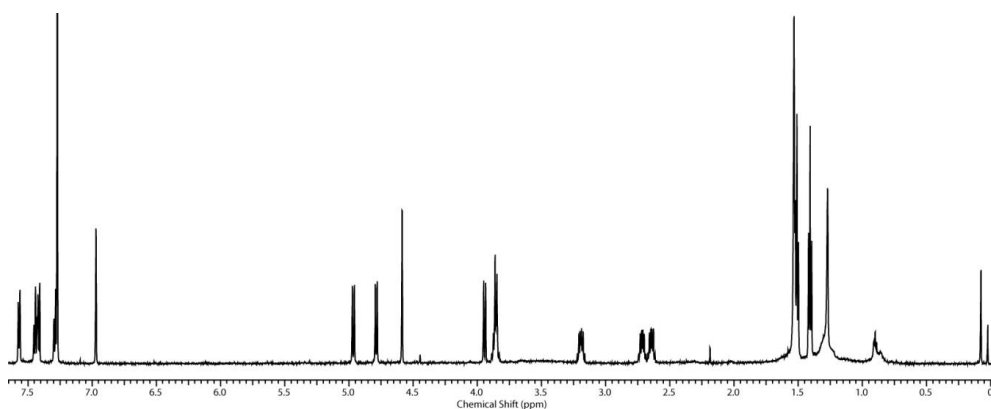


Figure C8. ¹H-NMR (600 MHz; CDCl₃/CS₂ (7/3), 298 K); Compound **3**: δ 7.57 (d, 1H_{Ar}, J=7.56 Hz), 7.45 (d, 1H_{Ar}, J=7.56 Hz), 7.42 (d, 1H_{Ar}, J=7.56 Hz), 7.29 (d, 1H_{Ar}, J=7.56 Hz), 6.97 (s, 1H, N-CH), 4.97 (d, 1H, N-CH₂-C₆₀, J=9.62 Hz), 4.78 (d, 1H, N-CH₂-C₆₀, J=8.64 Hz), 4.58 (s, 1H, N-CH), 3.94 (d, 1H, N-CH₂-C₆₀, J=9.62 Hz), 9.85 (d, 1H, N-CH₂-C₆₀, J=8.64 Hz), 3.86 (m, 1H, N-CH₂-CH₃), 3.19 (m, 1H, N-CH₂-CH₃), 2.71 (m, 1H, N-CH₂-CH₃), 2.64 (m, 1H, N-CH₂-CH₃), 1.51 (m, 3H, CH₃, J=7.57 Hz), 1.41 (m, 3H, CH₃, J=6.87 Hz) ppm.

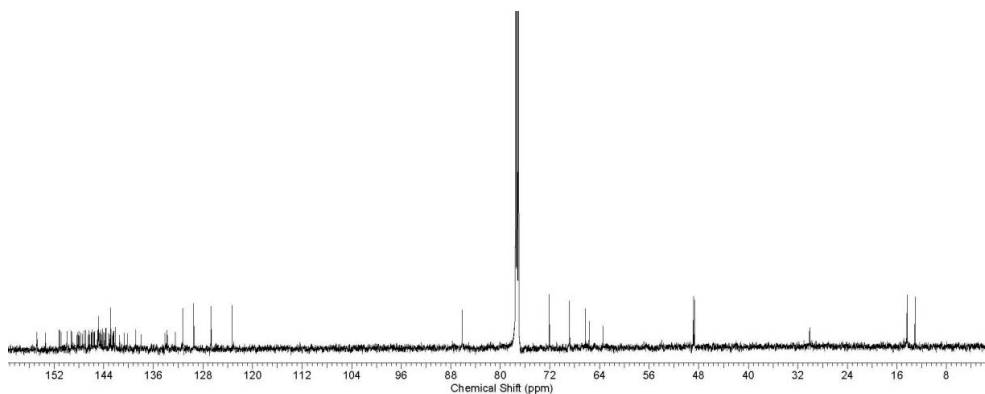


Figure C9. ¹³C-NMR (150 MHz; CDCl₃/CS₂ (7/3), 298 K); Compound **3**: δ 151.16, 150.91, 149.93, 149.30, 149.11, 148.38, 148.26, 148.07, 147.98, 147.72, 147.45, 147.14, 146.92, 146.47, 146.39, 146.29, 145.99, 145.89, 145.62, 145.54, 145.48, 145.03, 144.97, 144.84, 144.79, 144.55, 144.39, 144.21, 143.99, 143.84, 143.66, 143.19, 143.03, 142.92, 142.84, 142.58, 142.49, 142.38, 142.13, 141.43, 140.65, 140.24, 138.85, 137.97, 134.12, 133.81, 133.76, 132.46, 132.26, 129.47, 126.70, 123.26, 86.18, 72.11, 72.04, 68.87, 68.81, 66.26, 65.70, 63.42, 48.84, 48.66 ppm.

UV-vis Spectra

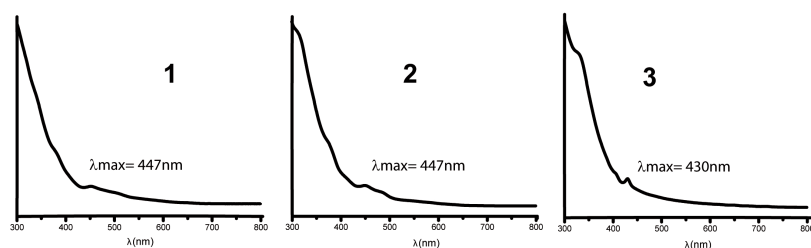


Figure C10. UV-vis spectra of compounds **1**, **2** and **3** in toluene.

Cyclic voltammetry

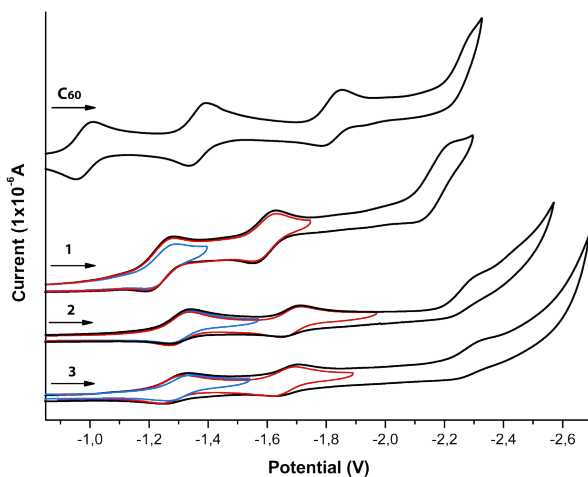


Figure C11. Cyclic voltammetry of C_{60} and compounds **1**, **2** and **3** (dichloromethane containing 0.1 M $n\text{-Bu}_4\text{NPF}_6$; using the redox couple Fc/Fc^+ as internal reference).

Electrochemistry

Table C1. Redox Potentials (V)^a of **1**, **2**, **3** and C_{60}

	C_{60}	Isomer 1	Isomer 2	Isomer 3
$E^{0/-}$	-0.977	-1.218	-1.282	-1.224
$E^{-/2}$	-1.369	-1.574	-1.658	-1.608
$E^{-2/-3}$	-1.817	-2.158	-2.197	-2.222
$E^{-3/-4}$	-2.253	-	-	-

^a Values obtained by SWV in V vs Fc/Fc^+ Correction with Fc .

Crystallographic Data

SCXRD was obtained at 100 K on a APEX CCD Bruker diffractometer, the sample was fixed on a fiber glass with paratone oil. The data refinement and solution of the structure was done in the suite APEX2.^[1]

Crystal Data **1**: C_{75.5}H₂₀N₂S₃, Fw=1051.11, Monoclinic P2₁/c, a=16.77(4) Å, b=10.12(2) Å, c=24.23(5) Å, β=100.13(4)°, V=4050(16) Å³, Z=4, R1=0.1812 [1377 ref, I>2σ(I)], wR2=0.4186 [all 6904 data]. 349 parameters, 0 restraints.

Crystal Data **2**: C₇₅H₂₀N₂S₂, Fw=1013.05, Orthorhombic Pnmn, a=13.975(2) Å, b=22.943(3) Å, c=13.824(2) Å, V=4432.2(12) Å³, Z=4, R1=0.0590 [2506 ref, I>2σ(I)], wR2=0.1812 [all 4050 data]. 368 parameters, 0 restraints.

The crystal packing of **1** shows that each fullerene interacts with two other fullerenes through C⋯C interactions [3.315 and 3.367 Å] (Figure C16a). In the case of **2**, each fullerene interacts with five other fullerenes through C⋯C interactions [3.208–3.385 Å] (Figure C16b). A particularly interesting motif is observed in the packing of **2**, where two phenyl groups from adjacent molecules show π⋯π interactions [3.853 Å] (Figure 6.12b). Based on the X-ray data it is possible to assign the stereochemistry (summarized in Scheme 6.1) for the pure bisadducts **1** and **2** (*cis*-2).

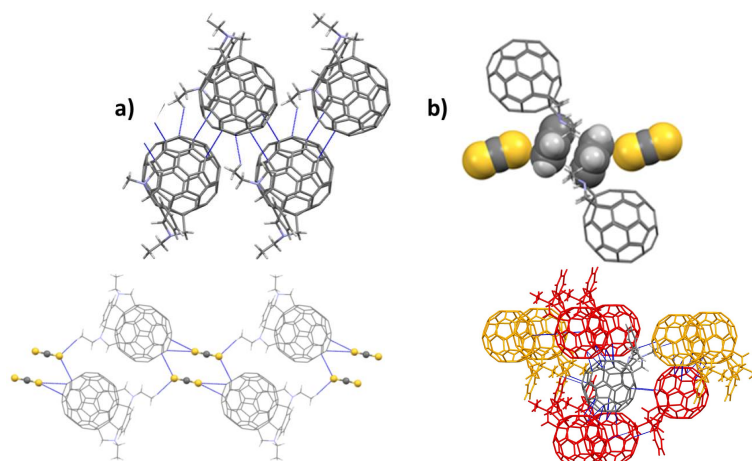


Figure 6.12. a) Short contacts formed by a second CS₂ molecule in the crystal structure of **1**. b) Parallel orientation of the phenylene groups in compound **2**. c) Crystal packing of compound **1**. The short contacts are shown: H⋯π [2.793 Å], π⋯π [3.315 and 3.367 Å]. The view is through the c axis with the b axis horizontal. d) Environment of each fullerene motif in the crystal packing of compound **2**. The fullerenes forming C⋯C interactions are in red color, while the yellow ones correspond to those interacting through H⋯C contacts.

- [1] a) APEX2 v2010.7-0. , Bruker AXS, (2010); b) Platon. A. I. Spek, Utrecht University, Utrecht, The Netherlands (2011).

6.3.2. Thermodynamic and kinetic aspects

Table C2. Conformation of the different products of the bis-Prato reaction. "N-Endo" and "N-exo" labels are referred to N, according to Figure 6.2; "axial" and "equatorial" (or "eq.") are related to the pyrrolidine conformation. In parenthesis, relative energies in kcal·mol⁻¹, computed in the gas phase (BP86-D/TZP).

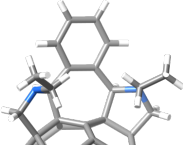
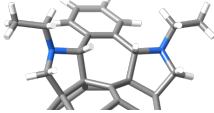
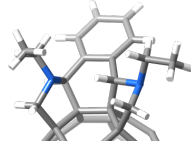
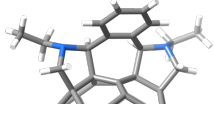
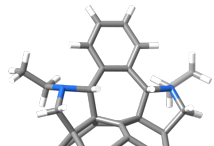
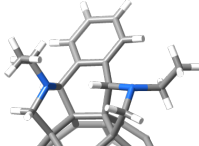
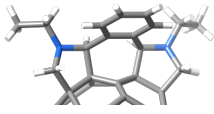
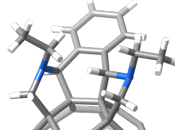
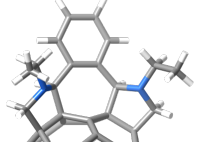
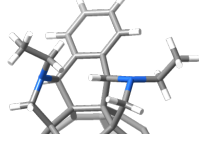
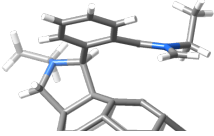
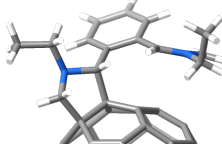
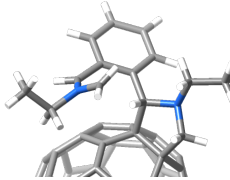
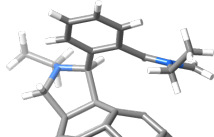
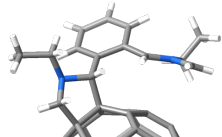
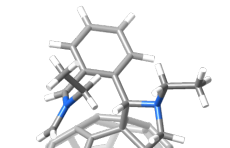
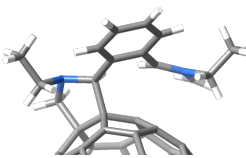
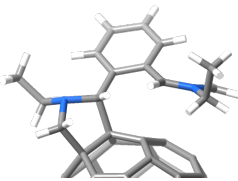
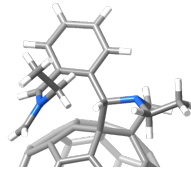
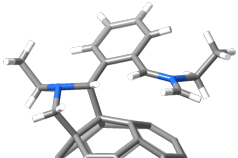
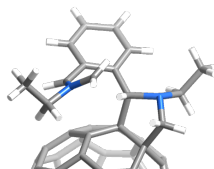
1	2	3
 N-endo axial (7.2)	 N-exo equatorial (4.8)	 N-endo eq./N-exo eq. (0.0)
 N-exo axial (7.3)	 N-exo axial (10.5)	 N-endo eq./N-exo axial (1.1)
 N-exo equatorial (13.9)	N-endo leads to N-exo	 N-endo axial./N-exo eq. (7.1)
 N-endo equatorial (17.2)		 N-endo axial/N-exo axial (8.9)
		N-exo leads to N-endo

Table C3. Relative energies (in kcal·mol⁻¹) of the different isomers for the bis-Prato reaction in C₆₀ using several computational methods, in the gas phase.

Isomer	Opt	Opt	SP ^b	Opt	SP ^c	SP ^c	Opt	Opt
	AM1 ^a	BP86 TZP	KT2 ET-pVQZ	BP86-D TZP	B3LYP-D TZP	PBE-D TZP	PBE-D TZP	B3LYP-D def2-TZVP ^d
3	9.5	0.0	0.0	0.0	0.0	0.0	0.0	
2	2.6	2.2	2.6	4.8	2.6	2.5	2.8	0.0
1	0.0	6.3		7.2	6.6	5.9	6.2	4.2

^a Computed with GAUSSIAN-09 program.^b From the optimized geometry at the BP86/TZP level.^c From the optimized geometry of BP86-D/TZP.^d Computed using TURBOMOLE program.

Table C4. Conformation of the different intermediates of the Prato bis-(addition). "N-Endo" and "N-exo" labels are referred to N-pyrrolidine, according to Figure 6.2; "axial" and "equatorial" (or "eq.") are related to the pyrrolidine conformation; "endo" and "back" labels are referred to the ethylene of the ylide conformation, according to Figure 6.2. In parenthesis, relative energies in kcal·mol⁻¹ computed in the gas phase.

Int-1	Int-2	Int-3
 N-exo axial/exo (3.8)	 N-exo equatorial/endo (0.0)	 N-exo equatorial/ exo (1.8)
 N-exo axial/endo (7.3)	 N-exo equatorial/exo (2.2)	 N-exo equatorial/ endo (4.8)
 N-endo axial/endo (10.3) Identical to <i>int-2</i> N-exo axial/exo	 N-exo axial/ endo (8.8)	 N-endo axial/ endo (10.9)
	 N-exo axial/ exo (10.6)	 N-exo axial/ exo (10.9)

6.4. Isomerization from 1 to 2

6.4.1. Mechanism 1: both H flipping simultaneously

The two H linked to the stereogenic centers rotate to the other side of the benzyl simultaneously to give rise to bisadduct **2**. Only the two internal bonds of the bisaddition should be broken; a schematic path is represented in Figure C13. To study it, we have calculated specific points of the reaction path, to have a general idea of the amount of energy required. The results are plotted in Figure C14, together with the geometric representation of the final structure of each point. We have chosen isomer **2** as the starting geometry. As reaction coordinate we have chosen the dihedral angle between the flipping H and the plane formed by the two stereogenic centers and the cage (remarked in red in the plot). These results showed that almost 100 kcal·mol⁻¹ are required to turn to reach half of the way, *i. e.*, until both H atoms stay perpendicular to the fullerene surface. We can also perceive that the benzyl group is spontaneously bent to the other side of the molecule.

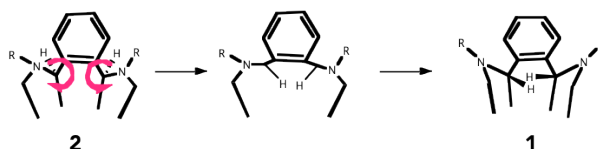


Figure C13. Schematic mechanism of the simultaneous flip of the H atoms.

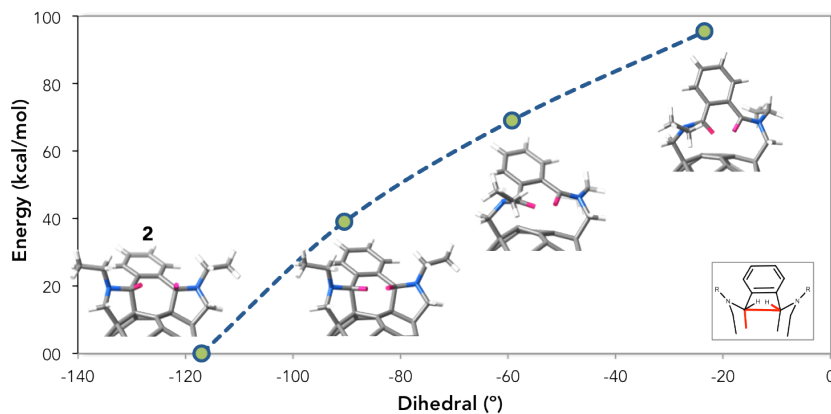


Figure C14. Plot of the first proposed mechanism for the isomerization from **1** to **2**. The flipping H are colored in pink). The initial point was bisadduct **2**. The x axis correspond to the torsion angle of the H atoms, highlighted in red in the inset.

6.4.2. Mechanism 2: One-by-one H flipping

This is a modified version of the previous mechanism. Here, the two H linked to the stereogenic centers flip both but not the same time. Again, only the two internal bonds of the bisaddition should be broken. Figure C15 shows a schematic representation of this one-by-one H flipping. We have performed a scan of the two flipping processes, and the most significant points are plotted in Figure C16, together with the geometric representation of the final structure of each point. The plot must read from right to left, being the orange points the ones corresponding to the first flip and the green points to the second one. As reaction coordinate we have chosen the dihedral angle between the flipping H and the plane formed by the two stereogenic centers and the cage (remarked in red in the plot). According to the results, a barrier of 60 kcal·mol⁻¹ is required for each flipping. The benzyl group is spontaneously bent to the other side of the molecule with the rotation. Furthermore, a minimum is found, which corresponds to the *trans* isomer of the *cis*-2 bisaddition; this isomer is never observed in the experiments.

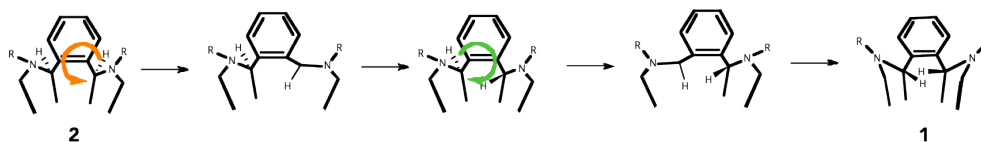


Figure C15. Schematic mechanism of the one-by-one flip of the H atoms.

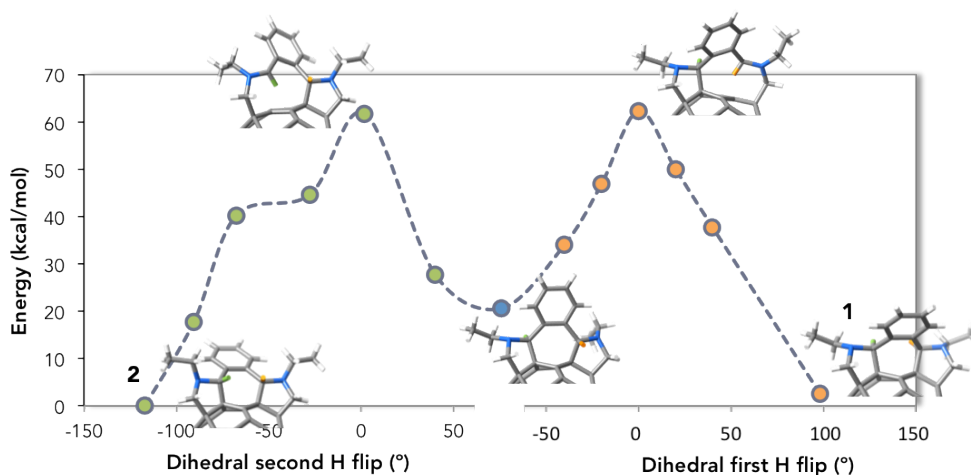


Figure C16. Plot of the second path studied for the isomerization from **1** to **2**. According to it, the isomerization takes place by the flip of one H (in pink) and then the other one. The horizontal axis correspond to the torsion angle of the H, which is highlighted in red at

6.4.3. Mechanism 3: H flip via intermediates

A retro-1,3-dipolar-cycloaddition has been studied starting from bisadduct **1**. During the retrocycloaddition process **Int-1** is formed, and then it rearranges (orange in figures below) to give the *exo,endo* or *endo,exo cis-2* bisadduct (blue circle). Another retrocycloaddition process from *exo,endo* or *endo,exo cis-2* produces a new pyrrolidine-ylide species that after rearrangement and cycloaddition yield **Int-2** (green circle), which finally leads to compound **2**. This mechanism requires to overcome an energy barrier of about 6 kcal·mol⁻¹ higher with respect to the proposed mechanism described in Figure 6.14.

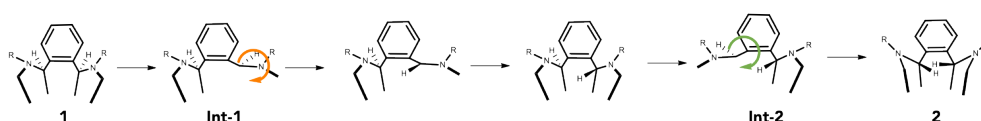


Figure C17. Schematic representation of the retro-1,3-dipolar-cycloaddition followed by flipping of the hydrogens.

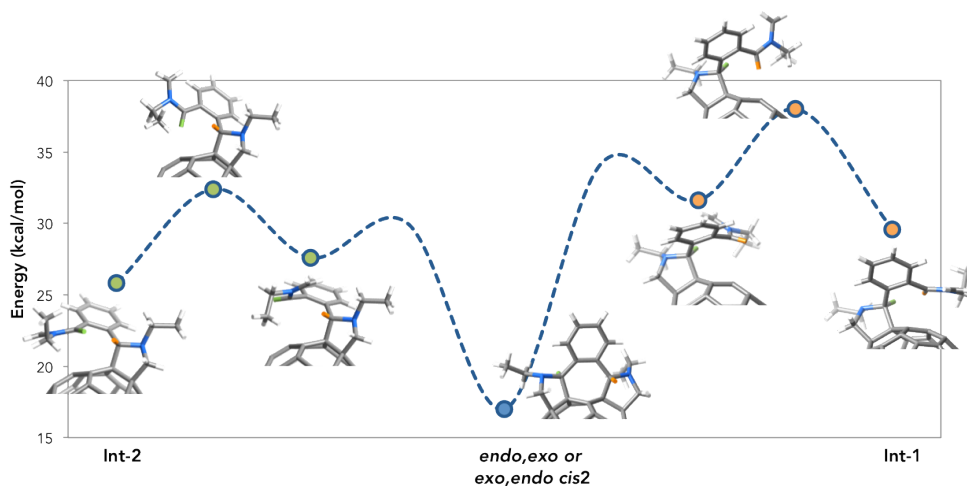


Figure C18. Energy profile of the retrocycloaddition followed by flipping of the hydrogen atoms.

Résumé

Publications

Related to this thesis

- [1]. **The maximum pentagon separation rule provides a guideline for the structures of endohedral metallofullerenes**
A. Rodríguez-Forteza, N. Alegret, A.L. Balch, J.M. Poblet. *Nature Chem.* (2010), 2, 955-961
- [2]. **Bingel-Hirsch reactions on non-IPR $Gd_3N@C_{2n}$ ($2n=82$ and 84)**
N. Alegret, M.N. Chaur, E. Santos, A. Rodríguez-Forteza, L. Echegoyen, J.M. Poblet. *J. Org. Chem.* (2010), 75, 8299-8302
- [3]. **Electronic Structure of IPR and non-IPR endohedral metallofullerenes: Connecting orbital and topological rules**
N. Alegret, M. Mulet-Gas, X. Aparicio-Anglès. A. Rodríguez-Forteza, J.M. Poblet. *C. R. Chimie* (2012), 15, 152-158
- [4]. **Bingel-Hirsch Addition on Endohedral Metallofullerenes: Kinetic Versus Thermodynamic Control**
N. Alegret, A. Rodríguez-Forteza, J.M. Poblet. *Chem. Eur. J.* (2013), 19, 5061-5069.

- [5]. **Bingel-Hirsch Addition on Non Isolated Pentagon Rule $Gd_3N@C_{2n}$ ($2n=82$ and 84) Metallofullerenes: Products Under Kinetic Control**
N. Alegret, P. Salvadó, A. Rodríguez-Forteza, J.M. Poblet. *J. Org. Chem.* (2013), 78, 9986-9990.
- [6]. **Unprecedented Isomerism in cis-2 Bispyrrolidino[60]Fullerene Diastereomers**
M. Izquierdo, M.R. Cerón, N. Alegret, A.J. Metta-Magaña, A. Rodríguez-Forteza, J.M. Poblet, L. Echegoyen. *Angew. Chem. Int. Ed.* (2013), 52, 12928-12931.
- [7]. **Endohedral Fullerenes. In "Comprehensive Inorganic Chemistry II"**
A. Rodríguez-Forteza, N. Alegret, J.M. Poblet. Kenneth Poeppelmeier and Jan Reedjik Eds; Elsevier: Oxford, UK (2013); 9, 907-924.
- [8]. **Sinfonía de Fullerenos: la magia de la encapsulación**
N. Alegret, A. Rodríguez-Forteza, J.M. Poblet. *Anales de Química*. (Submitted)
- [9]. **Looking for the identity of the first non-IPR $Sc_2@C_{66}$**
N. Alegret, A. Rodríguez-Forteza, J.M. Poblet. (To be submitted)

Not related to this thesis

- [10]. **Disruption of Double Stranded DNA Molecules in Presence of Carbon Nanotubes: Relevance of the Nucleotide Number**
N. Alegret, E. Santos, A. Rodríguez-Forteza, F.X. Rius, J.M. Poblet. *Chem. Phys. Lett.* (2012), 525-526, 120-124
- [11]. **Endohedral Metallofullerenes Containing Lanthanides: A Robust Yet Simple Computational Approach**
X. Aparicio-Anglès, N. Alegret, A. Clotet, A. Rodríguez-Forteza, J.M. Poblet. *J. Phys. Chem. C* (2013), 117, 12916-12921.

Posters and Oral Presentations

Solving the cage dilemma in Sc₂@C₆₆

43rd IUPAC World Chemistry Congress • July 30th – August 7th 2011

Colegio de Químicos de Puerto Rico and IUPAC • San Juan • Puerto Rico

Participation type: poster presentation

Maximum Pentagon Separation Rule (MSPR). A guide for the characterization of endohedral metallofullerenes

Setena Trobada de Joves Investigadors dels Països Catalans • February 2012

Junta de la Societat Catalana de Química • Mallorca • Spain

Participation type: oral presentation

Path of the Bingel-Hirsch Reaction on IPR and non-IPR endohedral metallofullerenes

8th Congress on Electronic Structure: Principles and Applications (ESPA) • June 26th – 29th 2012

University of Barcelona • Barcelona • Spain

Participation type: poster presentation

Awards: Best poster in the topic of Chemical Reactivity

Computations on Endohedral Fullerenes

Southern Catalonia Nobel Campus • July 1st – 4th 2012

CEICS-URV • Port Aventura Convention Center • Tarragona • Spain

Participation type: oral and poster presentation

Collaborations



Prof. Luis Echegoyen
University of Texas at El Paso (El Paso)



Prof. Alan L. Balch
University of California (Davis)

Research Abroad



Projects	Synthesis, characterization and functionalization of endohedral and empty fullerenes. Application in solar cell technology.
Supervisor	Prof. Luis Echegoyen
Center	University of Texas at El Paso
Period	January – April 2013 March – June 2014

Notes and Comments

